The Effect Of Flow Structure On The Combustion And Heat Transfer In A Scramjet Combustor

by

Scott David Stouffer

Dissertation Submitted to the Faculty of
Virginia Polytechnic Institute and State University
in Partial fulfillment of the requirements for the degree of

DOCTOR OF PHILOSOPHY

in

Mechanical Engineering

APPROVED:

Dr. Uri Vandsburger, Chairman

Dr. W. F. O'Brien

Dr. J. A. Schetz

Dr. C. L. Dancey

Dr. G. B. Northam

July, 1995
Blacksburg, Virginia

The Effect Of Flow Structure On The Combustion And Heat Transfer In A Scramjet Combustor

by

Scott David Stouffer

Committee Chair: Uri Vandsburger

(Abstract)

A combined experimental and computational study of two different swept-ramp injector configurations was conducted in a scramjet combustor. The object of the study was to determine the effect of mixing augmentation, resulting from the streamwise vortices generated by injector ramps, on scramjet engine operation characteristics, combustion, and heat transfer. Hydrogen was injected from the base of swept compression and expansion ramps in direct-connect tests that simulated flight at Mach 6.6.

The experimental effort included combustor wall pressure and heat flux measurements with Gardon gages and surface thermocouples for the two injector configurations. A novel, side-view laser light sheet technique was developed to obtain images of the combustion product distribution at selected planes in the closed combustor duct downstream of the swept-compression ramp injectors. In addition, a miniature refractory probe was developed to determine the pitot pressure at the exit of the combustor. Three-dimensional computations were made for mixing and reacting cases of the swept-compression ramp injector using the SPARK computer code. The flow field calculations were compared to the experimental measurements.

The experimental tests demonstrated combustor performance with parallel injection comparable to that reported using normal injection. This unusually rapid parallel jet mixing and combustion was obtained using swept ramp injectors with near-parallel injection. The experiments and calculations showed that the injectors were effective in promoting lateral spreading of the fuel jets. The incomplete penetration of the fuel jets in the

direction normal to the walls was a major limiting factor in the amount of mixing that could occur for both configurations. In addition, the proximity of the burning shear layer to the injector wall led to increased heat transfer on the injector wall. The effect of the flow structure on the heat flux was not principally through a large increase in the film coefficient caused by the vortical flow. Instead, it was due to the proximity of the reacting fuel jet to the wall, which led to high adiabatic wall temperatures near the wall.

Acknowledgments

First I would like to thank Dr. G. Burton Northam of NASA Langley for providing me with the opportunity and funding to conduct this research. I also want to thank my advisor Uri Vandsburger along with rest of my committee: Professors Clint L. Dancey, Walter F. O'Brien, and Joseph A. Schetz.

I wish to thank Dean Eklund for all of his help and guidence in the numerical computions for this study. I wish to thank Ned Baker of Lockheed for his help and advice on the experimental phase of this work.

I wish to thank Diego Capriotti, Mike Smith, Glenn Diskin, Earl Andrews, Troy Middleton, and Olin Jarret, of the Hypersonic Airbreathing Propulsion Branch for all of their help and advice while I was at NASA.

I wish to thank my fellow graduate students: Bon Calayag, Karl Nelson, Donna Kraus, and Brian Levey, for all of their help and emotional support over the past four years at Langley.

I am deeply grateful for the technical support provided by Barry Lawhorne, Dennis Williams, Richard White, Lois White, and Clint Reese of the operations support division.

I wish to thank John Franke, Stephen Jones, and David Rhodes of NASA Langley for their help with the laser scanners used in the Mie scattering experiment.

I appreciate the useful conversations with Dr. Tom Diller of VPI on the application of Gardon gages.

A special thanks goes to my parents, Dale and Jean, and my sisters Jamie and Suzanne, who have given me love and emotional support through my life.

My deepest thanks go to my wife Susan for all of the sacrifices she has made in the last year.

Table of Contents

List of Illustrations

List of Tables

Nomenclature

a = Speed of sound
b = Thickness of Gardon gage foil
c = Specific heat
h = Enthalpy
k = Thermal conductivity
q = Heat flux
r = Radial distance
r = Velocity ratio (U_1/U_2)
s = Entropy
t = Time
w = combustor width
x = Axial distance
y = Spanwise distance
z = Transverse distance

EMF = Electromotive Force
F = Pressure integral
G = Gap Length = twice the combustor inlet height
M = Mach number
Mc = Convective Mach Number
R = Foil radius
P = Pressure
S = Gage sensitivity
T = Temperature
U = Axial Velocity
U_c = Convective Velocity
U1 =Velocity of the high speed stream
U2 = Velocity of the low speed stream
V = Velocity
Y = Mole Fraction

Greek

α = ramp angle

β = Lumped thermal parameter $= \left(\beta = \left(\rho c_p k \right)^{1/2} \right)$

δ = Shear layer thickness

η = Efficiency

ρ = Density

ϕ = Fuel-air equivalence ratio

θ = Combustor divergence angle

ω = vorticity

Δ = change

Subscripts

c = Compression

c = Combustion

c = Convective

c = Center

e = Expansion

e = Edge

f = Fuel on

nf = No fuel

r = Reacted

T= Total or stagnation conditions

Chapter 1

Introduction and Background

Ever since the Wright brother's first flight, mankind has desired to fly higher and faster. The pace of high speed aircraft development is presently limited by the available propulsion systems. Rockets can be used to propel an aircraft from rest to any speed but have the disadvantage of requiring that both fuel and oxygen be carried onboard the vehicle. For this reason, air breathing propulsion is preferred for flight within the atmosphere. Turbojet and turbofan engines are commonly used at speeds up to Mach 3.5. At higher speeds the rotating compressor can be eliminated and the inlet can be used to compress the air before it enters the combustor, as in the ramjet engine. In the conventional ramjet engine, air is diffused from supersonic to subsonic speeds in the inlet, so that the combustor flow is subsonic. The temperature and pressure in the conventional subsonic ramjet combustor increase dramatically as the vehicle speed increases, requiring stronger, and therefore heavier, engine structures. In addition, the stagnation pressure losses across the normal shock, as well as the dissociation losses caused by the high temperatures, increase dramatically as the Mach number increases. Therefore, at speeds greater than Mach 5-6, the supersonic combustion ramjet (SCRAMJET) engine, in which supersonic air flow is maintained throughout the entire engine, is more promising than the conventional ramjet.

The design of a supersonic combustor is more challenging than conventional subsonic combustors because the high velocities limit the residence time in the combustor. During this time the fuel must mix and react with the high velocity air stream. From a practical engine design standpoint, it is desirable to shorten the combustor length in order to reduce engine weight and internal drag. Therefore, methods to enhance the fuel/air mixing rates are crucial for the design of the combustor.

In engine cycles based on subsonic combustion, the design goal of 99-100% combustion efficiency with little total pressure loss is possible due to

the low air velocity in the engine. In the scramjet cycle the tradeoff between energy release in the combustor and total pressure losses must be considered. Because of the losses that must occur to achieve complete combustion, the optimal combustion efficiency, in terms of overall vehicle performance, may be less than 100%.[1] Unavoidable total pressure losses occur due to the heat release in the supersonic air stream (Rayleigh losses) and the molecular level mixing of the fuel and air. Other losses, such as skin friction and shock losses, must be minimized. Because of the supersonic velocity in the combustor, the effect that the injection scheme has on the stagnation pressure losses, through shock waves, is important.

Another problem in practical scramjet combustor design is that of the wall heat transfer rates. Even at low hypersonic speeds (Mach 6-7) the stagnation temperature of the air entering the combustor is higher than the melting point of most metals. Fuel reacts with the high enthalpy air in the combustor further increasing its temperature, and the potential heat transfer to the combustor walls. For this reason, both the airframe and engine of a scramjet-powered aircraft will be actively cooled.

Hydrogen is preferred over hydrocarbon fuels for a reusable, high-speed vehicle design because its high specific heat, and large working temperature range, allows regenerative cooling of the airframe and engine. However, because of its low density, hydrogen requires more storage volume than hydrocarbons, which translates into higher vehicle drag and structural weight. For this reason other fuels, such as higher density slush hydrogen (50 % liquid hydrogen/50% solid hydrogen), are being considered.[2] Slush hydrogen also allows more heat to be absorbed from the structure since the solid portion of the fuel will undergo two phase changes prior to gaseous injection.

In addition to increasing the net amount of energy released by combustion, using the hydrogen to regeneratively cool the structure allows the thrust to be augmented if the regeneratively-heated fuel is injected parallel to the main flow in the combustor. At high Mach numbers, thrust augmentation by parallel injection of the fuel can be used to provide a significant fraction of the total thrust.[3] Parallel fuel injection, however, has

the disadvantage of requiring longer combustor lengths for mixing and combustion than perpendicular fuel injection. The problem of mixing in parallel compressible flows is discussed in the following section.

1.1 Mixing In Compressible Shear Layers

A schematic of a planar free shear layer is shown in Fig. 1.1. The effect of velocity ratio, $r = u_2 / u_1, (u_1 > u_2)$ on the growth of planar shear layers was studied by Sabin.[4] The following expression for the growth of shear layers with equal density ratios was proposed:

$$\frac{\delta}{x} \approx C_\delta \frac{(1-r)}{(1+r)} = C_\delta \frac{\Delta u}{(u_1+u_2)} \qquad (1\text{-}1)$$

where δ is the shear layer thickness, C_δ is a constant that depends on the initial conditions and $\Delta u = u_1 - u_2$. As Δu increases from 0 to u_1, the spatial shear layer growth rate, δ / x, increases.

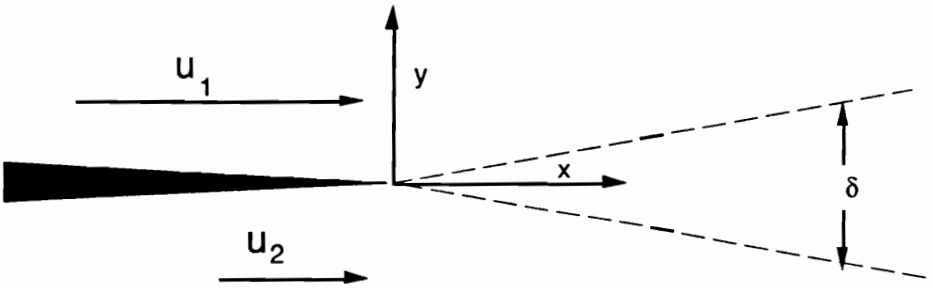

Figure 1.1 Schematic of Free Shear Layer.

Early experiments with supersonic jets showed that the spreading angle of the mixing layer decreased as the Mach number of the jet increased. This decrease in shear layer thickness was initially attributed to the effect of density ratio. Brown and Roshko[5] studied the effect of density ratio on a planar mixing layer between nitrogen and hydrogen. Nitrogen and helium were used to create large density ratios, which were typical of those observed in high speed mixing experiments. The effect of the density ratio on the shear layer spreading rate, due to the density ratio alone, was found to be much less than the effect that was due to the increase of the Mach number in previous studies. Therefore, it was concluded that the decrease in the shear

layer spreading rate was due to compressibility rather than the effect of density ratio.

To address compressibility effects, Bogdanoff[6] proposed that the shear layer growth should be correlated with a reference Mach number, M^+, in a coordinate system that travels at the speed of the large scale structures in the flow. Papamoschou and Roshko[7] expanded on the work of Bogdanoff and proposed the convective Mach number to correlate shear layer growth in compressible shear layers. The convective Mach number is defined as the Mach number in a coordinate system that moves at the velocity of the large scale structures of the mixing layer. In shear layers with two different gases there are two different convective Mach numbers which are defined by the following:

$$M_{c1} = (u_1 - u_c) / a_1 \qquad (1\text{-}2)$$

$$M_{c2} = (u_c - u_2) / a_2 \qquad (1\text{-}3)$$

where u_c is the velocity of the convecting structures of the flow and a_1 and a_2 are the sound speeds in gases 1, and 2, respectively. As the convective Mach number, M_{c1}, increased from 0 to 0.8, the ratio of the shear layer growth rate to that for an incompressible shear layer at the same velocity and density ratio decreased to $\approx$ 1/5. At convective Mach numbers, $M_{c1} > 0.8$, the ratio of the compressible shear layer thickness to the incompressible shear layer thickness was approximately constant. Early investigations averaged the two computed values of convective Mach number. Later, it was shown by direct measurement that the convective velocity tends toward the low velocity stream in a shear layer between two supersonic streams[8], resulting in large differences between the two convective Mach numbers. However, the same conclusion still holds; for shear layers with the same density and velocity ratio, the spreading rate of the shear layer decreases with an increase in the flow velocity.

Although compressible axisymmetric mixing layers have not been studied as much as planar mixing layers, the same type of decrease in shear layer thickness with convective Mach number has also been observed.[9-12]

The reasons for the low growth rate and subsequent decrease in the overall mixing rate associated with compressible shear layers are not yet fully understood. However, several theories have been presented.

Papamoschou[13] examined the propagation of sound waves within the shear layer. In that study it was shown that increased Mach number hinders communication between parts of the flow. The inhibited acoustic interaction was proposed as the fundamental explanation for the increased stability of high speed shear layers. Nixon, et al.[14] proposed that the decreased mixing rate is caused by the lower flow energy that is available for entrainment because of the compression work that occurs during deflection of the free stream fluid into the shear layer. Hussanni et al.[15] proposed that the formation of transient eddy shocklets could distort the eddy, decreasing its length scale.

1.2 The Effect of Combustion on Mixing

Before continuing, it is useful to consider the relationship of supersonic mixing to supersonic combustion, and the effect that combustion has on fuel/air mixing. Most of the studies that were discussed in the previous section were performed with cold (non-reacting) flow. Mixing studies allow examination of complex flowfields without the added complications of chemistry, and heat release. Mixing is important for the obvious reason that combustion cannot occur unless fuel and oxidizer are mixed. A further complication in reacting flows is the effect of the heat release on the flowfield and thus the fuel-air mixing.

There are several ways that combustion could alter the mixing rate. One effect is that combustion and the resultant pressure rise can change the flowfield near the injectors. For example, a fuel injector that is slightly underexpanded could become overexpanded as a result of the combustion-induced pressure rise near the injector.

The entrainment rates can also be changed as a result of heat release. McMurtry et al.[21] performed direct numerical simulations of a reacting two-dimensional flow. The growth rate of large scale structures in a shear layer was found to decrease with moderate levels of heat release. Hermonson and Dimotakis[22] conducted an experimental study of shear layer growth in a reacting shear layer and showed that the thickness of the shear layer decreased slightly with increasing heat release. The fact that the shear layer growth rate did not increase implies that the entrainment rate also decreases

due to the decreased density at the fuel/air interface. Therefore, less fuel/air mixing occurs in a reacting shear layer than in a nonreacting layer.

Another effect of combustion is that the vorticity at the center of the vortex is reduced because of the expansion of the fluid due to the heat release, as discussed by McMurtry.[21] Note that many of the mixing enhancement strategies add streamwise vorticity to a flow in order to increase the mixing rates.

To overcome the difficulties associated with mixing in supersonic combustor flows, many strategies have been proposed and studied. Due to the large number of papers on supersonic mixing enhancement, a comprehensive survey is beyond the scope of this dissertation. Therefore, the following discussion is intended to show the general types of mixing enhancement techniques that have been proposed for use in supersonic combustors.

1.3 Fuel Injection and Mixing Enhancement Techniques

Much of the early work on scramjet fuel injection focused on normal injection[16-17] resulting in correlations for fuel mixing and penetration. In comparison to parallel injectors, normal injection offers relatively rapid mixing. However, none of the fuel momentum contributes to the thrust, and there are large total pressure losses associated with the shock system. In addition, when a fuel jet ignites near the injector, the heat transfer can be severe.

Film injectors, in which a near-tangential stream of fuel is injected from the wall have also been studied.[18-19] This configuration allows all of the fuel momentum to be contributed to the thrust with little total pressure loss. Also, in the case of a film injector that extends across the width of a combustor, a large fuel-air interface is provided which is desirable from the standpoint of mixing. The major disadvantage of film injectors is that the penetration is limited by shear layer mixing, which as previously discussed, is small for high flow velocities. The result of inhibited penetration is that the fuel will not mix and react with air in the center of the combustor. Therefore, although high mixing efficiencies can be achieved for low

equivalence ratios (due to the large fuel-air interface area) tangential injection is not effective at high equivalence ratios because mixing is penetration-limited. Also, heat release near the wall can lead to high wall heat transfer rates, which is a major disadvantage in practical combustors.

Thomas et al.[20] presented a review of the data base for mixing with transverse injectors, slot film injectors, and coaxial injectors. It was shown that the spacing of coaxial and transverse jets below a critical value could decrease the mixing rate. In addition, it was shown that when the maximum fuel concentration for all configurations was plotted on the same plot, the maximum fuel concentration decreased with a decay rate that was roughly proportional to $x^{-0.8}$.

The rest of this section contains a review of techniques to enhance the mixing of parallel flows. Most of the methods impart streamwise vorticity to the mixing region between the fuel and air. Streamwise vorticity enhances the mixing in parallel flows primarily by increasing the surface area of the fuel/air interface. In addition, recalling Crocco's theorem, the entropy increase and thus the decrease of total pressure can be related to the vorticity by the following relationship: $T\nabla s = \nabla h_T - U \times \omega$. For the case where the vorticity and velocity vectors are aligned, the last term is zero. Therefore, longitudinal vorticity is an efficient way of enhancing the large scale mixing.

The combination of normal and tangential injection was studied by King et al.[24] A nearly pressure-matched Mach 1.7 film injector was used as the tangential injector. A row of normal injectors was mounted 1/2 of the film injector height downstream of the film injector. The normal injectors were created from circular tubes that protruded through the film so that they were equal to the film injector height. Both sonic and supersonic (M =2.2) normal injectors were used. It was found that sonic normal injectors increased the total mixing layer thickness by up to 70 % over that for the slot injector alone.

Flush wall-mounted, angled fuel injectors have been studied by several investigators to obtain the advantages of both tangential and normal injectors. McClinton[25] studied sonic hydrogen injection at injection angles of 30° to 90° into a Mach 4 airstream. The ratio of jet total pressure to the

airstream total pressure was held constant. It was found that for lower injection angles, faster mixing and improved fuel penetration resulted. Also, the total pressure losses due to the shock system decreased as the injection angle decreased.

Mays et al.[26] extended the work of McClinton by studying pressure-matched and under-expanded helium injection from nozzles angled at 30° and 15° into a Mach 3 freestream. An increase in the injection angle was found to increase the mixing in the near field by increasing the penetration; however, mixing in the far field was not significantly affected. A fivefold increase in the jet exit pressure to the effective back pressure ratio was found to increase the rate of downstream mixing by 30 %.

Fuller et al.[27] studied the effect combining yaw and transverse injection angles in the mixing of flush-mounted helium jets with Mach 3 and Mach 6 airstreams. The addition of yaw angle significantly increased the fuel plume cross-sectional area over that for no yaw angle, while slightly decreasing the transverse penetration.

Cox et al.[28] expanded on the work of Mays et al. and Fuller et al. and studied a novel injector with nine separate injectors arranged in a 3x3 array. The first row of injectors was angled at 15° with respect to the main flow. The next two rows of injectors downstream were slanted at increasing angles transverse to the main flow in 15° increments. In addition, the outer two injectors in each of the two downstream rows were angled inward toward the centerline of the injector array. The purpose of the design was to produce large scale longitudinal vorticity and increase the fuel penetration from a flush wall injector, while avoiding the large pressure drag associated with devices which protrude into the flow, such as strut or ramp injectors. The yawed jets created vorticity, while the penetration of the fuel was improved due to the staged injection, similar to previous studies of staged normal injection.[23] Experiments with helium injection as well as CFD calculations showed that the large-scale vortical structures produced by the injection scheme were effective in enhancing the mixing..

Various non-circular injector configurations have also been studied, mainly in coaxial injector configurations. A major feature of such injectors is the phenomena of axis switching, in which the fuel jet spreads more in the minor axis plane flow than in the major axis plane. Eventually, the minor and major axis of the fuel jet switch. Axis switching has been observed in elliptical and rectangular jets by Gutmark et al.,[29] resulting in enhanced mixing rates for noncircular injectors as compared to the circular injectors. In addition to large scale structures, which are useful in spreading the fuel, small scale structures, which are useful for molecular level mixing, are generated at the corners. In reacting flows the small scale structures created at the corners can enhance flameholding. Other noncircular injector geometries such as triangular, and tapered (rectangular throat to round exit) injectors have also been studied by Gutmark et al.[30-31] and have shown increased mixing rates as compared to circular injectors.

Other groups have studied mixing enhancement due to the fuel injector geometry. Samimy et al.[32] used tabs at the exit of the nozzles to enhance the mixing of supersonic jets. In a study of mixing of an air jet into air they found that the use of small tabs (blockage area = 1.5 % per tab) increased the entrainment of ambient air into the jet. The use of one, two, and four tabs was examined at several streamwise positions using Mie-scattering. The flow visualization results suggested that each tab created two counter-rotating vortices. The use of two tabs mounted opposite of each other caused bifurcation of the jet, increasing the mass entrainment by 13 % more than that for a plain nozzle. Zaman[33] showed that the addition of tabs to circular nozzles could increase the entrainment by 20 % over that observed for plain rectangular nozzles. Also, flow visualization showed that the addition of tabs to noncircular injector nozzles could either enhance or prevent axis switching, depending on the location of the tabs.

Yu et al.[34] used five swept-ramps located around the internal circumference of an injector nozzle to enhance the mixing of air with a coaxial flow of air. Flow visualization by Mie scattering showed that the ramps appeared to enhance shear layer growth by creating large-scale structures. Total pressure profiles showed that the addition of the ramps to the inside of

the nozzle caused the shear layer growth rate to increase by 110 % over that for a plain circular nozzle.

An increase in the mixing rates of coaxial mixing layers by even smaller modifications to the internal nozzle geometry has been demonstrated by King et al.[35] Triangular pieces of ordinary adhesive tape that were 0.2 % of the exit diameter of a pressure-matched Mach 1.8 nozzle were found to increase the mixing rates while causing little thrust loss due to exit area blockage.

The addition of swirl to the fuel inside the injection nozzles has also been studied as a mixing enhancement method. In the investigations of Levey, Cutler and Kraus,[36-40] the mixing growth rate of a Mach 1.7 air jet, as measured by probes, focusing schlieren, and Rayleigh scattering, was found to increase with an increase in the amount of swirl.

Kraus and Cutler[39] studied the effect of swirl on the mixing of a 30 degree wall jet into a Mach 2 airstream. Instantaneous Rayleigh scattering images were used to study the mixing of both helium and air into the airstream. It was observed that the penetration of the wall jet into the freestream increased little. However, the addition of swirl preferentially increased the lateral spreading of the fuel in one direction. The interaction of the vortex from the supersonic nozzle with the two counter-rotating vortices generated by injection of the fuel was thought to be the cause of the lateral movement of the jet mixing region.

An unsteady vortex breakdown mechanism has been suggested as a major cause of the increased mixing observed in overexpanded swirling jets. Metwally et al.[41] studied a streamlined, axisymmetric, strut-mounted supersonic swirl injector in a Mach 2 airstream. Air was used for the injectant and the nozzle flow was over-expanded. Schlieren films showed that, with a strong vortex, the normal shock formed downstream of the nozzle rapidly oscillated ($f \approx 4$ kHz) in the streamwise direction. As the shock moved forward it curved. A mechanism based on the vortex breakdown downstream of the normal shock, and the resultant formation of a high pressure

stagnation point was proposed as the cause of the forward movement of the shock.

The interaction of oscillating shocks with a hydrogen-air mixture was studied computationally by Kumar et al.[42] The geometry studied was a duct with a 10° compression surface on one side that created an oblique shock along with a 15° expansion on the opposite wall. It was found that disturbances from the wall region propagated along the shock resulting in an unsteady shock that enhanced the turbulence behind the shock. Other methods for producing oscillating shocks were also discussed.

The effect of an unsteady shock on the mixing characteristics of the 15° angled jet, previously studied by Mays, was studied by Wood and Schetz.[43] The shock was generated by normal injection of a small jet of water injected from the opposite wall. Waves generated along the column of the water jet were thought to be responsible for the shock oscillation. By adjusting the liquid jet diameter, the power spectrum of the pressure measured on the opposite wall was altered. It was found that mixing was enhanced or inhibited depending on the shock oscillation frequency.

The interaction of shock waves with a fuel jet has also been studied as a way of mixing enhancement through the baroclinic torque mechanism. In the baroclinic torque mechanism the cross product of the density gradient and pressure gradient produces vorticity as shown in the following equation:

$$\frac{D\omega}{Dt} = \frac{1}{\rho^2}(\nabla\rho \times \nabla P) \qquad (1\text{-}4).$$

The baroclinic torque interaction is illustrated in Fig. 1.2. As shown in Fig. 1.2a, pressure and density gradients occur at the intersection of a fuel/air interface with a shock wave. This two-dimensional non-steady interaction was studied computationally by Yang et al.[44] A qualitative picture of the subsequent interaction is shown in Fig. 1.2b-d. The induced vorticity is a maximum at the sides of the fuel jet where the gradients of pressure and density are perpendicular to each other, and is zero at the top and bottom of the fuel jets where the gradients are parallel. The vorticity induced at the edges of the jet cause it to assume the kidney-bean shaped structure shown in

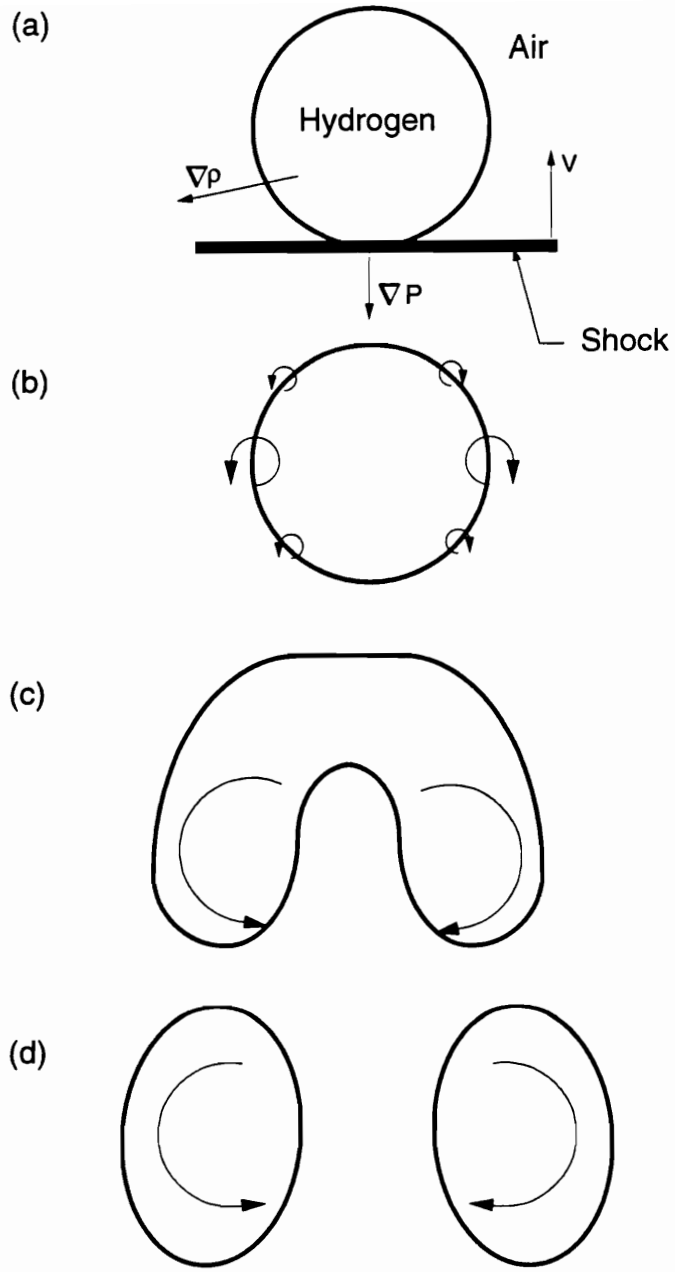

Figure1.2 Unsteady Two-Dimensional Baroclinic Interaction With a Round Fuel Jet: (a) Approaching Shock Wave (b) Initial Vorticity Distribution (c) Initial Roll-up (d) Development Into Separated Counter-Rotating Cores. (Adapted from Yang et al. [44]).

Fig. 1.2c. The fuel jet separates into a pair of counter-rotating vortical structures. In addition, the fuel jet moves in the direction of the shock wave after the interaction. Yang found that the induced velocity increased as the pressure ratio and density ratio across the shock increased.

The use of the baroclinic mechanism in a steady flow was first suggested by Marble et al.[45] As shown in Fig. 1.3, the interaction of a steady oblique shock with a fuel jet is analogous to the problem of the moving shock-fuel jet interaction. Traveling in a reference frame along with the fuel jet, the shock wave moves through the fuel jet as the fuel moves downstream. The passage of the shock causes a large increase of the fuel/air interface area due to the distortion of the fuel jet by the axial vorticity.

Fuel injection through the base of ramps angled to the airstream has been the subject of numerous studies for mixing enhancement in scramjet combustors.[46-66] Ramp injectors provide a method for near-parallel injection along with the creation of large scale vortical structures that are effective in increasing the mixing rate. Waitz et al.[46-47] studied the mixing of helium into air using a class of contoured wall fuel injectors shown in Fig. 1.4. The ramps were designed to produce axial vorticity through two mechanisms:

1. The cross-stream shear associated with the pressure gradient between the high pressure on the ramp top and the low pressure region between the ramps.

2. The baroclinic torque mechanism that occurs as the fuel jet is passed through the oblique shock.

Note that the tunnel wall opposite of the injectors was high enough that the reflected shock from the ramps did not interact with the fuel jet in the test section.

Waitz compared the baseline ramp geometry shown in Fig. 1.4 $\left(\alpha_c = 4.76^\circ, \alpha_e = 4.76^\circ\right)$ with two other injector ramp configurations to evaluate the relative effects of the two axial vorticity mechanisms on the

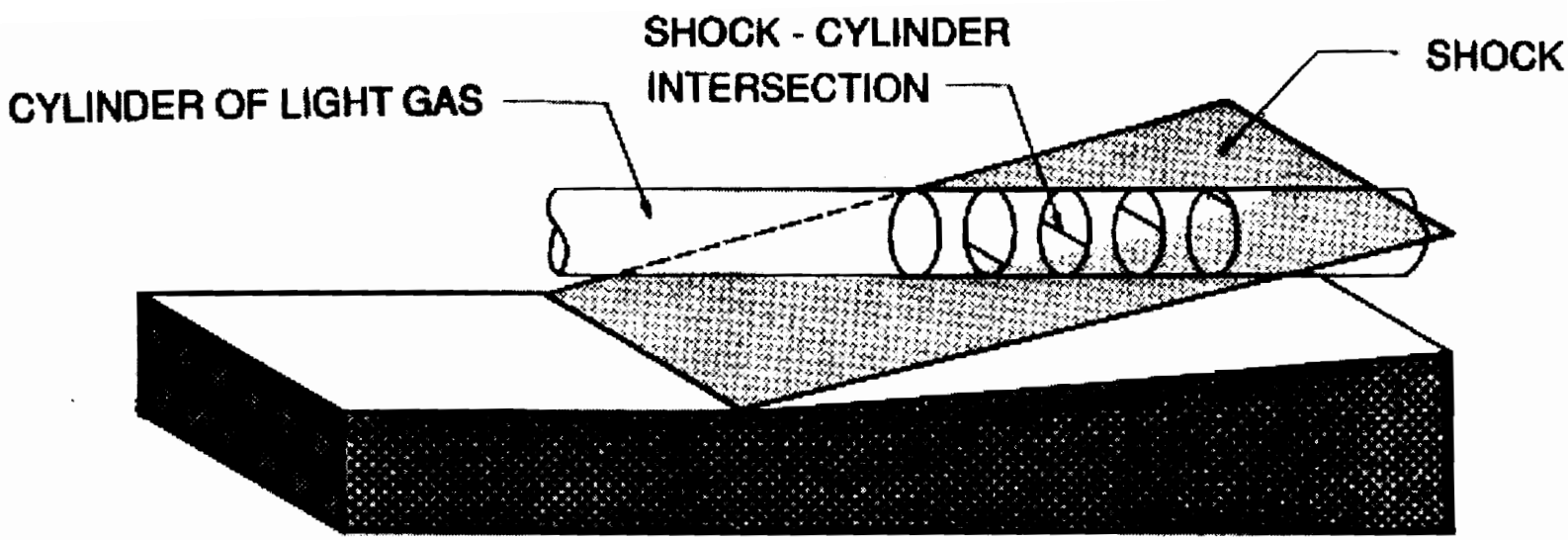

Figure 1.3 Baroclinic Interaction in a Steady Three-Dimensional Configuration (from Waitz et al.[46])

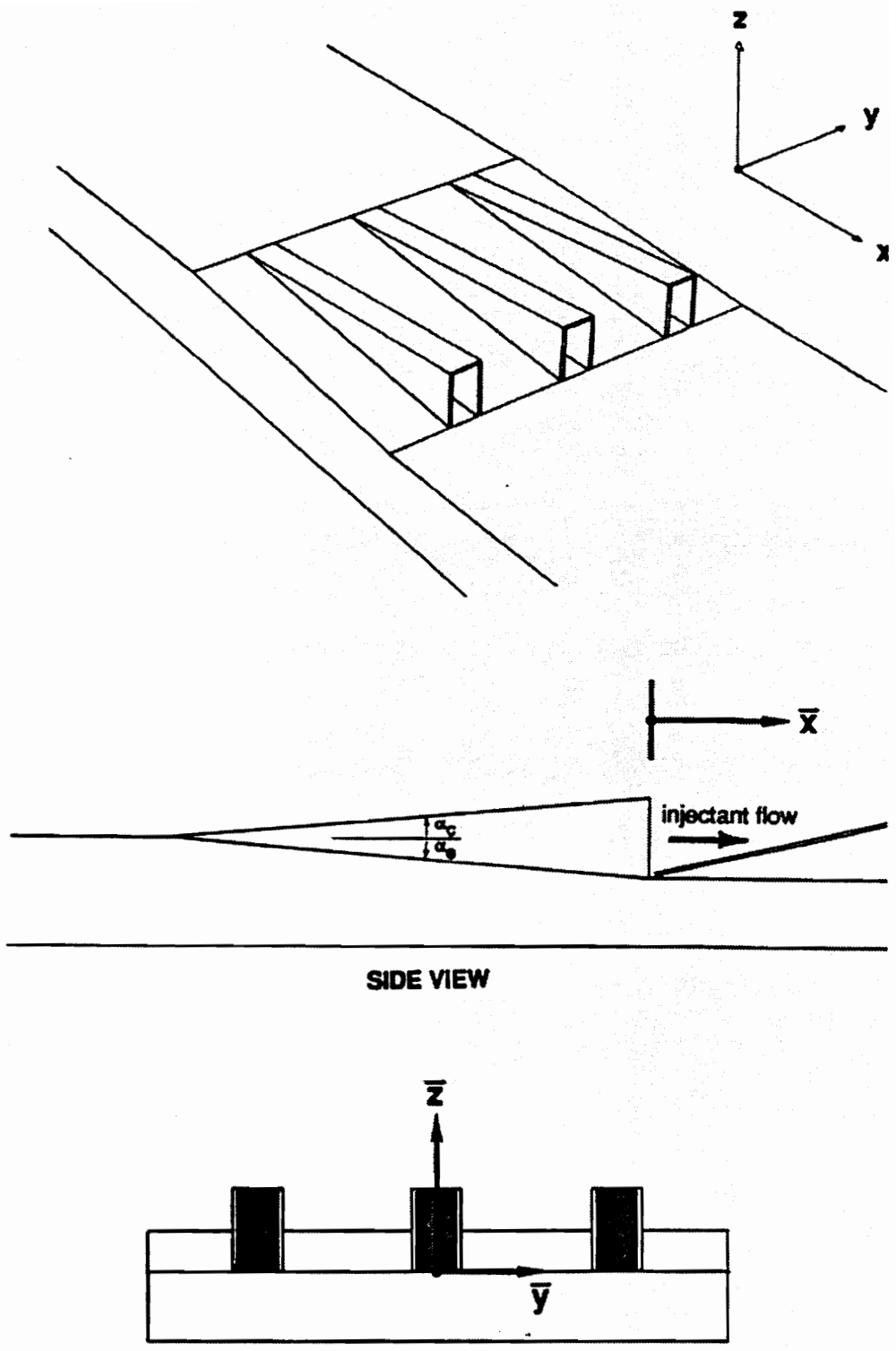

Figure 1.4 Contoured Wall Injectors (From Waitz et al. [46]).

mixing. The second injector was a straight-sided expansion ramp $\left(\alpha_C = 0°, \alpha_e = 4.76°\right)$ that was designed to produce approximately the same amount of baroclinic torque on the fuel jet as the baseline configuration. The third ramp was a straight compression ramp $\left(\alpha_C = 9.76°, \alpha_e = 0°\right)$ that was designed to produce the same amount of cross stream shear with no baroclinic torque. Computations of the helium/air mixing showed that the decay of helium concentration was more rapid for the two injectors that used the baroclinic mechanism than it was for the compression ramp. The enhanced mixing was attributed to the fact that vorticity produced by the baroclinic mechanism was produced directly at the fuel/air interface while the center of the vortex generated by the compression surface of the ramps was located away from the fuel/air interface.

1.4 Swept Ramp Injectors

Northam et al.[48-52] introduced the swept ramp fuel injector that is shown in Fig. 1.5. In the swept ramp design, axial vorticity is created as the flow spills from the high pressure region on the top of the ramp to the region between ramps in the same manner as it is for the straight-sided compression ramps. However, because the ramp surfaces are swept in the direction of flow, more flow is drawn over the top of the ramps, resulting in a stronger vortex than that produced by the straight compression ramps. Combustion tests were conducted at combustor inlet Mach numbers of 2 and 3 for both swept ramps and straight compression ramps.

The swept ramps were found to provide flameholding downstream of the ramps, with autoignition limits of T_T = 1400 K, and T_T = 1670 K for Mach 2, and Mach 2.9 test conditions, respectively. The performance, based on the combustion efficiency, was found to be better for the swept-compression ramps. In fact, the combustion performance nearly equaled the performance expected from empirical correlations of the mixing from perpendicular injectors. In addition, the performance of the swept-ramp injectors was much less sensitive to the total temperature of the incoming flow than it was for the unswept-compression ramp injectors.

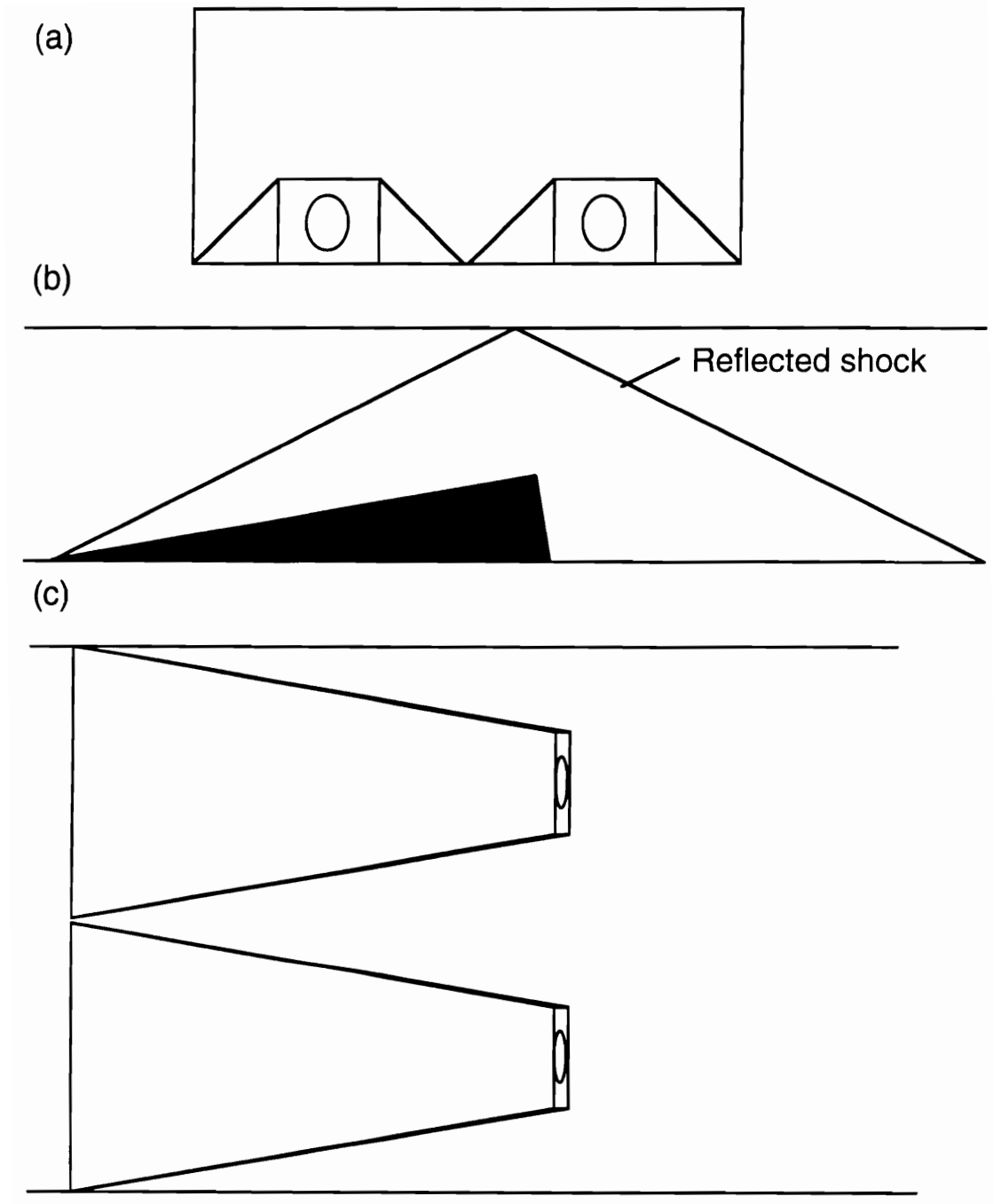

Figure 1.5 Swept-Compression Fuel Injectors (a) End View (b) Side View With Oblique Shock (c) Top View.

Planar laser induced fluorescence (PLIF) was used by Hartfield et al.[59] to study the mixing of iodine-seeded air from a swept-ramp injector into cold Mach 2 and Mach 2.9 airstreams. Concentration profiles in the crossflow planes for the Mach 2.9 case are shown in Fig. 1.6. Near the injectors the flowfield was found to be dominated by the action of the two counter-rotating vortices on the fuel jet. The vortices greatly distorted the fuel jet in the lateral direction, increasing the fuel/air interface area. Several ramp heights downstream of the ramps, as the vortex structures closed the plume contours, the plume assumed an almost circular shape. The plume contours closed closer to the ramps in the Mach 2 tests. Also, the fraction of the combustor area that was within the flammability limits of hydrogen/air was highest at Mach 2.

Davis[63] conducted a numerical study of the amount of vorticity production and total pressure loss resulting from several ramp injectors, including swept, and unswept-compression ramps, and swept expansion ramps. Parabolized Navier-Stokes calculations, for the three ramp geometries at Mach 2, showed that the production of longitudinal vorticity by the ramp was greatest for the swept-compression ramp, followed by the unswept-compression ramp, and least for the swept-expansion ramp. The total pressure recovery was found to be best for the swept compression ramp, slightly better for the swept expansion, and best for the straight compression ramp. Davis suggested a geometry with a half of a cone cut out of the side as a compromise between vorticity generation and total pressure loss. Further reacting flow calculations showed that the combustion efficiency was best for swept-compression ramp, followed by the unswept-compression ramp, and was worst for the swept-expansion ramp.

Riggins and McClinton[56] performed both reacting and non-reacting elliptic Navier-Stokes calculations with 30° wall jets, and 10° unswept and swept-ramp injectors, with Mach 2 inlet conditions. The non-reacting mixing results showed that the swept-compression ramps had the highest mixing rate, the wall jet had the next highest, while the unswept compression ramp exhibited the worst mixing rates. Comparisons of the calculated thrust showed that the wall jet produced the most thrust and the swept compression

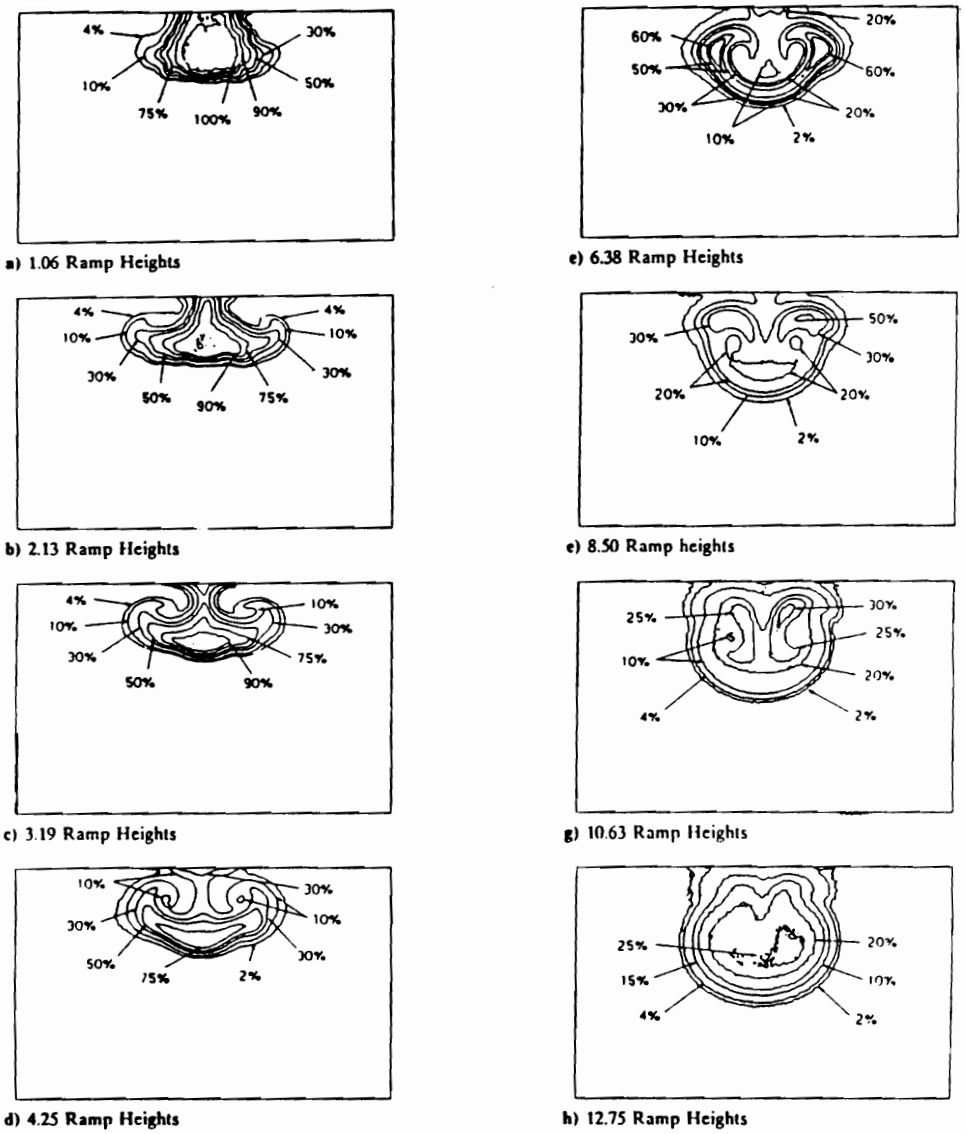

Figure 1.6 Injectant Mole Fraction Distributions by the Downstream of a Single Swept Compression Ramp (From Reference 59).

ramp produced the least amount of thrust. The reason for the decreased thrust in the case of the swept ramp was primarily due to the high pressure on the large forward facing surface of the swept ramp.

The calculations for the reacting flows showed that, in the nearfield, combustion efficiency was highest for the swept compression ramp while the combustion efficiency for the wall jet slightly lower. At the exit of the combustor the combustion efficiencies for these two configurations were approximately equal. Comparisons of the thrust for the two configurations showed the same trend as did further calculations by Riggins and McClinton[57] at Mach 3 combustor inlet conditions. The results for the unswept compression ramp showed that ignition did not occur at the ramp injector, but occurred a short distance downstream of the injectors. Even with a shorter distance to react, the unswept compression ramps had the highest combustion efficiency and thrust of the three configurations. Recalling that the unswept ramps had the worst mixing efficiency of the three configurations, the authors concluded that combustion near the injectors can decrease mixing.

Other mixing enhancement techniques have also been studied in combination with ramp injectors. Capriotti et al.[49] found that small normal injectors located downstream, directly in line with swept compression ramp injectors, improved the combustion efficiency slightly. A greater improvement was found for the combination of unswept-compression ramps and normal injectors. The improvement was attributed to the additional longitudinal vorticity introduced to the fuel plume at the intersection of the normal jet and main fuel jets.[65]

The effect of combining noncircular injector geometry with a single swept-ramp injector on the mixing performance was studied by Hamovich[64] in a cold flow mixing study. Six different noncircular nozzles, including ellipsoidal and tapered rectangular nozzles, were studied. Although large differences were found in the fuel plume cross-section near the jet exit, only minor differences were observed between the fuel plumes in the farfield. The similarity in the farfield was attributed to the fact that the flow in the farfield appeared to be dominated by the longitudinal vorticity from the ramps.

1.5 Heat Transfer in Scramjet Combustors

1.5.1 Background

A brief survey of the open literature concerning heat transfer in scramjet combustors is presented below. It should be noted that other studies involving heat transfer measurements in scramjet combustors have been made in recent years as part of the National Aerospace Plane (NASP) program. However, these studies cannot be addressed here due to classification or ITAR restrictions.

Early experimental studies of scramjet heat transfer involved energy balances on the cooling water to large surface plugs located in the far-field of the fuel injectors.[66-68] Later studies provided more spatial resolution by using heat flux gages to measure the flux over much smaller areas.

Guy and Mackley[69] studied the heat flux distribution in a copper scramjet engine at Mach 7 flight conditions and found that the heat flux distributions resembled the pressure distributions. Diskin et al.[70] used a single heat flux gage mounted near the end of a Mach 2 scramjet combustor to investigate the wall heat flux in direct-connect tests with hydrogen and hydrocarbon/hydrogen mixtures as fuels. One of their main objectives was to determine if the heat flux increased when using hydrocarbon fuels. Increased heat transfer was expected with hydrocarbon fuels because of blackbody radiation from soot. With pure hydrogen fuel no particulates are formed; therefore, the only radiation from the burning fuel to the walls is in the form of descrete spectral lines. They found that the heat transfer to the walls increased as the fuel equivalence ratio increased when using hydrogen as a fuel. When using hydrogen/hydrocarbon mixtures, the trends of heat flux vs. equivalence ratio were approximately the same, implying that the effect of radiation was small.

Morgan and Stalker[71] studied the heat transfer to the combustor and nozzle walls of a scramjet in a shock tunnel. The fuel injector was a strut that was mounted in the center of the tunnel, so that the reaction zone was separated from the wall. The combustion products did not penetrate to the wall. Thus, the only influence that the combustion had on the heat flux level was through freestream pressure increase. Measured heat fluxes that were

below the turbulent predictions in the nozzle were discussed with the possible explanation of relaminarization of the boundary layer.

Perhaps the most striking evidence of the high wall heat transfer levels in scramjets is provided by the numerous examples of melted and burnt scramjet combustor parts displayed in the offices and laboratories of engineers around the world. In previous combustion tests of swept ramps, Northam et al.[51] noted large melted areas of the combustor duct downstream of the ramp injectors. A photograph of the melted combustor wall from these experiments is shown in Fig. 1.7. In these tests the injector wall suffered extensive melting, in contrast to the opposite wall that was virtually damage free.

1.5.2 SCRAMJET Combustor Cooling

In the design of a scramjet engine it is obvious that some form of cooling will be required. From weight and thermodynamic considerations it is desirable to use fuel to regeneratively cool the engine components. The cooling requirements for the engine can be further reduced by cooling the internal combustor walls with the fuel. The fuel forms an insulating layer between the wall and the high enthalpy freestream. Two methods of cooling the hot side of the combustor walls, film and transpiration cooling, are shown in Fig. 1.8.

Film cooling is illustrated in Fig. 1.8a. Film cooling is used to protect large areas of the walls downstream of a slot injector. It has the advantage that the fuel momentum is used to produce thrust. Film cooling has been demonstrated to be effective in cooling large areas of scramjet nozzles by Baker et al.[72] Film cooling has the disadvantage that incident oblique shocks can degrade the film cooling effectiveness.[73] In addition, a strong adverse pressure gradient in the freestream due to combustion may also degrade the film effectiveness.

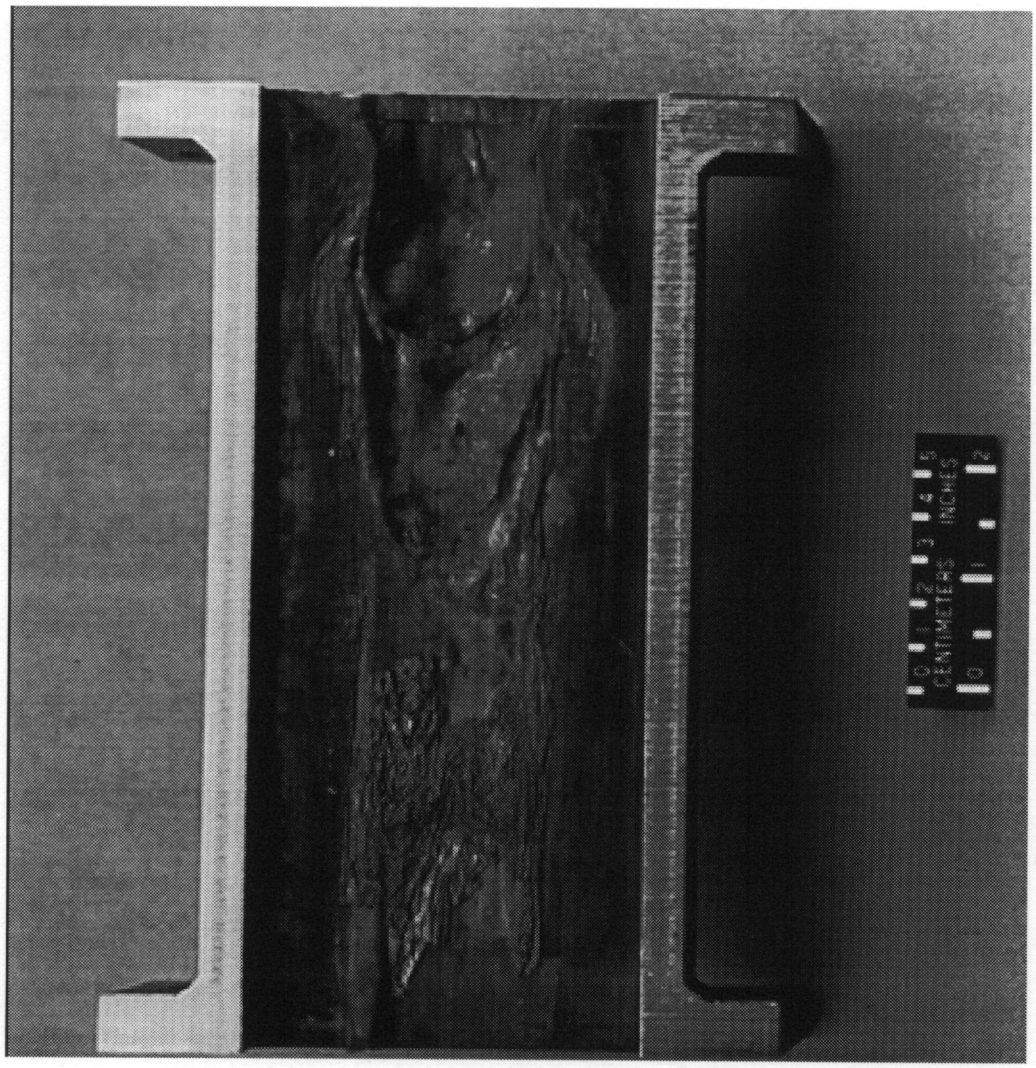

Figure 1.7 The Melted Combustor Duct Downstream of the Swept Compression Ramp Injectors.

Transpiration cooling is illustrated in Fig. 1.8b. In transpiration cooling fluid is injected perpendicular to the wall. Transpiration cooling has been used extensively in cooling gas turbine blades. Typically, less of the combustor area downstream of the transpiration injector is protected in this method. In addition, none of the momentum of the coolant is used to produce thrust. Another concern with transpiration cooling is that flameholding characteristics can be altered when using transpiration near fuel injectors. Byington et al.[74] studied transpiration film cooling around a normal

hydrogen fuel jet in a Mach 3 freestream. They found that transpiration cooling was effective in reducing the high heat fluxes in the vicinity of normal injectors. However, in open jet tests it was found that there were limits on the amount of transpiration cooling which could be applied without flameout.

Before an effective cooling strategy can be devised for a combustor, it is essential to identify regions of the combustor that suffer the most severe heat fluxes. It is even more important to understand the reasons for the severe heat flux.

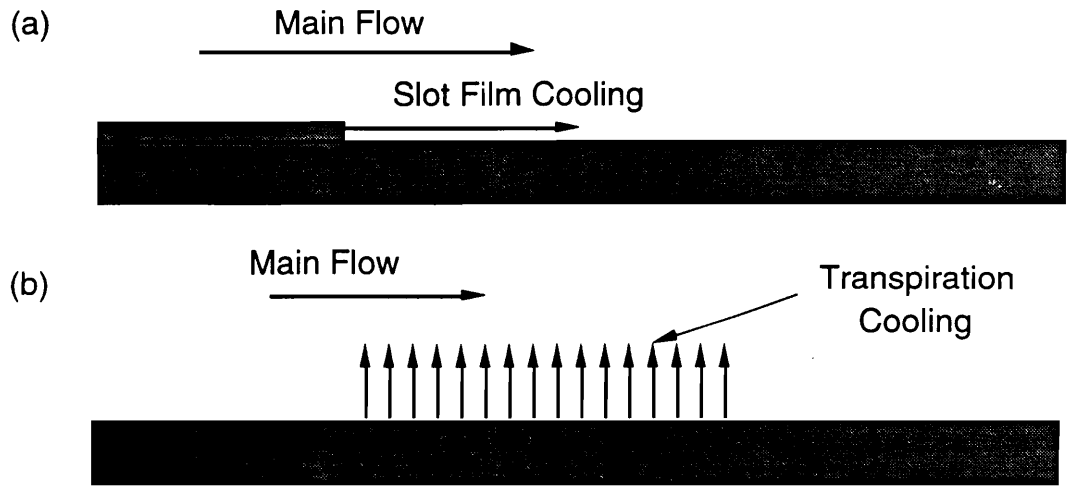

Figure 1.8 Combustor Wall Cooling Methods (a) Film Cooling (b) Transpiration Cooling.

1.6 Dissertation Objective and Approach

The objectives of the present study were to determine the effect of mixing augmentation, resulting from streamwise vortices generated by swept injector ramps, on scramjet engine operation characteristics, combustion, and heat transfer. To achieve these objectives, a combined experimental and computational study of a scramjet combustor employing two different swept-ramp injector configurations was conducted. The experimental study was conducted in a direct-connect combustor test facility, simulating flight at approximately Mach 6.6. The combustor inflow conditions for the tests were: $M = 2.63$, $T_T = 1940$ K, and $P = 1$ atm.

The experimental measurements included combustor wall pressure and heat flux measurements for the two injector configurations. Measurements of the heat flux were made by both cooled Gardon gages, and by a transient analysis using the combustor surface temperature. A unique side-view laser light sheet technique was developed to obtain Mie-Scattered images of the combustion product distribution at selected planes in the scramjet combustor. Further instream information was obtained by a miniature refractory probe which was developed for this research.

Computations of the flowfield using a three-dimensional, Navier-Stokes code were conducted to provide further insight into the effect of the flowfield structure on combustion and wall heat transfer. The flowfield calculations were then compared to experimentally determined values of wall pressure, heat flux, pitot pressure, and Mie scattering flow visualization.

1.7 Outline of the Dissertation

The background and motivation for the following study have been presented in this chapter. Chapter Two describes the combustor hardware and the direct-connect combustor test facility used in the experimental portion of the study. The experimental methods and measurements used to acquire the data are discussed in Chapter Three, followed by the presentation of the experimental data in Chapter Four. The results of the computational study of the flowfield structure are presented in Chapter Five along with comparisons between the numerical and experimental results. The conclusions are presented in Chapter Six, followed by the recommendations for further work in Chapter Seven. A discussion of the uncertainty analysis is presented in the Appendix along with data reduction techniques, and a tabulation of test conditions.

Chapter 2
Experimental Apparatus

2.1 Test Facility

All tests were conducted in the Direct-Connect Supersonic Combustor Test Facility at the NASA Langley Research Center. The direct-connect test apparatus, shown in Fig. 2.1 simulates scramjet combustor inflow conditions at flight Mach numbers from 4-7. In direct-connect tests, the air flow from a scramjet inlet is simulated by the facility nozzle. The direct-connect facility has two distinct practical advantages over a free jet facility in which the complete engine is tested. The first advantage is that the required mass flow is lower because there is no airflow external to the engine. The second advantage is that the required facility stagnation pressure is much lower because there are no inlet losses (shock losses and viscous losses). The high enthalpy air at the combustor inlet was provided by a hydrogen-air vitiated heater with oxygen replenishment to 21 percent by volume. The mass flow rates of air, hydrogen and oxygen were set to achieve the desired total pressure, temperature and oxygen content. Detailed information about the vitiated heater design is presented in reference 75.

For the tests reported here, the total temperature and pressure were approximately 1950 K and 2.8 MPa, respectively, simulating the stagnation enthalpy of air at Mach 6.6. The inlet Mach number was set at 2.63 by a water-cooled copper nozzle, so that the ratio of the combustor inlet Mach number to the flight mach number was 0.4. A commonly accepted "rule of thumb" for low hypersonic speeds that the ratio of the combustor inlet Mach number to the flight mach number should be between 1/3 and 1/2. Therefore, the combustor inlet Mach number used for the current tests is appropriate for the flight Mach number. The oxygen content of the vitiated air was calculated from the heater mass flow rates during the tests and only runs with oxygen levels of 21.0 ± 1.0 % were analyzed. The required heater mass flow rates to obtain the operating conditions were:

Air flow rate = 2.75 kg/s
Oxygen flow rate = 1.0 kg/s
Hydrogen flow rate = 0.082 kg/s

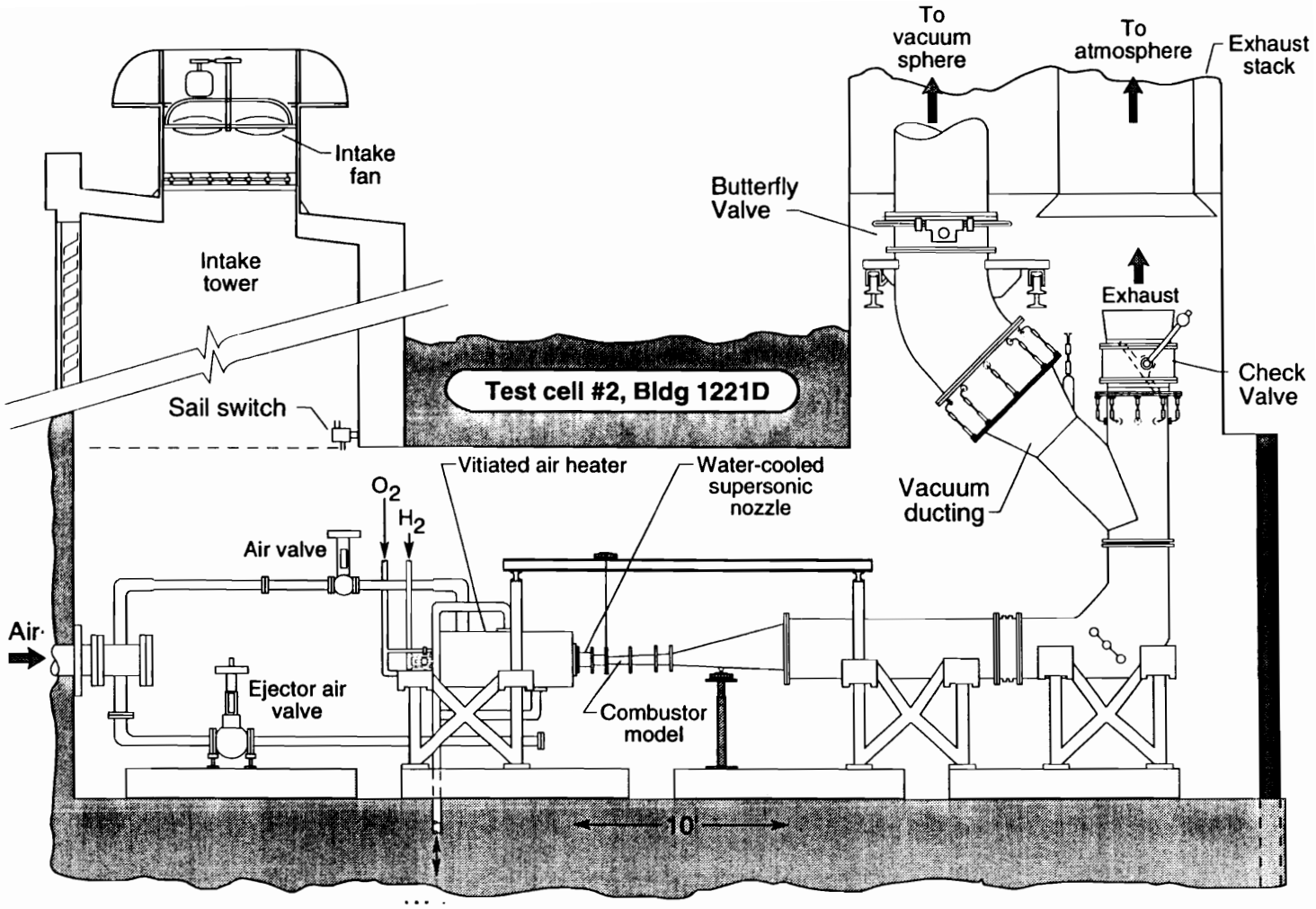

Figure 2.1 Schematic of Direct-Connect Scramjet Combustor Test Facility

A complete uncertainty analysis of the measured and calculated combustor inlet properties is presented in Appendix A. With the Mach 2.63 nozzle, the static pressure at the combustor entrance was approximately one atmosphere. A vacuum duct was connected to the end of an expanding nozzle-duct assembly to allow operation at reduced back pressure without separation. The vacuum ducting was connected to a 21.3-m vacuum sphere that was evacuated to a few Torr by a three-stage steam ejector. For the short run times of the tests and total mass flow rates of under 5 kg/s there was no increase in the back pressure at the scramjet combustor/nozzle exit.

2.2 Injector Designs

Figure 2.2 shows the two injector blocks that were constructed for this investigation. These designs are referred to as the swept-compression and swept-expansion ramp injectors. The injector blocks consisted of a 90 mm long constant area section, followed by the injector ramp, which was then followed by a 70 mm long constant area section. A single fuel injector nozzle was mounted in the base of each ramp.

The swept-compression ramp injector is similar to the swept-ramp model that was previously studied in this facility,[50-52] except that the width of the combustor is twice as wide. The wider hardware allowed the use of four injector ramps, which reduced the effect of the side walls on the flow. The swept-compression ramps have a 15.2-mm wide by 12.7-mm high base. The ramp angle and the fuel injection angle were both 10.3° with respect to the base of the injector block. The ramp angle was much less than the 29° shock attachment limit predicted by oblique shock-wave theory; thus, the flow should have remained attached to the ramp and the reflected shock should have been stable. The sweep angle was 10 degrees on each ramp side wall. There was a 70 mm long constant area section downstream of the base of the ramps. The duct height at the entrance of the combustor, upstream of the ramps, was 38.1 mm. The blockage area of the compression-ramps was about 12%. The base area and the ramp angle were selected to minimize the flow losses and flow separation over the rearward-facing step. The compression-ramp has been shown to produce vortical flow as the higher

pressure on the ramp face is relieved. Mixing in this configuration was also enhanced by the baroclinic torque mechanism as the reflected shock passed through the density gradient caused by the hydrogen fuel jet (see Section 1.3). At Mach 2.63 inflow conditions, an estimate based on two-dimensional, oblique-shock theory predicted that the shock from the 10 degree compression-ramp was reflected back to the fuel injector wall about 79 mm downstream of the injectors. Also, flameholding in this configuration was promoted by recirculation behind the swept, rearward-facing steps.

A second injector block with expansion-ramps was also constructed to reduce the flow losses associated with the oblique shock generated by the compression-ramp. For this injector, the top surface of the ramps were flush with the wall upstream of the ramps and the recesses between the ramps were used to generate vorticity (see Fig. 2.2). As it was for the swept-compression ramp, the pressure was higher on the top surface of the ramp than it was in the interstice, leading to formation of longitudinal vortices. The flow turning at the intersection of the expansion between the injector ramps and the constant area section produces an oblique shock, which can interact with the hydrogen jet to enhance mixing through the baroclinic torque mechanism. The recesses were 13 mm deep and the other dimensions of the injector block were the same as for the compression-ramp design. The duct height at the end of the expansion-ramp injector was thus increased from 38 to 51 mm. This design resulted in the hydrogen being injected into a higher Mach number expanded flow with a lower pressure and temperature compared to the compression-ramp design.

The fuel injector nozzles, which were mounted in the base of the ramps, were indentical for both configurations. The exit Mach number for the injector nozzles was 1.7 with an exit diameter of 7.1 mm. Also, the injection angle, relative to the constant area section upstream of the ramps, was the same (10.3°) for both ramps, so that the fuel was injected nearly parallel to the airstream. Hydrogen fuel was supplied from fuel tanks at a stagnation temperature equal to ambient conditions (~ 30 K). The fuel total pressure increased as the fuel equivalence ratio increased. For an equivalence ratio of one, the 3.27 MPa. Hence, in the absence of a

combustion-induced pressure increase, the flow from the Mach 1.7 injector nozzles was highly underexpanded for both injector configurations.

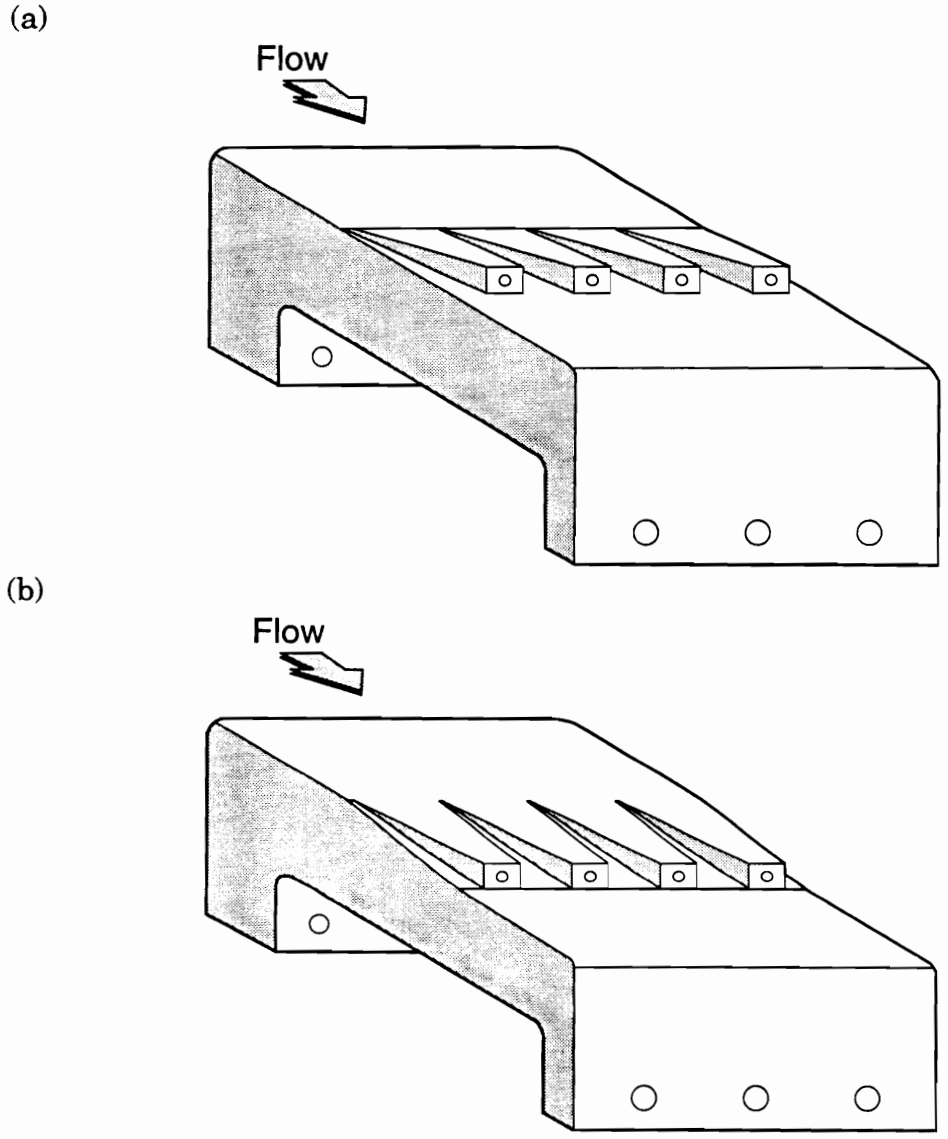

Figure 2.2 Swept Ramp Injectors (a) Swept Compression (b) Swept Expansion.

2.3 Duct Configuration

The combustor area distribution is based on previous experience with similar combustors at low hypersonic speeds ($M_\infty = 4-8$)[48]. Constant area combustors lead to high temperatures and pressures in the combustor, which is helpful from the standpoint of ignition and flameholding. However, at low hypersonic flight speeds, a limited amount of heat addition may occur before thermal choking occurs in a constant area combustor. As the flight speed increases, the fraction of energy that can be added by complete combustion of the fuel becomes small relative to the total enthalpy of the airstream. Therefore, if the flight speed is high enough, a constant area combustor cannot be thermally choked by combustion. Note that in order to reach flight speeds where choking is not a concern, the engine must first fly at lower speeds where choking is a concern. An expanding combustor duct allows more heat addition without thermal choking. The combustor area distribution used in this study consisted of a short constant area section immediately downstream of the injectors followed by a diverging combustor duct. The intent was to promote combustion in the nearfield of the injectors by the constant area section, while avoiding thermal choking by expanding the flow throughout the combustor.

The combustor duct is shown in Fig. 2.3 for both injector configurations. The dimensions are normalized by the gap length, G, which is defined as twice the combustor inlet height (G = 76.2 mm for both of the injectors). The combustor was constructed from an injector block that was followed by a 4.3° included-angle divergent combustor duct. The exit of the combustor was attached to a 22° divergent nozzle that was used for a related study of heat transfer and film cooling in a scramjet nozzle.[72] The nozzle exited into the vacuum system. The combustor duct consisted of three divergent duct sections bolted together for the compression-ramp combustor and two ducts for the expansion-ramp combustor. The first duct (Duct A), which was used only for the compression-ramp case, was 167 mm long and had a height that increased from 38 to 50.8 mm. This duct was removed when the expansion-ramp injectors were used. As shown in Fig. 2.3, the expansion-ramp equipped combustor is shorter because the expansion to the

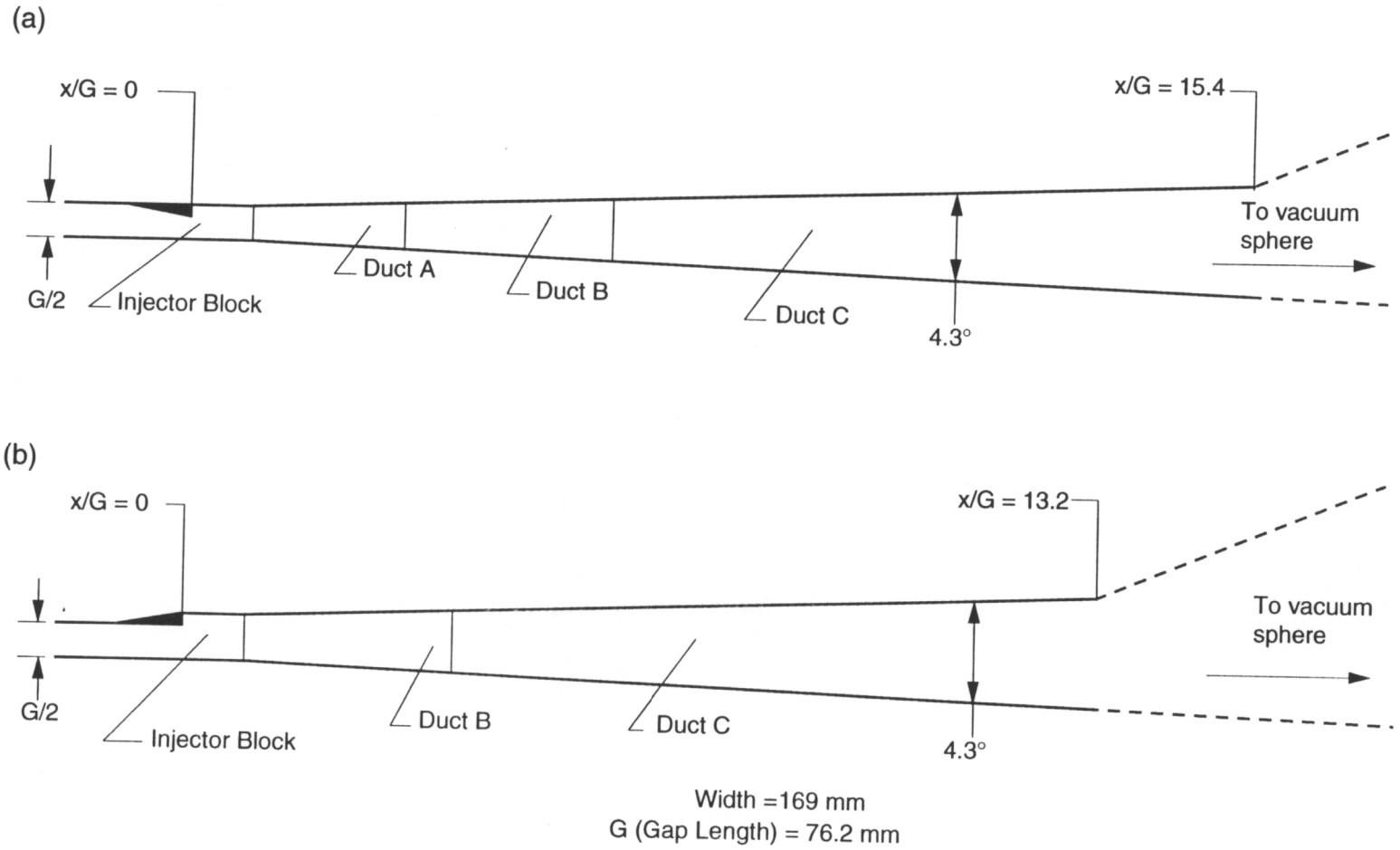

Figure 2.3 Combustor Duct Geometry (a) Compression Ramp (b) Expansion Ramp

height of 50.8 mm occurs in the injector block section. The second diverging duct (Duct B) was 228 mm long and was connected to a third duct (Duct C)that was 710 mm long. The injector blocks and the two diverging ducts immediately downstream of the injector region were constructed of ARMCO 15-5 stainless steel, and the final duct, which was available from previous tests, was constructed of low carbon steel. The ratio of the exit area to the inlet area was 3.2 for both combustors, and the nozzle expansion ratio was 5.6.

The combustor walls were uncooled and the run times were limited to 10 seconds total and 4 seconds with fuel on, to avoid excessive wall heating. A photograph of the combustor installed in the test cell is shown in Fig. 2.4.

2.4 Test Cell Operation

The vitiated heater is turned on in three stages, low air flow, pilot fuel mode, and vitiated heater on. Figure 2.5, which shows the stagnation pressure inside the heater and the combustor fuel line, illustrates the run timing. In cold air operation only the air flows through the combustor. During the pilot fuel mode, 60 % of the heater flow is diverted around the main fuel valve and is ignited by a spark ignitor. After a pressure rise is sensed in the heater, a mechanical run timer is used to open the valve controlling the main heater fuel. At this point the vitiated heater is fully on. The valve controlling the combustor main-fuel system was then opened after a delay supplied by another mechanical timer.

The flowrates through the air and fuel lines were set by manually operated dome-loaded regulators before each test. Because of the short run times, there was usually no time to further adjust the supply pressures by hand. This lack of control resulted in some tests with unsatisfactory inlet temperature, pressure, or oxygen content that were not analyzed.

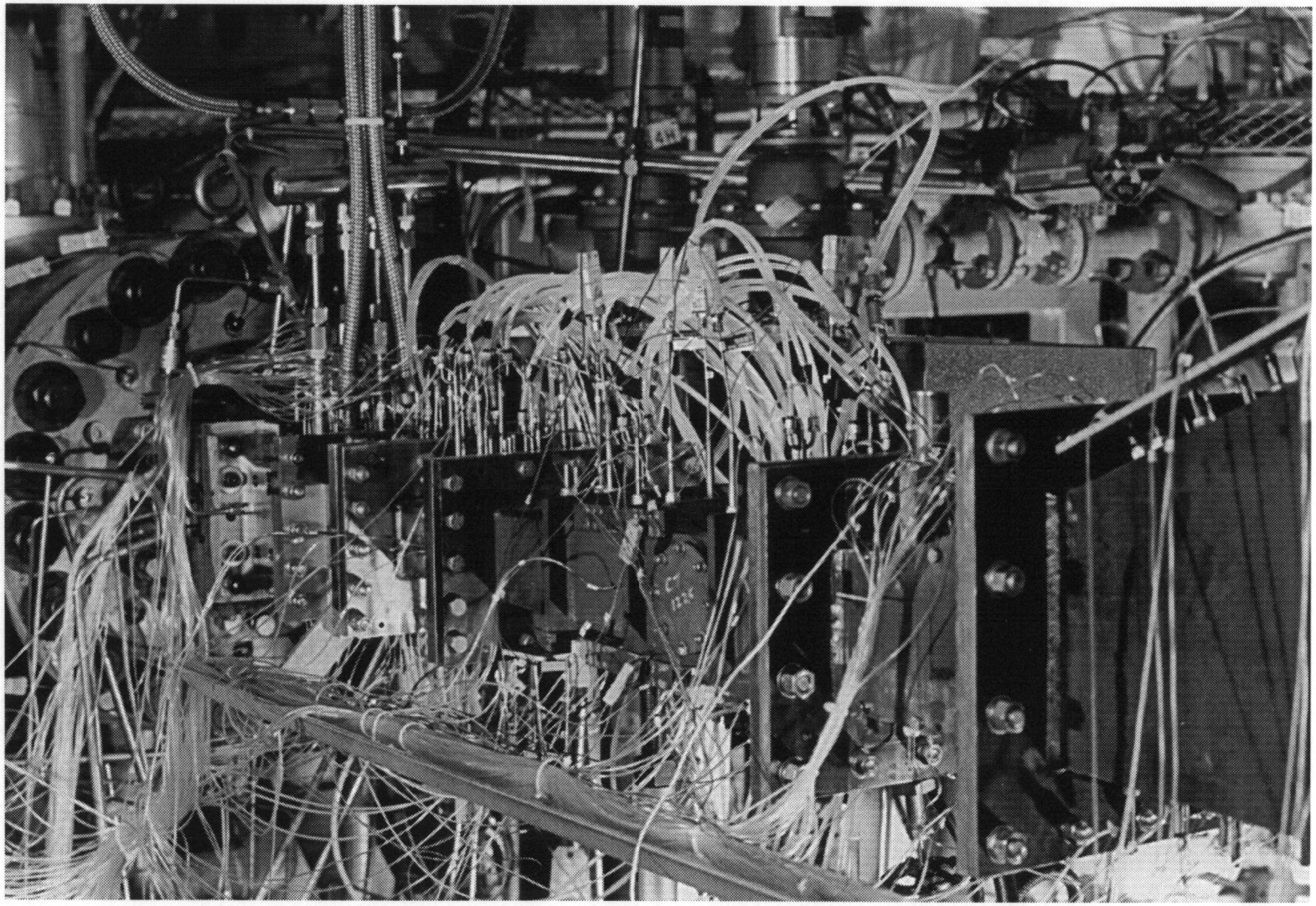

Figure 2.4 Combustor Installed In The Test Cell.

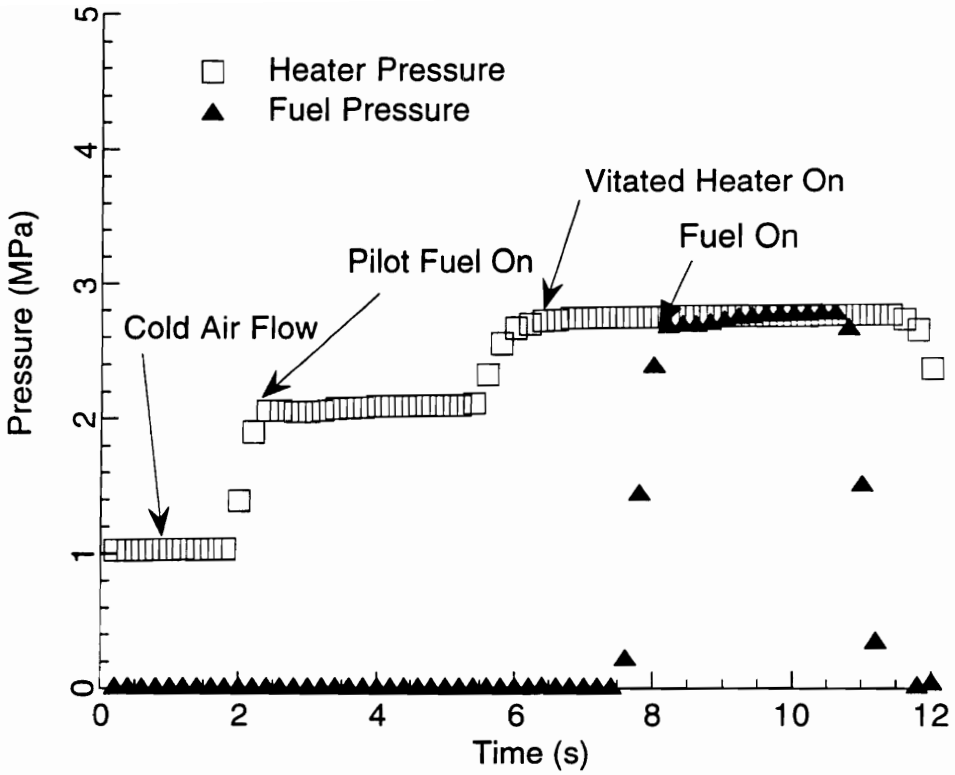

Figure 2.5 Vitiated Heater and Model Fuel Supply Pressure During a Typical Test.

In addition to the heater and main fuel systems, there were seven auxiliary fuel systems which were controlled by a Modicon programmable logic controller (PLC). These fuel systems were used to control silane/hydrogen ignition sources during some of the tests. Further information about silane/hydrogen ignition sources is presented in Chapter 4 section 4.1.

Chapter 3

Experimental Methods and Measurements

3.1 Wall Pressure Measurements

Combustor wall pressures were measured with an Electronically Scanned Pressure (ESP system 780-B) measurement system built by Pressure Systems Incorporated. Up to 140, 1 mm-dia. taps were used to measure pressure along the combustor walls. Stainless steel tubing was welded to the outside of the combustor walls at each tap location and connected to the ESP system by Tygon tubing.

Wall pressures were recorded on the data system at a rate of 5 Hz. The time response of the ESP/tube system was an obvious concern due to the long lengths (greater than 1 m) of small diameter tubing used to connect the pressure taps to the ESP modules. However, during tests the system was observed to respond to a step change in combustor pressure in less than two data cycles (0.4 s).

3.2 Wall Temperature Measurements

Inside wall temperatures are useful in a qualitative sense to determine where the largest heat flux occurs. In addition, the time history of surface temperature can be used to calculate the heat transfer by the transient finite difference method discussed in Appendix B. Past techniques for determining surface temperatures have included discrete measurements by surface thermocouples,[76] optical methods such as infrared emission,[74] and phosphor thermography.[77] Although optical methods offer high spatial resolution, and planar wall temperature profiles, they are difficult to apply in a closed supersonic combustor. The requirement of optical access is just one of the major problems that has to be solved. For example, in infrared measurements, depending on the wavelength of the signal, special materials must be used for the windows. Some of these materials are hygroscopic and therefore would have limited useful lifetimes in the humid combustor environment. Other factors, such as the change of surface emissivity with oxidation and temperature, emission from the windows, and water vapor, further complicate the experiment.

Because of the difficulties with optical measurements, surface thermocouples were used in the present investigation. Surface thermocouples are specially designed to determine the temperature only at the surface. Embedding thermocouples at specified positions was not attempted because of the large errors that can occur due to uncertainties in the depth.[78] The error due to position becomes especially important in low conductivity materials, such as stainless steel, because of the large temperature gradient normal to the wall. Two different types of thermocouples were used in the combustor, eroding thermocouples, and coaxial Chromel-constantan thermocouples.

3.2.1 Eroding Thermocouples

Eroding thermocouples made by NANMAC have previously been used to determine the internal surface temperatures in other harsh environments, such as Diesel engines.[79] A drawing of the thermocouple is shown in Fig. 3.1. This particular thermocouple used the Chromel-Alumel (type K) thermocouple pair. The wires are in the form of 0.64 mm thick ribbons, which were insulated by thin (25 μm) sheets of mica. A small junction is formed by abrading the surface with 80-grit sandpaper. This practice ensures that small junctions are formed at the surface where the two wires intersect. The thermocouple ribbons were placed between two tapered pins, which were secured inside a thick walled tube. Both the tube and the tapered pins were made of the same material as the walls.

Recall that the upstream half of the combustor was constructed of stainless steel, while the downstream half of the combustor was constructed of carbon steel. Therefore, surface thermocouples were designed with both materials. The thermocouple wires have a higher thermal conductivity than the wall material. However, because the small thermocouple junction is in intimate thermal contact with the relatively massive tapered pins, the temperature measured is that of the wall material. Also, the two-dimensional geometry of the thermocouple ribbons minimizes conduction errors.

The carbon-steel eroding thermocouples, which were installed in the second half of the combustor, performed as desired. During the test program only two failures occurred. The thermocouples failed by the opening of the junction at the surface. The failure of the junctions was corrected by lightly sanding the surface. The stainless steel thermocouples were less reliable than the carbon steel thermocouples. Apparently the higher surface temperatures, caused by the larger heat fluxes and lower conductivity material, caused the junctions to open. An effort was made to renew the junctions by sanding; however, the thermocouples failed after a few runs. In addition to the junction failure, the response time of some of the stainless steel thermocouples lagged that of the carbon steel thermocouples indicating that junctions were formed below the surface. For these reasons, no data obtained from the stainless-steel thermocouples is presented.

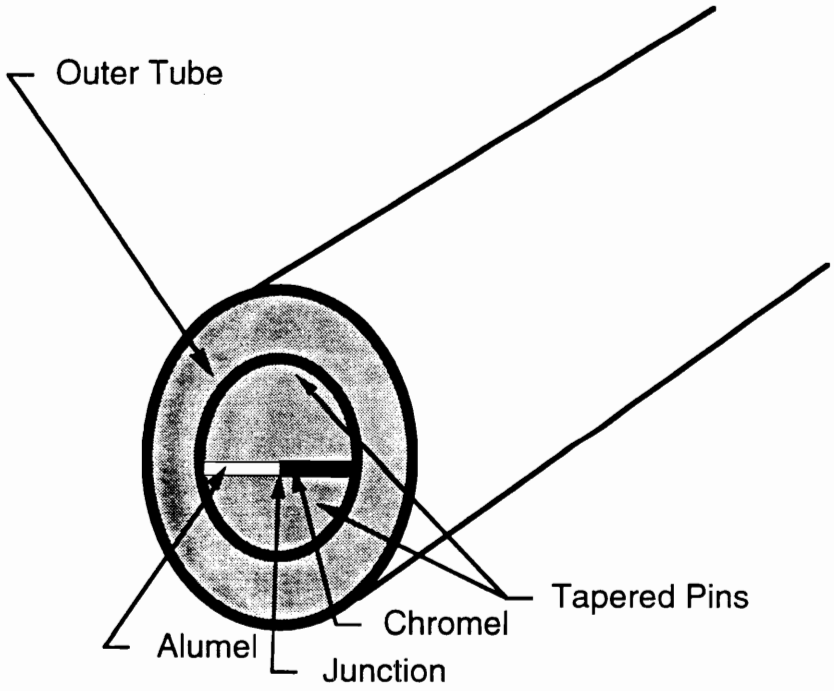

Figure 3.1 The NANMAC Eroding Thermocouple.

3.2.2 Coaxial Thermocouples

Chromel-constantan (E-type) coaxial thermocouples were examined as a method of measuring the surface temperatures in the stainless steel sections of the combustor. The coaxial thermocouples are constructed from

an inner rod of Chromel surrounded by a layer of insulation and outer tube of constantan. The outer diameter of the thermocouples was only 1.6 mm (1/16 in). The small size was desirable to obtain a high spatial density of temperature measurements. Because of the low thermal conductivity, the stainless steel walls can be considered as semi-infinite for the short test times (see Appendix B). For a semi-infinite medium, the surface temperature is determined by the heat flux, run time, and the thermal properties of the wall material through the lumped thermal parameter β $\left(\beta = \left(\rho c_p k\right)^{1/2}\right)$. An examination of the lumped thermal parameter shows that β differs by less than 1 % for Chromel and constantan. In addition, β for Chromel and constantan differ less than 10 % from that for stainless steel. The favorable match of thermal properties makes type E coaxial thermocouples a good choice for stainless steel surface temperature measurement.

Thirty type-E thermocouples were obtained from the NANMAC Corporation. The thermocouples were installed in the first duct downstream of the combustor by using high temperature Saureisen cement. The thermocouples appeared to be robust during the tests; few open junctions occurred. However, during a separate investigation of the surface heat flux associated with the normal injection of fuel from a flat plate (note: the details of this investigation are not covered in this dissertation), it was found that the surface temperature varied widely for thermocouples at similar locations. Further examination of the thermocouples showed that the insulation was at fault. The insulation, made from Teflon, melted at the high surface temperatures, causing the junction to be formed below the surface. Thus the measurements of temperature were at an unknown depth below the surface, and no useful quantitative information was obtained from the coaxial thermocouples.

3.3 Heat Flux Measurement

Many of the measurement techniques that have been used in other investigations of wall heat transfer could not be used for heat flux measurement in this facility, because of the unique requirements imposed on the sensor by the test conditions. Schmidt-Boelter gages, and most of the layer-type gages could not be used because of the high heat fluxes. Slug and

null-point calorimeters, which are used to measure high heat fluxes in shock tube tests (test time < 1ms), could not be used because the usable run time of the gage is much less than the time required to start the tunnel.

A promising gage design is the Vatell Heat Flux Microsensor reported by Hager et al.[80] The microsensor consists of two thermopiles that measure the temperature difference across a thin (less than 1μm) resistance layer. The measured voltage is proportional to the heat flux. The gage had a high sensitivity due to the small thickness of the layer and the large number of thermocouple pairs that were used. The layers of the gage are sputtered directly onto the surface of the models. In order to sputter the layers onto the gage, the ceramic gage surface must be polished to a mirror-like finish. Because the gage material was not compatible with the combustor wall materials, the microsensor was not considered as an option at the initiation of this study.

Two methods were used for most of the heat transfer measurements, the calculation of the heat transfer from measurements of the wall temperature history (see Appendix B), and circular foil gauges, commonly known as Gardon gages,[81,82] which are discussed in the next section.

3.3.1 Gardon Gage Theory

The Gardon gage was initially developed as a sensor for thermal radiation, but has also been widely applied as a sensor for convective heat transfer. A sketch of a typical Gardon gage is shown in Fig. 3.2a. A thin constantan foil is welded to the end of a copper cylinder. A small copper wire is welded to the center of the foil. Heat is transferred in the gage by radial conduction to the copper body, which is maintained at a lower temperature by heat sinking or water cooling. The thermocouple junctions formed at the center and the edge of the foil measure the radial temperature gradient. This radial temperature gradient can then be related to the gage heat transfer rate.

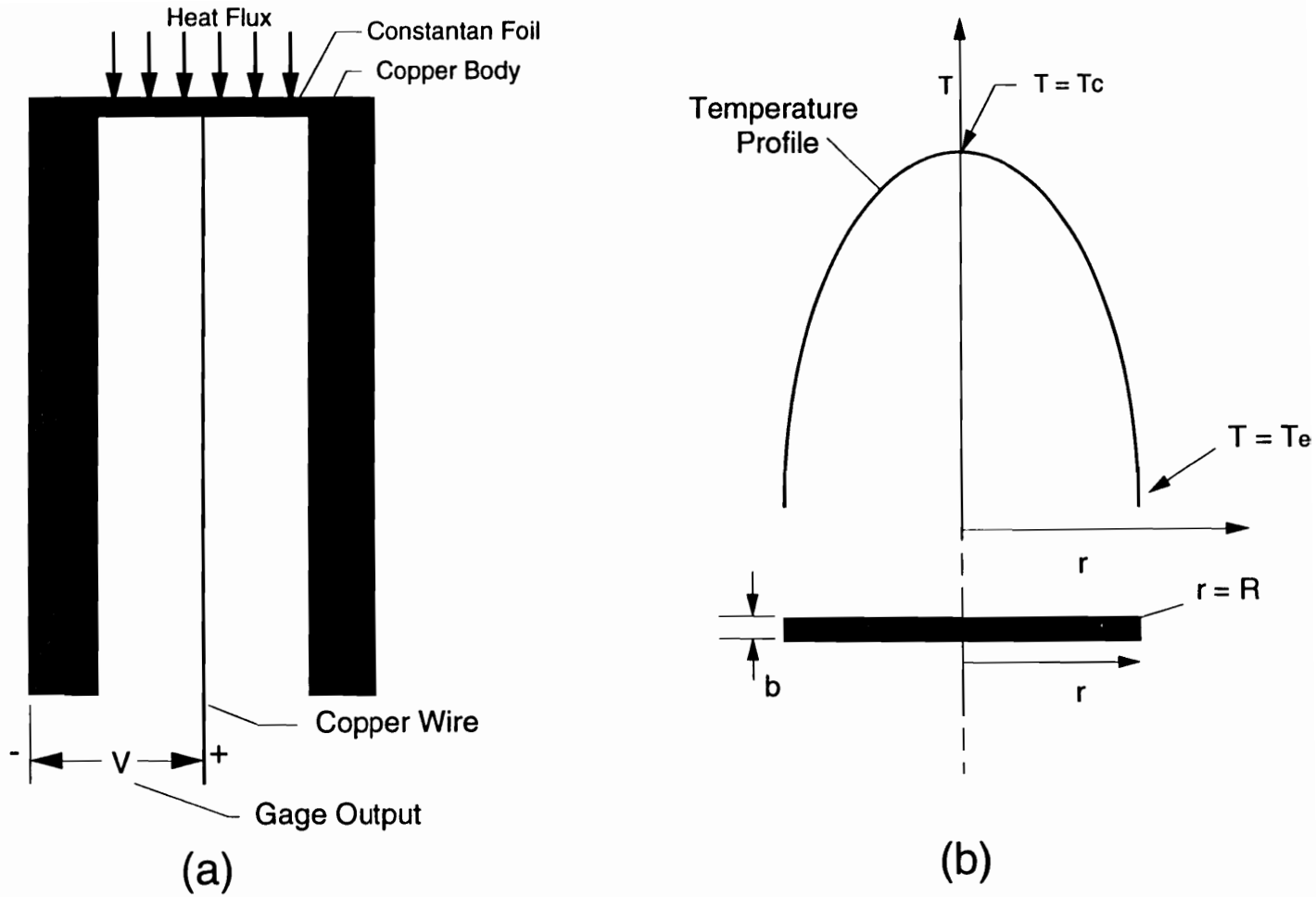

Figure 3.2 Gardon Gage: (a) Schematic (b) Radial Temperature Profile

The relationship between a constant heat flux to the foil surface and the resultant temperature difference between the center and the outside of the foil, which is shown in Fig. 3.2b, can be found by solving the following differential equation:

$$\frac{-q}{bk} = \frac{1}{r}\frac{\partial T}{\partial r} + \frac{\partial^2 T}{\partial r^2} \tag{3-1}$$

with the boundary conditions : $T = T_e$ at $r = R$
and $dT/dr = 0$ at $r = 0$.

Where k is the thermal conductivity, b is the thickness of the gage foil, and R is the radius of the foil. The solution to this equation is given by:

$$T = T_e + q\frac{R^2 - r^2}{4kb} \tag{3-2}$$

Thus, the relationship between the heat flux and the temperature difference between the edge and the center of the foil is given by:

$$q = (T_c - T_e)4kb / R^2. \tag{3-3}$$

Since the radius and the thickness of the foil are constant the flux can be expressed as: $q = Ak(T_c - T_e)$ where A is a constant of the geometry, and the conductivity is evaluated at the mean foil temperature.

The temperature difference is measured by two type T (copper vs. constantan) thermocouples. The thermoelectric potential of this pair is well known[83] and can be fitted with a third order polynomial. The thermal conductivity of constantan foil is a linear function of temperature between 270 and 1200 K.[84,85] Thus, the sensitivity, S, may be calculated by the following expression:

$$S = \frac{\Delta EMF}{q} = \left[\frac{a_1(T_c - T_e) + a_2(T_c^2 - T_e^2) + a_3(T_c^3 - T_e^3)}{Ak_o(1 + 0.5\alpha(Tc + Te))(T_c - T_e)}\right] \tag{3-4}$$

where a_1, a_2, and a_3 are coefficients for the thermoelectric potential and k_o and α are the constants in the linear relationship of conductivity vs. temperature. Gardon[81] reasoned that, at low temperatures, the third order term of the temperature can be neglected with an error (in the thermoelectric potential) of less than 2.5 % at 190 C and 5 % at 300 C. With this assumption, the sensitivity is written as follows:

$$S = \frac{\Delta EMF}{q} = A'\left[\frac{1+\beta(T_c+T_e)}{1+\gamma(T_c+T_e)}\right] \qquad (3\text{-}5)$$

where A', β , and γ are constants. Fortuitously, Gardon also found that the constants β and γ are approximately the same for gages with constantan foil and copper bodies, so that the sensitivity is not strongly dependent on the gage temperature at low gage temperatures.

3.3.2 Gages and Installation in the Present Investigation

Two different models of Gardon gages made by Thermogauge were used for the present investigation. The dimensions of both gauges are given in Table 3.1. The sensitivity of each of the gauges was obtained by a radiation calibration (see Appendix C) and ranged from 1.6 to 1.96 mV/(MW/m^2). The response time, which was supplied by the manufacturer, is also listed in Table 3.1. Both gauge types were mounted in water-cooled copper tubes with an outside diameter of 7.9 mm. At the initiation of this research there were 12 gages of type 1 available. Because of concern about possible temperature-mismatch effects, 14 additional gages of type 2 were acquired. These gages were equipped with an additional thermocouple to measure the temperature at the junction of the foil edge and the copper body.

Table 3.1 Dimensions of the Heat Flux Gauges.

Type	Foil Diameter (mm)	Wire Diameter (mm)	Foil Thickness (mm)	Edge Thermocouple	Response Time (sec)
1	1.0	0.05	0.064	no	0.10
2	2.0	0.05	0.25	yes	0.22

Swagelok compression fittings with Teflon ferrules were used to mount a maximum of 24 heat flux gages flush with the internal combustor wall. Seventy-eight gage locations were machined into the top and bottom walls of the combustor. Gages were either placed in line with one of the two center fuel injectors or in line with the interstice between two adjacent injectors. In order to map the heat flux with a limited number of gages, the gages were moved between each series of tests. Composite heat flux distributions were formed from tests that have similar combustor inlet conditions and fuel

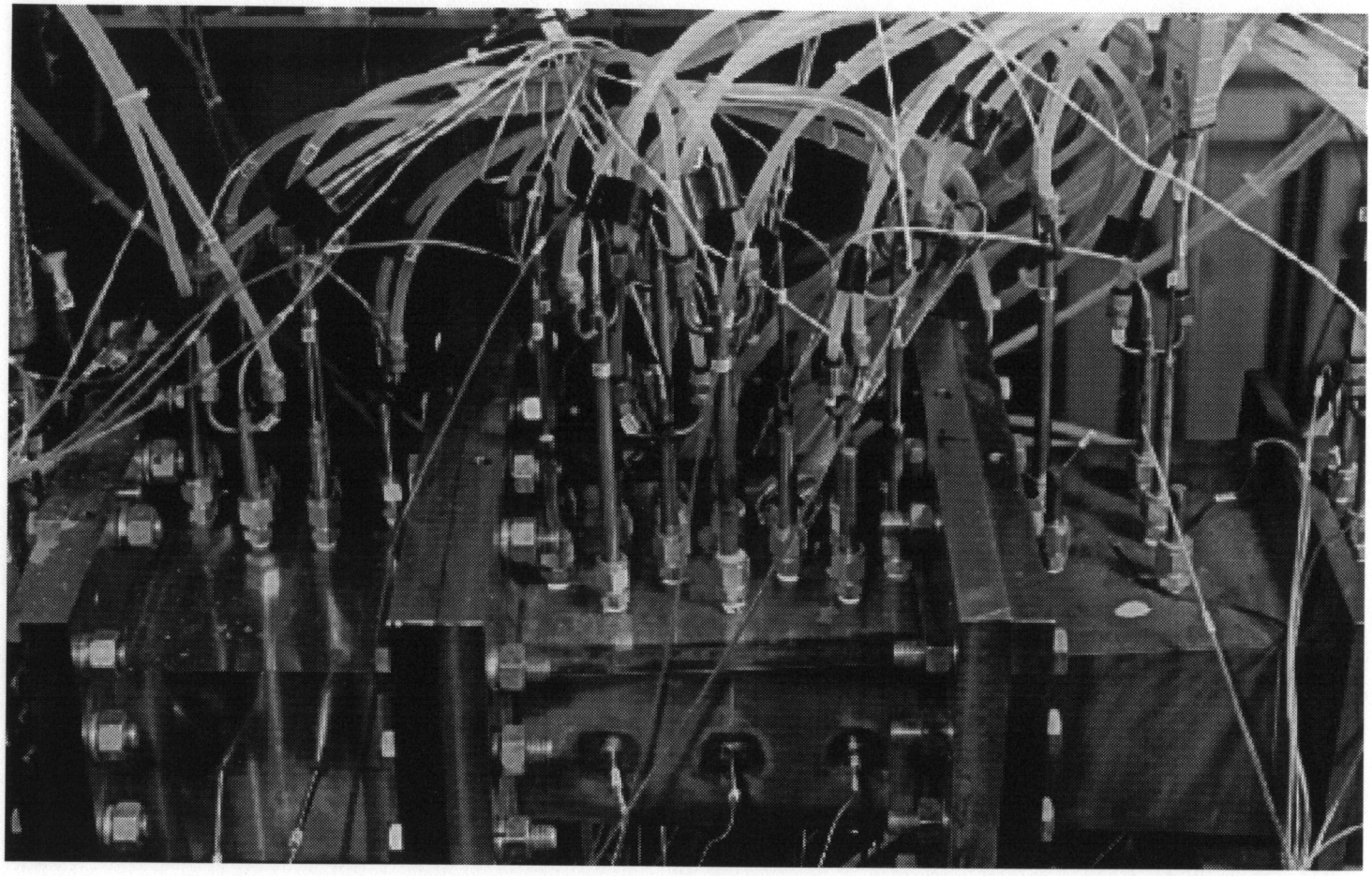

Figure 3.3 Close-Up of Gardon Heat Flux Gages Installed in the Combustor Walls.

equivalence ratios. Figure 3.3 is a photograph of the top of the combustor showing the heat flux gages along with the required cooling tubes and wiring.

3.3.3 Uncertainty Factors in the Use of Gardon Gages

While it is true that the Gardon gage provides an output that is proportional to the flux at the foil surface, there are other factors that need to be considered in the application of the Gardon gage to high heat flux environments. These factors can be separated into two categories:

1. Departures of the gage sensitivity from the idealized model.
2. Installation effects due to temperature mismatch with the wall.

The first category includes the effect of conduction by the center wire and the effect of neglecting the higher order terms in the thermoelectric potential at higher temperatures. The second category is due to the difference between the gage surface temperature and the surrounding wall temperature. Note that even if the edge temperature matches the surrounding temperature, the center of the foil will be at a higher temperature. Thus, it is impossible to measure the wall heat flux without changing it by changing the wall temperature profile. An uncertainty analysis is given in Appendix C that quantifies the above mentioned effects for the gages used in this research.

3.4 Data Acquisition System

A computer-based data acquisition system was used to record measurements. A Neff 620200 amplifier and analog to digital converter (A/D) were used to measure the output voltages of the various gages. Data was collected at a rate of 5 Hz. The resolution of this system was 14 bits. Further specifications of the A/D along with an error analysis are given in Appendix A. The digitized data from the A/D was recorded on a MODCOMP 92500 computer.

3.5 Flow Visualization

3.5.1 Mie Scattering Background

Mie scattering was used to qualitatively visualize the reacted fuel distribution in the combustor. Mie scattering is elastic light scattering by particles that are roughly the same size as the wavelength of the incident light. The intensity of the scattered light is dependent on the intensity and

polarization of the incident light, the size of the particles relative to the wavelength of the light, the particle index of refraction, and the scattering angle. The solution of this problem was first presented by Mie.[86] Solutions to the Mie scattering problem as well as other elastic light scattering problems are presented in a book by van de Hulst.[87] Although a strict definition of Mie scattering only applies to spherical particles, the term Mie scattering is commonly used to describe the scattering by arbitrarily shaped particles that are roughly the same size as the wavelength of the incident light. The same convention is used here. Several other researchers have also used this technique. A brief discussion of Mie scattering for flow visualization in previous experiments is presented in this section.

Mie scattering by water vapor droplets formed in the expansion of a supersonic wind tunnel was first used by McGregor[88] to study the large scale vortices formed by flow over a delta wing. This study was conducted before the availability of lasers, so a mercury lamp was used to illuminate the particles. Most subsequent studies have used lasers as a light source.

Mie scattering has also been used to study mixing in compressible planar shear layers by Clemens et al.[89] and Messersmith et al.[90] In these studies the mixing was studied by seeding one of the air streams upstream of the splitter plate with ethanol at temperatures high enough to prevent condensation. Condensation occurred as the vapor-laden air stream mixed with an air stream that was below the saturation temperature of the ethanol. Imaging of the ethanol droplets allowed the molecular-level mixing to be studied. Short pulse length lasers were used to freeze the motion in both studies. Cattafesta and Settles[91] also used ethanol as a particle seed in order to study shock-vortex interaction downstream of an over-expanded swirling supersonic jet. In their study, the ethanol seed crystallized after expansion through the nozzle and melted after passing through a normal shock.

Product formation has also been used to generate seed particles for flow visualization. The reaction of steam with $TiCl_4$, which forms solid TiO2 particles, has been used by Wey et al.[92] to study a reacting shear layer. One drawback of this method is that toxic HCl is also produced by the reaction.

Smith and Northam[93] used silane-seeded hydrogen to provide instantaneous flow visualization in a reacting supersonic flow. Silane (SiH4), a pyrophoric compound, reacts when it mixes with air. A mixture of 20 % silane and 80 % hydrogen was used as the fuel. When the fuel mixture reacted, so did the silane, forming small solid silica (SiO_2) particles as a product. Silica is a solid powder that melts at 1950 K, and vaporizes above 2500 K. If the local conditions in the combustor are such that the kinetics of the hydrogen/air reaction is not significantly altered by the presence of the silane, then the silica particles generated can be used to provide visualization of the products of the hydrogen/air reaction. These conditions can occur in regions of the combustor with high static temperatures and velocities low enough so that the rate of reaction is mainly mixing-limited rather than kinetically limited.

Although no measurements were made of the silica particle size, they are thought to be small. Previous measurements of the silica particle size in counterflow diffusion flames by Zachariah et al.[94] have shown that most of the particles had effective diameters in the range of 0.1 to 0.25 μm.

All of the silane flow visualization tests conducted by Smith and Northam[93] were conducted in semi-free jet mode. That is, several walls of the combustor were removed for optical access. The light source used for the light sheet was a frequency-doubled (532 nm), pulsed Nd:YAG laser. Because of the short pulse length (10 ns), the motion of the particles was effectively stopped in time, providing instantaneous visualization of the extent of the products. With the powerful (100 mJ per pulse) laser, the signal from the silane particles was strong enough that, even with the camera set at f/22, neutral density filters were required to avoid camera saturation. It was noted that the fraction of silane required for effective visualization could probably be reduced significantly.

3.5.2 Present Study

In the silane flow visualization experiments conducted for the present study, the goal was to visualize the distribution of the combustion products across the closed combustor. The images that were acquired during the test qualitatively represent the average extent of the reacted product across the

combustor duct. Obtaining optical access to the severe thermal environment of the combustor required several design modifications to the combustor hardware that will be discussed below. Also, because of the possible density ratio effects on mixing, an effort was made to use lower silane concentrations than had been used previously.

3.5.3 Design of the Optical System

Optical access to the tunnel was obtained by using three slits cut into a 50 mm long flange which was mounted between the combustor ducts. Figure 3.4 shows the design of the novel optical system that was developed for this study. During operation, a continuous-wave laser beam that shines vertically through the top of the combustor is scanned across the width of the combustor. While the laser was scanned across the top of the combustor, a small mirror was used to scan the scattered light, viewed from a slit in the side of the combustor, across the detector of a CCD camera. The exposure time of the camera was slightly greater than that of the scan time. Therefore, the image that was formed is that of an average image of Mie-scattered light that would be seen looking upstream from the exit of the combustor.

The laser used for the tests was a continuos-wave, argon-ion laser. The laser was operated at a single line (λ = 514.5 nm). The laser power output was up to 5 W, as indicated by the built-in power meter. However, the power output was restricted to less than 2.5 W to avoid damaging the first scanning mirror. The light from the laser first passes through a polarization rotator to achieve correct polarization of the beam. A mirror that was mounted on a galvanometer-driven scanner was used to rotate the laser beam at a constant angular rate. A folding mirror, that was attached to the top of the combustor, was then used to direct the light vertically though the test section, resulting in an almost vertical beam of light that was moved across the test section at a constant rate. Because the laser scanner was mounted on the wall of the test cell, approximately 3.3 m away from the combustor, the maximum departure of the beam angle from the vertical was limited to 1.6 degrees. The same ramp signal that was used to drive the laser scanner was also used to drive a small mirror mounted on a scanner in front of the CCD camera.

A Photometrics AT 200 CCD camera system was used to acquire the images. A photograph of the camera and the camera scanner is shown in Fig. 3.5. The camera and scanner were mounted on a tripod that was bolted to the floor and weighted down to reduce vibrations. The dynamic range of the camera was 14 bits. The CCD was thermoelectrically-cooled to -40 C to reduce the dark current noise. The camera was controlled from a personal computer using the PMIS software. The exposure time for the CCD was software-adjustable between 0.1 ms and 9999 s. For the present series of tests, the exposure time was set to slightly longer than the 1/4 second laser scan time. The software also allowed selection of any rectangular portion of the square (512x512) pixel array to be read as the image. Typically, the width of the image was set to 512 pixels and the number of pixels in the vertical direction was adjusted to fit the height of the combustor section. The camera also allowed "binning" of an integer number of pixels into a larger pixel. The intensity of the resultant pixel is the average of the component pixels. Binning is used to reduce the number of pixels in the image, which reduced the time required to read the CCD and the storage requirements of the images, at the expense of decreased spatial resolution. During most of the tests, the bin factor was set equal to two in each direction, so that four pixels were averaged and read as one pixel.

The camera controller, which was triggered by a personal computer, opened the shutter on the camera, and triggered the sweep generator, which operated the scanners. Subroutines written in the camera control software were used to acquire a sequence of ten images during each test. The speed of the camera scanner was the limiting factor in the scan speed (scan period $\geq$1/4 s). The time between images was limited by the time to reset the scanners and download the image data to the computer. The camera was started after the vitiated heater was turned on. Images were acquired while the silane seeding was on, as well as before and after the silane was turned on. Typically, three to four images were taken while the silane seeding was on.

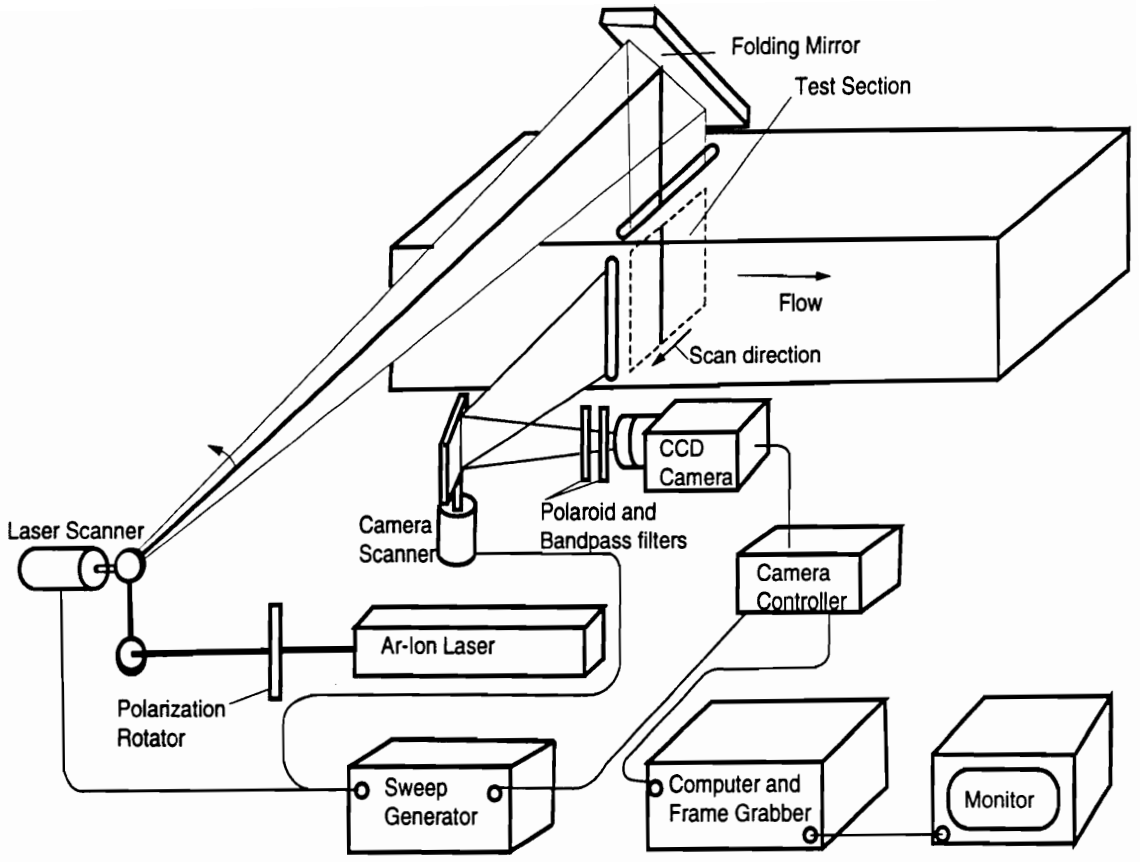

Figure 3.4 Schematic of the Optical System Used for the Mie Scattering Images.

Bandpass and Polaroid filters were used to improve the contrast of the scattered light from the luminosity of the hot silica particles and the hot combustor walls. A 2 nm wide bandpass filter centered at the wavelength of the laser was mounted in front of the camera. The rotation of the polarization was used to assure that the light is properly polarized when it illuminated the particles. Theoretically, for small spheres at a 90 degree scattering angle, the reflected intensity of light polarized perpendicularly to the plane defined by the incident light and the receiving optics is much greater than that of light polarized parallel to this plane. A Polaroid filter mounted in front of the camera was used to further discriminate between the randomly polarized light and the polarized scattered laser light.

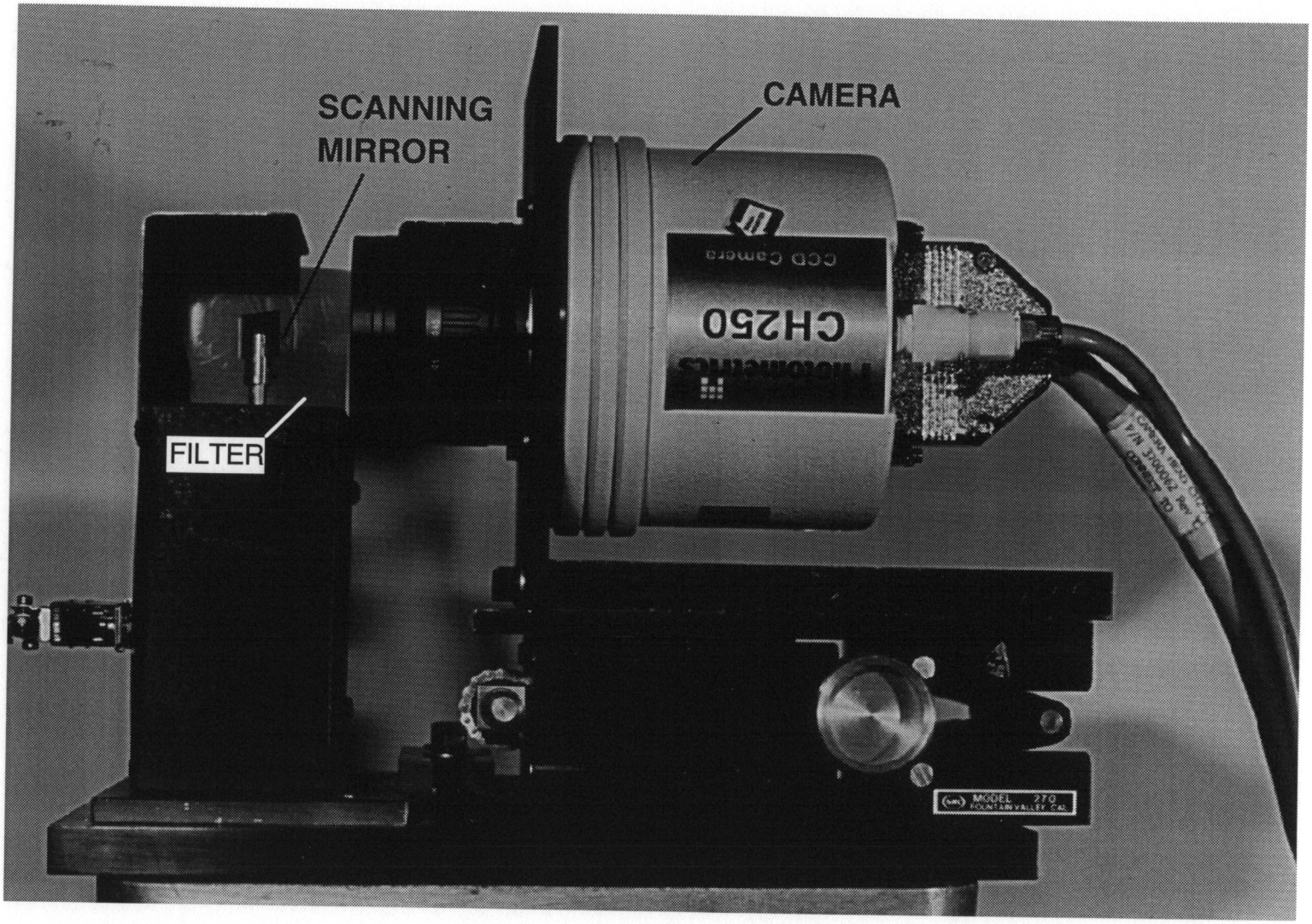

Figure 3.5 Photograph of Camera and Scanning Mirror.

3.5.4 Optical Access

The window design that was used for optical access is illustrated in Fig. 3.6. The window design was based around a single flange made of stainless steel with 6.4 mm-wide slots on the top and sides for optical access. Three sets of four insert pieces were machined out of stainless steel to match the internal dimensions of the tunnel at each of the three axial test sections. The inserts were designed to allow thermal expansion in order to prevent warping due to thermal stresses. All of the inserts had 3.2 mm wide slots for optical access. The slot in the bottom of the insert was used as a light trap for the incident beam of light.

The windows were constructed of 12.7 mm thick quartz and were first mounted on the outside surface of the flange between an aluminum plate and a rubber gasket. Although the windows were separated from the flow by more than 100 mm, silica particles, moisture, and other tunnel debris quickly clouded the windows. Therefore, purge window assemblies were designed. Figure 3.6 shows a cross-sectional view of the purge system mounted on the outside of the flange. High pressure air was blown through narrow slits on both sides of the slot, creating a high velocity flow across the window surface, to purge debris without large (potentially disruptive) additions of air flow to the tunnel. The purge air cooled the window enough to condense the humid room air on the outside of the windows. Therefore, a single purge tube was used to blow dry air across the outside surface of the window. The side window was mounted on an aluminum box offset about 200 mm from the flange and was purged with the flow from a single tube mounted at one side of the window.

3.5.5 Silane Seeding

A large quantity of premixed 20 % silane-80 % hydrogen by volume was available for silane seeding. For the flow visualization tests it was desired to mix a smaller fraction of silane with the fuel. Figure 3.7 shows the apparatus used to dilute the silane concentration. The 20/80 silane-hydrogen mixture was injected normally through a small orifice (3.18 mm or 2.36 mm) into the subsonic main hydrogen fuel line. The silane/hydrogen was allowed to mix with the hydrogen in the 8m-long main fuel line before entering the

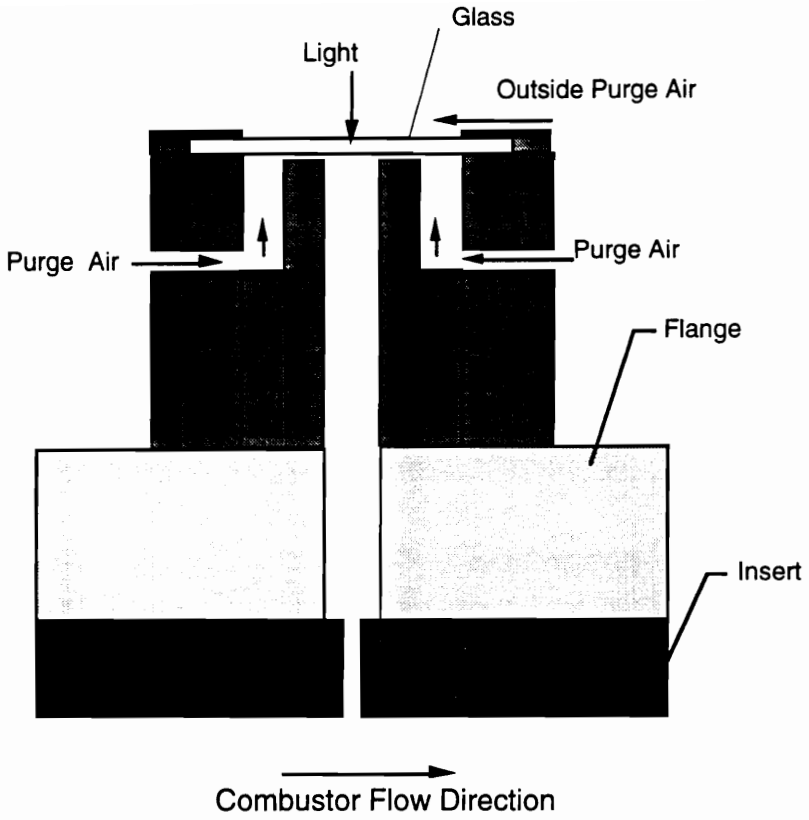

Figure 3.6. The Purge Window Assembly for the Top Window.

fuel injector manifold. It was assumed that the length of the fuel line was sufficient to allow the silane and hydrogen to be completely mixed. The pressure ratio across the silane orifice was sufficient to choke it. The amount of silane added to the fuel was increased by either increasing the pressure or the orifice area. After performing a calibration of the discharge coefficient of the orifices, the mass flow of silane added to the main flow was calculated from measurements of the pressure and temperature upstream of the orifice. The silane flow rate was used along with the fuel and heater massflow rates to calculate the silane mole fraction and equivalence ratio (based on hydrogen flow).

Because silane is pyrophoric, special precautions were taken to assure that the silane could not propagate upstream into the hydrogen storage trailers or accumulate elsewhere in the fuel lines where oxygen can ignite it.

The valve that controls the silane mass flow was triggered by the PLC to open after the main fuel flow was turned on. About 1/2 second before the end of the run the silane was turned off and a high pressure purge of hydrogen was used to sweep the rest of the silane out of the fuel lines.

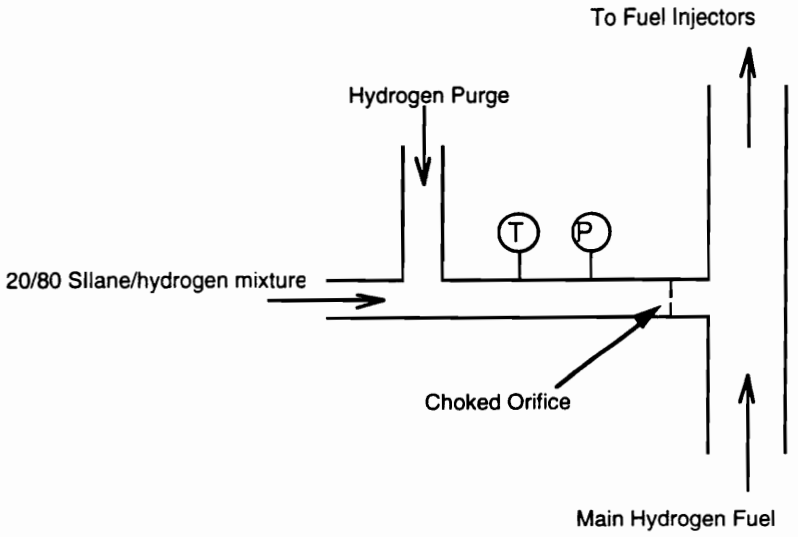

Figure 3.7 Silane Seeding and Metering Apparatus.

3.5.6 Image Processing

The images were processed on a workstation using the PV-WAVE command language, a commercially available language that is similar to the language APL. Subroutines were created in this language for image enhancement. A brief description of the sequence of the processing steps is presented below.

The first step in the sequence was to read the raw image files and store them in a form readable by the PV-WAVE routine. The images for each run were then sorted into images obtained with the fuel on and those with fuel off (background images). During a typical test, three to four images were obtained with the fuel on, while the rest were background images. The background images were summed and divided by the number of background images to obtain an average background. The average background image

was then smoothed using a 5x5 kernel before subtracting it from each of the fuel-on images.

Because the camera was closer to the one side of the combustor, a geometrical distortion due to the change in magnification across the image was introduced into each of the images. This effect is shown in Fig. 3.8a. In addition, the aspect ratio of the image was not equal to the actual aspect ratio of the tunnel cross-section, resulting in different spatial resolutions in the vertical and horizontal directions. This effect is shown in Fig. 3.8b. The combined effect of these two distortion sources is shown in Fig. 3.8c. The PV-WAVE routines POLYWARP and POLY-2D[95] were used to correct for distortion. Given four pixel locations on the distorted images (control points) and the four corresponding ideal pixel locations, the POLYWARP routine was used to calculate the coefficients to be used in a first degree polynomial transformation. The routine POLY-2D was then used to perform the distortion correction.

Two of the control points for the warping were determined by imaging a triangular Plexiglas wedge which ran diagonally, almost corner to corner, across the cross-section. The intersections of the wedge and the wall were chosen as control points. The other two control points were the other two corners of the tunnel, which were selected by examining images obtained while spraying small droplets into the tunnel cross-section. After selecting the four control points, the original image of the wedge was corrected using the transformation, printed out to size, and compared to the actual wedge as a test of the correction procedure.

Vertical striations occurred in the images obtained during tunnel operation. It is thought that the striations were caused by the relative motion of the tunnel and scanners. The first strategy to correct for this was to determine the spatial frequencies of the striations by calculating the Fourier transform for each row of the image and subtract the peaks due to the striations. This method did not work because the frequencies due to vibrations were in the same region as the spatial frequencies used to represent the image.

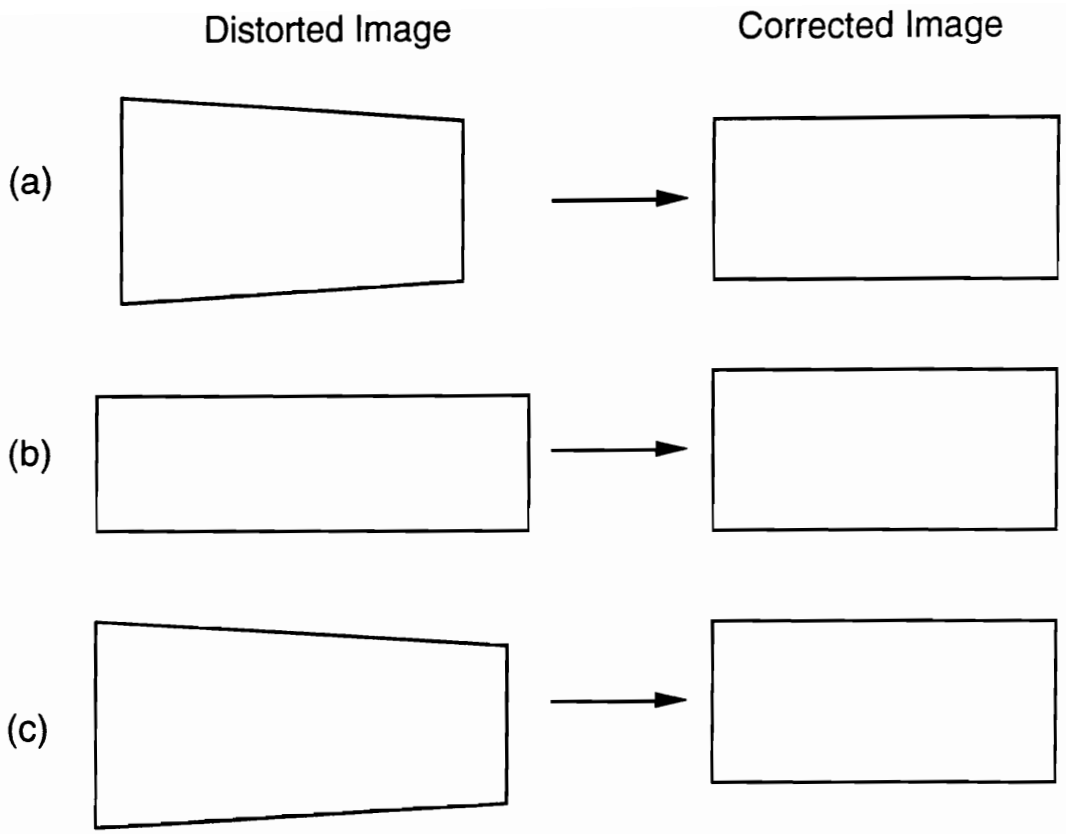

Figure 3.8 Image Distortion Mechanisms:(a) Magnification (b) Unequal Pixel Resolution (c) Combined Effects.

The method used to correct for the striations was convolution of the image array. The convolution used a 13x13 kernel that had elements equal to zero on all rows except for the center row. On the centerline of the kernel, the elements had a Gaussian distribution with a peak at the center element. The effect of convolution of the image with the kernel was that the intensity of each pixel in the resultant image was a Gaussian-weighted sum of the pixel and the six pixels before and after it in the same row of the original image.

The images were then averaged to form an average image. Typically three to four separate images were used to form the average image for each run. The final step in the image processing procedure was the gray scale adjustment, to enhance the contrast. Figure 3.9 shows the cumulative probability distribution of the pixel intensity for a typical image. The

horizontal axis shows the pixel intensity and the vertical axis shows the fraction of pixels in the image that are lower than the intensity shown on the horizontal axis. For hardcopy output, this region was mapped to an 8 bit (0 to 255) range. The image contrast can be modified by setting the maximum and minimum values of the pixel values to different values (clipping). The low intensity side of the cumulative probability distribution corresponds to the cut-off between the (brighter) edge of the illuminated product plume and the (darker) background, which contains no particles. Note that because the cumulative probability distribution is steep at the low intensity side of the plot, the choice of the lower cut-off can vary widely without significantly changing the value of the lowest intensity pixels. The cut-off value of the high intensity side of the distribution relative to the low intensity cut-off value controls the contrast within the image. Due to the "tail" at the high intensity section of the plot, the selection cut off at the high intensity section is more difficult to set. Therefore, the contrast within the bright region of the image is sensitive to the selection of the high cut off. The gray scales of the final images were clipped at the 3 % and 97 % values of the source image. This set of cut-off values was used for all of the images.

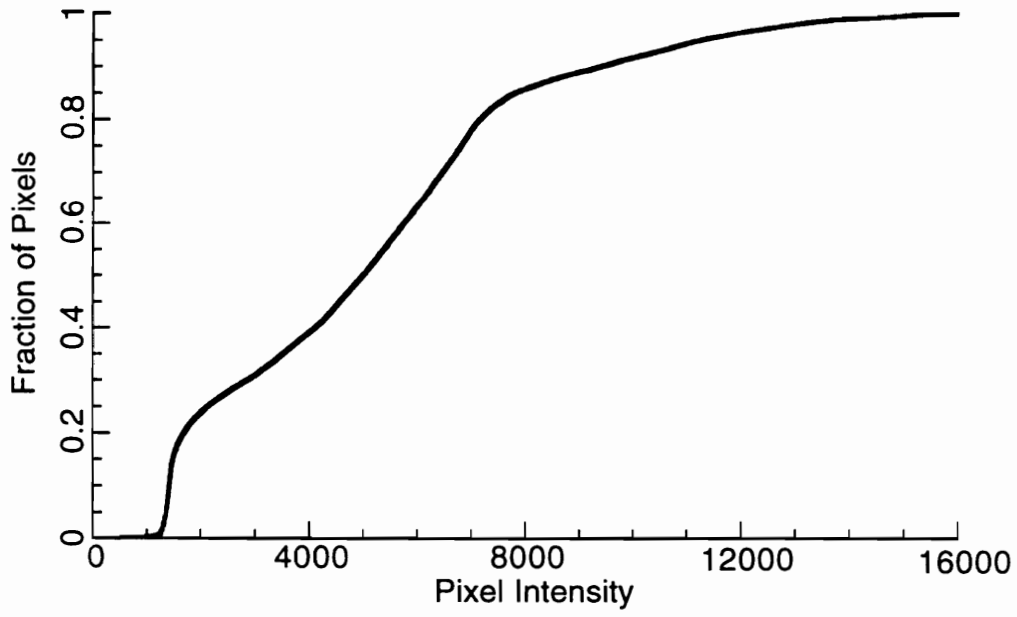

Figure 3.9 Typical Cumulative Probability Distribution of the Pixel Intensity.

Figure 3.10 shows two consecutive raw images of the Mie scattering acquired during a typical test. Figure 3.11 shows the results of applying the image processing operations to the raw images.

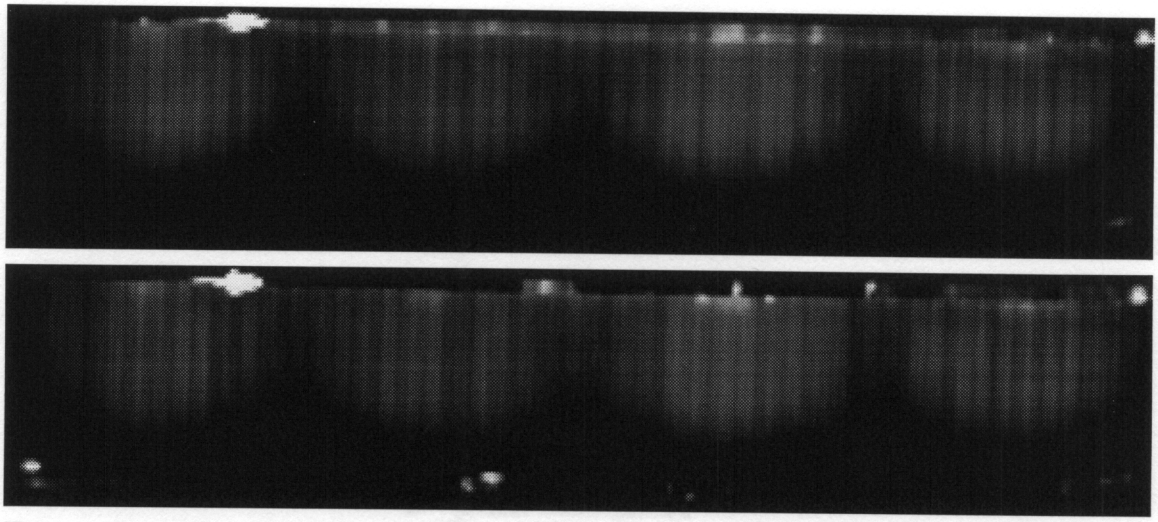

Figure 3.10 Two Consecutive Raw Images Acquired During a Single Test.

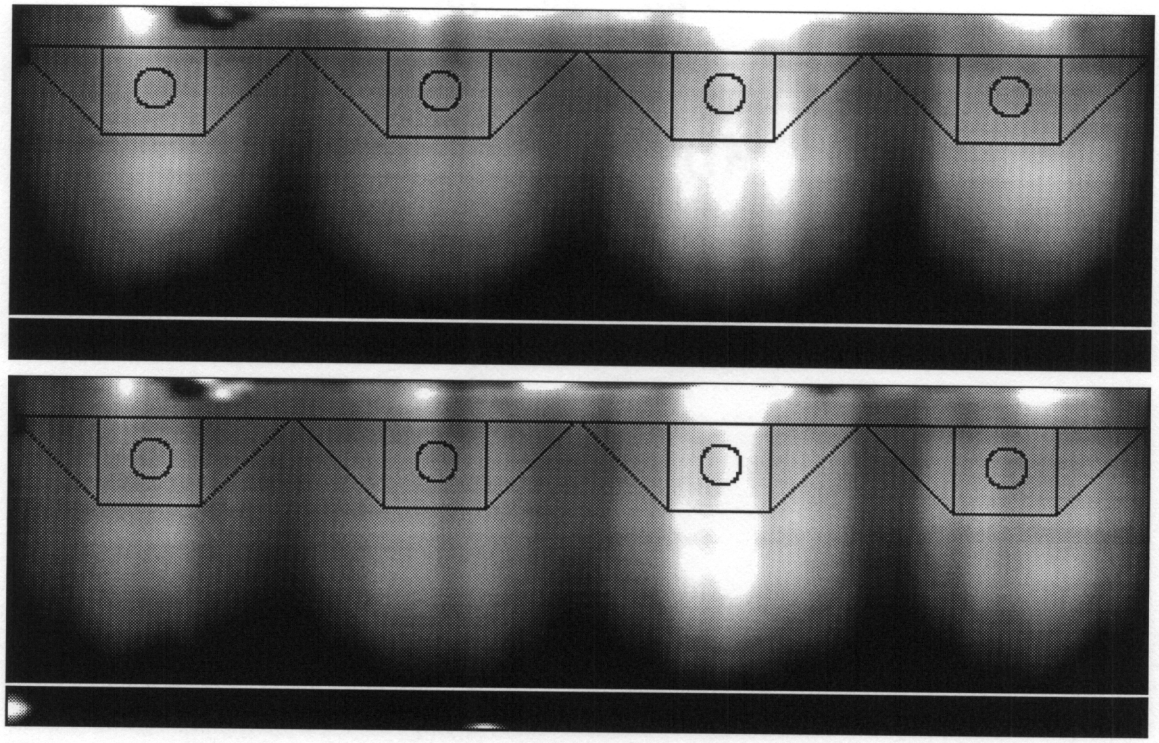

Figure 3.11 The Two Images After Image Processing Operations.

3.5.7 Limitations on Image Interpretation.

As stated earlier, the goal of the current study was to visualize the combustion products. The final processed images, which will be shown in the next chapter, qualitatively show the distribution of the combustion products. Quantitative interpretation of fuel-air mixing by interpretation of Mie scattering has been attempted by other researchers in a different experiment.[96] However, quantitative interpretation was not attempted for the present investigation because of the required assumptions, which are discussed below.

The first assumption is that of uniform incident illumination of the particles. In the experiment the incident light on the particles was not measured. Variations in the incident light could have occurred due to temporal variations in the laser intensity and/or debris on the window at the top of the combustor duct. Assuming that the flow is optically thin, a linear array camera at the bottom of the test section could be used to correct for the variation of incident light intensity with spanwise position across the combustor.

A large uncertainty in the amount of reflected light is due to the uncertainty in the size distribution of the silica particles. The intensity of the scattered light is a strong function of the particle size. Large changes in the particle size distribution could occur due to agglomeration. Optical methods, such as combined absorption and scattering measurements can be used to determine the size distribution. However, this is not a simple diagnostic to apply across the entire product plume. Further difficulties are caused by phase changes in the silica particles (melting at 1950 K, and vaporization at 2500 K). As will be shown in Chapter Five, the computed static temperatures near the injectors exceeded the vaporization temperature of silica.

3.6 Pitot Pressure Probe

3.6.1 Background

A pitot probe and traverse system was designed for use at the exit of the scramjet combustor. Pitot pressure traces were acquired to allow a comparison of instream measurements with CFD calculations. A secondary objective of the pitot surveys was to provide information for a separate study

of the effect of combustor exit conditions on the thrust produced in the nozzle.[102] The design of a pitot probe for a scramjet engine is challenging because it must be able to withstand stagnation point heating in an oxidizing environment. The stagnation temperatures in the combustor model reached 1950 K without combustion and up to 3000 K with combustion, whereas the melting point of stainless steel, a typical probe material, is 1700 K.

Previous probe designs for high-speed, high-enthalpy flows have been large water-cooled designs that dumped water over the side of the probe and into the flow causing large disturbances, particularly near the tunnel walls. A notable exception is a water-cooled probe designed by Lagen[97] that used a closed coolant system and was tested at temperatures up to 1400 K.

The goal for the current study was to create a miniature probe that could withstand high stagnation temperatures without dumping coolant into the flow. For this reason, the probe was based on an uncooled design constructed of tungsten. Tungsten has an extremely high melting point (3670 K), which is higher than the expected stagnation conditions. However, tungsten has the drawback that it oxidizes at high temperatures. Most handbooks state that tungsten, as well as other refractory metals (molybdenum, tantalum, and rhenium), "rapidly" oxidize at high temperatures. It was not known at the beginning of this design effort how fast the tungsten would oxidize in this environment. Data on the recession rates of these metals as a function of temperature and pressure is available,[98] however, nearly all of it applies to quiescent flows. It was thought that the oxidation rates would be worse due to the erosion of the tungsten oxide layer in the high-speed oxidizing flow. One approach around the oxidation problem is to coat the refractory metal with a non-oxidizing coating. Examples are $MoSi_2$, and Iridium film on Rhenium.[99]

Several design constraints were imposed on the probe and probe support. First, it was desired to traverse from the top to the bottom of the combustor while maintaining a seal between the combustor flow and the outside. In addition, the probe and traverse mechanism had to fit within a 51 mm-long flange section that was mounted between the combustor exit and the scramjet nozzle model entrance.

3.6.2 Probe Design

A drawing of the probe and probe support is shown in Fig. 3.12. The pitot probe was made out of a 3.2 mm-dia. x 16.5 mm-long tungsten rod. The hole was burned through the rod by electrode discharge machining (EDM). The design of the probe support was based around cooled stainless steel tubes. Although it is readily recognized that the drag is large for a cylinder compared to a wedge or diamond cross-section, a cylinder fits within the short flange section and could be readily sealed with an O-ring. The probe support centerpiece was machined out of stainless steel and was welded to the two AISI 347 stainless steel tubes (12.7 mm-dia. x 1.24 mm-thick) a TIG tube welder. The tungsten probe was press-fitted into the center piece and sealed with high-temperature silver solder.

The probe support was cooled by high pressure water. The coolant flow rates and pressures were selected to provide forced convection cooling of the interior of the probe support without boiling the water. Although the heat transfer coefficient is known to increase with incipient boiling, it also drops (catastrophically) once a layer of vapor is formed. Thus, the increase of film coefficient with boiling was viewed as an added safety factor. To provide maximum cooling with a minimum amount of coolant, an narrow annular passage was created between the outer tubes of the probe support and the spacer rod and tube. Slots for the water cooling passages in the probe center piece were burned out by using EDM. The coolant flow rate was set at 26 liters/min with an inlet pressure of 2.4 MPa. The coolant exit pressure was set at 1.4 MPa in order to increase the boiling point of the coolant from 100 C to 194 C, allowing the heat transfer from the interior walls to be increased.

A brief summary of the stress and heat transfer analysis of the probe design is presented in Appendix D. The complete set of design drawings for the probe and associated hardware is available from the NASA-Langley drawing files under the numbers 1099136-1099143.

The probe was installed in a flange that was fitted between the combustor and nozzle so that it could be traversed, from top to bottom, along the centerline of the combustor. A photograph of the flange, probe, and

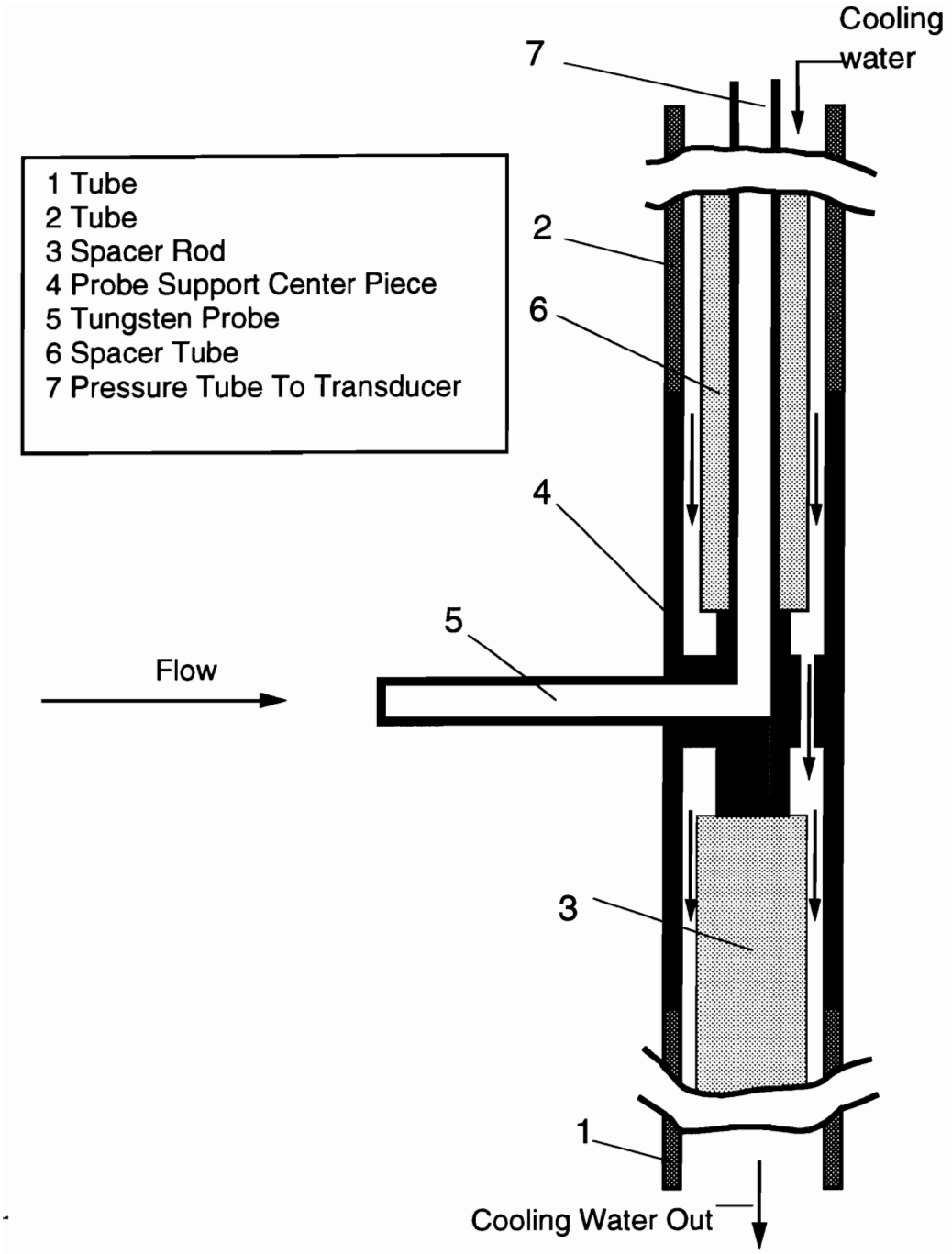

Figure 3.12 Schematic of Probe and Probe Support Tube.

traverse mechanism is shown in Fig. 3.13. The flange was split so that it could be assembled around the probe. Four oil-soaked, sintered bronze, journal bearings were used to guide the probe through the flange. An inner frame piece that was fitted inside the flange was used to hold two of the bearings in place. The frame also provided 12 mm deep recesses on each side of the probe travel so that the probe could be retracted from the flow in order to limit exposure to the tunnel flow. Leakage to the inside of the tunnel was prevented by two O-rings that were installed on the outside of the flange.

A close-up of the probe and the probe recess region of the flange is sketched in Fig. 3.14. Because the tip of the probe was mounted two probe diameters behind the corner of the recess, the interaction of the probe with the expansion-fan compromised the measurements of the pitot pressure near the walls. A minimum height, z_{min}, beyond which the expansion fan had little influence, was calculated. The distance, z_{min}, was calculated by adding 1 probe diameter to the position at which the probe crossed the expansion fan at the lowest average combustor exit Mach number (M_e = 1.7). Using this criterion, the pitot pressures within z/G = 0.1 of each wall were effected by the expansion and are not included in the results.

The probe drive mechanism was a commercial unit (Thompson Power Slide) which used a stepper motor to drive a ball screw/slider mechanism. The stepper motor controller was programmed from a personal computer over an RS-232 interface. The probe could be traversed across the tunnel at speeds up to 300 mm/s. Typical traverses across the tunnel were performed in 2 seconds. The velocity was constant over most of the traverse, with a short acceleration length at each side of the scan. The position of the probe was monitored by reading the output of a linear potentiometer that was calibrated before the tests. Data from the pressure transducer and potentiometer were acquired on a separate microcomputer-based data acquisition system at a rate of 60 Hz. The fuel and heater pressure were also acquired to allow comparison of data with the other facility parameters, which were recorded on the main computer at a much slower speed.

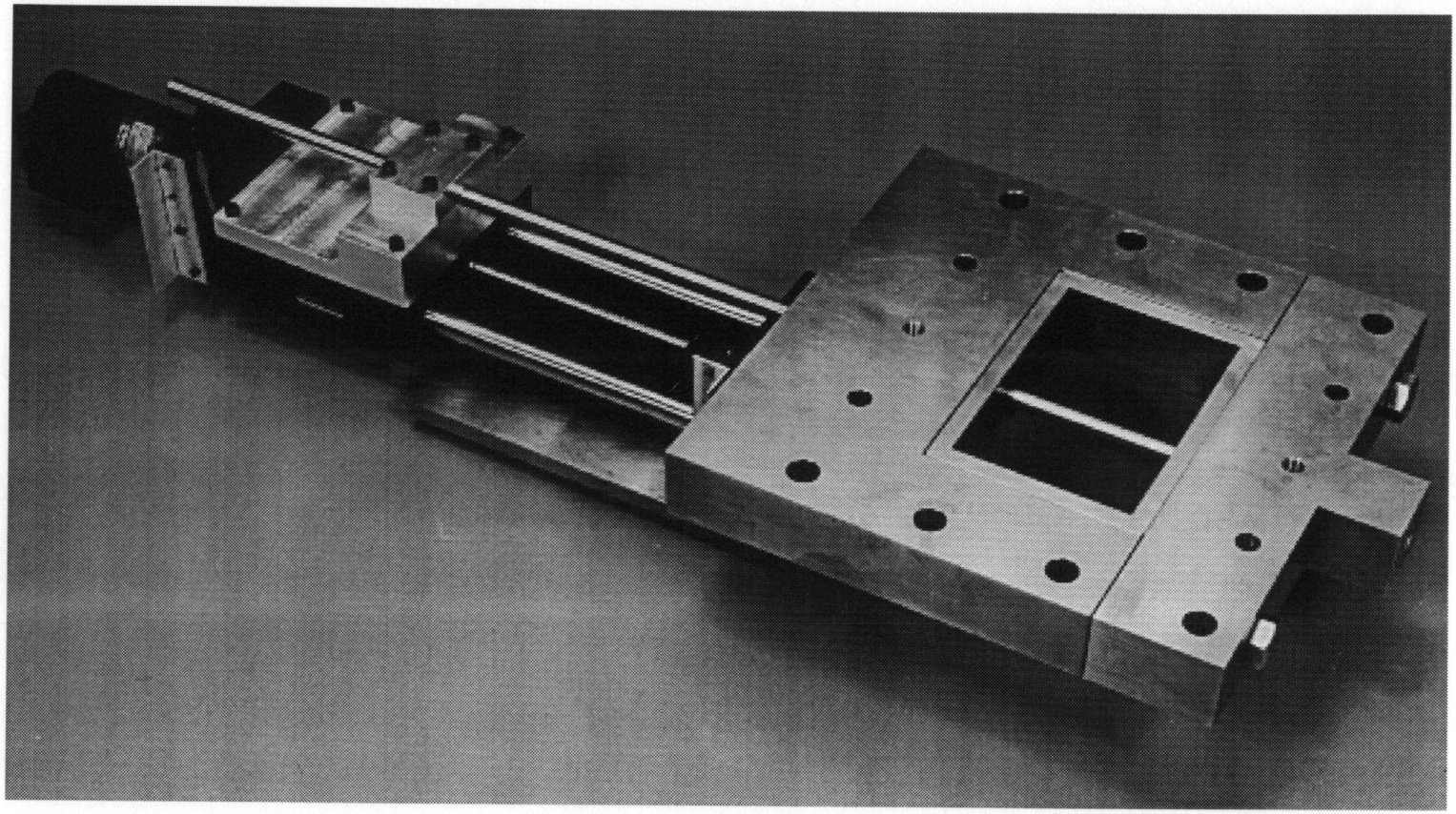

Figure 3.13 Photo of Probe Traversing Mechanism and Mounting Flange.

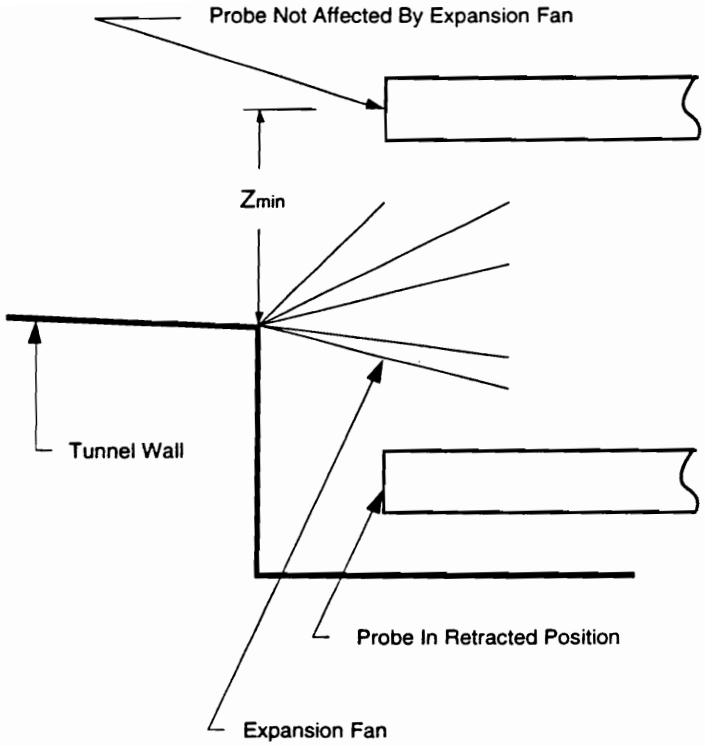

Figure 3.14 Effect of the Probe Recess on the Near-Wall Pitot Pressure Measurements.

The frequency response of the probe was a major concern. The temporal response of the pressure tube-transducer system increases with pressure, and internal tube diameter, and decreases with increases in tube length and volume. The internal tube diameter was set at a large diameter (1.8 mm) to allow fast response. The volume at the end of the pressure tube was minimized by using a small, fast (125 kHz) pressure transducer (Kulite XTME-190). The actual probe response time was not measured; however, bi-directional scans across the tunnel at twice the speed used during most of the tests showed little difference in the measured pressures. Therefore, the time response was adequate for two-second scans across the test section.

Chapter 4
Experimental Results

4.1 Ignition and Flameholding

Auto-ignition occurred with the compression-ramp model during all of the tests. The flowfield calculations (presented in Chapter 5) show that the static temperature downstream of the ramp shock was above 1000K, which is above the commonly accepted limit (900 K) for hydrogen/air autoignition. In contrast, for the same inlet conditions, auto-ignition would not occur with the expansion-ramp model and required an auxiliary ignition source or pilot. The flow expansion between the fuel injectors in the expansion-ramp model caused lower static temperatures and pressures to occur near the fuel injection location. Although the oblique shock, created at the base of the ramp, does increase the static temperature as it passes through the fuel jet, the static temperature increase was not high enough to support autoignition. For this reason, separate pilot injectors were used to ignite the fuel. The pilots consisted of 4.8 mm-diameter normal injectors within 6.4 mm-deep, 15.9 mm-diameter cavities, on both side walls upstream of the fuel injector ramps. The first step in the ignition sequence was to start the vitiated heater. A 20/80 (by volume) silane/hydrogen mixture was first injected through the pilot injectors to initiate combustion. The silane injection was followed by injection of pilot hydrogen through the same injectors. The hydrogen jet continued to burn after the silane was turned off, supplying hot gas and radicals to the main fuel injectors downstream. The main fuel to the ramp injectors was turned on while the pilot fuel was still on, and the fuel from the ramp injectors was ignited. After the fuel from the pilot injectors was turned off, the fuel injected from the main fuel injectors continued to burn. All of the data presented for the expansion-ramp configuration were acquired without the presence of auxiliary pilot fuel flow.

Two test points were chosen for further analysis from each of the tests; one with no fuel, and one with the fuel on. A true steady-state test point did not occur during the tests because the wall temperature increased during the tests. The test points were selected by examination of the facility parameters

(stagnation pressure, temperature, and fuel flow rate), heat fluxes, and the wall pressures vs. time. A criterion of three consecutive data cycles (1 cycle = 0.2 sec) with approximately the same combustor entrance conditions was imposed to select the data for further analysis. The mean of the tunnel conditions at the selected test points were calculated along with the standard deviation from the mean for each test point. Tests with tunnel conditions that were more than two standard deviations away from the mean tunnel conditions were rejected from further analysis. The measured facility conditions are tabulated in Appendix E.

4.2 Wall Pressure Distributions

Typical pressure distributions along the centerline of the injector wall for the swept ramp injector are shown in Fig. 4.1 and 4.2. The top wall pressures are shown plotted against the gap-normalized axial position. One gap was defined as twice the distance between the top and bottom walls of the combustor upstream of the injector ramps. Therefore, one gap length, G, equals 76 mm for both of the injectors. The fuel injection location at the base of these ramps was defined as the zero axial position.

The top wall pressure distributions for the combustor with swept-compression ramps are shown in Fig. 4.1 for three typical tests with $0.5 < \phi < 1.25$, and for no fuel injection ($\phi = 0$). The peaks in the pressure distribution for the no fuel case are evidence of oblique shock waves. Because a limited number of pressure taps were used, the exact locations of the shock waves were not determined. In all but one of the tests with fuel, the pressure increased immediately downstream of the fuel injectors, indicating that the fuel reacted near the base of the injector ramps. The one test in which flameholding occurred downstream in the expanding duct is discussed in detail in Appendix F. The maximum pressure occurred in the constant area section of the combustor for $\phi \leq 1$, while the maximum pressure occurred in the diverging combustor duct for $\phi = 1.25$. The measured pressure for $\phi = 1.0$ and $\phi = 1.25$ downstream of $x/G = 2$ is approximately equal, while the pressure for the fuel-lean case is lower.

Fig. 4.2 shows the pressures upstream of the injectors for $\phi = 0$, 0.5, 1.0 and 1.25, plotted vs. the spanwise position normalized by the combustor

width. A sketch of the injector ramps is also shown in the figure. The pressure difference between the top of the ramps and the interstice, which causes formation of the axial vortices, is shown in Fig. 4.2. Note that there is little change in the pressures upstream of the fuel injectors with fuel addition, demonstrating that any combustion-induced pressure rise was confined to the region downstream of the last pressure tap upstream of the ramp base (x/G = -0.19). This is important because further propagation of the combustion-induced pressure rise upstream to the inlet would result in disastrous inlet unstart.

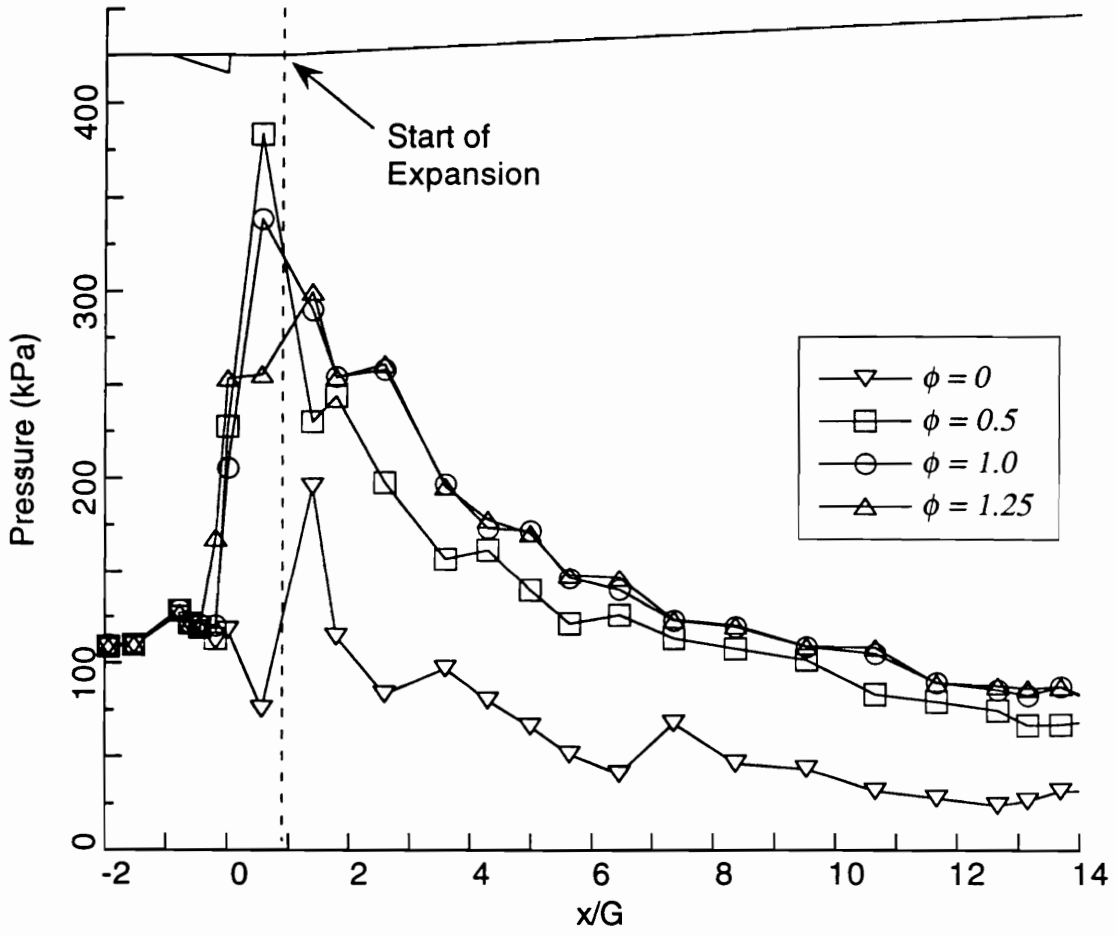

Figure 4.1 Axial Pressure Distribution Along the Injector Wall for the Swept Compression Ramp Injector.

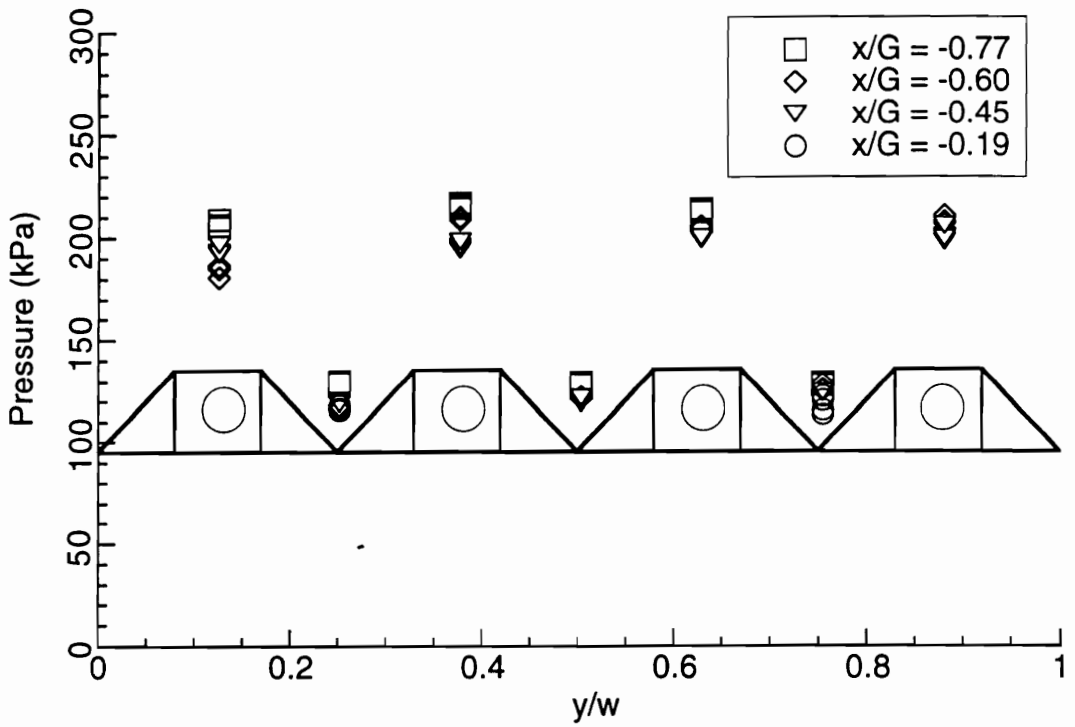

Figure 4.2 Spanwise Pressure Distributions Upstream of the Swept Compression Ramp Injector With ϕ = 0, 0.5, 1, and 1.25.

The top wall pressure distributions for the swept-expansion ramp combustor are shown in Fig. 4.3 for three typical tests with $0.5 < \phi < 1.25$ along with that for no fuel injection. The first peak at x/G = 0.6 in the pressure trace with no fuel is due to the oblique shock wave created at the beginning of the constant area section just downstream of the fuel injectors. The presence of other shocks can be seen along the rest of the combustor for ϕ = 0. The pressure at x/G = 0.6 increased with fuel addition to approximately the same value for each of the fuel settings. Downstream of the constant area section, the pressure distributions varied greatly with ϕ. In the fuel-rich case, the pressure increased due to combustion before x/G = 2.0. In contrast, in the tests with $\phi \leq 1$ the pressure decreased due to expansion in the combustor duct and did not increase until x/G = 2.4. The peak pressure occurred farther downstream as ϕ decreased. Also, the magnitude of the peak pressure decreased as ϕ decreased for $\phi < 1$. The magnitude of the peak pressures was lower than that observed in the swept-compression ramp cases.

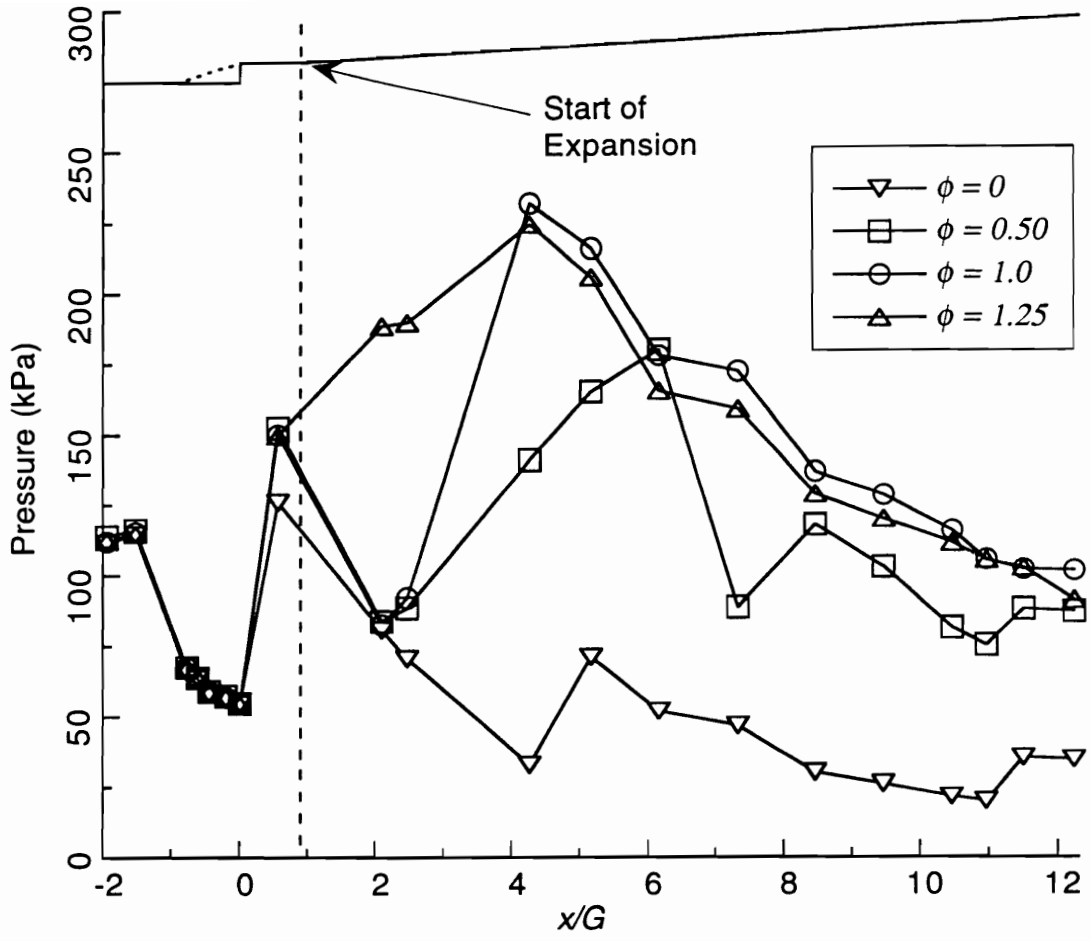

Figure 4.3 Top Wall Pressure Distribution for the Expansion Ramp Injector Configuration.

In contrast to the swept-compression ramp combustor where flameholding occurred near the ramp base, flameholding occurred in the farfield of the swept-expansion ramp after the silane pilot was turned off. Several possible ignition sources were present in the expanding combustor duct. The first was the presence of the reflected oblique shock train from the injectors. Shock-induced combustion has been observed in previous experiments elsewhere.[105-106] Another possibility is that the fuel-air mixture ignited in the boundary layer. Numerical studies have shown that ignition of hydrogen/air can occur within a turbulent boundary layer if the

viscous dissipation and/or wall temperature is high enough.[104] The large differences in the origin of the combustion-induced pressure rise shown in Fig. 4.3 imply that the flame could have been held differently depending on the equivalence ratio.

Figure 4.4 shows the spanwise pressure distribution upstream of the swept-expansion ramp injector, along with a sketch of the injector ramps. Similar to the swept-compression ramps, the large difference between the pressures on the top of the ramp and the interstice, which leads to the formation of the longitudinal vortices, is evident in Fig. 4.4. Like the swept-compression ramp model, the measured pressures upstream of the fuel injectors were the same for the fuel-on and fuel-off cases indicating no upstream propagation of the pressure rise due to combustion.

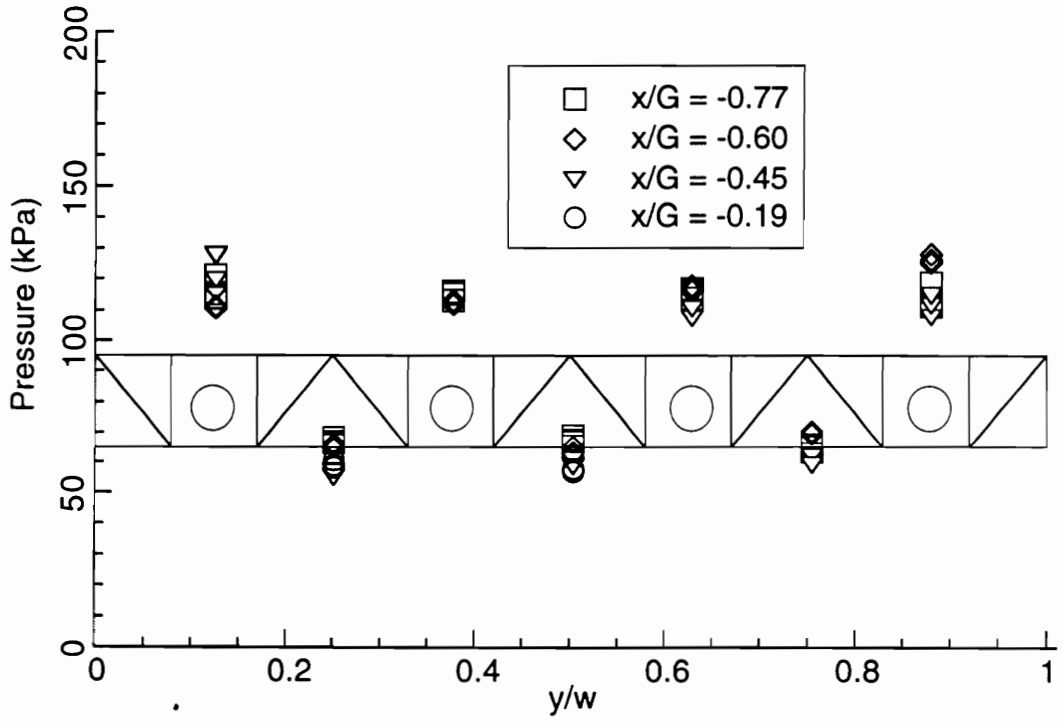

Figure 4.4 Spanwise Pressure Distributions Upstream of the Swept Expansion Ramp Injectors With ϕ = 0, 0.5, 1, and 1.25.

4.3 One-Dimensional Combustion Efficiency

The determination of combustion efficiency is one of the methods which has been used extensively in past experiments to measure SCRAMJET combustor performance. The combustion efficiency is defined as the amount of fuel that has reacted divided by amount that can possibly react, considering the overall stoichiometry. The one-dimensional combustor analysis program COMBAN, which was written by Anderson[100] of the NASA Langley Hypersonic Propulsion Branch and has been was used extensively at NASA and other laboratories, was used to calculate the combustion efficiency. The inputs to the program are the geometry of the combustor, the measured wall pressure distribution, the combustor inlet conditions, and the fuel flow rate. The chemistry was modeled with a ten-species (H_2, O_2, N_2, H_2O, O, H, OH, N, NO and Ar) equilibrium chemistry model for the hydrogen-air reaction. The skin friction and wall heat transfer are calculated by the model from van Driest.[101] With these assumptions, the program solves the one-dimensional equations of continuity, momentum, and energy conservation in a stepwise marching procedure.

The combustion efficiency, η_c, is related to the reacted equivalence ratio, ϕ_r, by

$$\eta_c = \phi_r / \phi \quad \text{for } \phi < 1, \text{ and} \qquad (4\text{-}1)$$
$$\eta_c = \phi_r / 1 \quad \text{for } \phi > 1$$

where ϕ_r is the ratio of the mass of fuel that reacts to the mass of stoichiometric fuel. The combustion efficiency is shown plotted vs. ϕ in Fig. 4.5 and 4.6, for the swept-compression and swept-expansion ramp models, respectively. For comparison, a correlation for the mixing efficiency of normal injectors, developed from studies of cold flow hydrogen/air mixing at NASA-Langley[143], is also plotted in Fig. 4.5-4.6. The mixing efficiency from the Langley correlation is given by: $\eta_m = 1.01 + 0.176 \ln \frac{x}{x_\phi}$ (4-2)

where: $x_\phi = 10.74 e^{1.72\phi}$ for $\phi < 1$

and $x_\phi = 200 e^{-1.204\phi}$ for $\phi > 1$.

The results in Fig. 4.5-4.6 are also compared to the combustion efficiency previously determined by Rogers[144] for normal injection of hydrogen in the same facility at approximately the same inlet conditions as the present study.

The combustion efficiency for the swept-compression ramp model is shown plotted versus the fuel equivalence ratio at several axial locations in Fig. 4.5. The combustion efficiency increased steadily with the axial distance. At x/G = 12 there is a plateau of 60 % at $\phi \geq 1.0$. Since there is no excess fuel or air when $\phi = 1$, complete molecular level mixing of all of the fuel with all of the airstream is required to achieve 100% combustion efficiency. Thus, the combustion efficiency would be expected to be the lowest for stoichiometric fuel/air. For $\phi < 1$ there is excess air and complete consumption of the fuel is required for complete combustion. Therefore, excess air traveling along the wall opposite of the injectors is not required to react with the injected fuel. The mixing correlation for normal injectors shows that the mixing efficiency is lowest for stoichiometric fuel/air and increases as ϕ decreases for $\phi < 1$, and increases with ϕ for $\phi > 1$. Figure 4.5 shows that as ϕ decreases (excess air increases) for the present experiment, the combustion efficiency increases, similarly to the mixing efficiency in the normal injector correlation. For $\phi > 1$ there is excess fuel and complete consumption of the airstream is required for complete combustion. However, unlike the mixing efficiency for the normal injectors, there was no observed increase in the combustion efficiency with fuel addition for $\phi > 1$. This implies that the excess fuel did not penetrate to mix with the air in this combustor configuration.

The combustion efficiency for the swept-compression ramp was higher than the mixing efficiency determined from the cold flow correlation for normal injectors at low equivalence ratios ($\phi < 0.65$). At higher equivalence ratios the difference mixing efficiency from the correlation is higher than the combustion efficiency for the swept ramps, and the difference between the two values increases as the equivalence ratio increases. The combustion efficiency for the swept-compression ramp injectors at $\phi \approx 1$ was approximately equal to that for normal injectors from reference 144. Thus, in addition to the advantage of near-parallel fuel injection, the combustion

efficiency for swept compression ramp injectors is comparable to that for normal injectors.

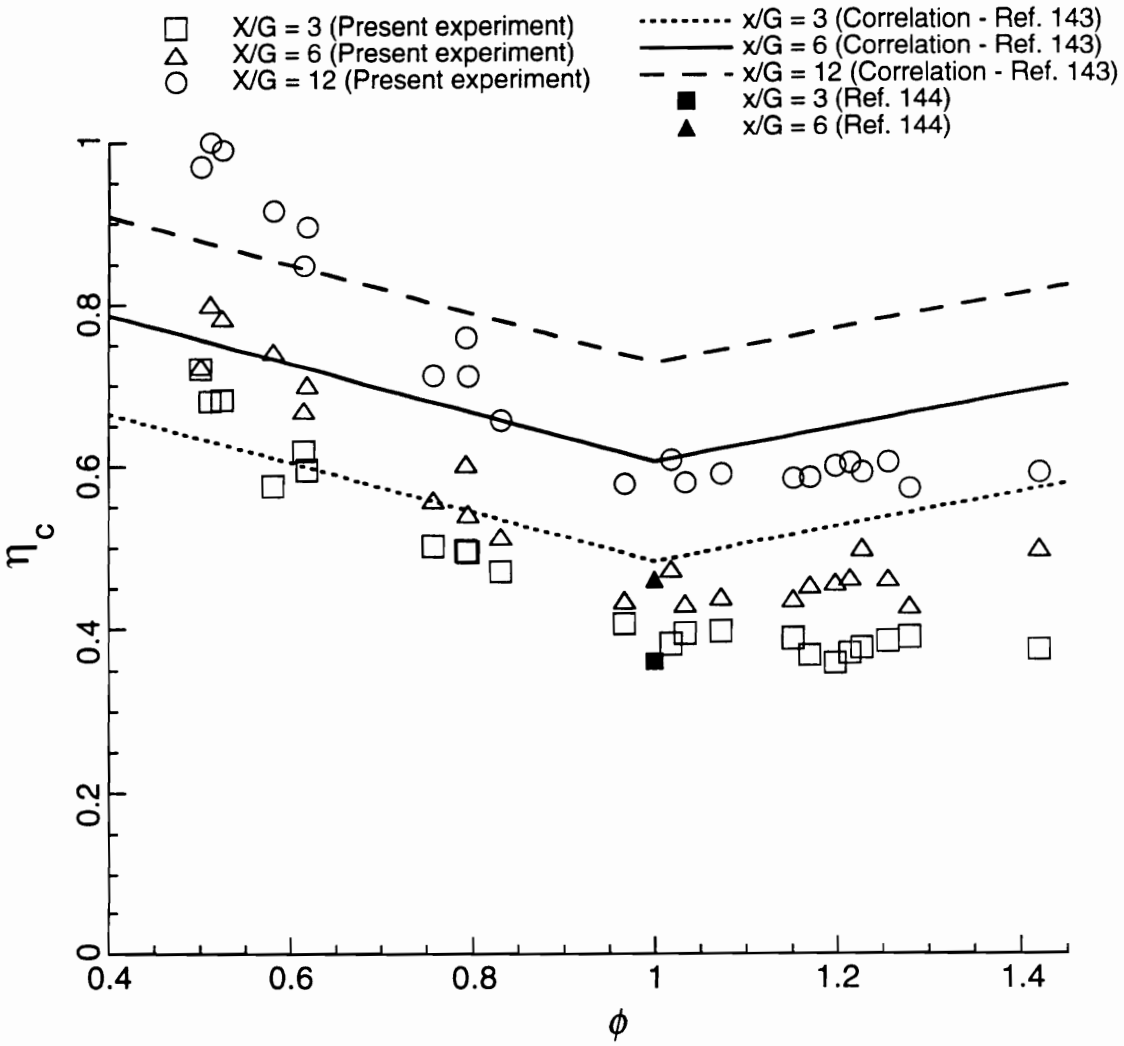

Figure 4.5 The Calculated Combustion Efficiency for the Swept Compression Ramp Configuration.

The calculated combustion efficiency for the expansion-ramp model is shown in Fig. 4.6. At a distance of x/G = 1.6 from the fuel injectors, the calculated combustion efficiency was zero for all values of ϕ tested. At a distance of x/G = 3 from the fuel injectors, the combustion efficiency increased as ϕ increased. Recall from Fig. 4.3 that the pressure rise due to combustion shifted upstream as ϕ increased. At distances greater than x/G = 6 the combustion efficiency decreased as ϕ increased from 0.5 to 1.0. The data at x/G = 6 and x/G = 12 show that for all of the values of ϕ, most of the fuel reacted within 6 gaps of the injectors. This implies that the combustor can be made shorter using expansion-ramp injectors. As in the compression-ramp model, the combustion efficiency curves showed that for $x/G > 6$ the efficiency did not increase with ϕ for $\phi > 1$. It is thought that the additional fuel was confined to the injector side of the combustor and did not penetrate to mix with the airstream.

The combustion efficiency for the swept expansion ramp injectors was higher than the mixing efficiency for the normal injectors for $\phi < 1.1$ in the farfield of the injectors (x/G = 6 and x/G = 12). As the equivalence ratio increased further, the combustion efficiency for the swept expansion ramp injectors was less than the mixing efficiency for normal injectors from the Langley correlation. In addition, the combustion efficiency for the swept-expansion ramp injector at x/G = 6 for $\phi \approx 1$ was greater than that for normal injectors.

4.4 Thrust Estimates

One of the major goals in scramjet engine design is to maximize the thrust. Thrust in a scramjet engine can be determined by three methods:

1. Directly measuring the net force.
2. Calculating the difference between the exit and inlet stream thrusts.
3. Integrating the forces along the combustor walls.

Methods are currently under development to measure the total thrust in the direct connect facility at NASA-Langley.[102] However, no direct thrust measurements were made for the current study. The second method was not

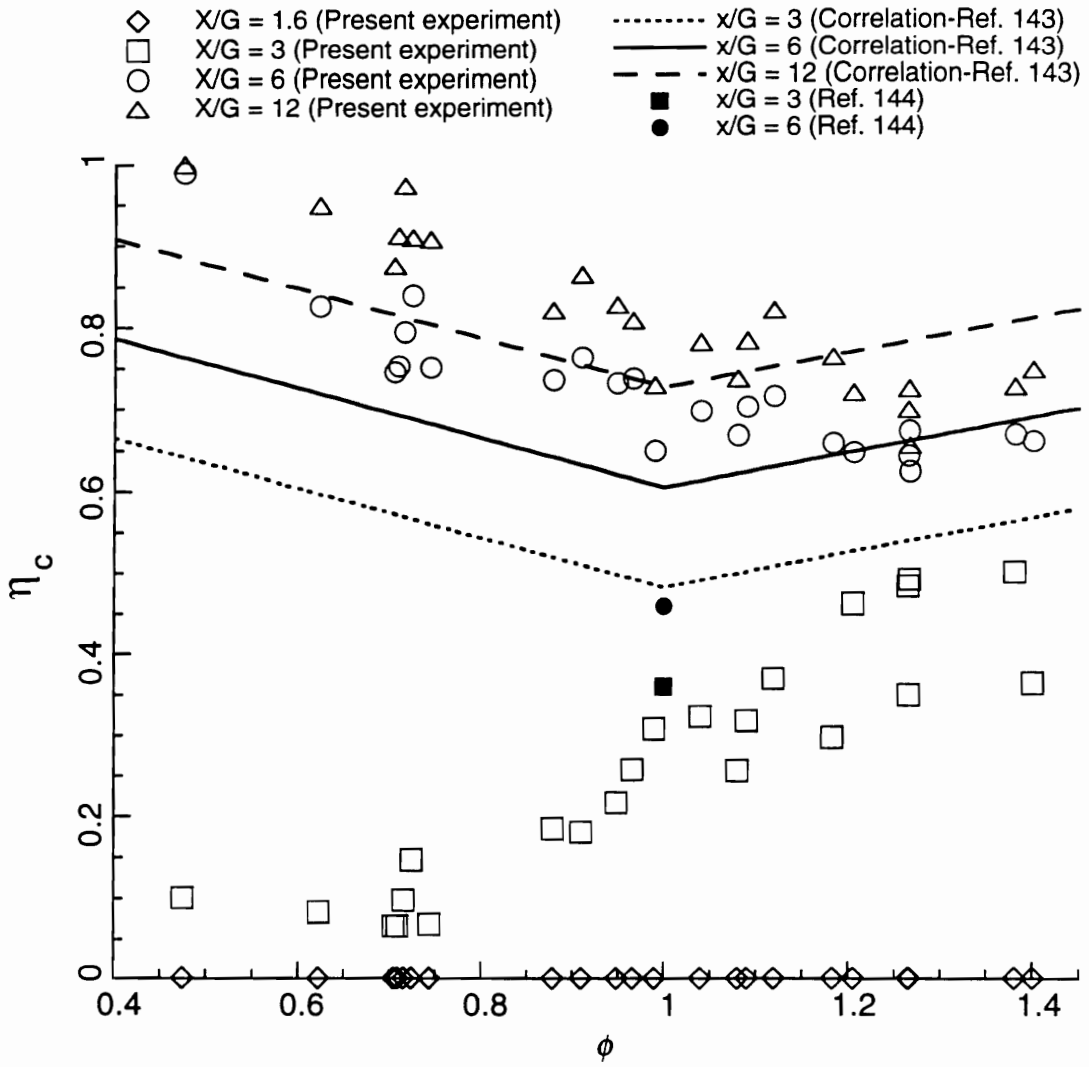

Figure 4.6 The Calculated Combustion Efficiency for the Expansion Ramp Injector.

attempted because of the difficulties involved in measuring the velocity, density and pressure across the combustor cross-section. Therefore, the sum of the forces along the surface was examined.

As shown in Fig. 4.7, the total thrust that is produced in a scramjet combustor or nozzle, is the sum of three terms: the pressure integral, the skin

friction integral, and the axial component of the momentum of the injected fuel. In conventional forms of air-breathing propulsion, the combustor thrust is negligible compared to the thrust produced in the nozzle. Although no thrust is produced by pressure acting on the walls of a constant area combustor, significant levels of thrust can be produced in diverging-area scramjet combustors.

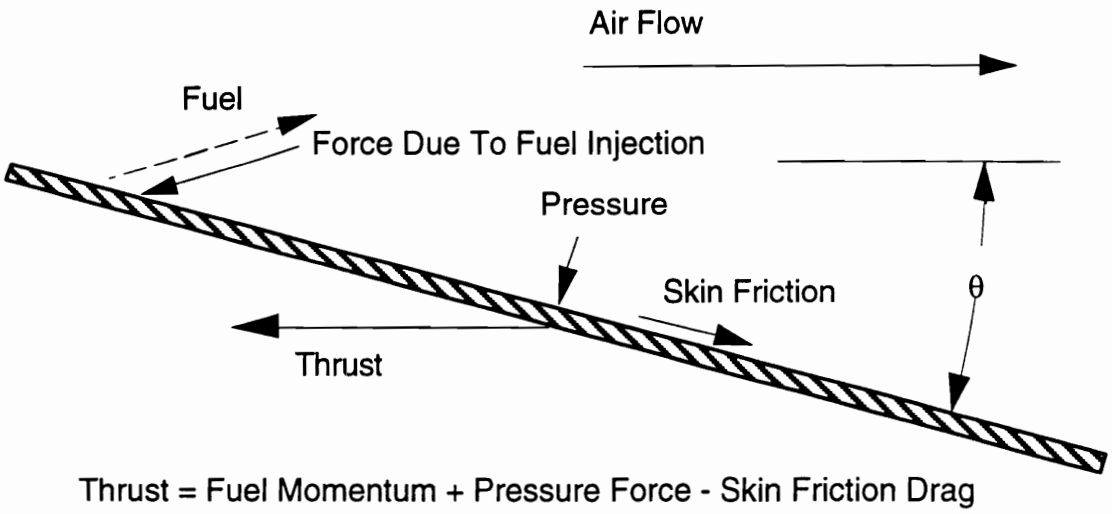

Figure 4.7 Components of the Net Thrust on an Expansion Surface.

4.4.1 Fuel Momentum

Since the fuel was injected through identical injector nozzles at the same angle, the thrust due to the momentum of the fuel is the same for both configurations. The ideal thrust due to the momentum of the fuel was calculated assuming isentropic expansion in the fuel injection nozzles. Figure 4.8 shows the thrust due to the momentum of the injected fuel at the test condition (T = 300 K) and for hydrogen regeneratively heated to a total temperature of 810 K. As shown in Fig. 4.8 the thrust due to fuel momentum increases linearly with equivalence ratio and as a square root of the temperature.

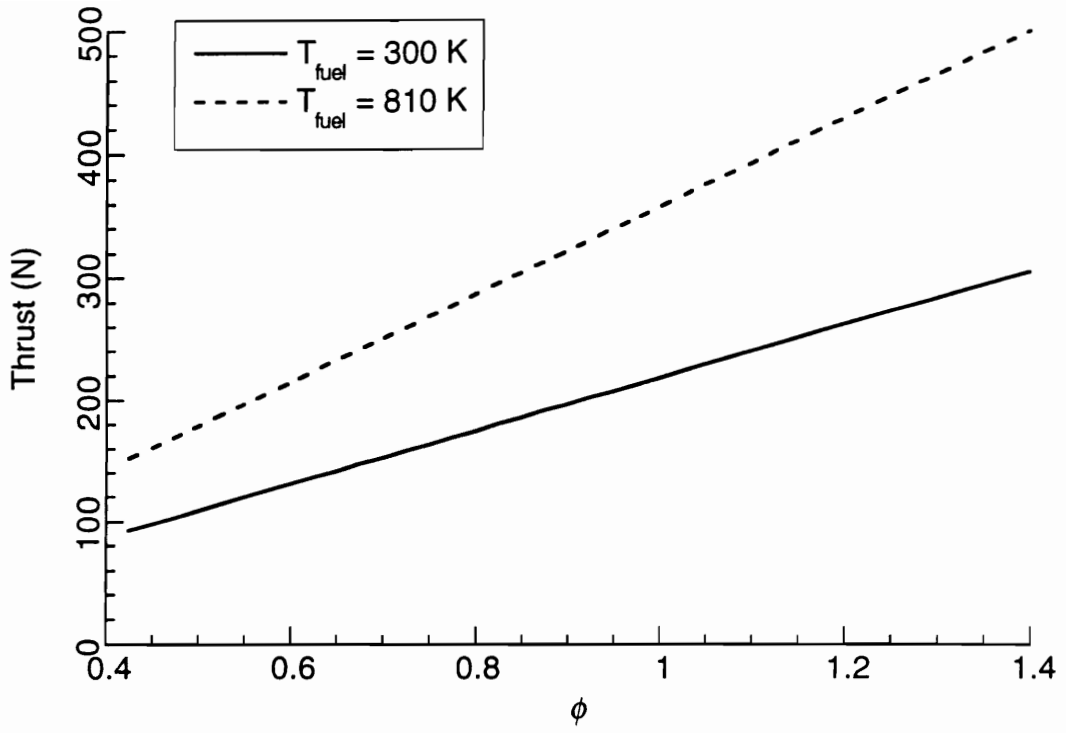

Figure 4.8 Contribution of the Fuel Momentum to the Thrust.

4.4.2 Skin Friction

Skin friction is the most difficult component of the engine forces to measure. Few direct measurements of skin friction have been made in supersonic combustors. Although measurements of the skin friction have been made in the direct connect facility for other combustors,[103] no measurements of the skin friction were obtained as part of this research. Computed values of the skin friction were obtained and are discussed in the next chapter.

4.4.3 Pressure Integrals

In order to assess the relative performance of the combustors the combined combustor/nozzle pressure integrals were computed. The pressure integral was calculated from the measured wall pressures along the combustor and nozzle walls from the following equation:

$$F = w\int_0^L P\tan\theta dx \qquad (4\text{-}3).$$

where P is the internal wall pressure, w is the width of the combustor, and the outside pressure was assumed to be zero.

The side walls of the combustor and nozzle do not diverge. Thus, the contribution of the side walls to the pressure integral is zero. Because the nozzle, which was used for both injector configurations, was asymmetric, the actual direction of the thrust produced was not aligned with the incoming flow. However, for the purpose of comparison in ground tests, the component of thrust in the direction of the incoming flow was calculated by equation 4-3.

The pressure integrals with no fuel injection for each of the combustor ducts (diverging section of the combustor) and the nozzle are shown in Table 4.1. The values shown are the average of all of the tests, and the bounds are twice the standard deviation of all tests. The combustor-duct pressure integral for the swept compression ramp was higher than that for the shorter combustor duct used in the expansion ramp tests. The nozzle pressure integral was slightly higher for the swept-expansion injector configurations without fuel injection. This was expected because of the higher combustor exit pressure for the swept expansion ramp configuration.

The pressure integral for the injector region of each model was calculated for the case of no fuel injection from a combination of measured pressures and calculated pressures obtained from 3-D Navier-Stokes solutions. The results are shown in Table 4.1. The injector region was divided into two parts, the injector surface upstream of the base, and the ramp base. As was shown in Fig. 4.2, and 4.4, little combustion-induced pressure rise occurred upstream of the injectors for either injector configuration. Therefore, the pressure integrals for the ramp region upstream of the injectors were the same with and without fuel injection. The pressure integrals for the ramp surfaces of the compression-ramp injectors were negative because of the forward facing surfaces while the pressure integral is positive for the expansion-ramp surface. The pressure integral for the ramp base is also shown in Table 4.1 for the no fuel case. Since the ramp base contains the fuel injectors, the pressure integral over that region increases with fuel injection. Further increases are possible due to combustion of the fuel near the injectors. The pressure integrals for the

entire combustor/nozzle combination shown in the last column of Table 4.1 are approximately the same for both injector configurations.

Table 4.1 Pressure Integrals (N) for No Fuel Injection.

Model	Combustor Duct	Nozzle	Ramp w/o Base	Ramp Base	Total
Swept-Expansion	507±10	431±17	53*	18*	1010
Swept-Compression	765±40	396±35	-200*	27*	988

* = calculated by SPARK

For a comparison between the two injector types, the difference between the pressure integral with and without fuel injection ($\Delta F = Ff - F_{nf}$) is examined for the two combustor ducts. The quantity ΔF is the change in pressure integral that is due to fuel addition and combustion. Since the pressure upstream of the ramp base changed little with injection, the quantity ΔF is independent of the region upstream of the injectors. Figure 4.9 shows ΔF for the combustor ducts used with the two swept-ramp injectors. The value of ΔF slowly increased with ϕ for both injectors. Also, the values of ΔF for the two injectors were approximately equal for $\phi > 0.8$ although the shapes of the pressure distributions were different. As was seen in Fig. 4.1 and 4.3, the combustion induced pressure rise occurred close to the injectors for the swept-compression-ramp while the pressure rise occurred further downstream for the swept expansion ramp. However, the pressure at the exit of the combustor is higher for the swept expansion ramp than it is for the swept compression ramp. For $\phi < 0.8$ the pressure rise occurred farther downstream for the expansion-ramp so that ΔF was lower than that for the compression-ramp.

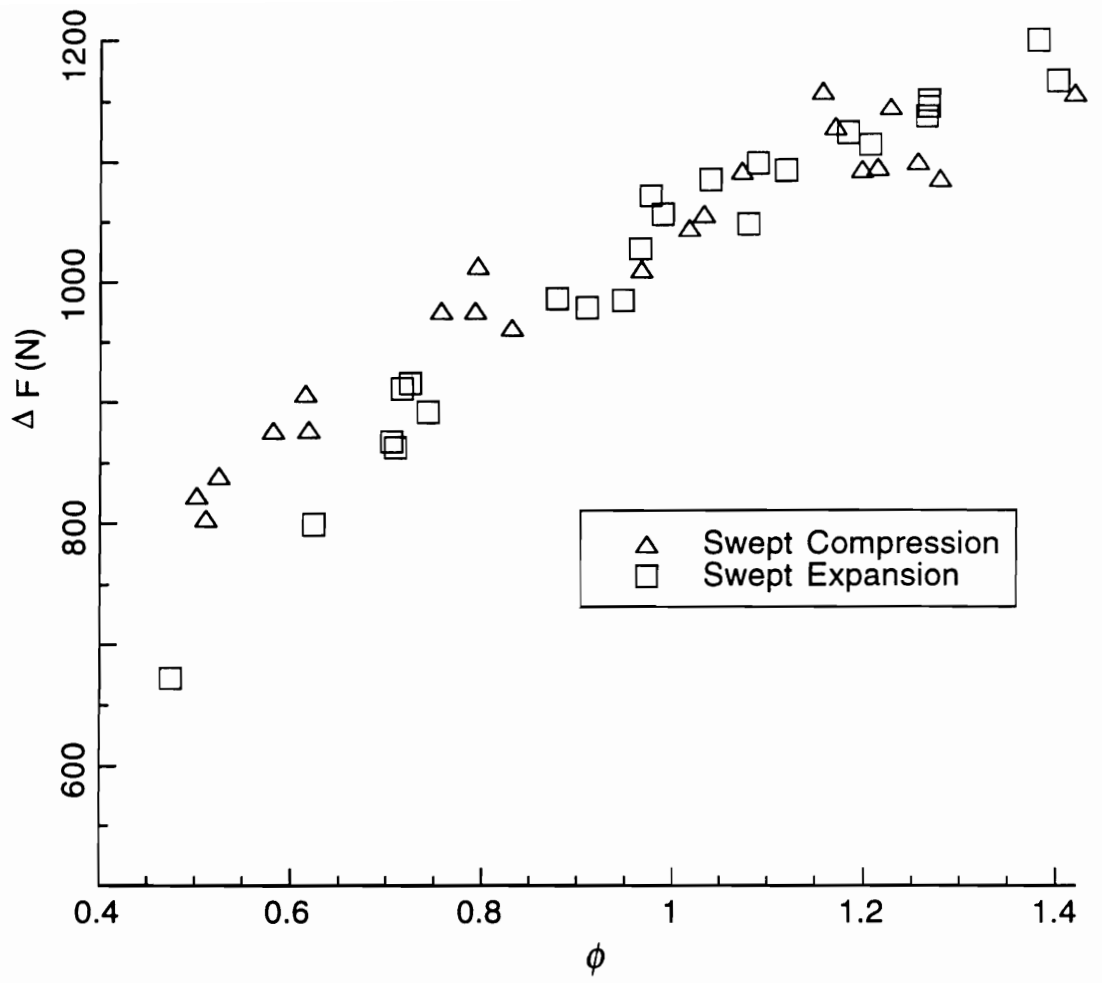

Figure 4.9 Pressure Integral for the Combustor ($\Delta F = F_f - F_{nf}$).

The pressure integral for the nozzle is shown along with the combined (nozzle-combustor duct) pressure integrals in Fig. 4.10. Note that, as shown in Table 4.1, the pressure integrals for the combustor-nozzle combination with no fuel injection were approximately the same for both injectors. Therefore, comparing the quantity ΔF for the combustor/nozzle combination is also equivalent to comparing the total pressure integral with fuel (F_f) between the two configurations. The nozzle pressure integral for the swept expansion ramp was higher than it was for the swept compression ramp at all values of ϕ. Referring to Fig. 4.1 and 4.3, this difference is expected because the combustor exit pressure was higher for the expansion-ramp configuration,

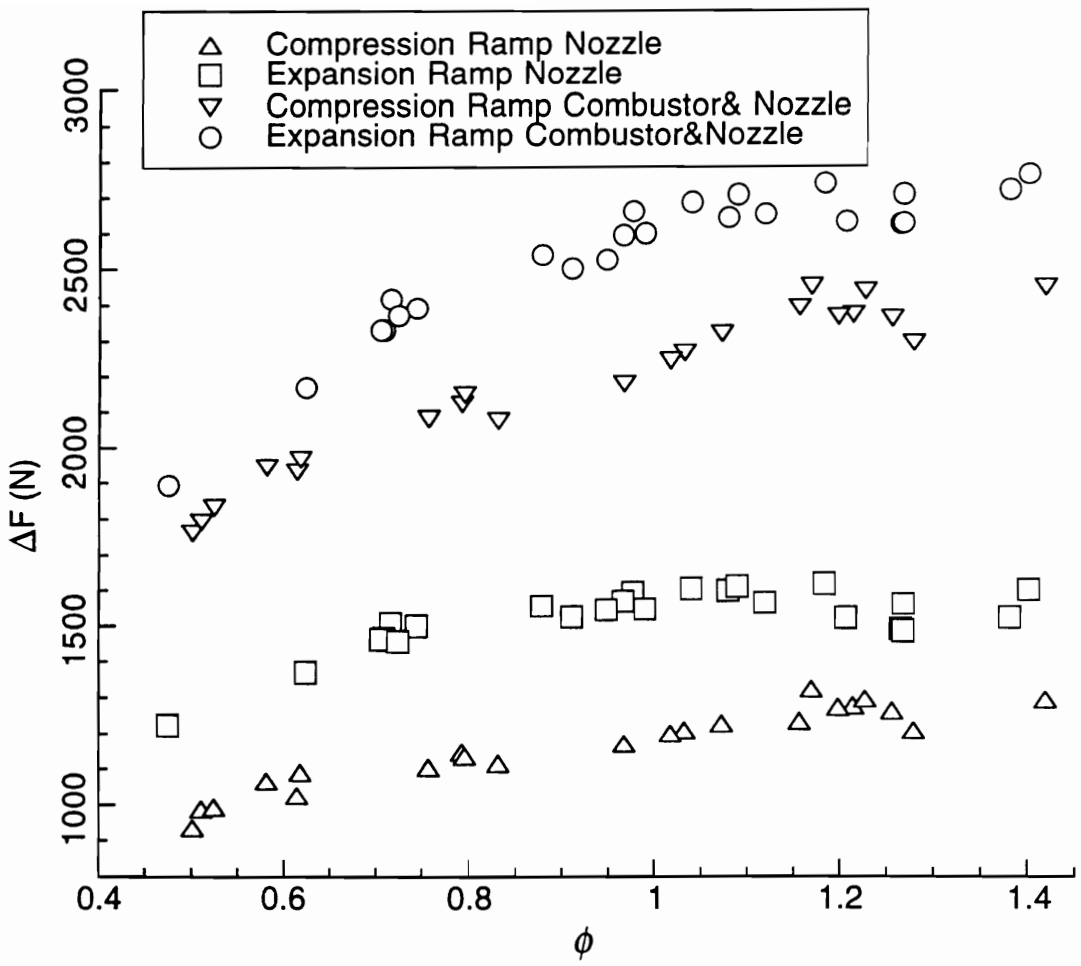

Figure 4.10 Pressure Integral for the Combustor Duct-Nozzle Combination ($\Delta F = F_f - F_{nf}$).

which, as shown in Fig. 4.11, resulted in higher pressures in the nozzle for the expansion ramp configuration. The combined pressure integral increased with ϕ for both the swept-expansion and the swept-compression ramps. For fuel rich tests the increase of ΔF with ϕ was small. At all values of ϕ, the pressure integral was higher for the expansion ramp than it was for swept-compression ramp. Because the combustor pressure integral was approximately the same for the two configurations, the difference between the two configurations was due to the nozzle pressure integral.

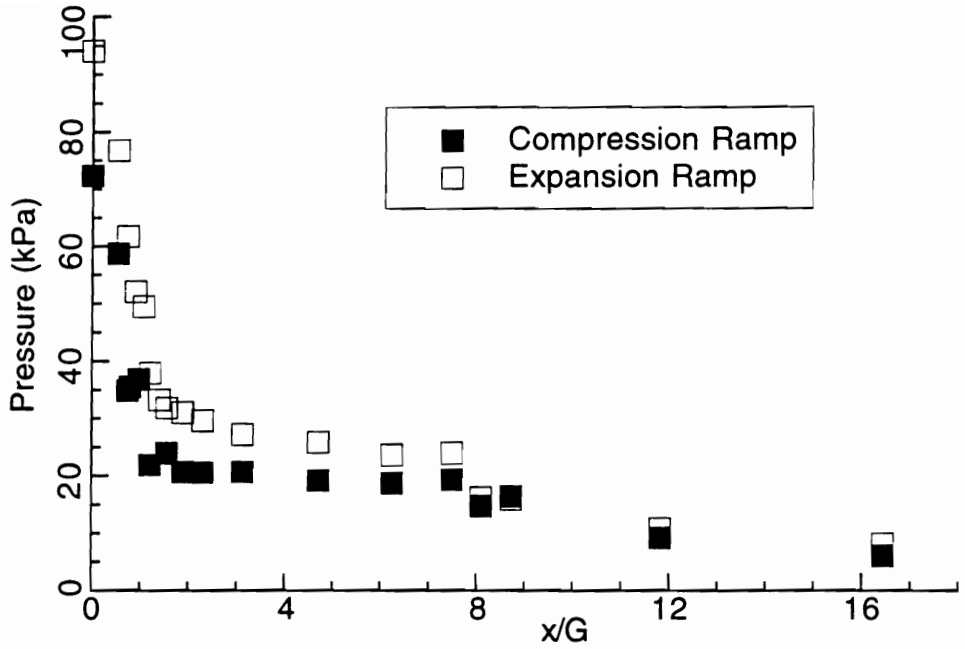

Figure 4.11 Pressures Along the Injector Wall of the Nozzle for $\phi = 1$.

The pressure integrals shown in Fig. 4.9 and 4.10 neglect the injector region. The pressure traces showed that the pressure did not increase upstream of the ramps with combustion. However, fuel injection and combustion increase the ramp base pressure. For the expansion-ramp injector, combustion did not occur near the injectors. The ramp base area is five times greater than the exit area of the injector nozzles. Therefore, in the absence of combustion near the injectors, little of the base area would be expected to reach the exit pressure of the fuel. Assuming that only the fuel-injector exit pressure increases due to fuel injection, the ramp base pressure integral increases by 45 N at $\phi = 1$. For the swept compression ramp, combustion occurred near the ramp base, which should have further increased the base pressure. No measurements of the ramp base pressure were made. However, an average base pressure increase of 660 kPa (twice the fuel pressure at $\phi = 1$), would be required for the compression ramp combustor-nozzle pressure integral to equal that for the expansion ramp. Calculations of the ramp base pressure for the compression ramp, which are presented in the next chapter, show that the average base pressure for the swept compression ramp with combustion was 200 kPa. Therefore, even with

large (>600 %) increases in the average ramp base pressure due to combustion, the pressure integral is higher for the swept-expansion ramp than it was for the swept-compression ramp.

4.5 Product Visualization By Mie Scattering

The results from the Mie scattering tests are presented in this section. The goal of the Mie scattering tests was to visualize the combustion product distribution at selected cross planes in a closed combustor. The images that were acquired during the test qualitatively represent the average extent of the combustion products across the combustor duct. Images were acquired in two cross-flow planes (x/G = 3.1 and x/G = 6.1) for the combustor using swept-compression ramp injectors. Attempts to image the flow at x/G = 1 were unsuccessful. It is thought that the high temperatures in this region resulted in the vaporization of the silica particles. Indeed, the computational results (presented Chapter 5) show that static temperatures in excess of the silica vaporization temperature were reached at this axial location.

The processed Mie Scattering images acquired at the x/G = 3.1 plane are shown in Fig. 4.12 in order of increasing ϕ. The ramp contours and the outline of the diverging walls are plotted over the image. For clarity, the bottom of the constant area section is indicated by the white line across the images. The equivalence ratio (based on hydrogen) and silane mole fraction, Y_{SiH4}, are listed for each of the runs. The equivalence ratio was approximately the same (0.69-0.81) for each of the images. The images show that the distribution of the products caused by the four fuel jets is symmetric about the centerline. Four distinct plumes are evident in the images. The product plumes from the two center injectors appear to penetrate slightly farther in both the transverse and spanwise directions than the two outer jets. With the exception of differences near the wall, the images are similar. The bright saturated regions near the wall are thought to be the result of reflections near the surface rather than product formation. The images clearly show that the combustion products have not penetrated to the opposite wall.

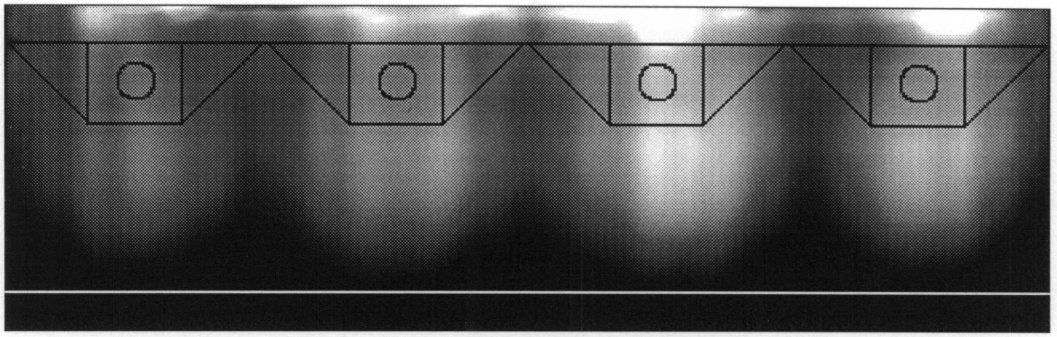

$\phi = 0.69$, $Y_{SiH4} = 2.5$ %

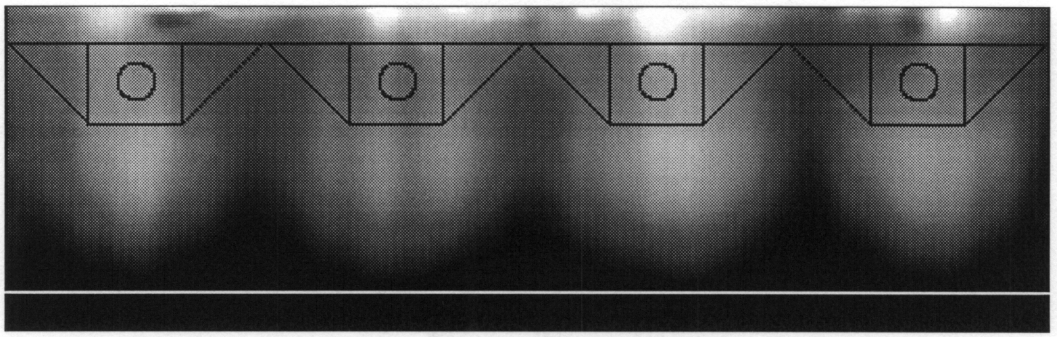

$\phi = 0.74$, $Y_{SiH4} = 2.2$ %

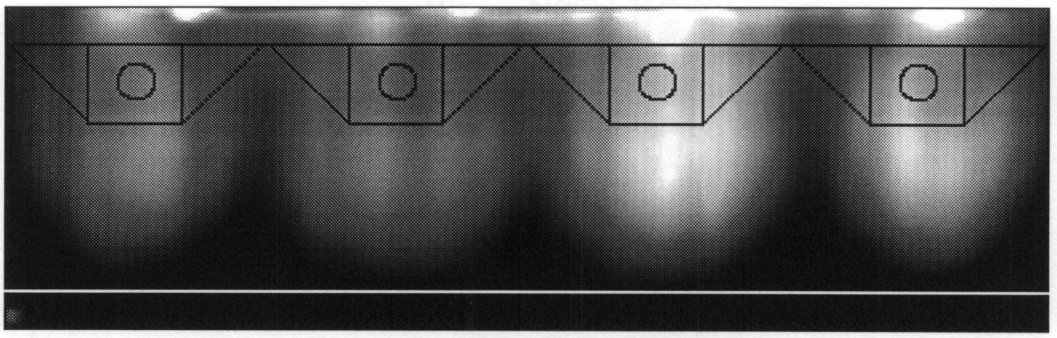

$\phi = 0.77$, $Y_{SiH4} = 1.7$ %

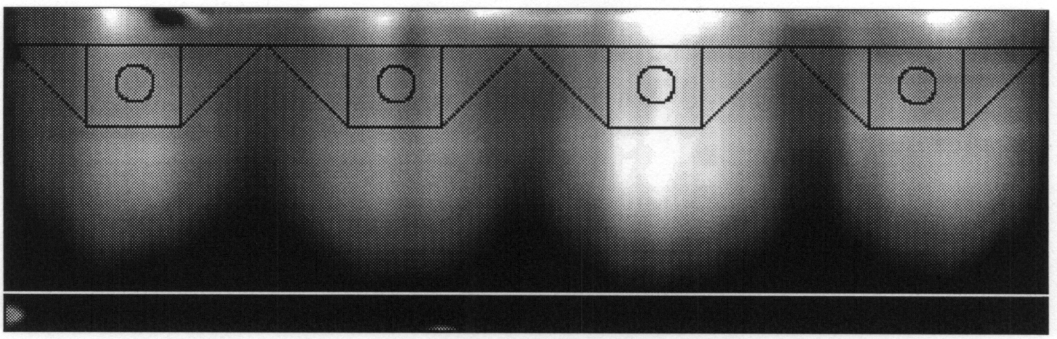

$\phi = 0.80$, $Y_{SiH4} = 1.6$ %

Figure 4.12 Processed Mie Scattering Images Acquired at x/G = 3.1.

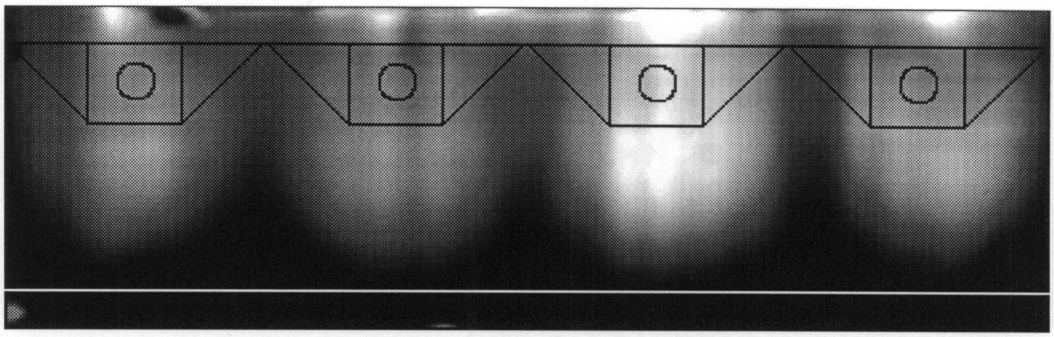

$\phi = 0.80$, $Y_{SiH4} = 1.6$ %

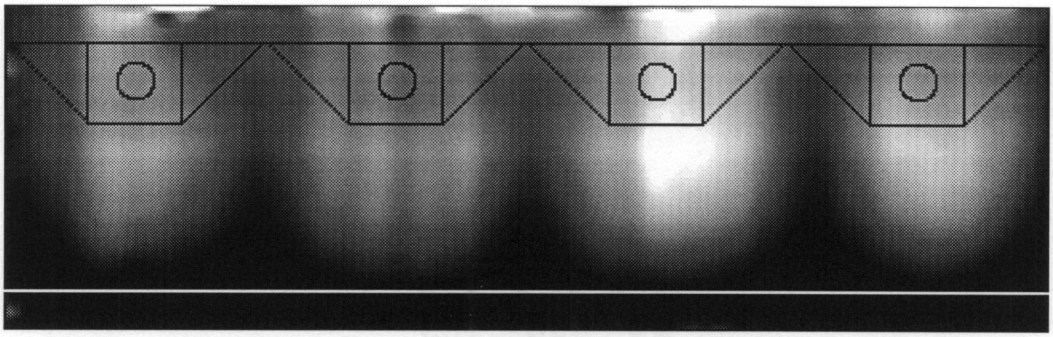

$\phi = 0.81$, $Y_{SiH4} = 1.6$ %

Figure 4.12 (continued) Processed Mie Scattering Images Acquired at x/G = 3.1.

The images acquired at x/G = 6.1 are shown in Fig. 4.13. The equivalence ratio for the images in this figure varied from $0.4 < \phi < 1.2$. The outer boundary of the product plume was approximately at the same height for all of the images. The contours in all of the images show a less regular structure than was observed at the upstream location. The products penetrated slightly farther in the transverse direction relative to the injector wall. However, the combustor walls expand between x/G = 3.1 and x/G = 6.1. The net effect was that the penetration of the combustion products did not keep up with the divergence of the combustor walls. The small increase in the fuel penetration, relative to the injector wall, between x/G = 3.1 and 6.1, suggests that the fuel jets lost most of their transverse momentum. Although no images were acquired farther downstream of x/G = 6, further penetration of the fuel was expected to be small. Note that as the equivalence ratio increased, penetration did not increase. For 100 % combustion efficiency in a fuel-rich combustor all of the air must react with the fuel. Thus, combustion in the swept ramp combustors was limited by the failure of the fuel to penetrate completely across the duct.

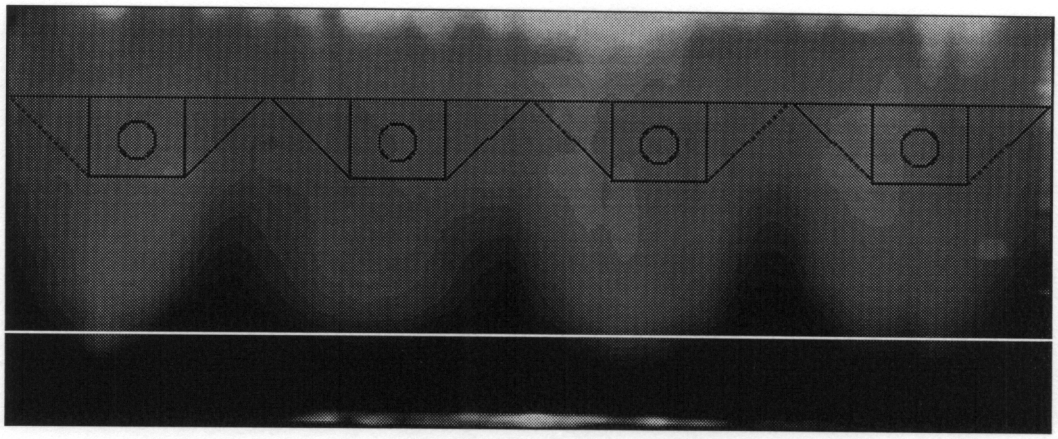

$\phi = 0.46$, $Y_{SiH4} = 2.5$ %

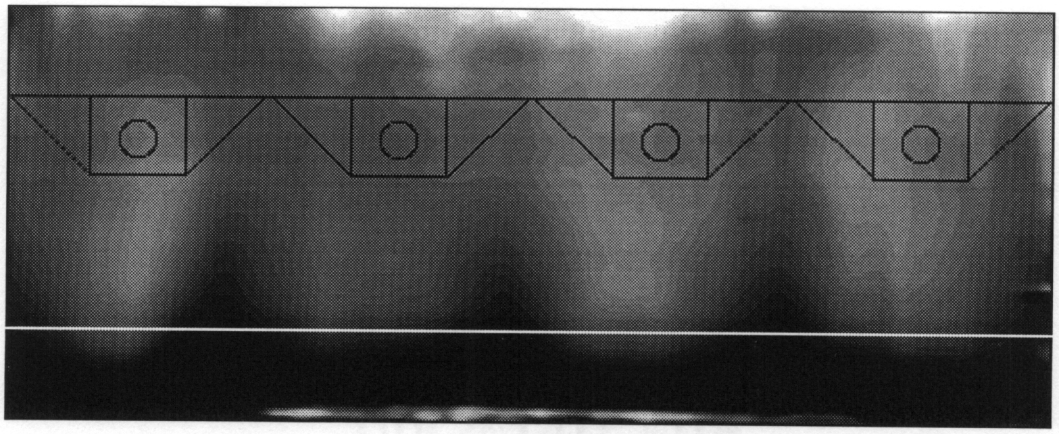

$\phi = 0.49$, $Y_{SiH4}=2.3$ %

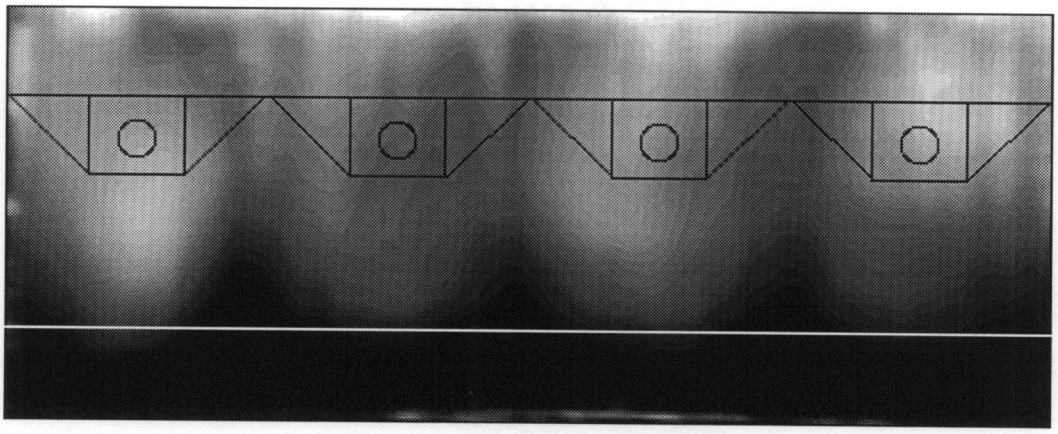

$\phi = 0.66$, $Y_{SiH4}=2.6$ %

Figure 4.13 Processed Mie Scattering Images Acquired at x/G = 6.1.

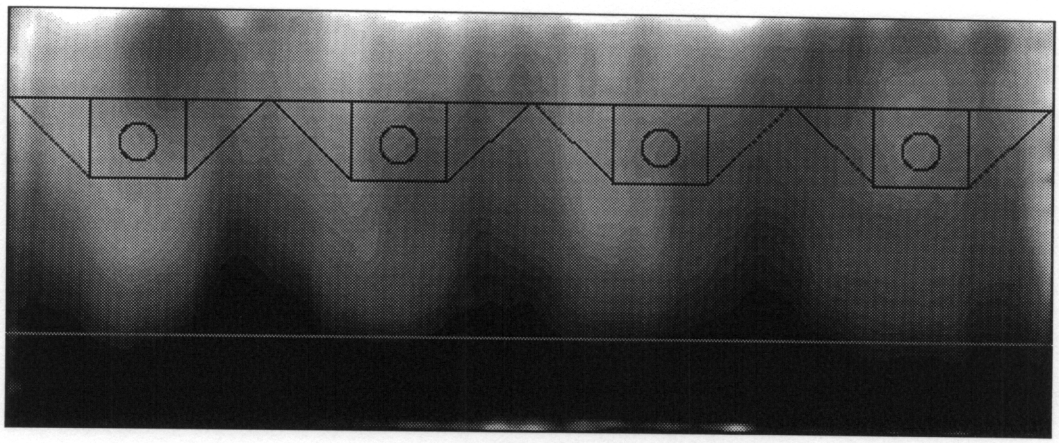

$\phi = 0.87$, $Y_{SiH4} = 2.0$ %

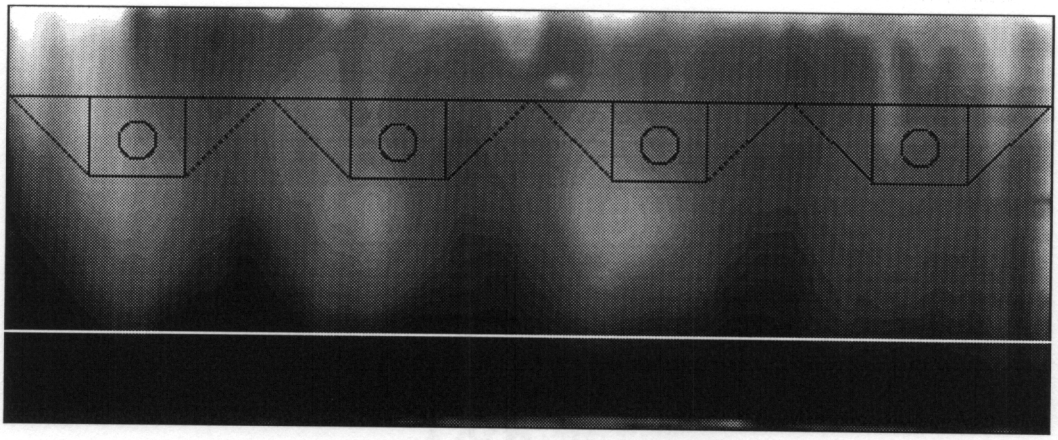

$\phi = 0.95$, $Y_{SiH4}=1.9$%

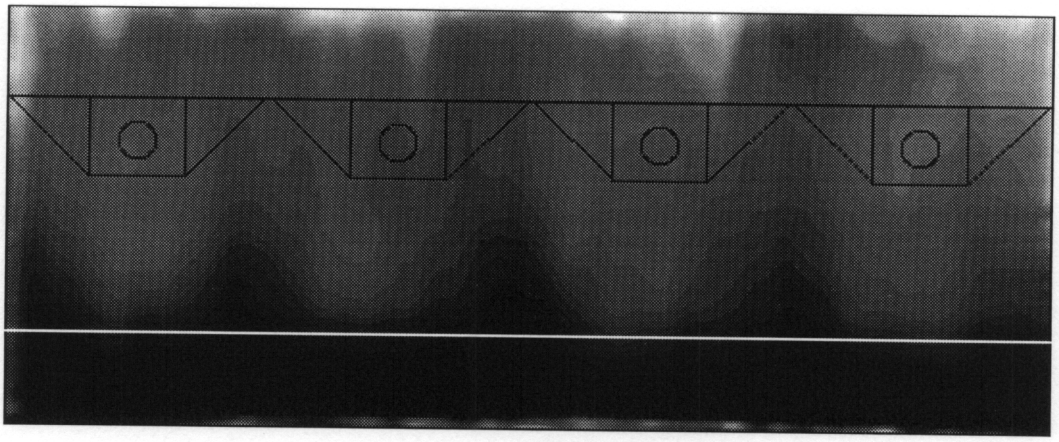

$\phi = 1.2$, $Y_{SiH4}=1.5$ %

Figure 4.13 (continued) Processed Mie Scattering Images Acquired at x/G =6.1.

4.6 Pitot Pressure Profiles

4.6.1 Probe Longevity

A total of 23 test runs were made with the pitot probe installed at exit of the compression ramp combustor (x/G = 14.1) in line with the interstice centerline. An inspection of the probe after runs 1 and 8 showed no noticeable change in the probe due to erosion. At the end of the test program 3/4 of the probe length was gone. The remaining probe material showed signs of recession. Curiously, the recession of the tungsten was greater on the inside diameter than it was on the outside diameter of the probe. It is thought that the probe failed by gradual oxidation, followed by a catastrophic break. A close examination of the pitot pressure traces showed that the response to the pitot pressure step, which occurred when the probe was withdrawn from the protective wall cavity (see Fig. 3.14), was slower for runs 18 onward. This result suggests that the probe failed during the 17th run, since the probe distance from the wall required to avoid the effect of the expansion fan, caused by the cavity, is larger for a shortened probe.

The first 15 tests were conducted without fuel injection and ϕ = 0.7, while the rest of the tests with the shortened probe were at other equivalence ratios.

4.6.2 Pitot Traverse Results

Figure 4.14 shows the pitot pressure profiles in the normal direction along the interstice centerline (normalized by the heater stagnation pressure) for two tests with no fuel added, and two tests with ϕ = 0.7. A sketch of the injector ramp, relative to the rest of the tunnel, is also shown at the side of the plot for orientation. Because of human error, the pitot traces shown for the no fuel case were conducted with the vitiated heater in the pilot fuel mode. Therefore, the total temperature and pressure were lower than that with the vitiated heater fully on. The heater total temperature was approximately 1500 K rather than 1940 K and the stagnation pressure was about 2.07 MPa rather than 2.76 MPa. However, the flow through the combustor was still supersonic at this lower pressure, and the normalized

pitot pressure trace can be expected to resemble that obtained while the heater is fully on.

Agreement between repeated tests for both the ϕ =0.7 and the no fuel cases was exceptional over most of the traverse. On the injector side of the trace, the pitot pressure traces for the no fuel case are higher than those with fuel. For z/G ≥ 0.3 the pitot pressure was greater for the fuel-on case. The pressure measured at the probe is the product of the stagnation pressure in front of the normal shock and the ratio of the stagnation pressure before and after the normal shock in front of the probe tip. Since the Mach number in the traverse plane was higher for the no fuel cases, the drop in the measured pressure across the normal shock was higher than it was for the ϕ = 0.7 case.

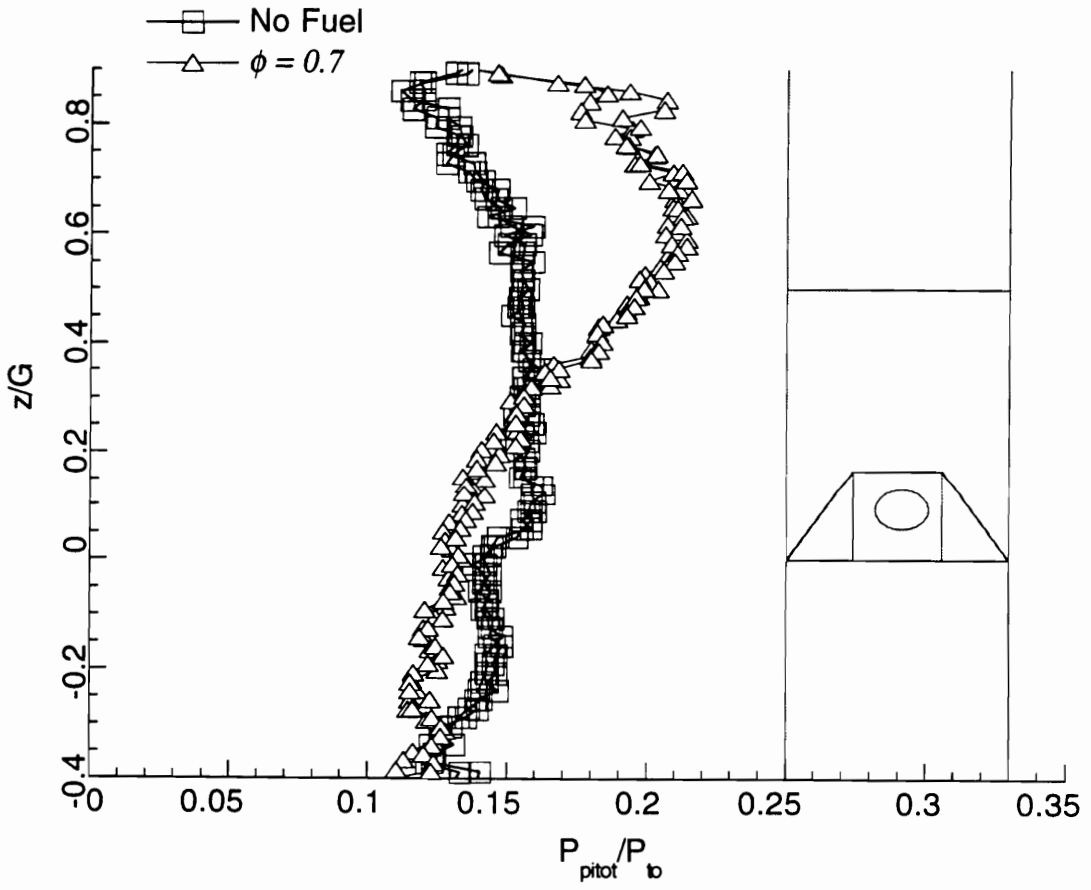

Figure 4.14 Pitot Pressure Profiles in the Normal Direction Across the Interstice Centerline of the Combustor at x/G = 14.1.

The pitot pressure increased from a minimum on the fuel injector side of the combustor to a maximum at approximately at z/G = 0.6 for the $\phi = 0.7$ case. The lower pitot pressure on the fuel injector side was caused by the drop in stagnation pressure associated with combustion, while the higher pitot pressure on the opposite side suggests that a smaller drop occurred in the stagnation pressure due to combustion. This is in agreement with the Mie scattering images. Recall that the Mie scattering images at x/G = 3, and x/G = 6 showed that the fuel did not penetrate completely across the duct by x/G = 6. Furthermore, the Mie scattering results suggested that the rate of fuel penetration across the duct would be lower further downstream in the duct.

The pitot pressure traces for the fuel-on case will be discussed further when they are compared with the computations in Chapter Six.

4.7 Heat Flux Measurements

Heat flux measurements were made with both Gardon gages ("cold wall" heat fluxes) and surface thermocouples ("hot wall" heat fluxes). A detailed discussion of the measurement uncertainty and the difference between the two types of heat flux measurement is presented in Appendix C. It was found that the difference between the measured cold wall heat flux and the actual heat flux is potentially large and continually increased with time during a test as a result of this wall temperature difference. Differences between the cold and hot wall heat fluxes of up to 25 % have been observed in the carbon steel portion of the combustor at the end of the tests. For the stainless steel section of the combustor, the difference between hot and cold fluxes is expected to be larger due to the lower thermal conductivity of stainless steel. Surprisingly, the cold wall heat flux was affected little by the large increase in the temperature mismatch between the wall and the gage. Examination of the heat flux measurements for all of the tests showed that, although the temperature mismatch often increased by more than 100% while the model fuel was on, the cold wall heat flux measurements changed by less than 5 % during the same period (see Appendix C).

Both the hot and cold wall heat fluxes are plotted together on the plots that are presented here. The hot wall fluxes were all determined 4 data cycles after the end of the fuel on transient. This was necessary in order to avoid numerical overshoot of the calculated heat flux, as discussed in Appendix B.

4.7.1 Swept Compression Ramp Heat Flux

The heat flux on the injector wall of the swept compression ramp combustor is plotted in Fig. 4.15, for the case of no fuel injection. The heat fluxes shown are average values from all of the tests. The reference heat flux is also plotted. The reference heat flux is the heat flux that was measured on the opposite wall of the combustor 1.6 gap lengths downstream of the combustor entrance (0.5 gap lengths upstream of the injectors). The reference heat flux gage was located upstream of the influence of the injector ramps, and thus represents the heat flux to the wall that is caused by the high enthalpy combustor inlet flow without shocks or combustion. Since the flow upstream of the injector ramps was the same for both types of injectors, the reference heat flux was the same for both injectors. The pressure along the interstice centerline is also shown in this figure.

As shown in Fig. 4.15, in the near field of the injectors, the heat flux was higher than the reference heat flux. Over most of the length of the combustor the pressures and heat fluxes followed the same trend. The highest heat fluxes occurred where the wall pressure was highest. The differences between the heat flux at the interstice and the fuel injector centerlines along most of the length of the combustor were small. The greatest difference was observed at x/G = 0.23, which was the closest gage location to the injectors. At this location the flux at the interstice centerline is about 25% lower than that measured at the injector centerline. Downstream of x/G = 2, at locations where gages were installed in line with both the interstice and the injector centerlines, the difference in the flux in the spanwise direction is within the uncertainty of the measurement. The hot wall heat fluxes, which are indicated by the solid symbols, were close to the cold wall heat fluxes.

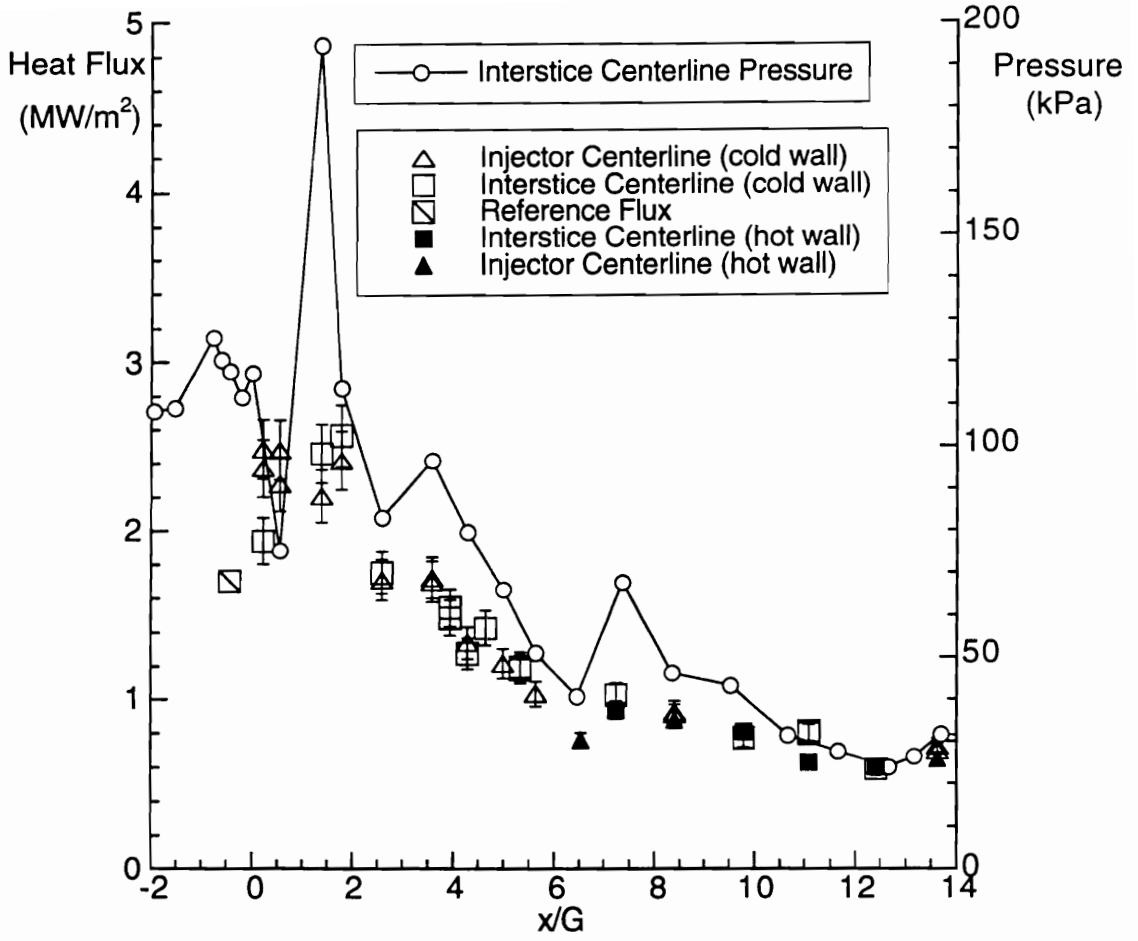

Figure 4.15 The Heat Flux and the Pressure Along the Injector Wall for the Swept Compression Ramp With No Fuel.

The heat fluxes along the injector wall of the combustor with fuel addition are plotted in Fig. 4.16 (ϕ =0.7), 4.17 (ϕ = 1), 4.18 (ϕ = 1.2). The plots are each a composite of several tests at approximately the same equivalence ratio. Therefore, in addition to small variations in the tunnel conditions, there is some variation in the heat flux due to differences between the amount of fuel injected. In general, the hot wall heat flux determined from the thermocouples was lower than that from the heat flux gages, but the two methods of measuring the heat flux show the same trend. The heat flux without fuel addition is also plotted along with the reference heat flux.

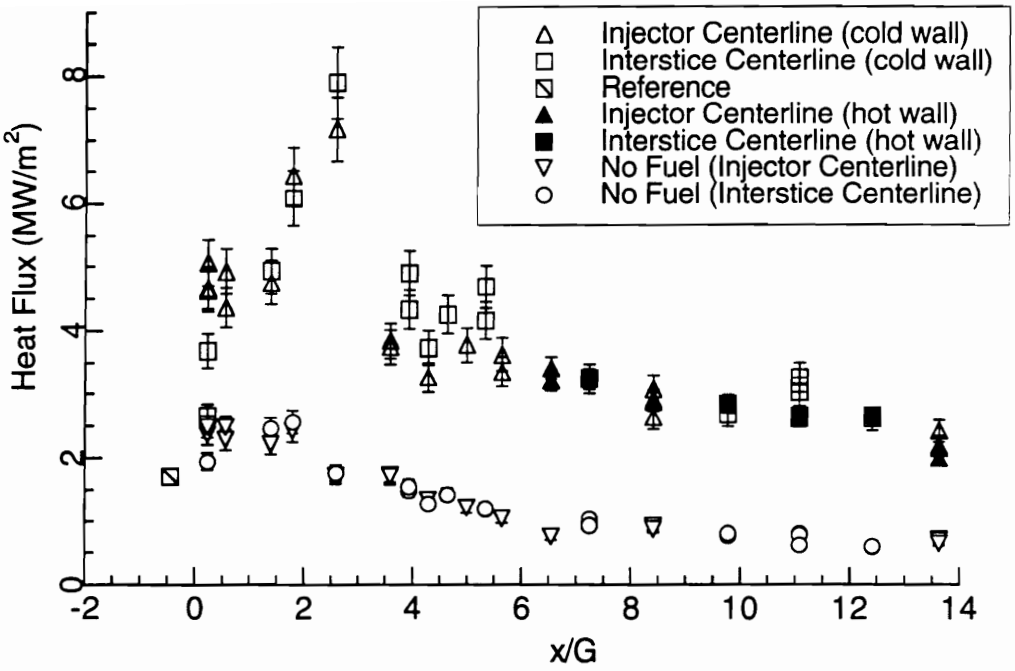

Figure 4.16 Injector Wall Heat Flux Distribution For the Swept Compression Ramp Model ($\phi = 0.68 \pm 0.06$).

The shape of the heat flux distributions did not vary significantly with ϕ. The heat flux at each location downstream of the injector ramps increased with fuel injection over that with no fuel. At the first gage location downstream of the ramps, at x/G = 0.23, the heat flux was significantly higher for the gages that were in line with the fuel jets than it was for those in line with the ramp interstice centerline. For any given equivalence ratio the gages in the constant area section of the combustor (x/G < 0.9) showed more test-to-test variation than those positioned in the farfield of the combustor. It is thought that the observed difference were due to small differences in the position of the reacting fuel jet relative to the wall. This will be discussed further in Chapter 5 when the reacting flow calculations are considered.

The heat fluxes increased in the expanding duct for x/G ≤ 2.6. A plot of the heat flux vs. ϕ in the region between the constant area section and x/G = 2.6 is shown in Fig. 4.19. At x/G = 1.4 and x/G = 1.8 the heat flux increased less than 25 % as ϕ increased from 0.5 to 1.25, and the fluxes were

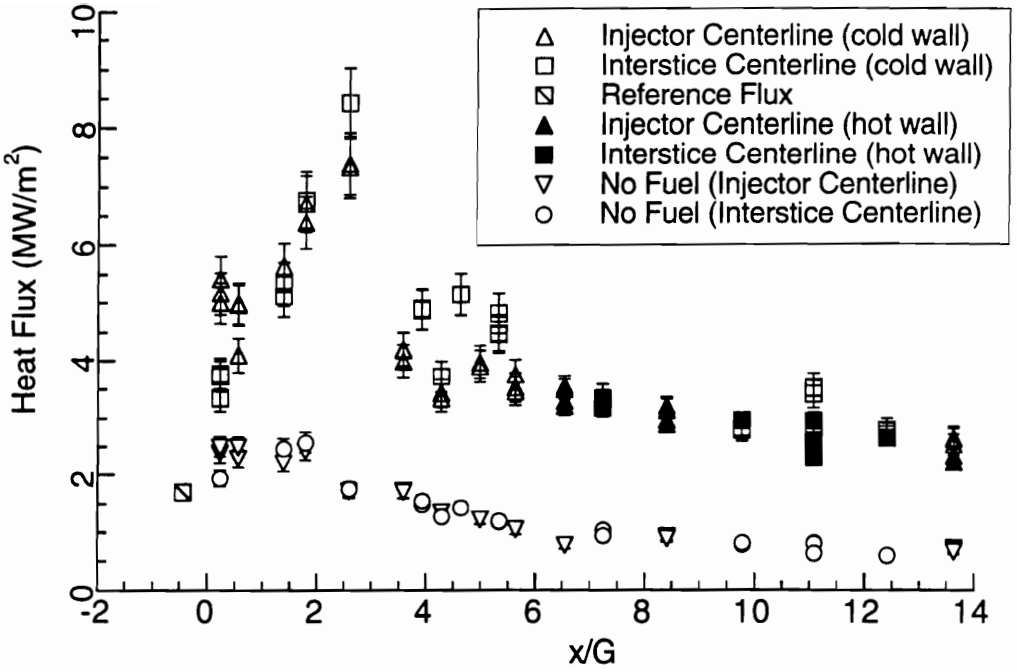

Figure 4.17 Injector Wall Heat Flux Distribution for the Swept Compression Ramp Model (ϕ = 1.0±0.04).

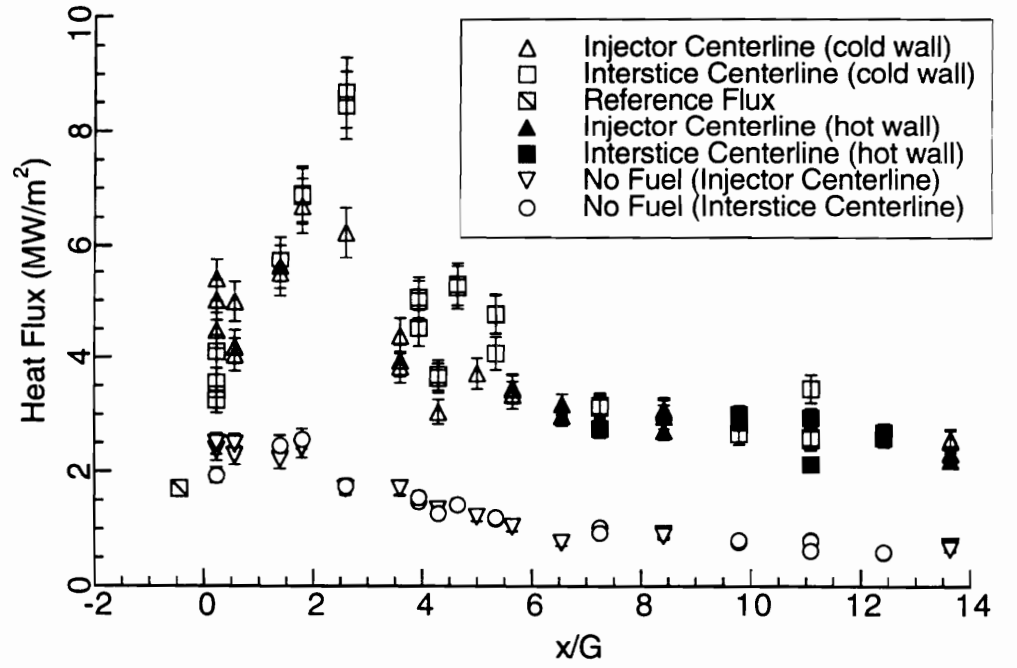

Figure 4.18 Injector Wall Heat Flux Distribution for the Swept Compression Ramp Model (ϕ = 1.20±0.05).

approximately the same along the interstice and the injector centerlines. The maximum measured heat flux occurred at x/G = 2.6 for all ϕ. At this location, the heat flux along the interstice centerline was higher than that along the fuel jet centerline. Note that the location of the maximum heat flux is in the expanding combustor duct, about 200 mm downstream of the injectors. At this location the pressure was less than the maximum pressure in the combustor, which occurred in the constant area section of the combustor. Thus, the maximum measured heat flux in the combustor was not coincident with the maximum pressure, but instead occurred in a favorable pressure gradient. From the standpoint of film cooling this is an encouraging result,

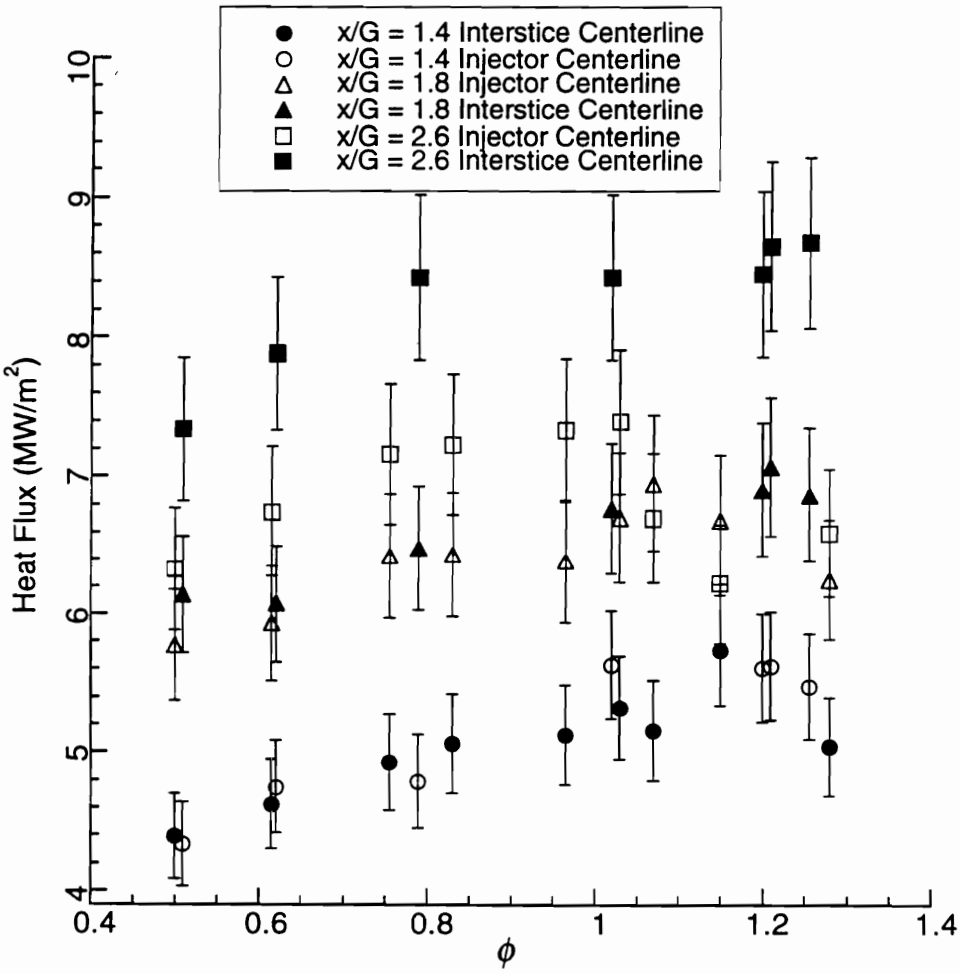

Figure 4.19 Heat Flux Between 1.4 ≤ x/G ≤ 2.6 vs. ϕ for the Swept Compression Ramp Combustor.

since it is expected that negitive pressure gradients would adversley effect the film integrity.

Downstream of the maximum measured heat flux at x/G = 2.6, the wall heat flux decreased in the expanding combustor duct. The heat flux along the interstice centerline was slightly higher than that along the injector centerline. The effect of ϕ on the wall heat flux is shown for several locations in the farfield of the injectors in Fig. 4.20. The heat flux in the far field of the injectors increased with ϕ for lean equivalence ratios. For $\phi \geq 1$ the heat flux changed little with additional fuel injection.

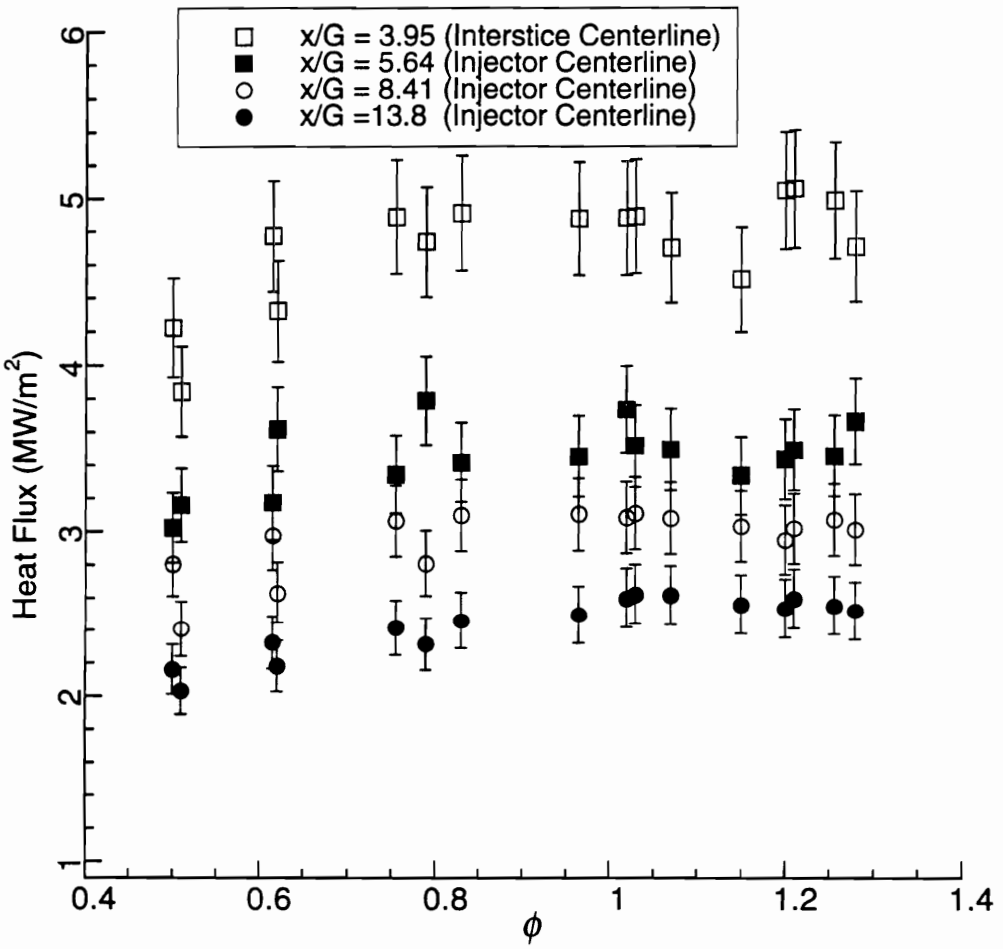

Figure 4.20 Injector Wall Heat Flux vs. ϕ in the Farfield of the Fuel Injectors for the Swept Compression Ramp Combustor.

The heat flux distribution on the wall that was opposite of the fuel injectors is shown in Fig. 4.21 for $0 \leq \phi \leq 1.4$. The maximum measured heat fluxes for the no fuel case occurred at x/G = 2.6. The maximum heat flux for the no fuel case is thought to caused by the pressure rise associated with the second reflection of the shock wave generated by the injector ramps. In the reacting flow cases the heat flux increased with fuel injection, and, at most measurement locations the heat flux increased with additional fuel. Note that the measured pressures also increased with additional fuel. At all measurement locations, the level of the heat flux with fuel injection was much lower than that measured on the injector wall side of the combustor. Recalling the Mie scattering flow visualization and exit pitot pressure surveys discussed earlier, this result was expected, since the hot products of combustion did not penetrate to the opposite wall of the combustor.

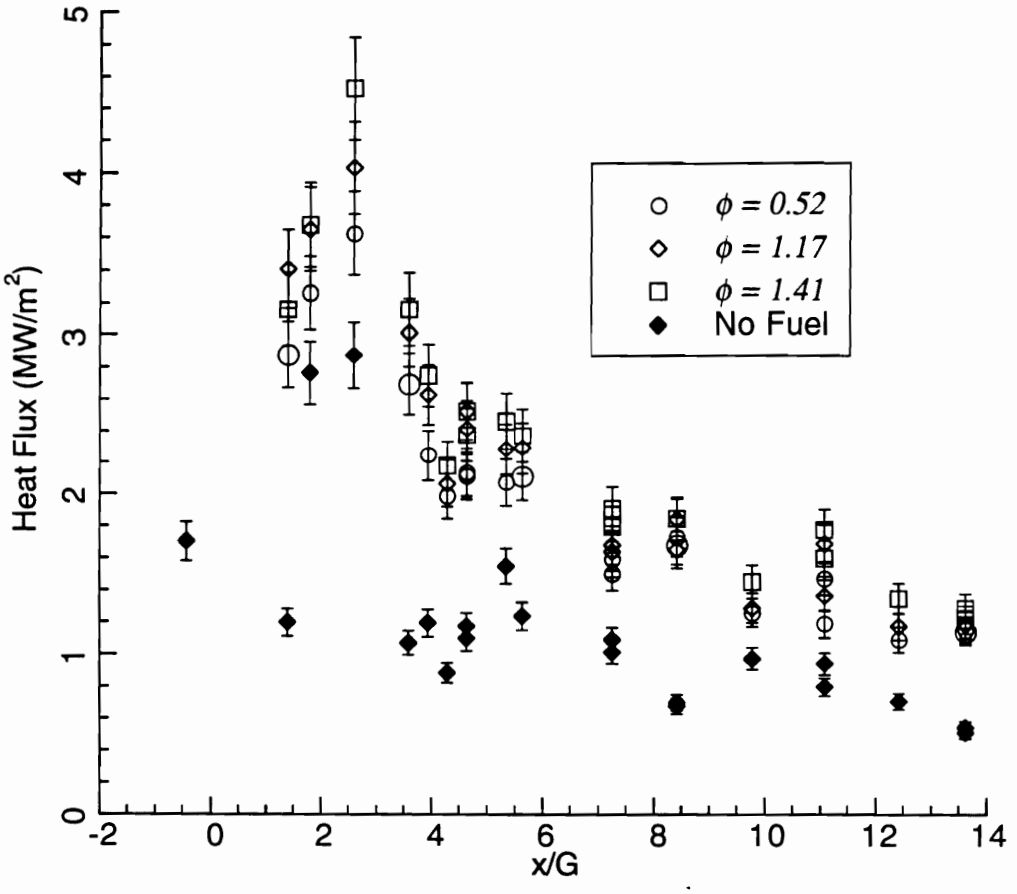

Figure 4.21 Opposite Wall Heat Flux Distribution For The Swept Compression Ramp Model.

4.7.2 Expansion Ramp Heat Transfer

The heat flux distribution for the swept expansion ramp combustor with no fuel injection is shown in Fig. 4.22, along with the interstice centerline pressure distribution. The heat fluxes shown are average values from all of the tests with no fuel. The measured heat flux distribution follows the same trend as the pressure distribution. The hot wall heat fluxes were significantly lower than the measured cold wall heat fluxes. The reason for this difference is that the data system was triggered about 1.6 seconds later than it was for the compression ramp case, resulting in an erroneous assumed initial wall temperature distribution. The error in the surface temperature was approximately 80 K. The effect of this error decreased with

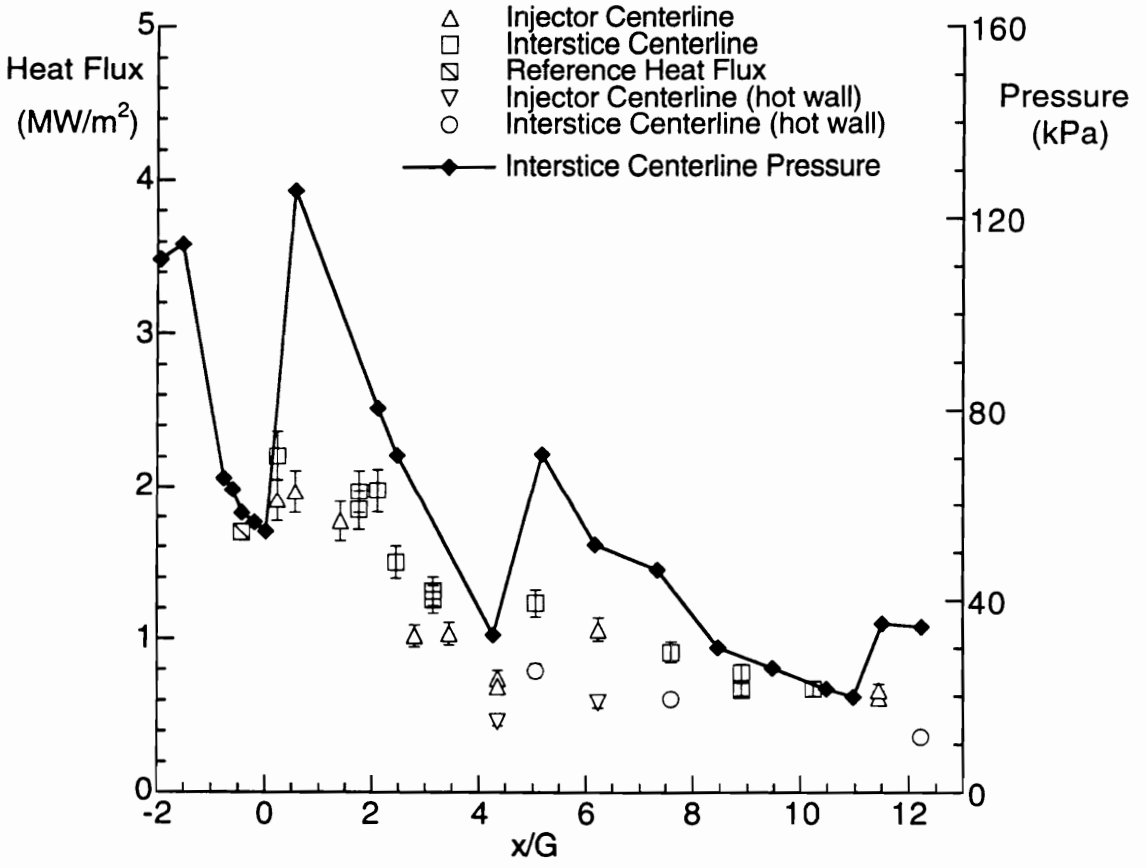

Figure 4.22 Injector Wall Heat Flux Distribution for the Swept Expansion Ramp Injector With No Fuel.

time during the tests because the initial temperature error was small compared to the final wall temperature.

The heat flux along the injector wall of the expansion ramp combustor with fuel injection is plotted in Fig. 4.23 (ϕ = 0.7), 4.24 (ϕ =1), and 4.25 (ϕ =1.25). The flux for no fuel injection as well as the hot wall heat flux is also shown. Note that the difference between the hot wall and cold wall heat fluxes was higher for the expansion ramp combustor than it was for the compression ramp combustor. There are two reasons for this difference. The first is the error in the assumed initial temperature. The second reason is a larger temperature mismatch between the wall and the gage. Recall that the expansion ramp was operated for several seconds with both pilot and main fuel injectors before data collection with only the main fuel injectors on. Thus, the wall temperatures were higher and as a result the hot wall heat fluxes were lower.

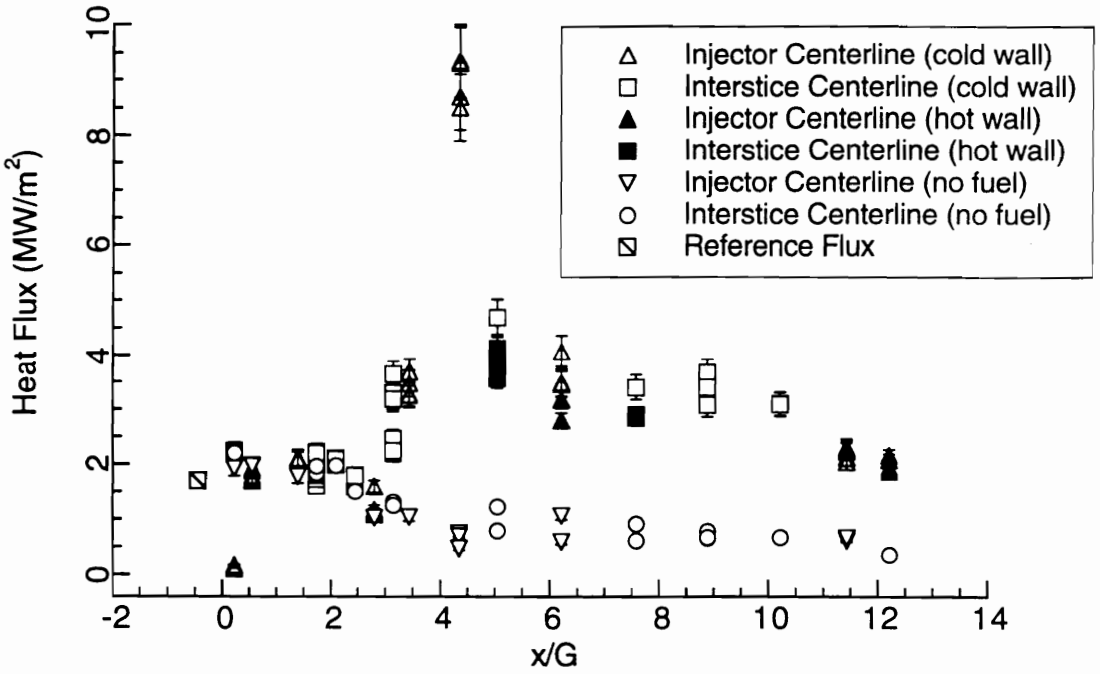

Figure 4.23 Injector Wall Heat Flux Distribution for the Swept Expansion Ramp Fuel Injector (ϕ = 0.72±0.02).

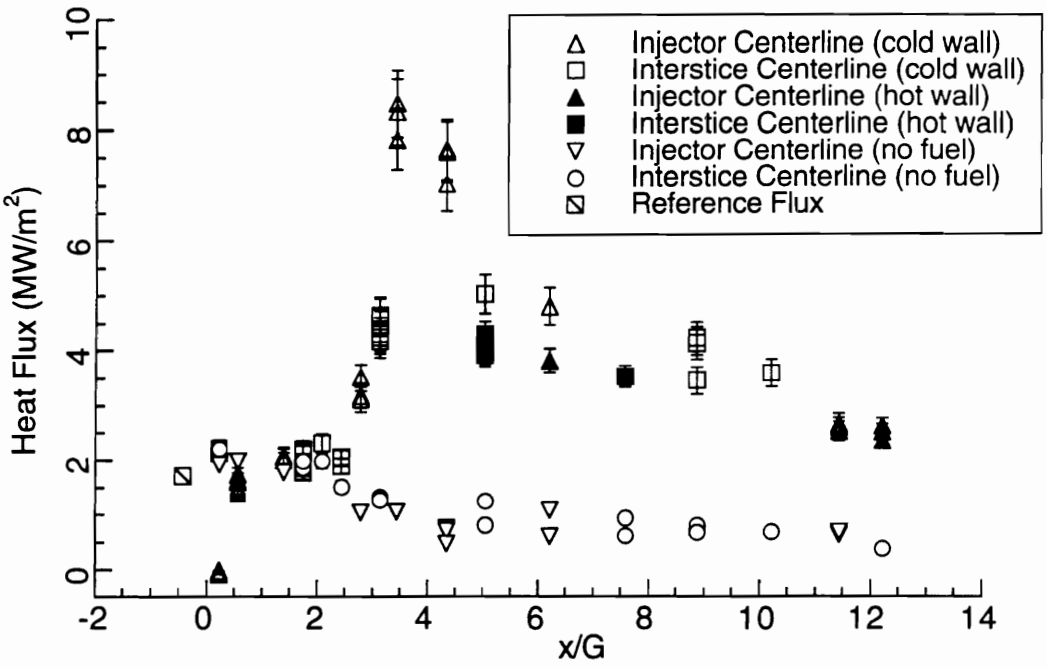

Figure 4.24 Injector Wall Heat Flux Distribution for the Swept Expansion Ramp Fuel Injector (ϕ =0.97±0.02)

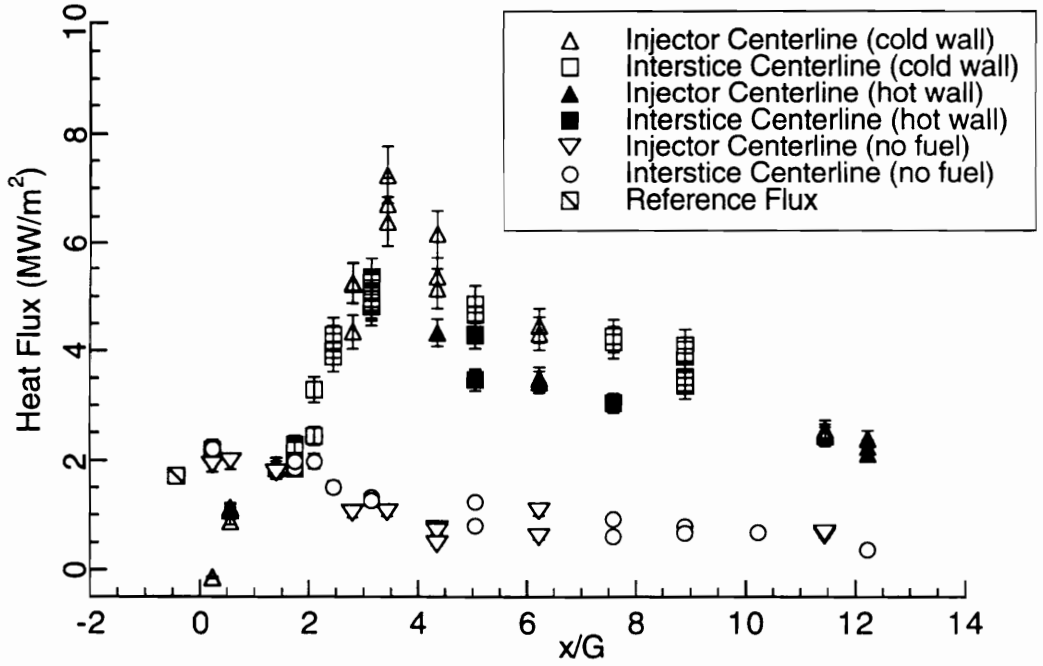

Figure 4.25 Injector Wall Heat Flux Distribution for the Swept Expansion Ramp Fuel Injector (ϕ =1.25±0.03)

The shape of the heat flux distributions is significantly different from those for the swept compression ramp and varied as ϕ changed. In the near field of the injectors the heat fluxes did not increase, but instead decreased with fuel injection. The variation of heat flux with ϕ in the constant area section of the combustor is further illustrated in Fig. 4.26. At the measurement location closest to the injectors (x/G = 0.23) there was little change in the heat flux at the interstice centerline. At the same axial location the heat flux measured in line with the injectors decreased with increased fuel injection so that for $\phi > 0.85$ the heat flux to the wall was negative, implying that cold hydrogen penetrated to the wall at this location without burning. At the next axial station, the heat flux in line with the fuel injectors also decreased with increased fuel injection for $\phi > 0.7$. However, the wall heat flux was still positive at this location.

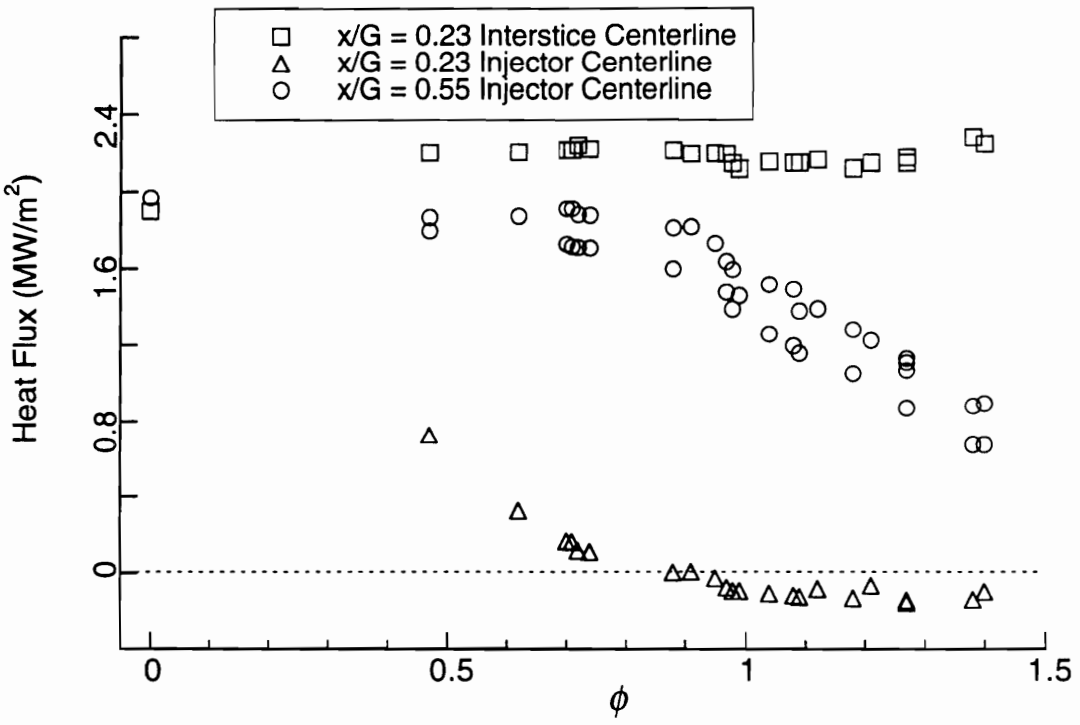

Figure 4.26 Injector Wall Heat Flux in the Constant Area Section of the Swept Expansion Ramp Combustor.

The heat flux in the expanding section of the injector wall was approximately equal to the no fuel heat flux at axial locations up to x/G = 2. The heat transfer increased dramatically between x/G = 2 and x/G= 4.4. The shape of the heat flux distribution in this region varied strongly with the equivalence ratio. Recall that the pressure distributions and one-dimensional combustion calculations presented earlier showed that the pressure rise due to combustion occurred in this region. In the tests with $\phi \leq 1$, the pressure decreased due to expansion in the combustor duct and did not increase before x/G = 2.4. The peak pressure occurred farther downstream as ϕ decreased. This is consistent with the heat flux distributions shown in Fig. 4.23-4.25. The increase in the wall heat transfer, as well as the calculated heat release, occurred closer to the injectors for the fuel rich tests than it did for the fuel lean tests. The peak measured heat flux occurred at x/G = 3.45 for the fuel rich cases, while it occurred further downstream at x/G = 4.36 for the fuel lean cases.

The dependence of the heat flux on the equivalence ratio in this region is further illustrated in Fig. 4.27. At x/G = 2.45 the heat flux increased with ϕ for $\phi > 1$. At locations further downstream of the injectors, the flux began to increase with ϕ at lower values of ϕ. At x/G = 3.45 the heat flux increased with ϕ in the fuel-lean region and slowly decreased with ϕ in the fuel-rich region, while at x/G = 4.36, the maximum flux occurred at $\phi \approx 0.7$ and decreased with further increases in ϕ. At locations further downstream, the heat flux decreased with axial distance and increased slightly with ϕ.

Except in the near-field of the injectors, no noticeable difference was seen between the heat flux along the interstice and the injector centerlines for the swept expansion ramp combustor.

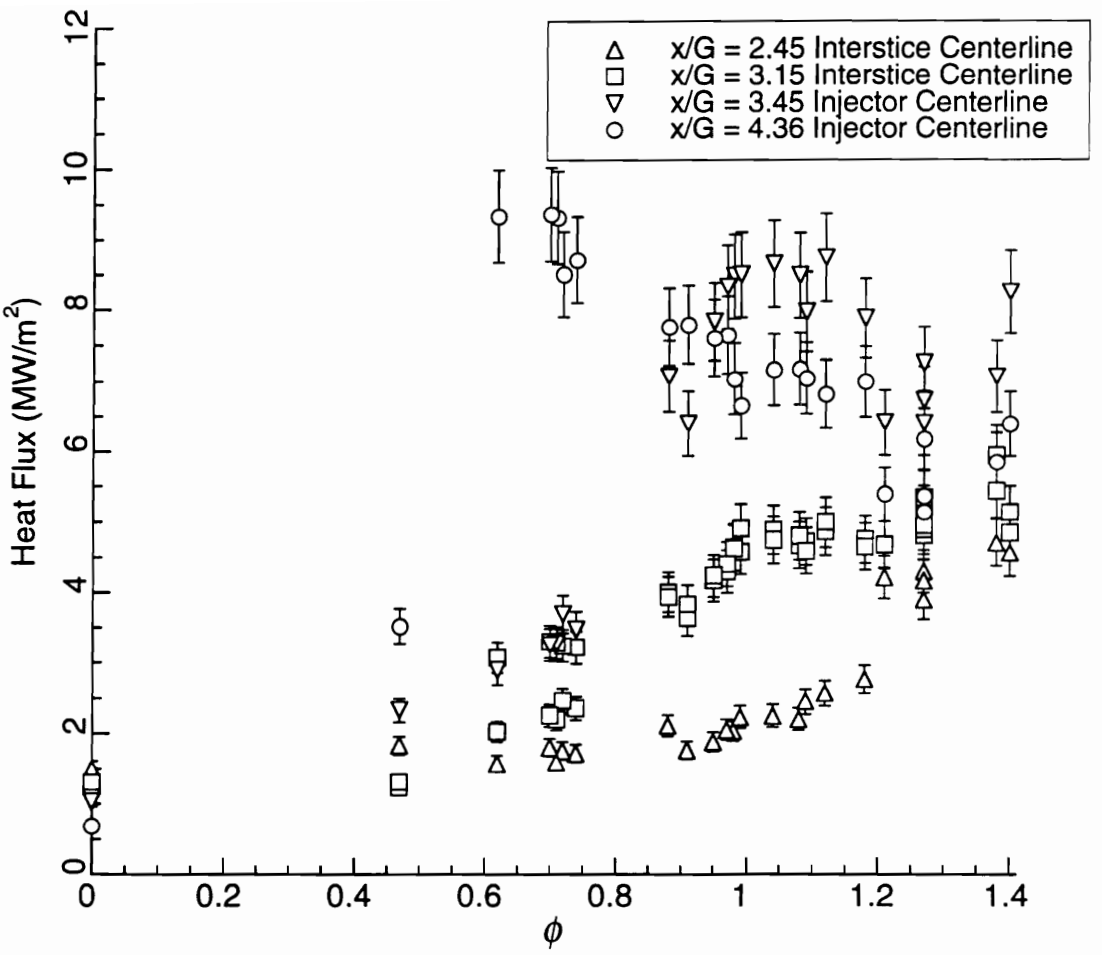

Figure 4.27 The Injector Wall Heat Flux Near the Flame Front for the Expansion Ramp Combustor.

The wall heat transfer opposite of the expansion ramp injectors was measured at a limited number of locations and is plotted in Fig. 4.28. Near the injectors, there was little difference between the heat flux with and without fuel. From x/G = 1.8 to 4 the heat flux was highest for the fuel rich case; note that the pressures in this region were highest. At the last axial station shown, the heat flux was almost equal for the cases with fuel injection. As was for the swept compression ramp cases, the wall heat fluxes were significantly less on the opposite wall, implying that the burning fuel had not penetrated to the opposite wall. Hence, the increase in the heat transfer on the opposite wall was caused largely by the pressure rise.

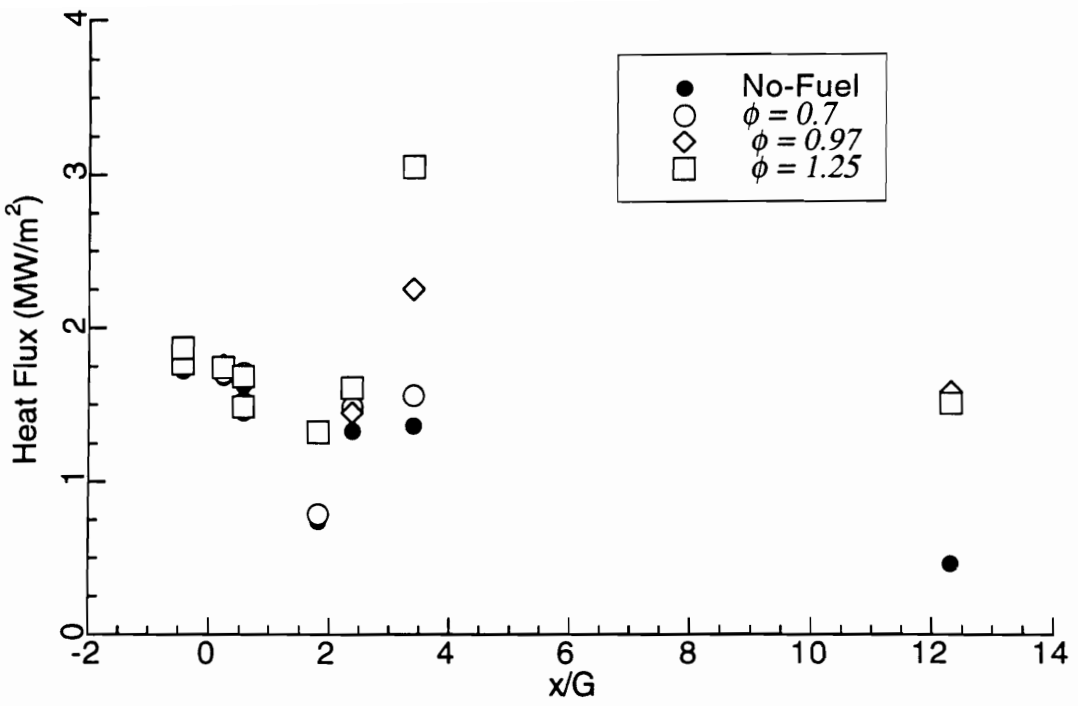

Figure 4.28 The Heat Flux on the Wall Opposite of the Fuel Injectors for the Swept Expansion Ramp Combustor.

4.7.3 Heat Flux Amplitude Ratio

Another way of examining the heat flux is the heat flux amplitude ratio, which is defined as the ratio of the heat flux with and without fuel at a given gage location. The heat flux amplitude ratio is plotted in Fig. 4.29, and 4.30 for the swept compression and swept expansion ramps, respectively. As shown in Fig. 4.29, the heat flux ratio for the swept compression ramp injector ranged from 1.5 to 5, and changed by less than 50 % at all gage locations as ϕ increased from 0.7 to 1.20. In contrast, the heat flux ratio for the swept expansion ramp ranged from 1 to 13. The onset of the heat release due to combustion occurred further downstream, where the heat flux for the no fuel case was lower for the expansion ramps; therefore it resulted in a higher heat flux ratio.

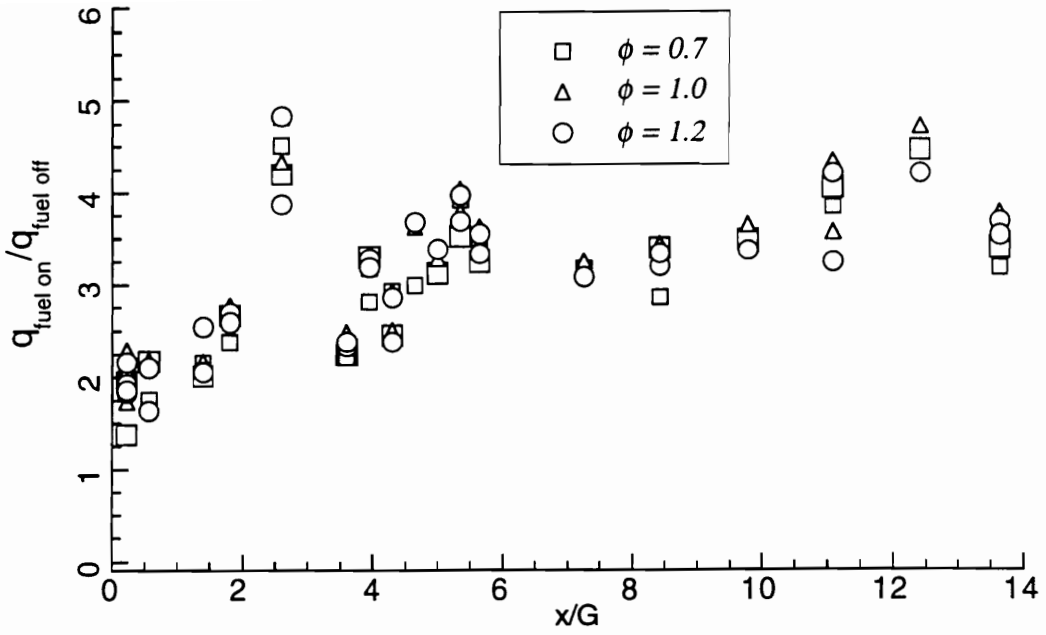

Figure 4.29 Heat Flux Amplitude Ratio ($q_{fuel\ on}/q_{fuel\ off}$) for the Swept Compression Ramp Combustor.

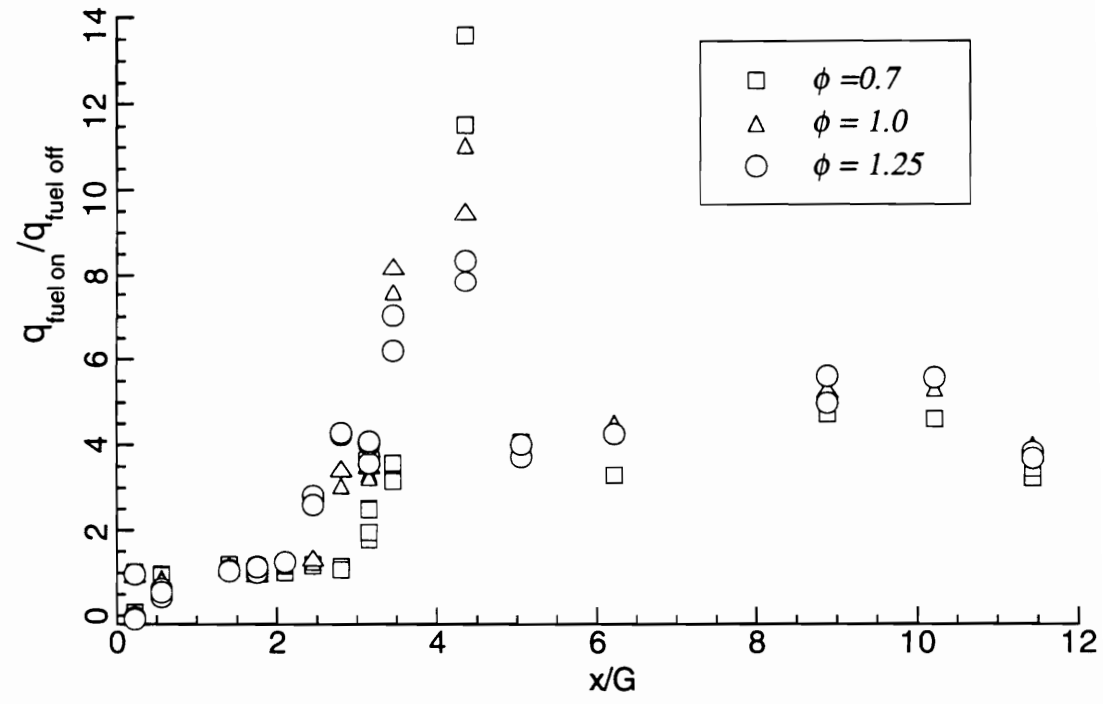

Figure 4.30 Heat Flux Amplitude Ratio ($q_{fuel\ on}/q_{fuel\ off}$) for the Swept Expansion Ramp Combustor.

Chapter 5

Results and Discussion of the Numerical Flowfield Analysis

5.1 Scope of the Numerical Study

The numerical simulations of the scramjet flow field were conducted in cooperation with other researchers at NASA-Langley as part of a joint investigation of the reacting flow fields downstream of swept-ramp fuel injectors. Solutions for the swept-compression ramp were achieved by the author and will be discussed in detail. Solutions for the expansion-ramp injectors were attained by other researchers and will be briefly discussed at the end of this chapter. Further details from the joint investigation are presented in reference 107.

Because of the large amount of computer time required to solve the complex flow field, the calculations presented here are for a single fuel equivalence ratio (ϕ=0.7). This equivalence ratio was chosen to facilitate comparison with the Mie scattering flow visualization. The results of four cases will be presented. The first case is a vitiated flow with no fuel injected, which corresponds to tunnel operation with no fuel injection. Two mixing cases with "non-reacting" hydrogen were also studied, one with laminar flow to investigate the inviscid mixing characteristics of the ramps, and a turbulent case to investigate the additional mixing due to turbulent diffusion. The last case is a turbulent reacting flow, which is intended to model the flow field with fuel injection and heat release.

5.2 Solution Technique

The flow through the combustor was modeled using the SPARK code which was developed at NASA-Langley Research Center by Drummond et al.[108-110] as a two-dimensional code and later extended to three dimensions by Carpenter.[111] The code uses the steady state cross-MacCormack algorithm, which is second order accurate in time and space, and is fourth-order accurate at steady state.

5.2.1 Turbulence Modeling

One of the most difficult issues in the numerical analysis of reacting turbulent flows is how to model the turbulence. The Boussinesq assumption, which states that the turbulent or Reynolds stress can be related to the local mean strain rate by an apparent turbulent viscosity, was used. With this assumption the effective transport coefficients can be expressed as the sum of the laminar and the apparent turbulent values. Thus,

$$\mu = \mu_l + \mu_t \tag{5-1}$$

$$k = C_p \frac{\mu_l}{\mathrm{Pr}_l} + C_p \frac{\mu_t}{\mathrm{Pr}_t} \tag{5-2}$$

$$D = \frac{\mu_l}{\rho Sc_l} + \frac{\mu_t}{\rho Sc_t} \tag{5-3}$$

where l and t refer to the laminar and turbulent components, respectively.

The turbulent Prandtl and Schmidt numbers were set to constant values of 0.9, and 0.5, respectively. The turbulent viscosity, μ_t, was calculated by analogy with the calculation of the laminar viscosity from kinetic theory, as follows: $\mu_t = c\rho vl$ (5-4)

where, c is a constant, v is the velocity scale, and l is the length scale.

A composite turbulence model formed from two algebraic turbulence models was used in this investigation. This composite turbulence model has been used with success in a previous validation study of the SPARK code for mixing of a normal jet in a supersonic flow.[114] In the region near the walls the Baldwin-Lomax model[112] was used. The length scale in the Baldwin-Lomax model is based on the distance from the wall and the velocity scale is based on the vorticity of the flow. The turbulent viscosity in the jet region was calculated from a simplified turbulence model which was a modification of the one suggested by Eggers.[113] This model used the velocity at the fuel jet centerline as the velocity scale and the average of the half-concentration width of the fuel jets in the normal and spanwise directions as the length scale.

In the outer region of the jet, where the hydrogen concentration drops to less than 1% of the maximum value, the turbulent viscosity was reduced by multiplying it by the ratio of the hydrogen concentration divided by a

concentration of 1 % hydrogen. In the region near the wall, the turbulent viscosity from the Eggers model was multiplied by the ratio $\left(\frac{z}{2\delta}\right)^2$ where z is the distance from the wall and δ is the boundary layer thickness. The value of the turbulent viscosity used at each point is the maximum value calculated from the two models. The turbulent viscosity was limited to less than 1000 times the laminar viscosity. This limitation on the turbulent viscosity is widely used.

In the initial calculations the constant c = 0.0164 was used in equation 5-4 as suggested by Eggers.[113] With this assumption the turbulent viscosity was more than 1000 times the laminar viscosity over most of the domain. Therefore, the constant, c, was lowered to 0.00328 for the turbulent cases that are presented here.

5.2.2 Chemistry Model

For the reacting calculations two different reaction models were used. The first model is a 7 species-7 reaction model adapted from reference 115 which uses the reactions listed in Table 5.1. The second model is a 9 species-19 reaction model adapted from reference 116, which includes the effect of HO_2 and H_2O_2, and is listed in Table 5.2. In both mechanisms nitrogen is assumed to be inert, but is allowed to act as a third body.

The reaction rates were found from the law of mass action. The forward reaction rate coefficients were calculated by the Arrhenius expression: $k_{f_i} = A_i\left(T^{b_i}\right)\exp\left(-T_{a_i} / T\right)$ where the constants A_i, b_i, and T_{a_i} are listed in reference 107. The backward rate coefficients were calculated from the forward rate coefficient and the equilibrium constant, K_i, where: $k_{b_i} = k_{f_i} / K_i$ and the equilibrium constant can be calculated from the change in the Gibbs function, ΔG°, for each reaction:

$$K_i = \left(\frac{1}{R_U' T}\right)^{\Delta n_i} \exp\left(\frac{-\Delta G_i^o}{R_U T}\right)$$

where Δn_i is the difference in the stoichiometric coefficients between the products and reactants.

Table 5.1 Reactions in the First Hydrogen-Air Reaction Mechanism.

$H_2 + O_2 \Rightarrow 2OH$
$H + O_2 \Rightarrow OH + O$
$OH + H_2 \Rightarrow H + H_2O$
$O + H_2 \Rightarrow OH + H$
$2OH \Rightarrow O + H_2O$
$H + OH + M \Rightarrow H_2O + M$
$H + H + M \Rightarrow H_2 + M$

Table 5.2 Reactions in the Second Hydrogen-Air Reaction Mechanism.

$H_2 + O_2 \Rightarrow HO_2 + H$
$H + O_2 \Rightarrow OH + O$
$O + H_2 \Rightarrow OH + H$
$OH + H_2 \Rightarrow H + H_2O$
$OH + OH \Rightarrow O + H_2O$
$H + OH + M \Rightarrow H_2O + M$
$H + H + M \Rightarrow H_2 + M$
$H + O + M \Rightarrow OH + M$
$O + O + M \Rightarrow O_2 + M$
$H + O_2 + M \Rightarrow HO_2 + M$
$HO_2 + H \Rightarrow OH + OH$
$HO_2 + O \Rightarrow OH + O_2$
$HO_2 + OH \Rightarrow H_2O + O_2$
$HO_2 + HO_2 \Rightarrow H_2O_2 + O_2$
$H + H_2O_2 \Rightarrow H_2 + HO_2$
$H + H_2O_2 \Rightarrow OH + H_2O$
$O + H_2O_2 \Rightarrow OH + HO_2$
$OH + H_2O_2 \Rightarrow H_2O + HO_2$
$OH + OH + M \Rightarrow H_2O_2 + M$

The third body efficiencies used for the termolecular reactions were 2.5 for M = H_2, 16.0 for M = H_2O, and 1 for all other species. Most of the calculations were made using the 7-reaction model. After obtaining a solution for the 7-reaction model, the 19-reaction model was used. An

examination of the flow field properties showed that the effect of including the additional radicals, H_2O_2, and HO_2, on the flow structure was negligible.

A major concern in the computation of reacting flows is the "stiffness" of the system of equations that are used to model the reactions. Stiffness in a system of equations is caused by a disparity between the time scales of the reactions. In the integration of a system of differential equations, the time step is dictated by the rate of the fastest reactions to ensure stability of the system. However, after the calculation of the initial transient, which is dominated by the fastest reactions, the calculation is still advanced with small time steps, which causes little change in the slower reactions. Thus a large amount of time is required to integrate the system of equations.

In past applications of the SPARK code, because of concerns about the stiffness, the chemical source terms were calculated implicitly. A preconditioning matrix was formed which allowed each reaction to be advanced at its own characteristic rate. Implicit evaluation of the source terms requires that, for n different species, an n x n matrix must be evaluated at each point for each time step. This requires large numbers of computations for large grids. For this reason, the stiffness of the equations was examined early in the study. It was determined that the chemical source terms could be calculated explicitly for the conditions of the test case. In fact, the explicit calculation of the chemical source required only 60 % of the time per iteration as the implicit calculations. Comparisons between the implicit and explicit calculations showed that 25 % more iterations were required with the explicit calculations.[107] Therefore, explicit evaluation of the chemical species equations resulted in a net computer time reduction of 25 %, and was used for the reacting flow calculations presented in this study.

5.2.3 Computational Grid, and Boundary Conditions

The combustor was split into upstream and downstream grids for the calculations. The grids were generated outside of the SPARK code using the exponential stretching functions from reference 141. The grids were then passed through an elliptic solver routine written by White[142]. Most of the computational effort was spent on the upstream region of the combustor. The

grid used for the computations on the upstream portion of the combustor is shown in Fig. 5.1. In the streamwise direction the grid extended from the beginning of the ramps, to 6.2 gap lengths (457 mm) downstream of the ramps. In the streamwise direction, the grid is compressed at the start and end of the injector ramp, at the end of the constant area section of the combustor, and at the outflow boundary. The grid extended from the top to the bottom walls of the combustor, so that the effects of the reflected shocks could be captured. In this direction the grid was also compressed at the top and bottom walls of the combustor and along the top of the injector. In the spanwise direction, symmetry was used to restrict the computational domain to 1/8 of the spanwise width of the combustor (from the fuel jet centerline to the interstice centerline), in order to reduce the computer time required for the calculations. Grid compression was used in the spanwise direction along the interstice and fuel jet centerlines, as well as at the edge of the injector ramp. The grid used 163, 39, and 75 grid points for the streamwise, spanwise, and normal directions, respectively, for a total of 476,775 grid points.

After obtaining solutions for the upstream section of the combustor, the grid shown in Fig. 5.2 was used to calculate the flow for the second section of the combustor. The grid for the second section of the combustor used 77, 20, and 101 grid points for the streamwise, spanwise, and normal directions, respectively. For the second grid, the number of nodes was reduced by progressively increasing the spacing of the grid points in the streamwise direction and decreasing the number of points in the spanwise direction by a factor of 2. This was possible because the grid compression that was required to resolve the flow features near the ramp was not required in the farfield of the injectors. The number of points in the normal direction was increased with the goal of better resolving the flow near the wall in order to improve the calculations of the heat transfer. The grid spacing in the normal direction at the wall was 1μm in this section of the combustor. The grid spacing in wall units, $\left(z^+ \equiv \frac{zu_*}{\upsilon} \right)$, where z is the distance of the first node from the wall was calculated and ranged between 0.9 to 0.4. Thus, the first node was inside the laminar sublayer. This is in contrast to the grid for the

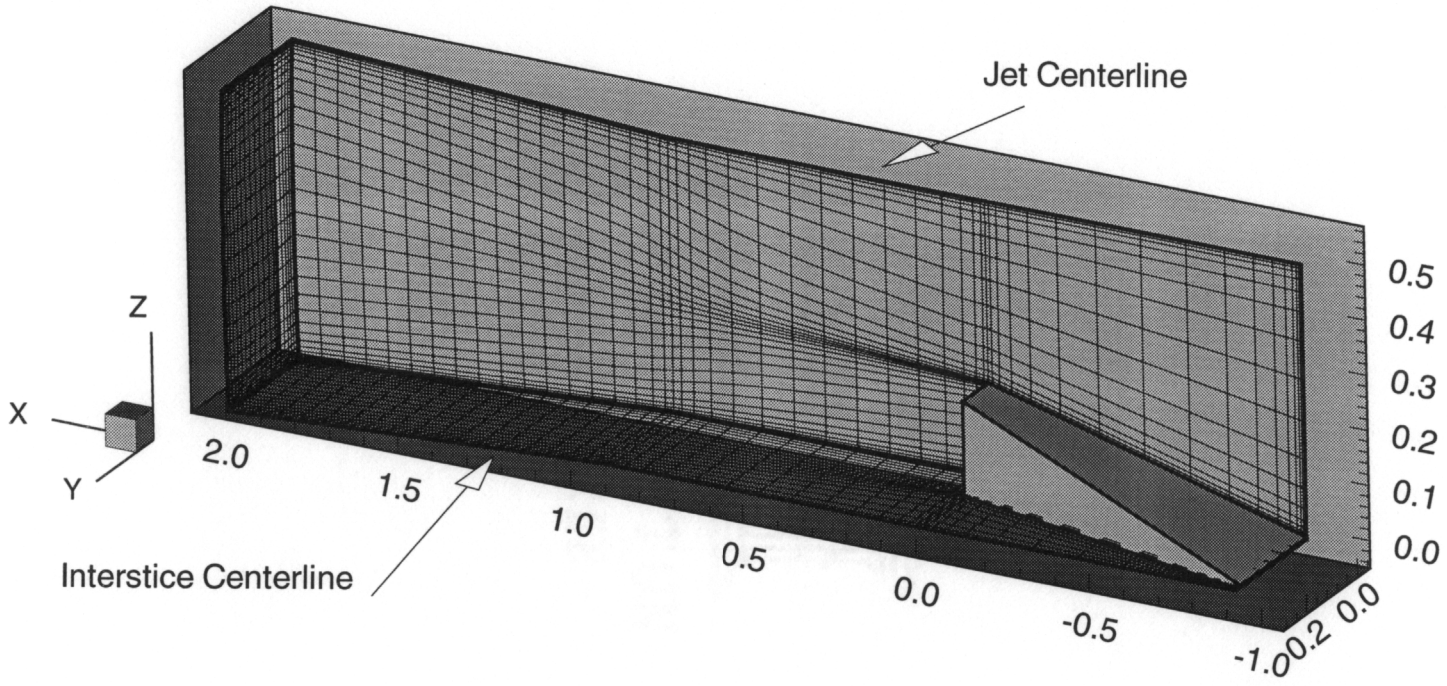

Figure 5.1 Computational Grid Near the Injectors.

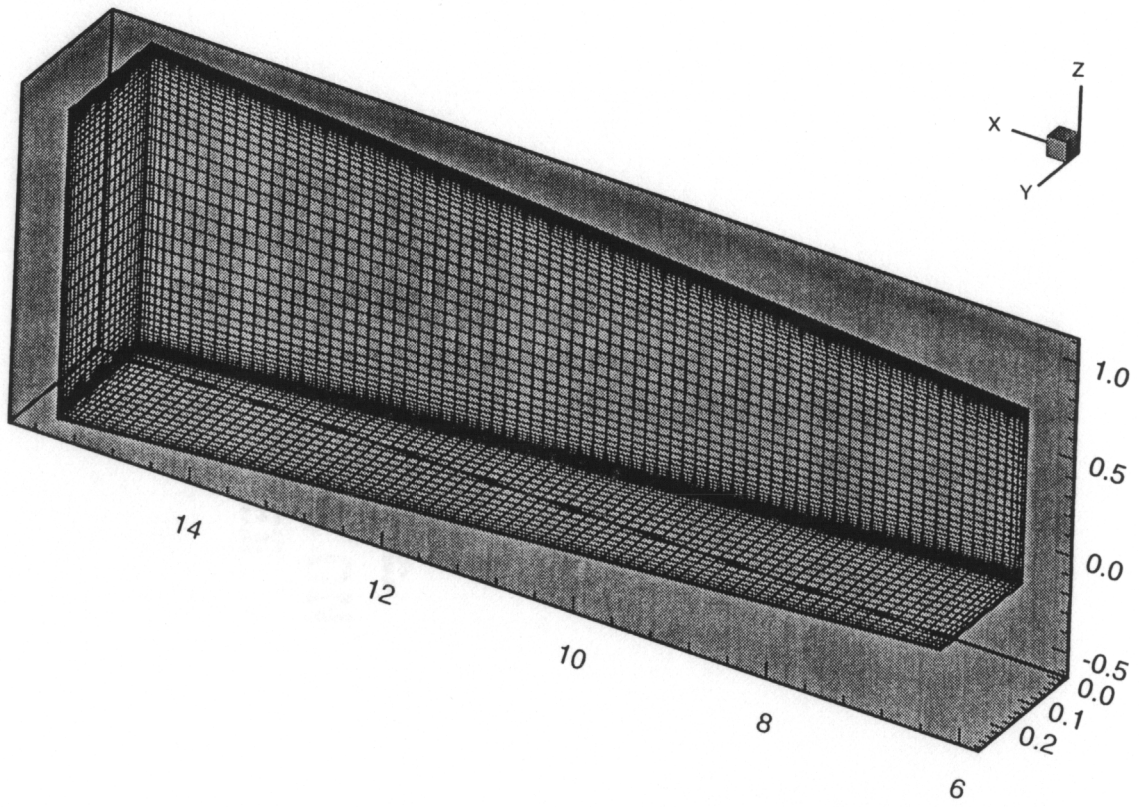

Figure 5.2 Computational Grid For the Second Half of the Combustor.

upstream section where the spacing of the first node from the wall is roughly 14 times larger than it is for the second grid. Therefore, the calculated values of the heat transfer and skin friction are expected to be less accurate for the upstream grid.

A known solution for the facility nozzle flow and the constant area section of the combustor upstream of the ramps was used for the inflow conditions. The static properties at the entrance of the combustor (M = 2.63, P = 104 kPa, T = 930 K) modeled the experimental conditions. Fuel injection from the conical nozzle was modeled as a point source. The injector was modeled with 87 points that were distributed to approximate a circle. The top and bottom walls were modeled as no-slip along with a zero normal pressure gradient. A constant surface temperature of 670 K was assumed for the walls in the first section of the domain. The wall temperature was estimated by calculating the wall heating by a compressible boundary layer at a total temperature of 1900 K. A linear curve fit of the measured wall temperatures was used for the second section of the domain. The two side planes of the domain were treated as symmetry planes, and the outflow boundary was modeled using first-order extrapolation.

A spline fit of the exit properties at the first section of the combustor was used for the inlet properties at the start of the second section of the combustor. Because the minimum Mach number at the exit for the first section of the combustor was supersonic (M=1.35 for the reacting case), splitting the computational domain into two sections should not have affected the solution.

5.2.4 Calculation Procedure

The system of equations was advanced in time using a local time step along with a Courant number of 0.5 for the turbulent mixing and reacting cases, and 0.3 for the laminar cases. The mixing solutions were started from the no injectant solution, and the reacting flow solution was started from the solution of the mixing case. Autoignition occurred in the reacting case without the aid of "numerical" ignition aids such as lowered activation energies.

The residual, which is defined as the normalized density change between successive iterations was monitored. The residual dropped to around 0.001 and then oscillated about this value. Thus, a true steady-state solution as defined by the residual approaching the round-off error of the computer was not obtained. Therefore, an inspection of the integrated mass flow, mixing efficiency, and combustion efficiency was used to assess the convergence of the solution. The conservation of mass was within 1 % for all of the turbulent cases, and within 2 % for the laminar mixing case.

The number of iterations required to solve the mixing cases was approximately 10,000, while the reacting cases required up to 70,000 iterations. The computations were performed on the CRAY-2 and CRAY-YMP computers at NASA-Langley. The total computer time required on the CRAY-2 computer was 23 cpu-hr. for the mixing cases and 330 cpu-hr. for the reacting case.

5.3 Flowfield Structure

5.3.1 No Injectant Case

Calculations of the flowfield structure for the no fuel case are shown in Fig. 5.3-5.8. Figure 5.3 shows the pressure and temperature along the jet centerline and interstice planes. The presence of shocks caused by the ramps and subsequent reflected shocks can be seen. Expansion fans were generated as the flow expanded around the side, and top of the ramp and interacted with the reflected shock waves generated by the ramp.

The contour plots of pressure at selected cross flow planes are shown in Fig. 5.4. Note that the domain extended from the injector centerline (y/G =0) to the interstice centerline (y/G = 0.28), or 1/8 of the combustor width. For clarity, the aspect ratios of the cross flow plots have been changed to exaggerate the spanwise (y) dimension. The pressure plot at x/G = 0 shows the high pressure region on the top of the ramp and the lower pressures on the sides of the ramp. The highest pressures occurred on the wall opposite of the fuel injectors immediately downstream of the location where the ramp

shock was reflected from the wall. The shock train weakened in the expanding portion of the combustor. Note that the plots of pressure in the cross flow plane show that the calculated wall pressure varied little in the spanwise direction for x/G > 1.5.

The Mach number contours are shown in Fig. 5.5. A small recirculation zone existed downstream of the ramp base. The axial velocity component was positive over the entire cross-flow plane at x/G > 0.25. For x/G > 0.5 the flow was supersonic except for the subsonic part of the boundary layer.

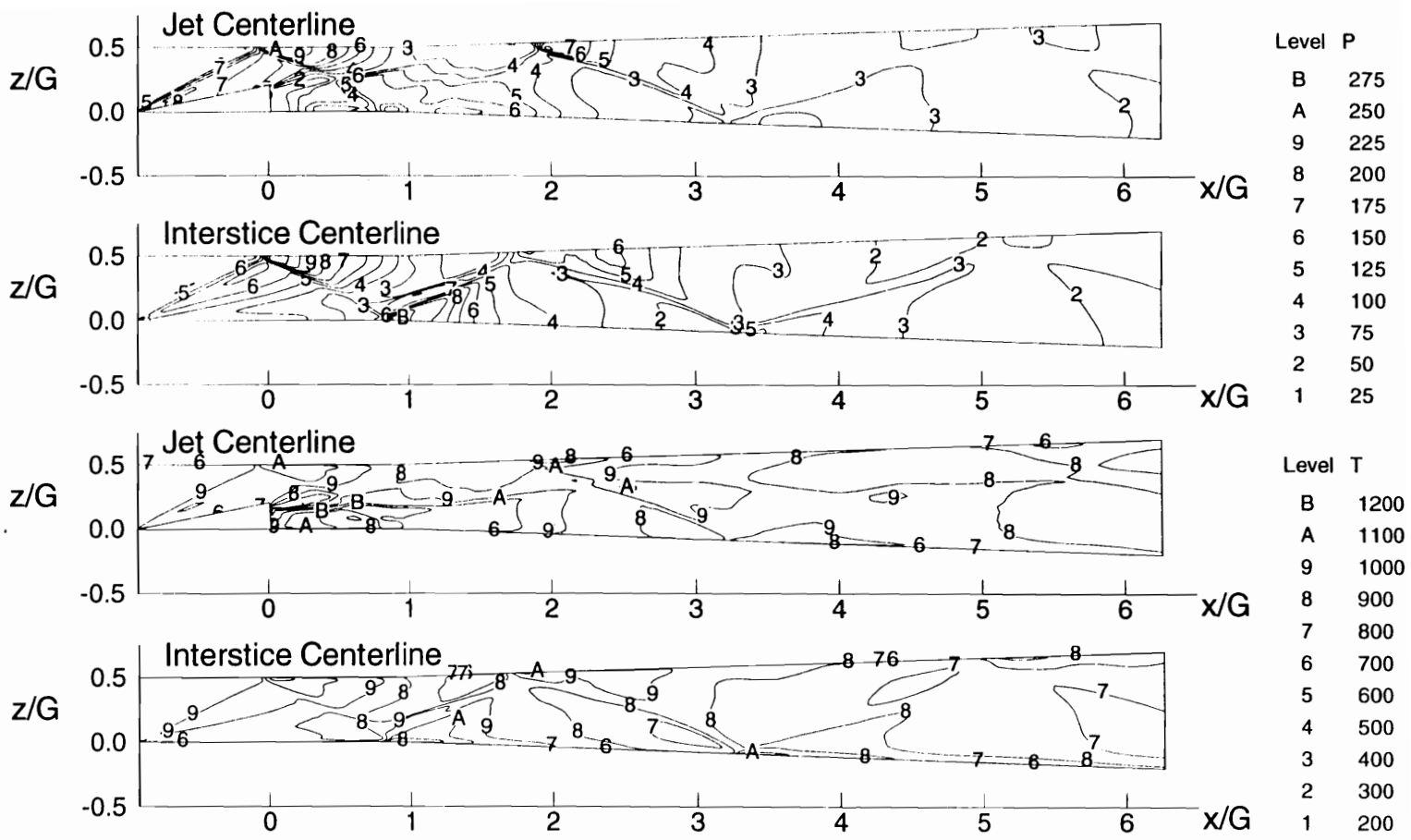

Figure 5.3 Pressure (kPa) and Temperature (K) Contours for the No Fuel Case.

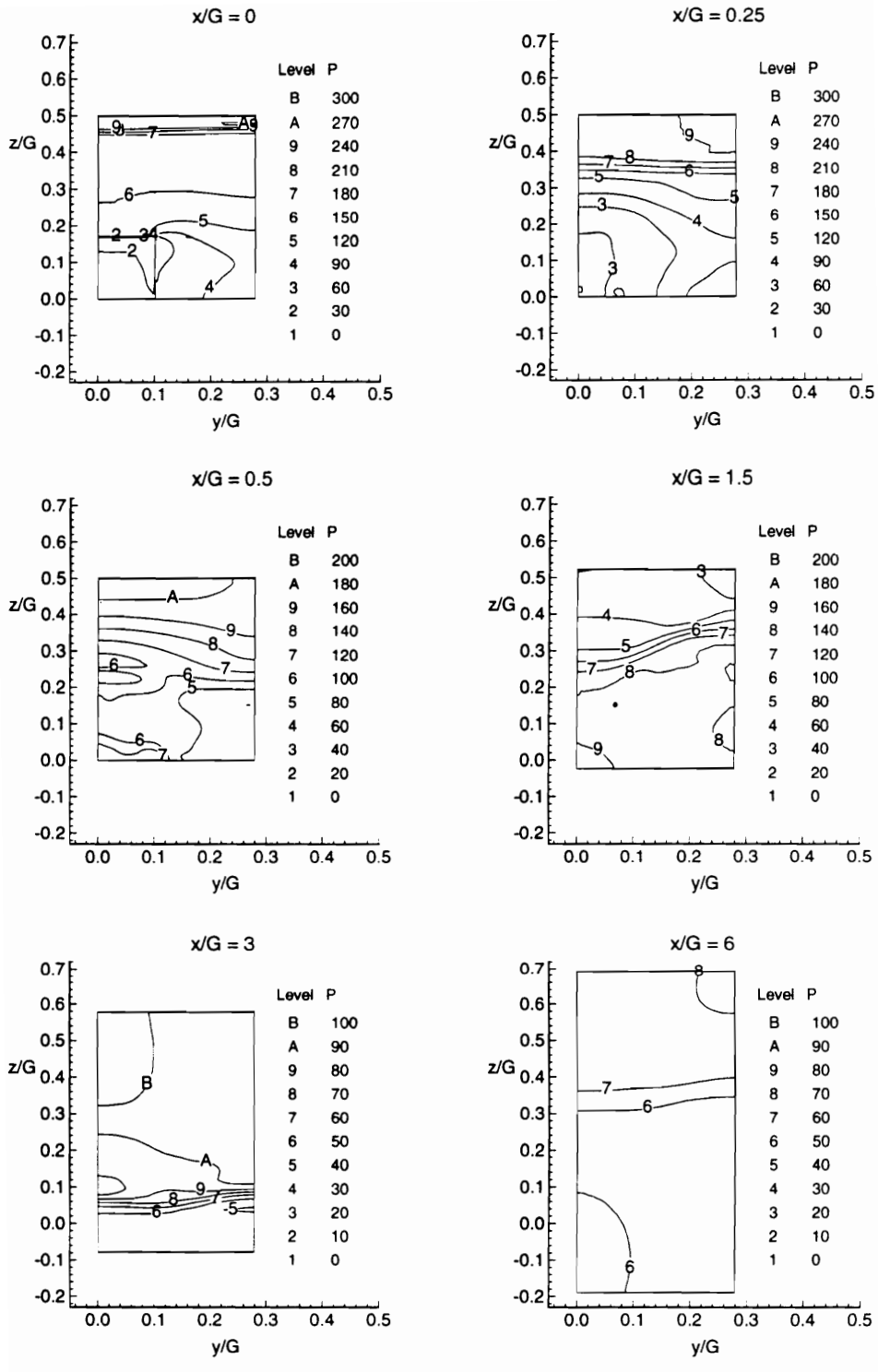

Figure 5.4 Pressure Contours (kPa) in the Cross Flow Planes for the No Fuel Case.

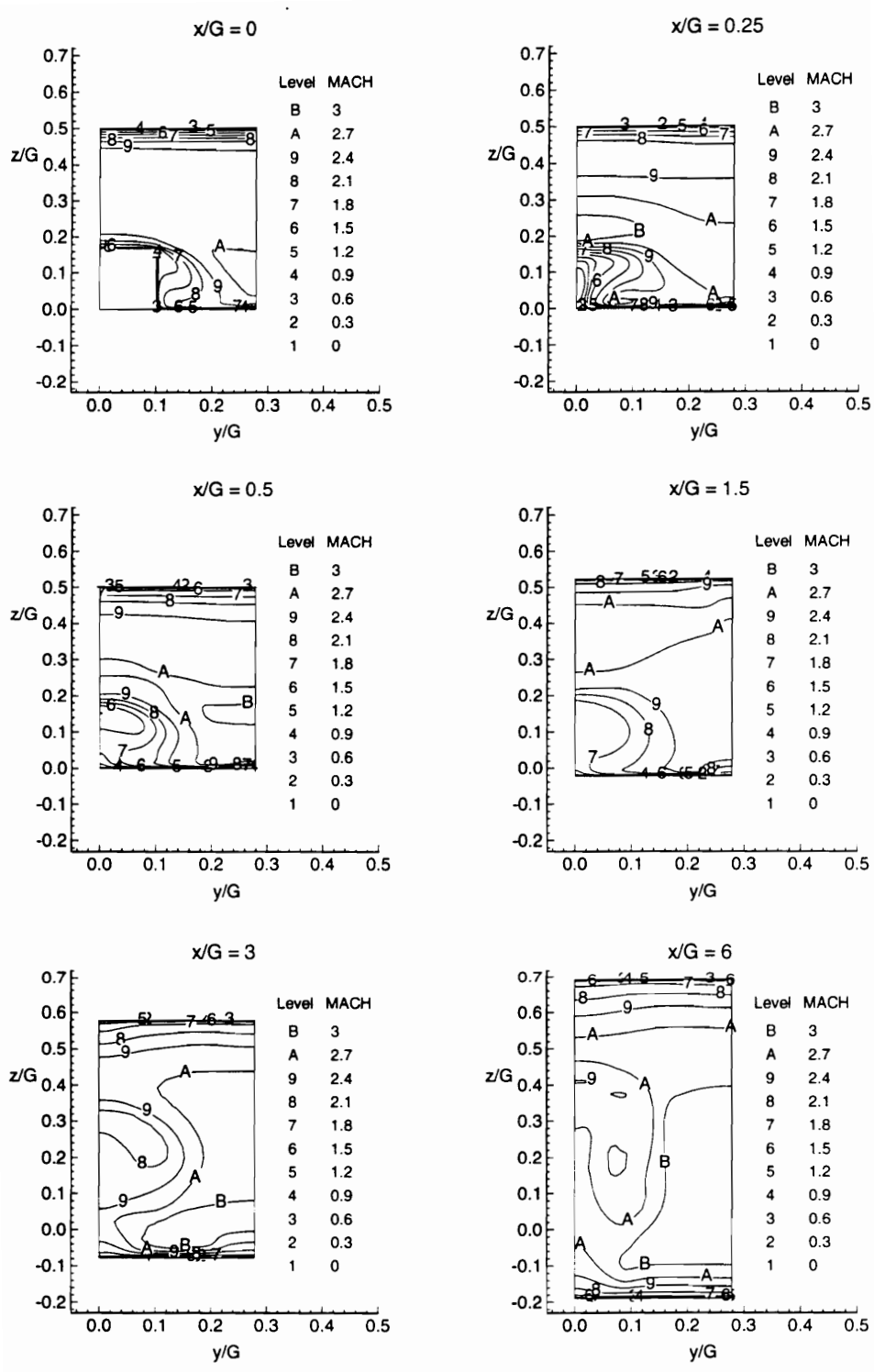

Figure 5.5 Mach Number Contours in the Cross Flow Planes for the No Fuel Case.

The velocity vectors in the cross flow planes are shown in Fig. 5.6. At the exit of the ramp the formation of the vortex is shown as the flow expands from the high pressure top of the ramp to the low pressure interstice between the ramps. Immediately downstream of the ramps, the flow expanded around the ramp base in the x-y plane resulting in large cross flow velocities near the bottom wall surface. At x/G = 0.5 a well-defined vortex that extended to the jet centerline is seen. The decay of the vorticity as the flow expanded along the rest of the combustor is shown in the plots for the downstream locations.

Another way of illustrating the vortical structure in the cross flow plane is the axial component of the vorticity vector. The axial component of the vorticity vector, $\omega_x \equiv \left[\frac{dw}{dy} - \frac{dv}{dz}\right]$, is plotted in Fig. 5.7. The sign convention used for the vorticity was the right hand rule, so that clockwise rotation (when looking upstream) corresponds to negative values of vorticity. Positive values of vorticity are shown by solid lines, and the dashed lines are used to indicate contours of negative vorticity. At the exit of the ramp the vorticity generated by the ramp can be seen. Downstream of the ramps, the vortex moved towards the jet centerline. At the x/G = 0.5 plane the edge of the vortex extended to the jet centerline, so that for each injector ramp there were two counter-rotating vortices that touched at their edges. Between x/G=0.25 and x/G=1.5 the vortex remained near the bottom wall of the combustor and grew little. The maximum vorticity decayed due to viscous dissipation and diffusion. At locations further downstream, the vortex eventually lifted off the bottom wall and weakened due to expansion and viscous forces.

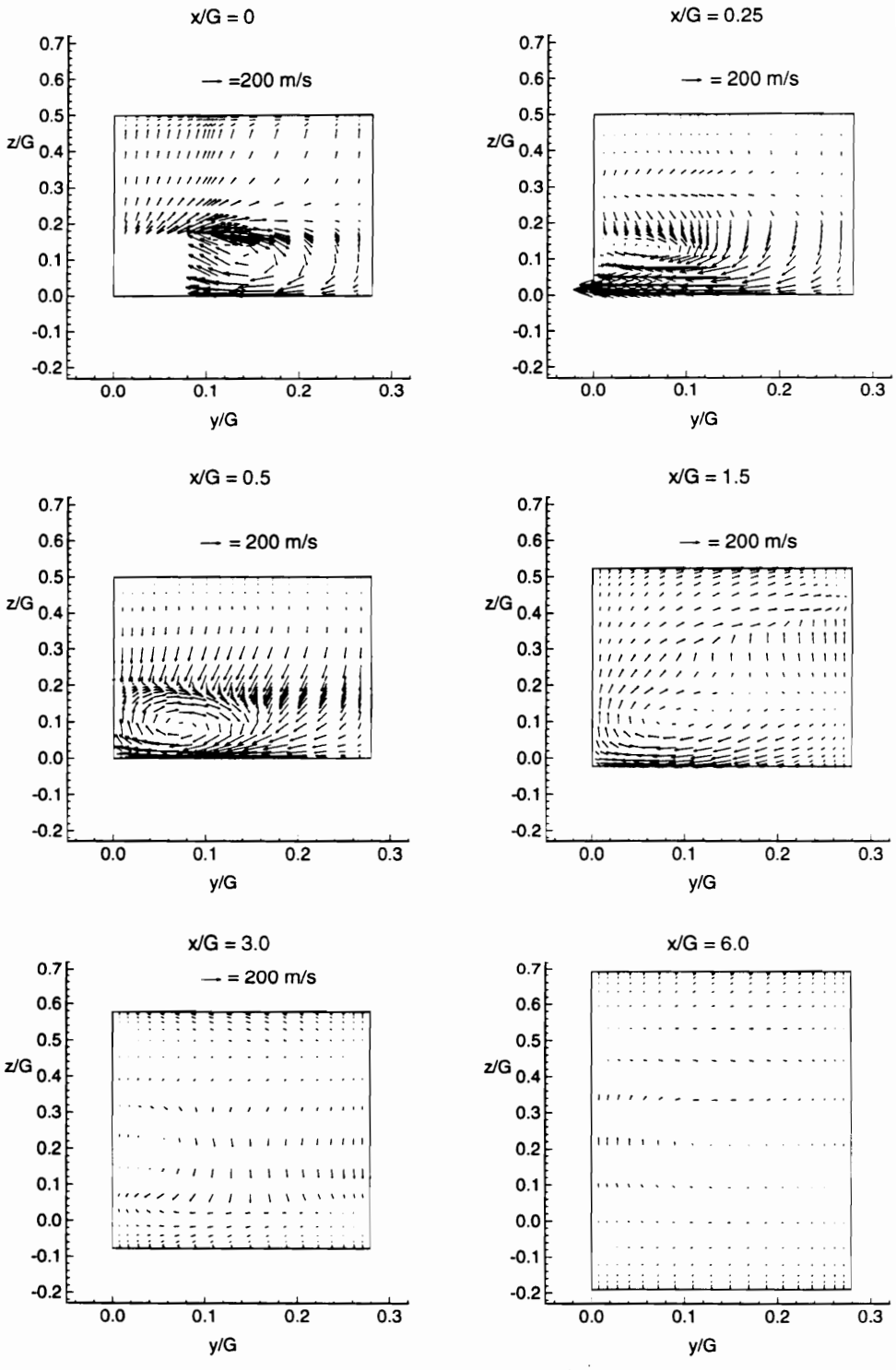

Figure 5.6 Velocity Vectors in the Cross Flow Planes for the No Fuel Case.

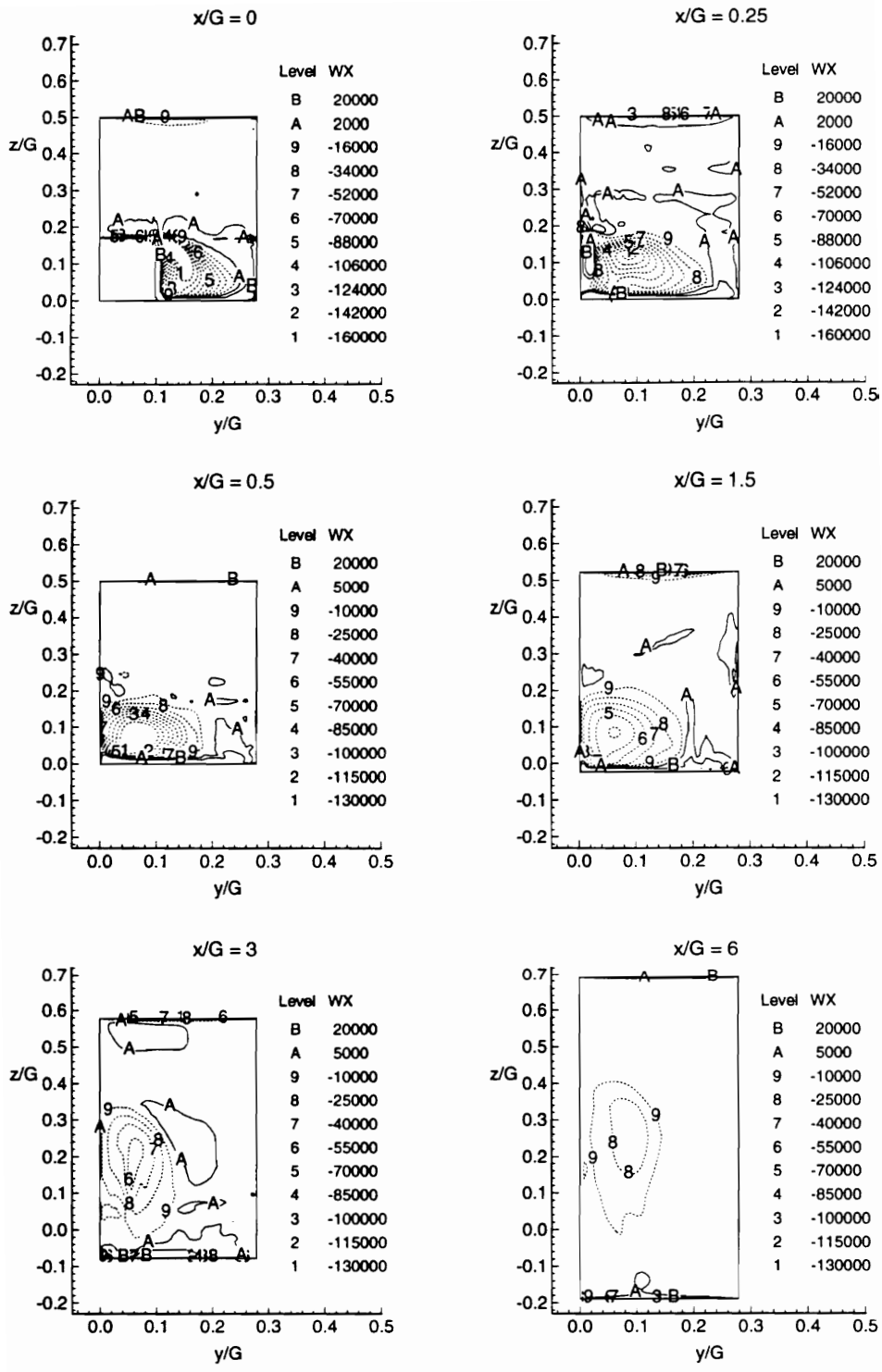

Figure 5.7 Axial Vorticity (1/s) in the Cross Flow Planes for the No Fuel Case.

5.3.2 Laminar Mixing Case

The flow structure for the laminar mixing case is shown in Fig. 5.8-5.11. The pressure and temperature contours are shown in Fig. 5.8. The pressure contours on the interstice centerline differ little from the no fuel case. The pressure contours on the injector centerline differ greatly in the near-field because of the effect of the fuel jet on the expansion and shock waves. The temperature contours along the jet centerline show that a low temperature region existed along the entire combustor, which was caused by the injection of the cold inert fuel. The fuel penetrated to the opposite side of the combustor by x/G = 5.3. The temperature contours for the interstice show that the cold fuel did not penetrate to the interstice.

The cross-flow velocity vector and the vorticity contours are shown in Fig. 5.9 and 5.10. At the ramp base plane the velocity vectors were slightly higher than those for the no fuel case. The vortex for the laminar mixing case was closer to wall and flatter for the laminar mixing case than it was for the no fuel case at x/G = 0.5. Also, the vorticity plots show that the vortex strength was significantly greater for the laminar mixing case than it was for the no fuel case. Because there is no turbulent diffusion for laminar flow, the viscosity was much lower for the laminar case than it was for the no fuel case, resulting in slower dissipation of the vortex for the laminar case. Downstream of the x/G = 0.5 plane, the vortex lifted off the injector wall and moved transversely across the combustor to the other wall.

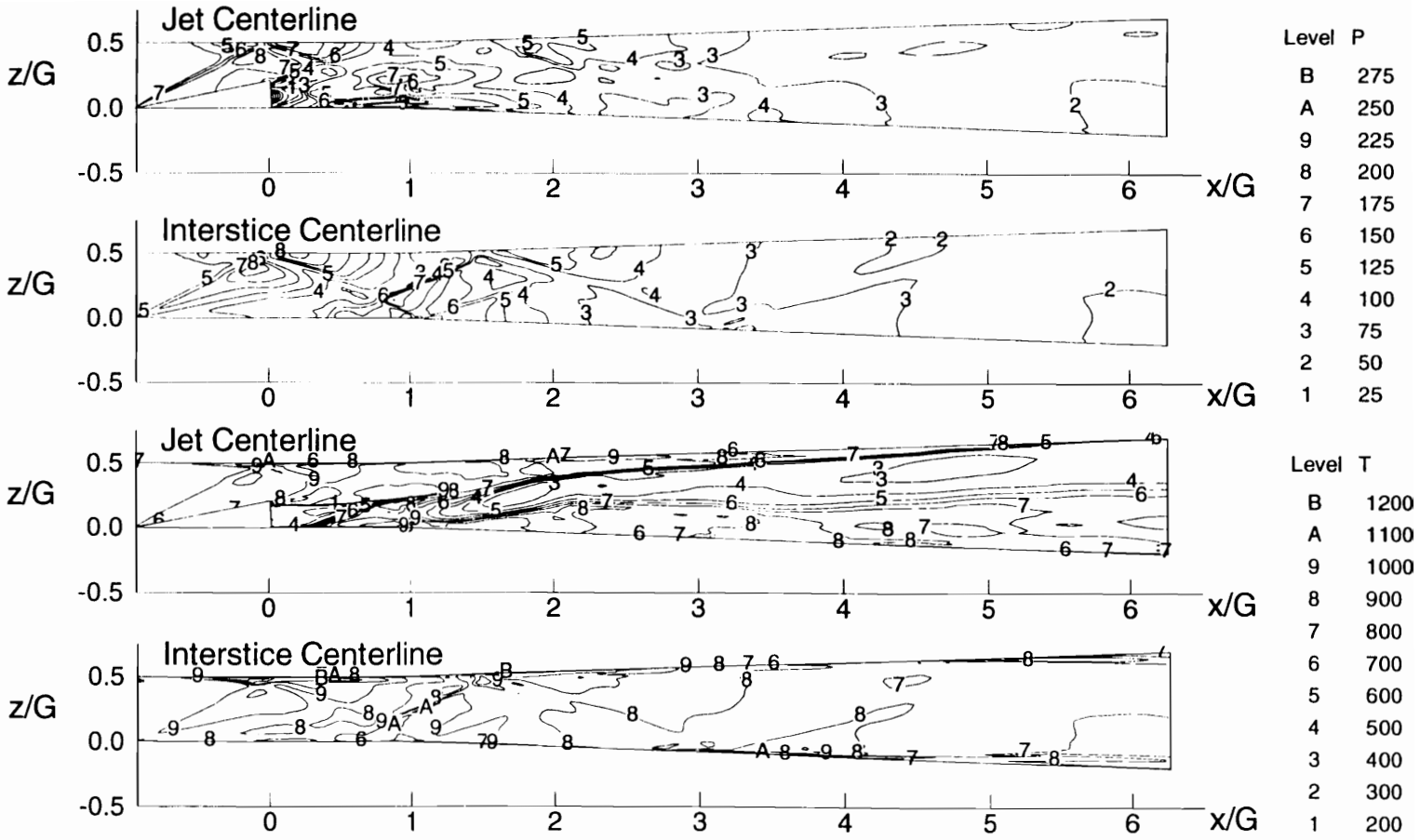

Figure 5.8 Pressure (kPa) and Temperature (K) Contours for the Laminar Mixing Case.

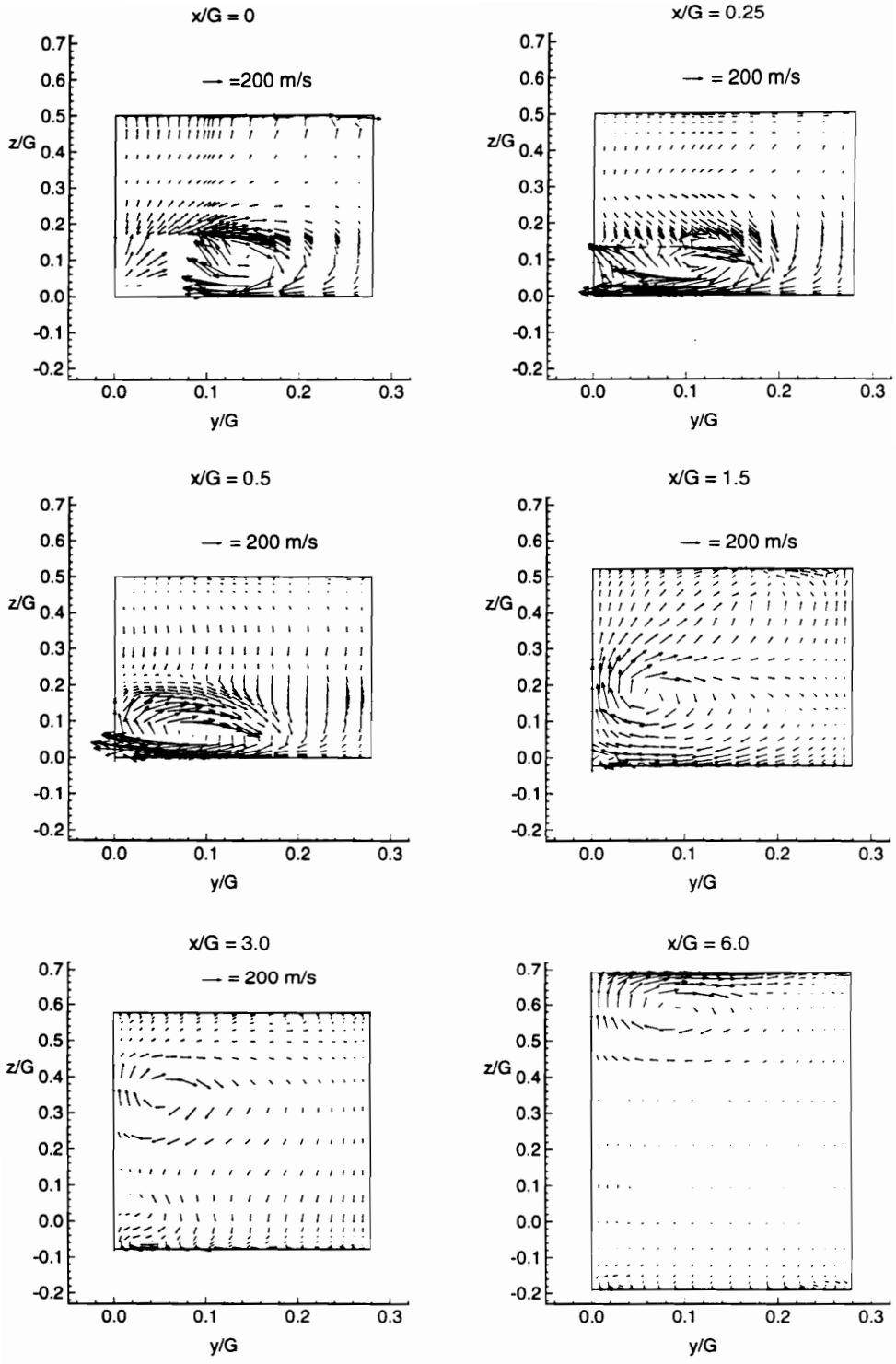

Figure 5.9 Velocity Vectors in the Cross Flow Planes for the Laminar Mixing Case.

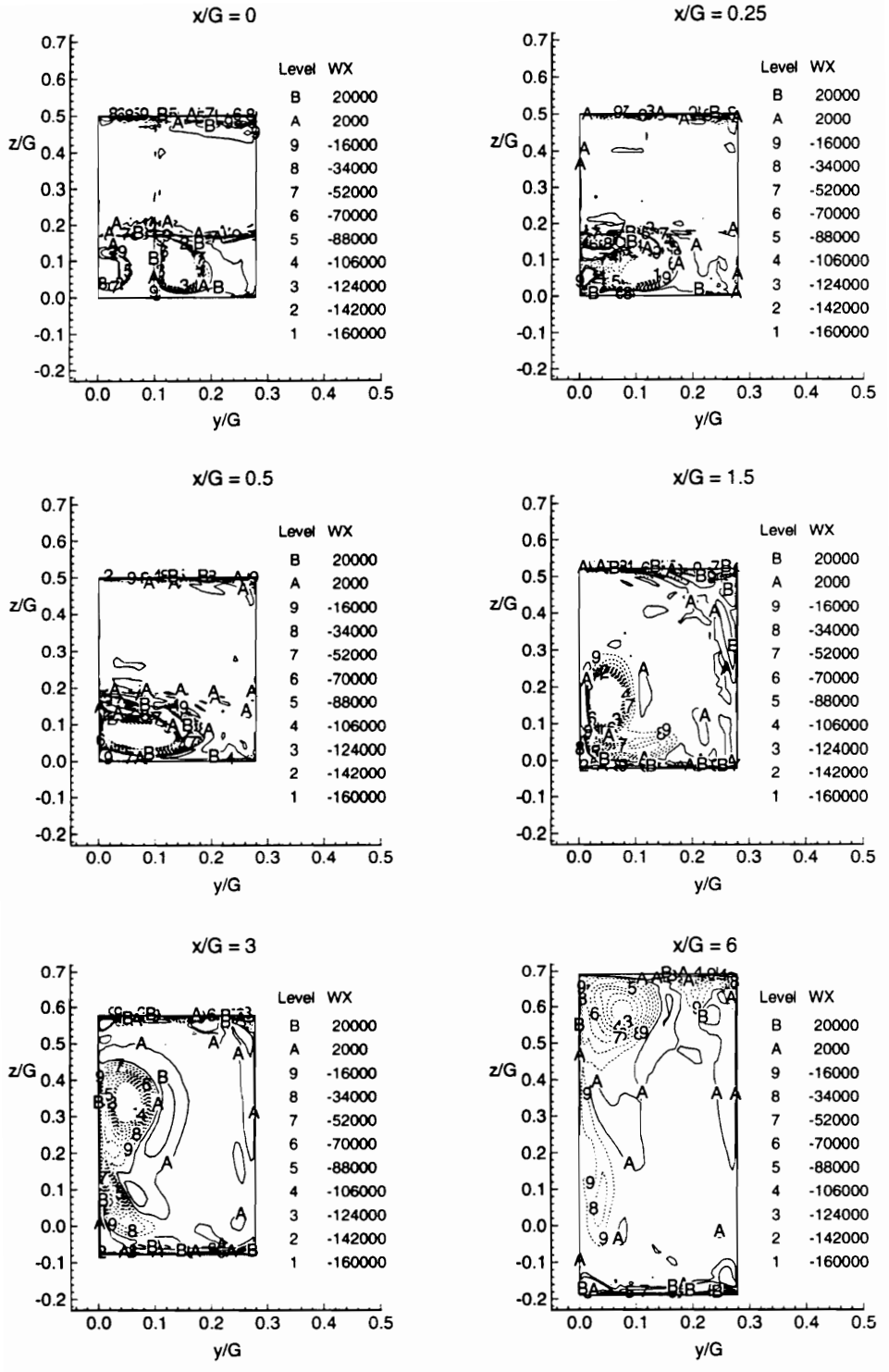

Figure 5.10 Axial Vorticity (1/s) in the Cross Flow Planes for the Laminar Mixing Case

The hydrogen mass fraction contours are shown in Fig. 5.11. In these plots the mass fraction contour line Y_{H2} = 0.031 corresponded to stoichiometric concentration. All contour levels higher than Y_{H2} = 0.031 correspond to locally fuel rich areas. The lowest contour level shown, Y_{H2} = 0.0012 corresponds to the commonly accepted lean flammability level of hydrogen-air (5 % by volume). The contours show large concentration gradients at x/G = 0.25. At locations further downstream the plots show that the fuel-air interface was "rolled up" by the vortical motion of the flow, increasing the length of the fuel-air interface, and thus increasing the mixing. A comparison of the vorticity plots and the hydrogen mass fraction plots show that the position of the hydrogen plume and the large vortex are closely correlated. Downstream of x/G = 1.5 the plots show that the fuel plume lifted completely off the injector wall. At the last plane shown the fuel plume penetrated to the opposite wall. Further baroclinic torque interactions occurred between the shock system and the density gradient associated with the fuel plume distorting the fuel plume as it moved further downstream in the combustor. However, the fuel plume spread little in the spanwise direction.

Note that the experimental study showed that the fuel did not penetrate completely across the combustor. Thus it is thought that the assumption of laminar flow is insufficient to model the actual turbulent flow in the combustor. For this reason, the rest of the calculations used the composite 2-zone algebraic turbulence model.

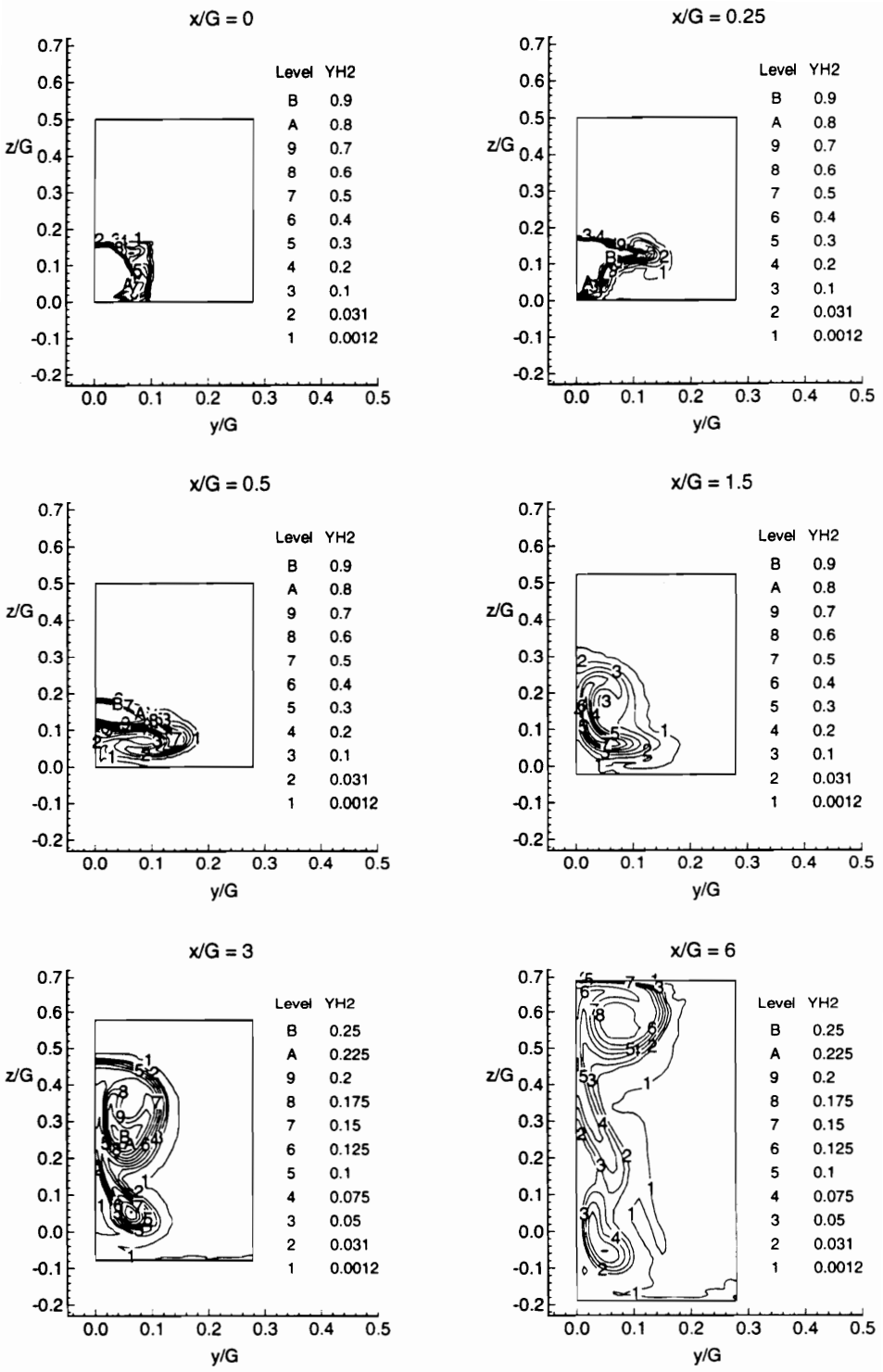

Figure 5.11 Hydrogen Mass Fractions for the Laminar Mixing Case.

5.3.3 Turbulent Mixing Case

The effect of turbulence on the mixing characteristics of the swept ramp injectors is shown in Fig. 5.12-5.14. The pressure contour plot for the interstice centerline is similar to that for the no fuel case. On the fuel jet centerline the pressure differs in the near field of the injectors but the presence of the reflected shock train is more apparent than it was in the laminar mixing case. The temperature contours showed that the fuel did not penetrate to the opposite wall by x/G = 6, as it did for the laminar case.

The hydrogen mass fraction plots in Fig. 5.14 show that the mixing of the fuel plume was significantly different than it was for the laminar case. Near the injector at x/G = 0.25 the most obvious difference is that the concentration gradient between the core of the fuel jet and air is more diffuse for the turbulent mixing case. At locations further downstream, the contour lines representing concentration were not rolled up into tightly spaced gradients as they were for the laminar case, but were made diffuse by the turbulent diffusion. Note that the turbulent flow solution represents the mean flow field. An instantaneous snapshot of the flow would vary greatly from the calculated contours shown in Fig. 5.14. However, a large collection of instantaneous mass fraction contours would resemble the calculated contours. The effect of the vortical flow on the fuel jet is still evident in the turbulent mixing case. Between x/G = 0.5 and x/G = 1.5, hydrogen is "pulled" from the centerline of the fuel jet towards the interstice, shifting the point of maximum concentration from the fuel jet centerline to y/G =0.1. Another major difference between the turbulent and laminar cases is the fraction of the cross-sectional area of the combustor that is covered by the fuel plume. The lateral penetration was much greater for the turbulent mixing case than it was for the laminar case. However, the hydrogen did not reach the opposite wall in the turbulent mixing case, as it did for the laminar case.

The axial vorticity contours for the turbulent mixing case are shown in Fig. 5.13. The vortex created by the ramps decays much faster for this case than it did for the laminar mixing case. Also, the center of the vortex only penetrated in the transverse direction to the center of the combustor. The

hydrogen mass fraction contours surround the vortex for x/G > 0.5. In contrast to the laminar mixing case, where the outer boundary of the fuel plume was close to the outer boundary of the vortex, the vortex was located entirely within the fuel rich region for x/G > 3.

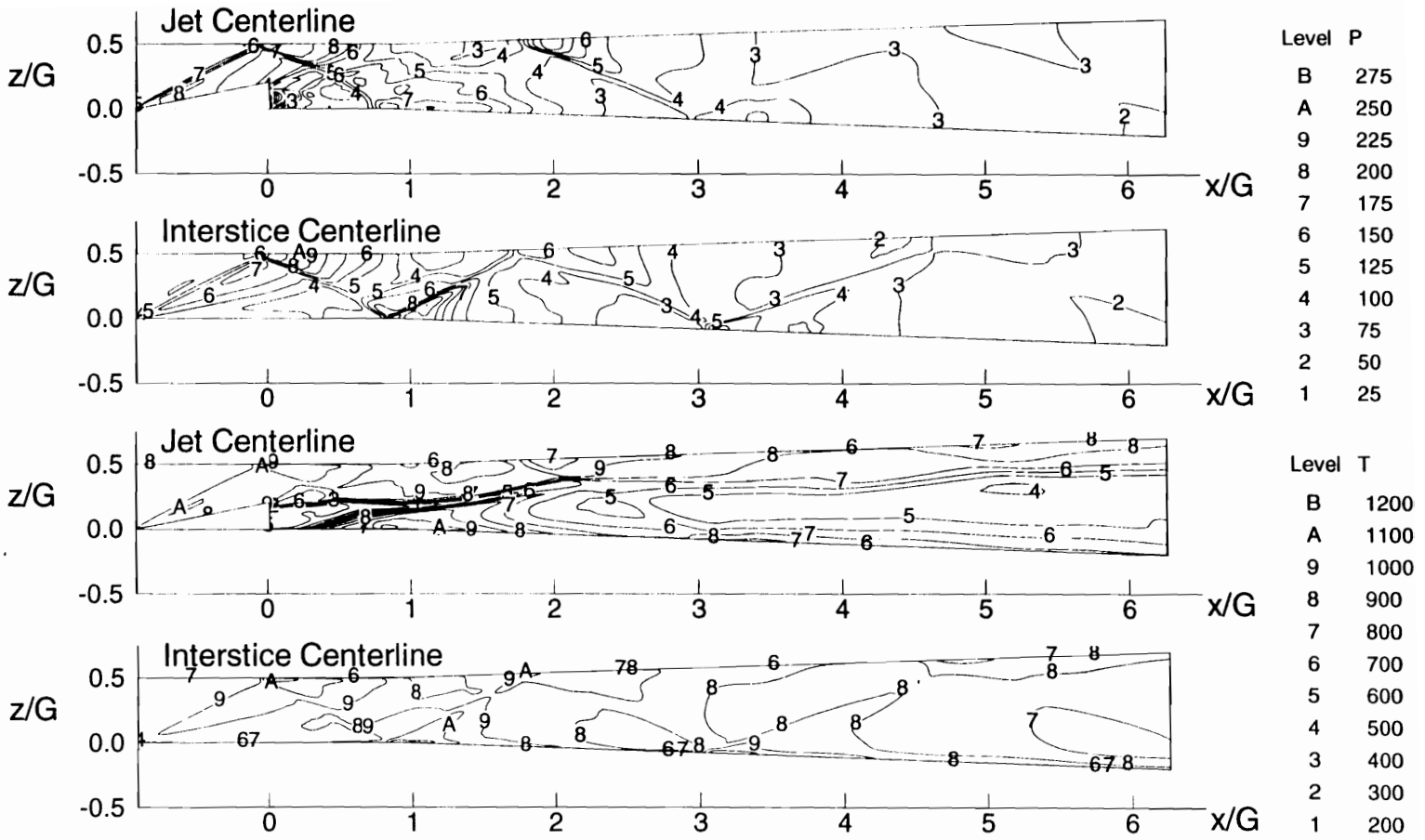

Figure 5.12 The Pressure (kPa) and Temperature (K) Contours for the Turbulent Mixing Case.

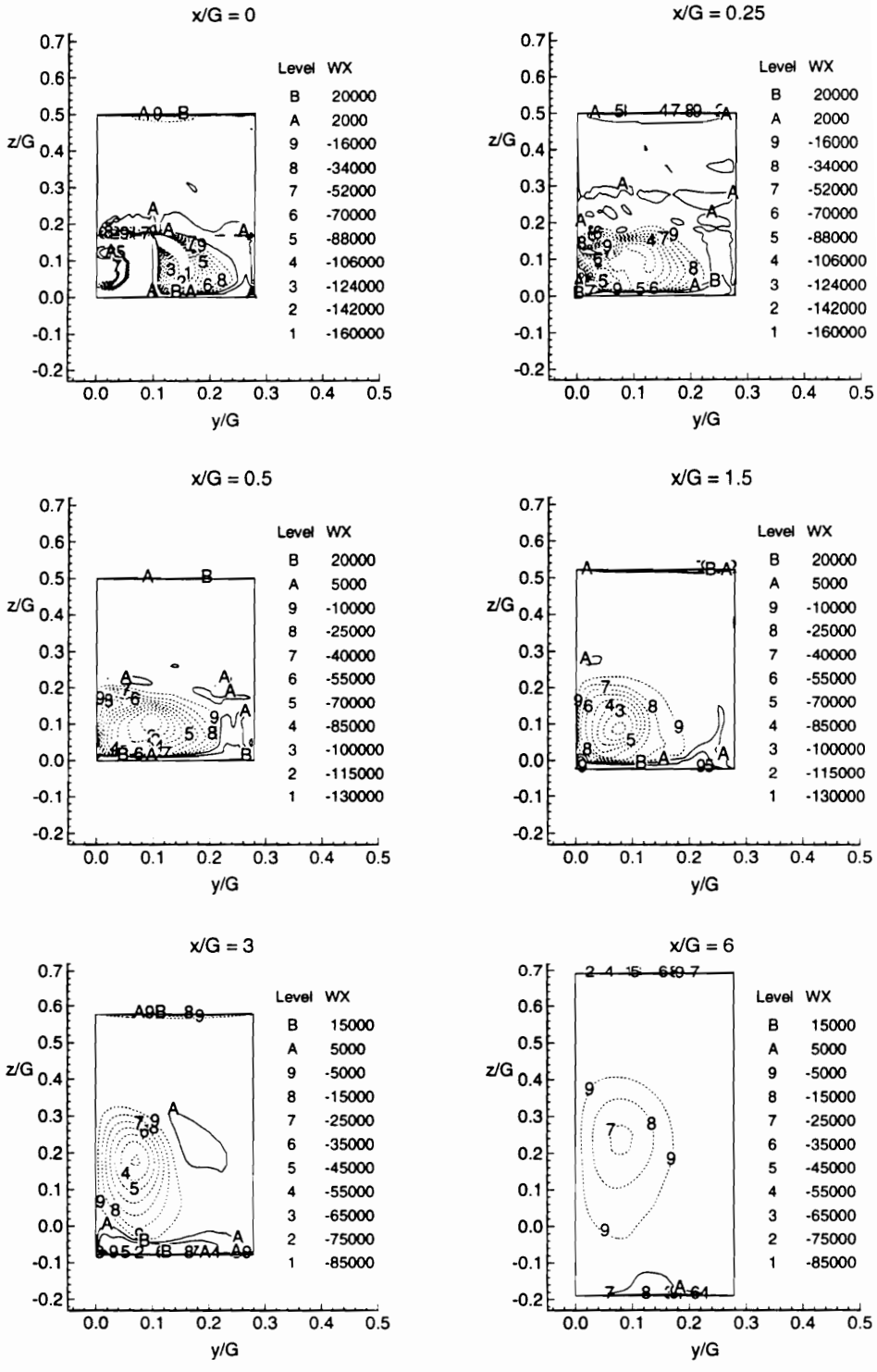

Figure 5.13 Axial Vorticity (1/s) for the Turbulent Mixing Case.

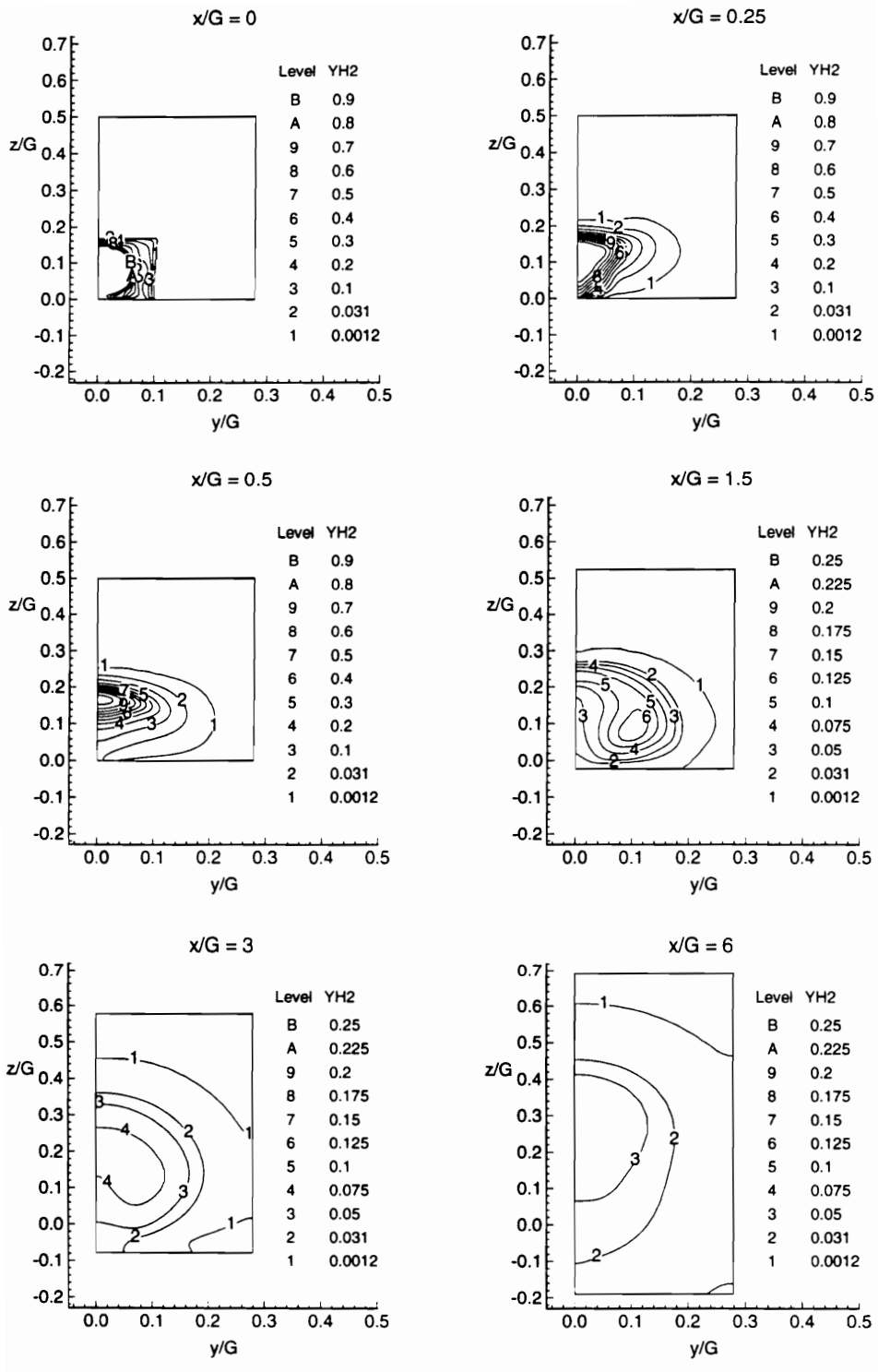

Figure 5.14 Hydrogen Mass Fractions For the Turbulent Mixing Case.

5.3.4 Turbulent Reacting Solution

The mixing and reaction of the fuel is illustrated in the contour plots of H_2, OH, and H_2O product shown in Fig. 5.15 to 5.18. The hydrogen mass fractions at the ramp exit show a much greater lateral penetration compared to the non-reacting turbulent case, due to a large recirculation zone that forced fuel upstream of the ramps. As will be shown later, the combustion pressure rise caused formation of a recirculation zone near the injectors. At locations further downstream of the ramps, the lateral penetration was also greater for the reacting case, but the hydrogen did not penetrate as far in the normal direction. However, recall that the contours represent unreacted hydrogen, and that hydrogen at the fuel/air interface reacts. Another major difference between the reacting and mixing cases, is that the peak hydrogen mass fraction in the farfield of the injectors was much higher for the reacting flow case. Also, the location of maximum hydrogen concentration was always along the fuel jet centerline for the reacting case, while the maximum hydrogen concentration was not always located at the fuel jet centerline for the mixing case.

At x/G = 0.5 the fuel jet spread to 85 % of the distance between the jet centerline and interstice centerline. Also, the fuel jet lifted completely off the surface of the injector wall at this location. The reflected shock from the injector ramps interacted with the fuel jet just downstream of the x/G = 0.5 plane. After passing through the shock, the fuel jet moved in the transverse direction toward the injector wall. The transverse penetration of the fuel was less on the interstice side of the fuel jet in the expanding section of the combustor than it was in the constant area section of the combustor. Thus, the fuel jet was attached to the injector wall.

The contours of the water product are shown in Fig. 5.16. Since there was already a background concentration of water due to vitiation the water product mass fraction, Y_{H_2OP}, was calculated by assuming that there is no differential diffusion between the nitrogen and the water in the vitiate stream. With this assumption the mass fraction of water product was calculated from the nitrogen and water mass fraction by the following

expression: $Y_{H_2OP} = Y_{H_2O} - A \times Y_{N_2}$ where A is the ratio of the mass fraction of water to that of nitrogen in the vitiated stream.

At the injector plane the contours show that water product was spread across much of the width of the combustor. This product was formed in the recirculation zone which forced fuel upstream of the ramps. The water product contours over the rest of the combustor length resembled hydrogen contours but extended further from the center of the hydrogen plume. This was expected because hydrogen was consumed and water was produced fuel/air interface.

The flame front can be located by the presence OH radicals. The OH contours shown in Fig. 5.17-5.18 show the reaction zone. The outer circumference of the fuel plume was surrounded by the OH for $x/G \leq 1.5$. Between $1.5 \leq x/G \leq 3$ the flame front near the wall vanished because the oxygen layer near the wall was consumed, and the reaction zone moved away from the fuel and product rich (oxygen depleted) jet centerline toward the interstice centerline.

The shapes of the temperature contours shown in Fig. 5.19 and 5.21 resemble those of the water product contours. As expected, over most of the length of the combustor, the maximum temperature occurred in the flame zone. A high temperature gradient existed near the wall, inline with the injectors ($y/G = 0$) in the constant area section of the combustor ($x/G < 0.9$) because of the proximity of the flame front to the wall. Recall that the heat flux gages in this section of the combustor showed more test-to-test variation than those in the farfield of the injectors. It is thought that this variation was caused by small differences in the position of the reacting fuel jet relative to the wall. In the near field of the injectors the temperature near the walls was higher on the fuel jet side of the combustor than it was for the interstice side, because the fuel had not penetrated to the interstice. The opposite occurred further downstream as the flame front near the injector wall moved toward the interstice. Thus, in the farfield of the injectors the flow near the wall at the fuel jet axis consisted mainly of fuel rich combustion products, while the flow near the interstice consisted of a lean reacting mixture.

The pressure contours, shown in Fig. 5.20 and 5.21 show that there was a large pressure rise associated with combustion near the injectors. The large combustion pressure rise caused a large recirculation region to form near the injectors. At x/G = 0.5 the reflected shock can be seen before crossing the fuel jet. The shock wave crossing the fuel jet was responsible for the transverse movement of the fuel jet towards the injector wall. The motion of the fuel jet toward the injector wall was caused by the change of main flow direction after passing through the shock, and by the baroclinic interaction. In the region downstream of the interaction of the reflected ramp shock and the reacting fuel jet, the shock train was severely damped out by combustion.

The Mach number and axial velocity contours are shown in Figs. 5.22, and 5.23, respectively. In contrast to the no fuel and mixing solutions, where there was a short subsonic region downstream of the ramp base, a large subsonic region extended from the interstice region slightly upstream of the ramps downstream to x/G = 2.5. The axial velocity plots show a large recirculation zone on the interstice that extended upstream to x/G = -0.2 and downstream to x/G = 0.85. The recirculation zone is further illustrated in Fig. 5.24 which was generated by shading the region of the flow which had a negative axial velocity component. The recirculation zone is enclosed by the shaded surface shown in the three perspective views of this figure.

The contours of the axial vorticity at selected positions are shown in Fig. 5.25. The contour plots show that axial vorticity at the ramp exit was much less than it was in the turbulent mixing case. A well defined pair of counter-rotating vortices is not apparent from the vorticity plots until the flow is downstream of the recirculation zone. Further downstream the axial vorticity decayed slightly faster for the reacting flow case.

The flow through the rest of the combustor showed further mixing and reaction. The pressure at the exit of the combustor for the reacting flow case was approximately uniform, varying by less than 5 % over the entire width of the combustor. The contours of temperature, OH and water product mass fraction in the combustor exit plane (x/G = 15.4) are shown in Fig. 5.26. The trends shown in this figure are similar to those shown earlier for the cross-flow plane at x/G = 6. The water product mass fraction contours show that

the injector side of the cross flow plane had large concentrations of products in it while the products of combustion had not penetrated to the opposite wall of the combustor. The flamefront is shown by the OH radical mass fractions. As seen in the OH and temperature contours, the flame front extended from the top of the fuel jet at the injector centerline to the interstice centerline near the wall, as it was at x/G = 6. In contrast, the flame did not penetrate into the fuel and product rich region at the injector centerline near the wall. The resultant temperature contours show that near the wall the temperatures are highest at the interstice centerline. Also, note the large difference between the temperature profile near the injector side as compared to the opposite wall.

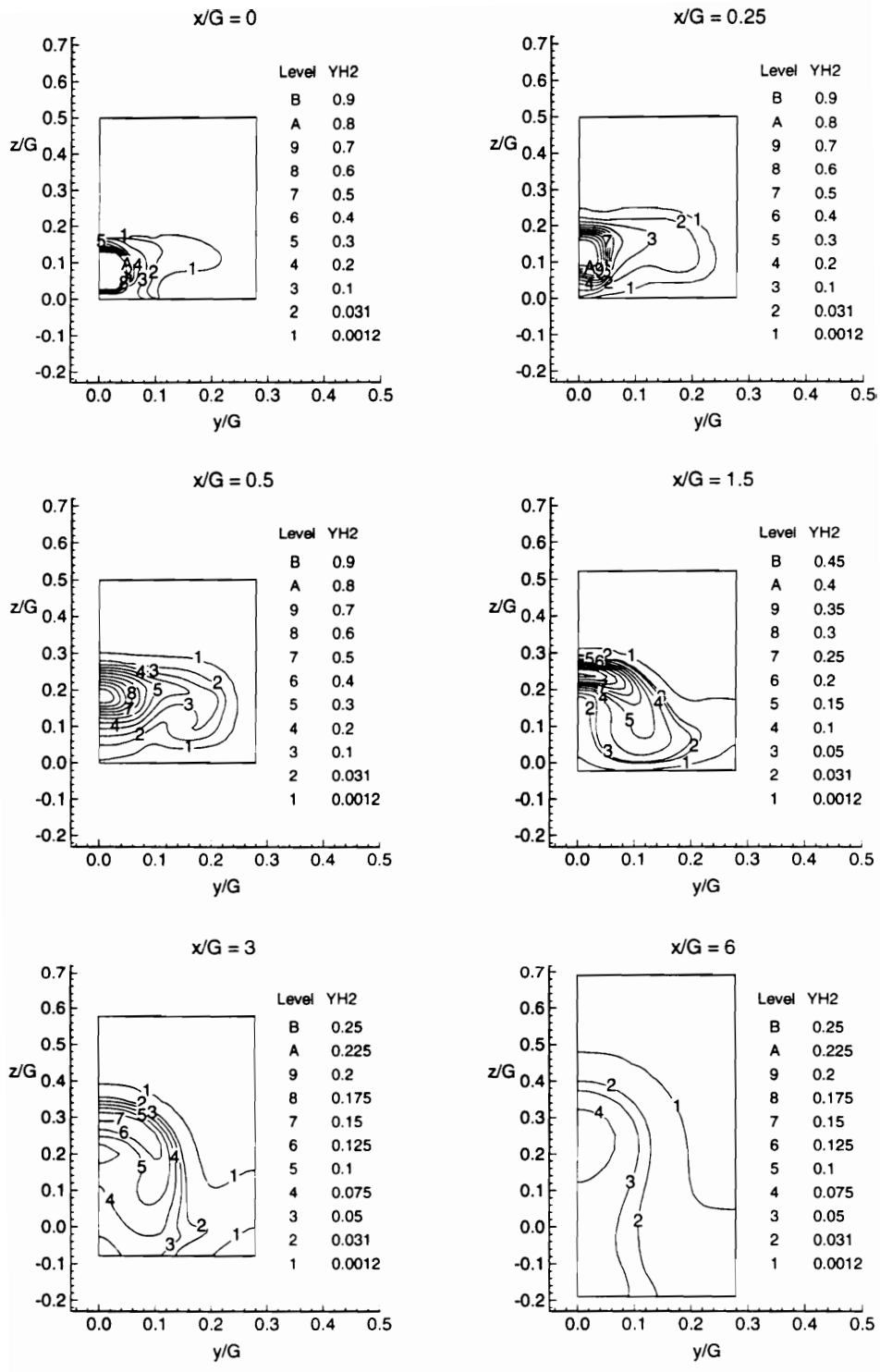

Figure 5.15 Hydrogen Mass Fraction Contours for the Reacting Case.

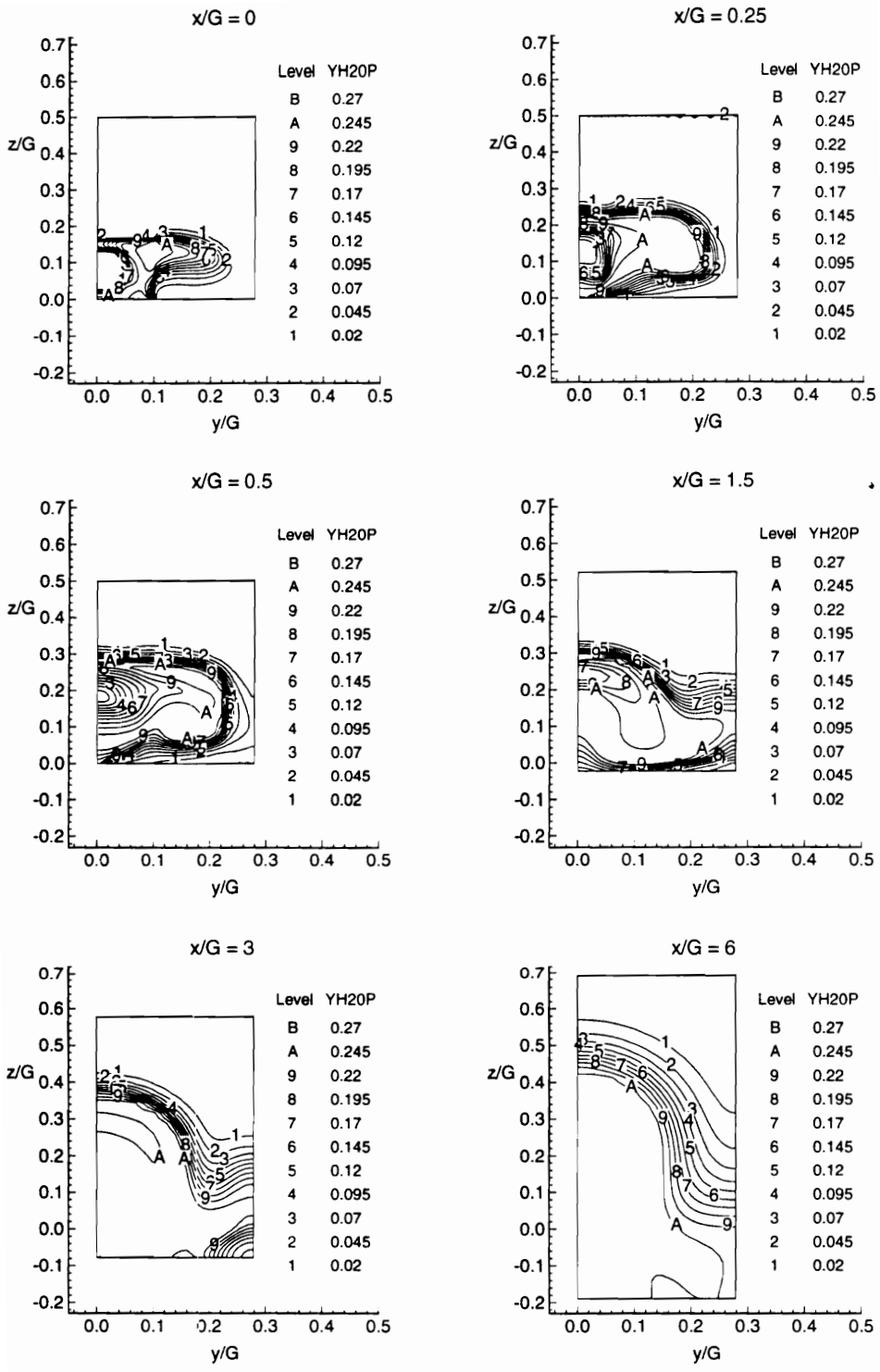

Figure 5.16 Water Product Mass Fraction Contours for the Reacting Flow Case.

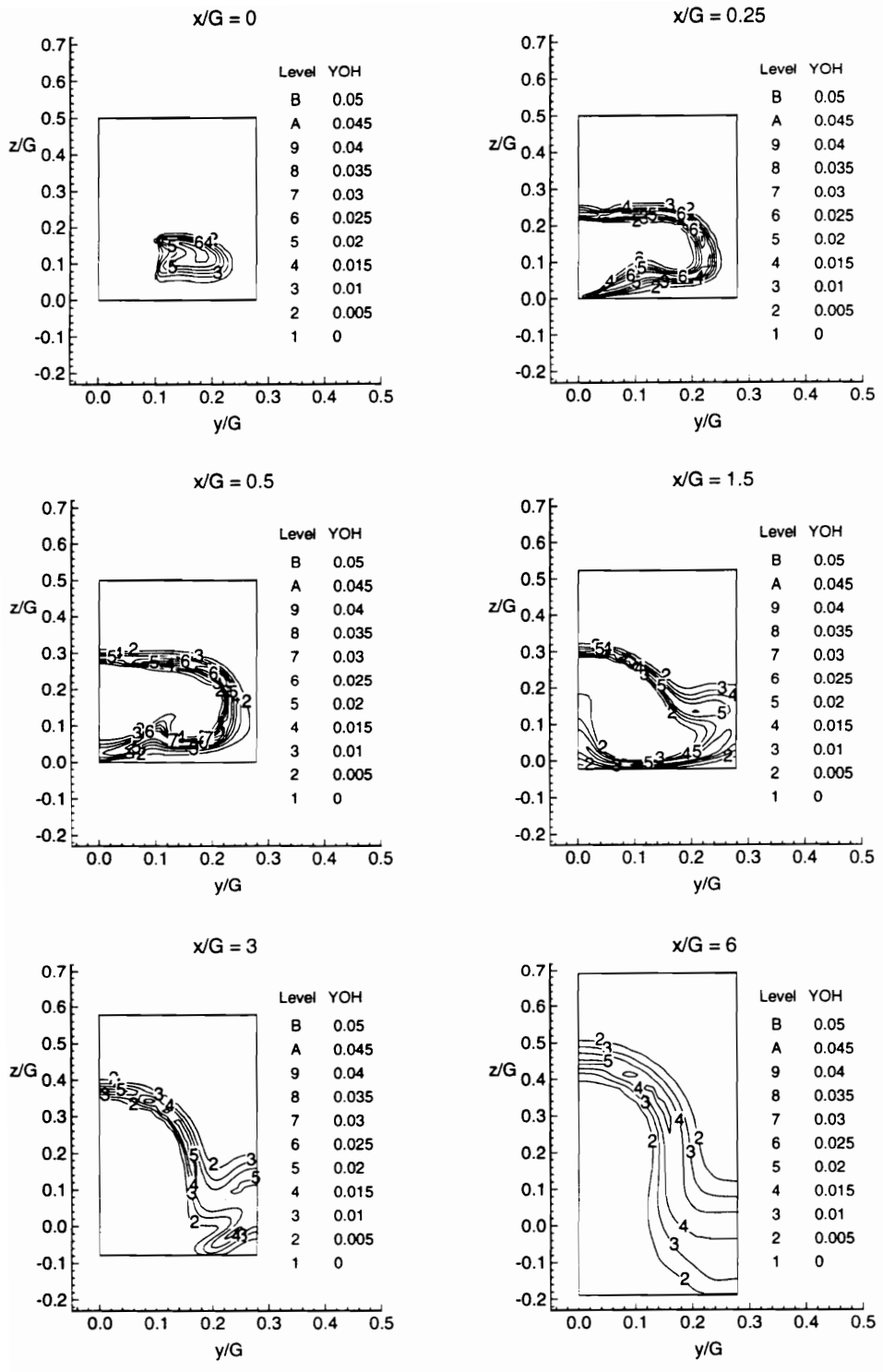

Figure 5.17 OH Mass Fraction Contours for the Reacting Flow Case.

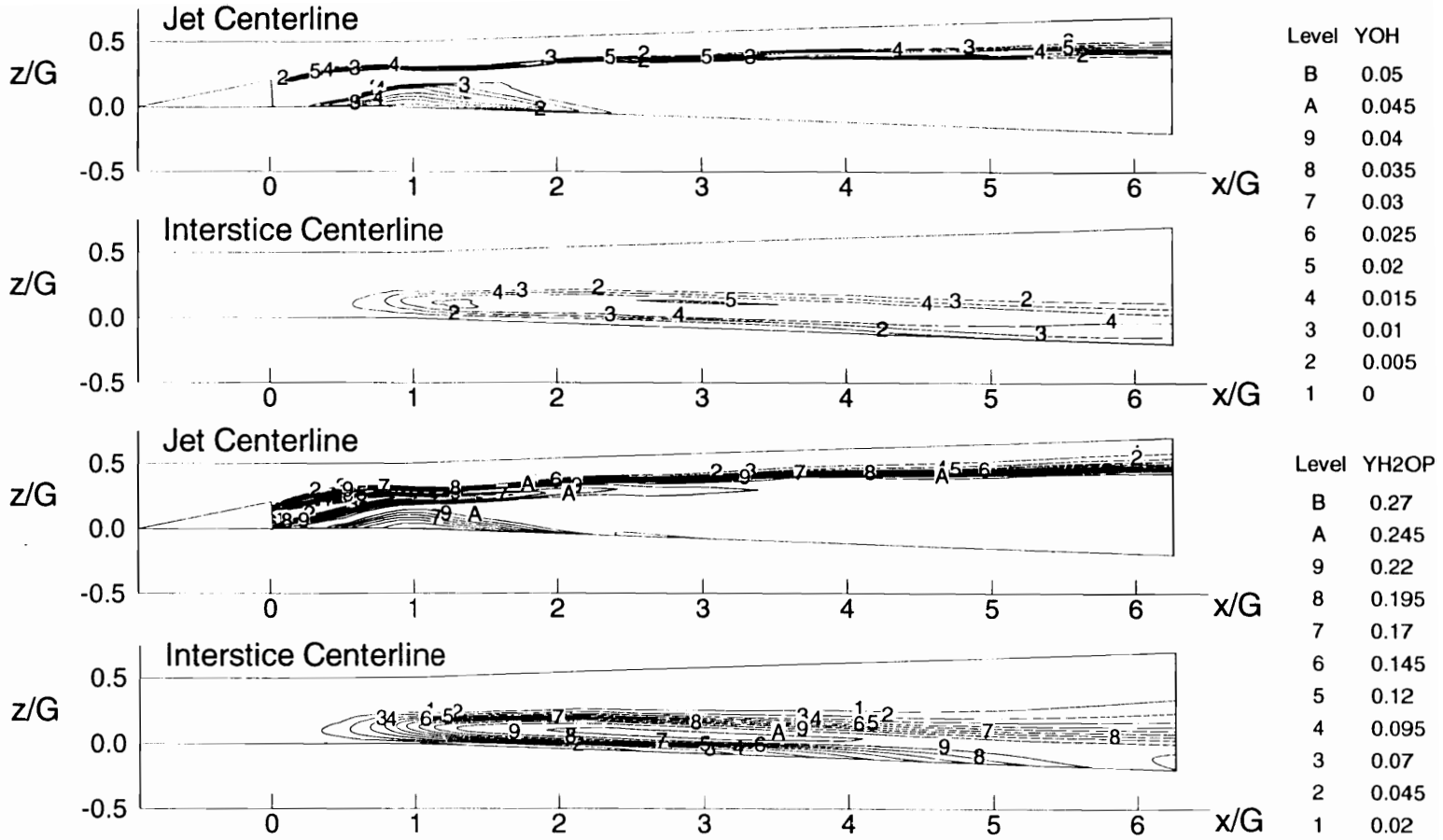

Figure 5.18 OH and Water Product Mass Fraction for the Reacting Flow Case.

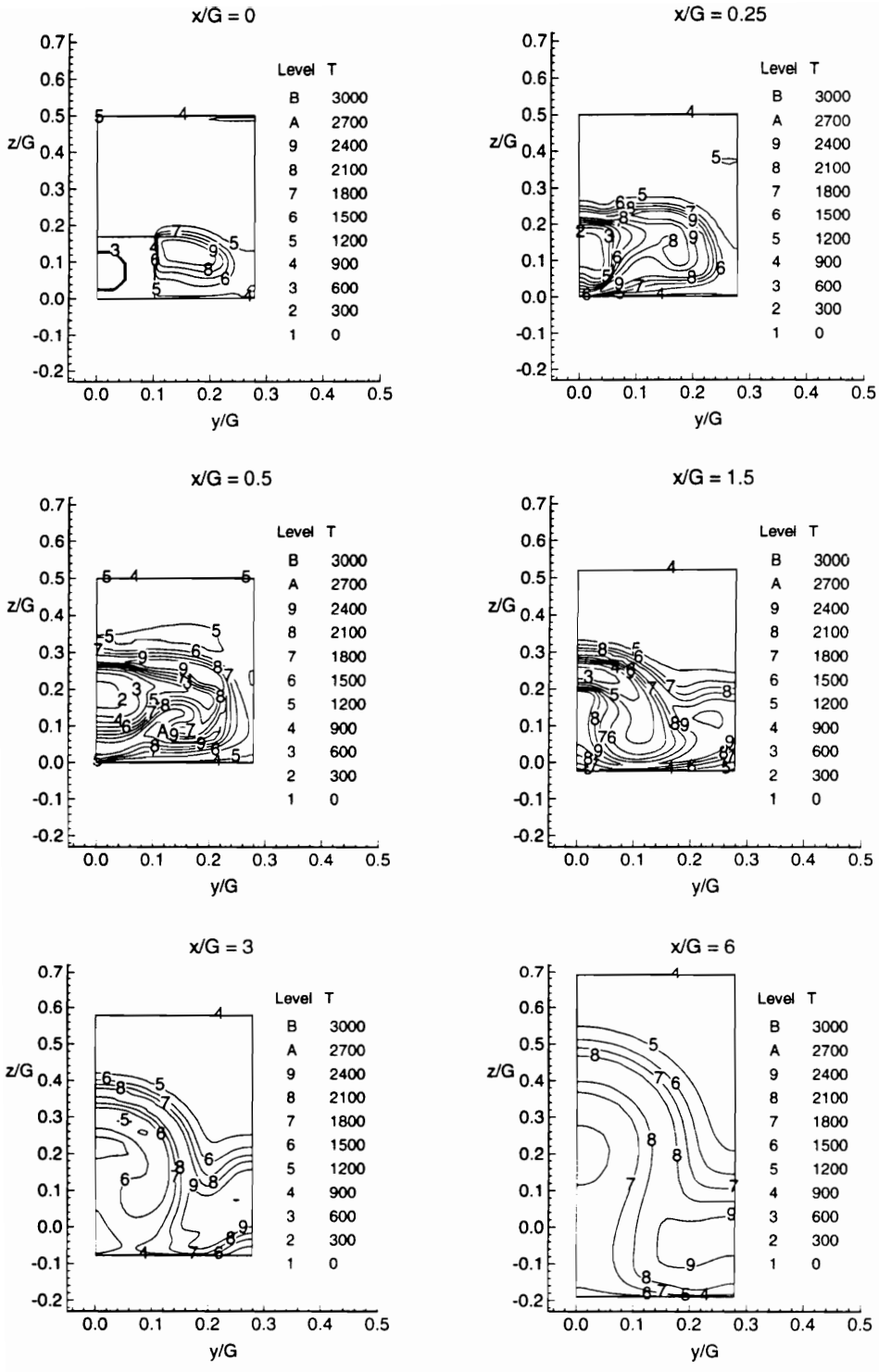

Figure 5.19 Temperature (K) Contours for the Reacting Flow Case.

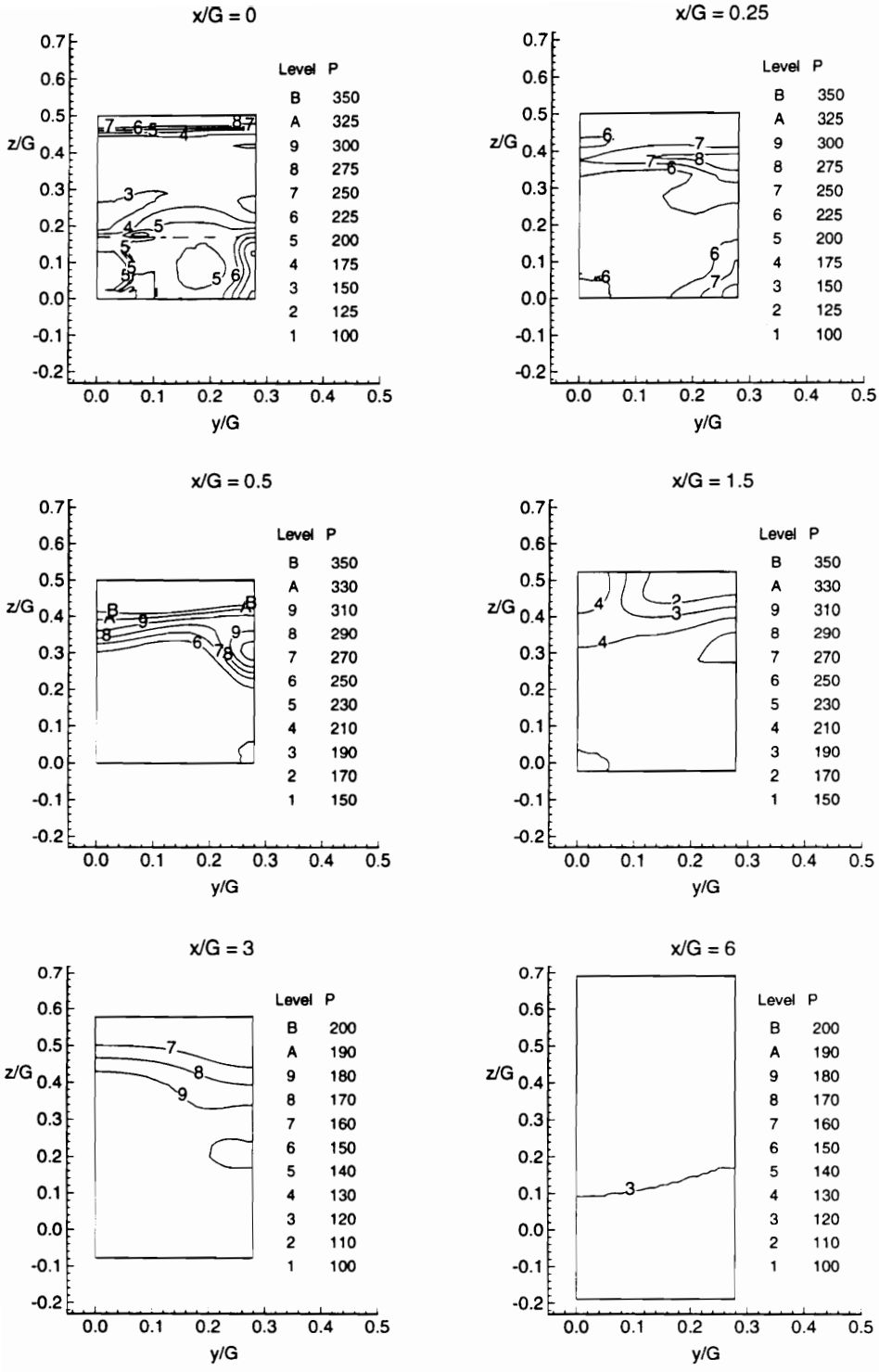

Figure 5.20 Pressure Contours (kPa) for the Reacting Flow Case.

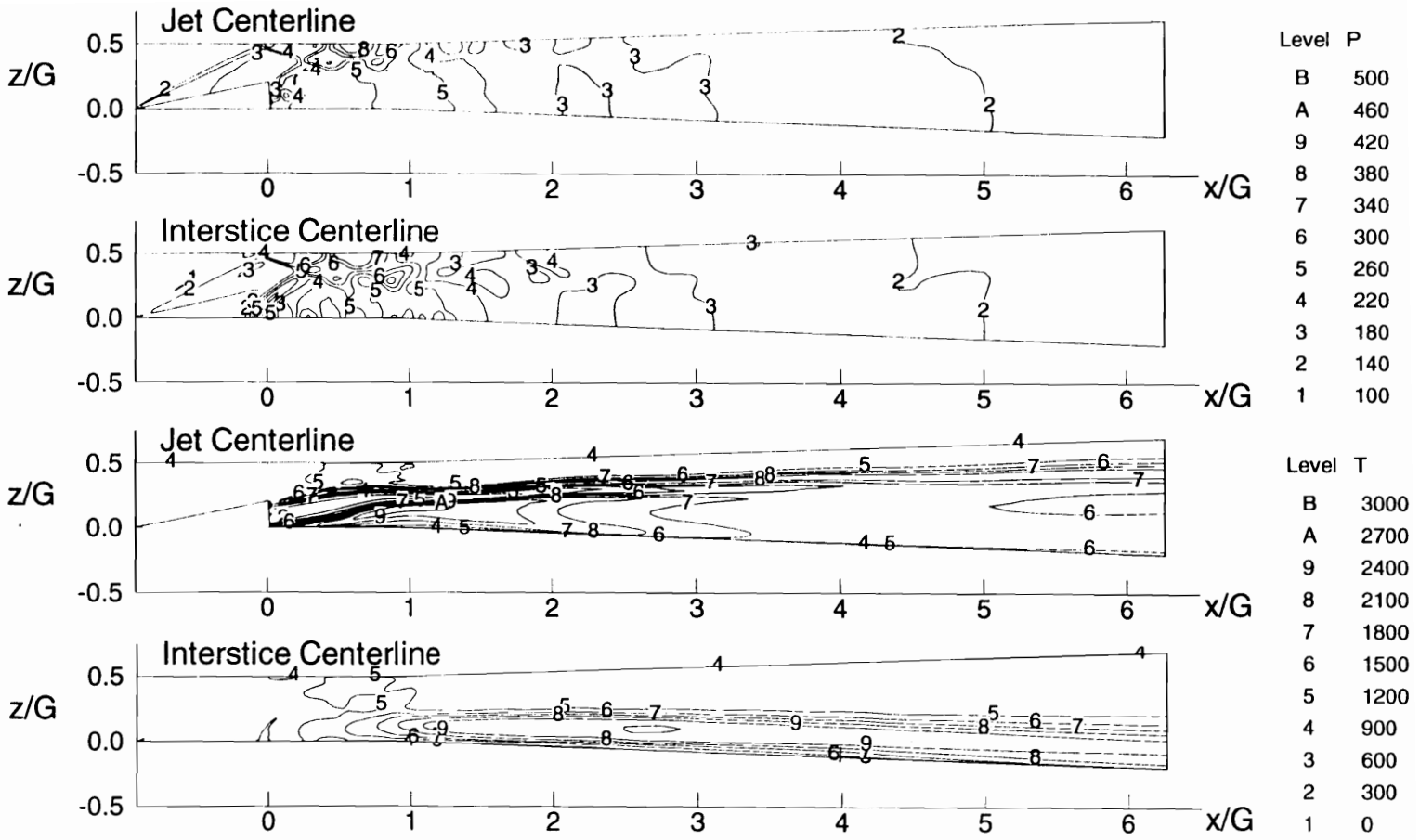

Figure 5.21 The Pressure (kPa) and Temperature (K) Contours for the Reacting Flow Case.

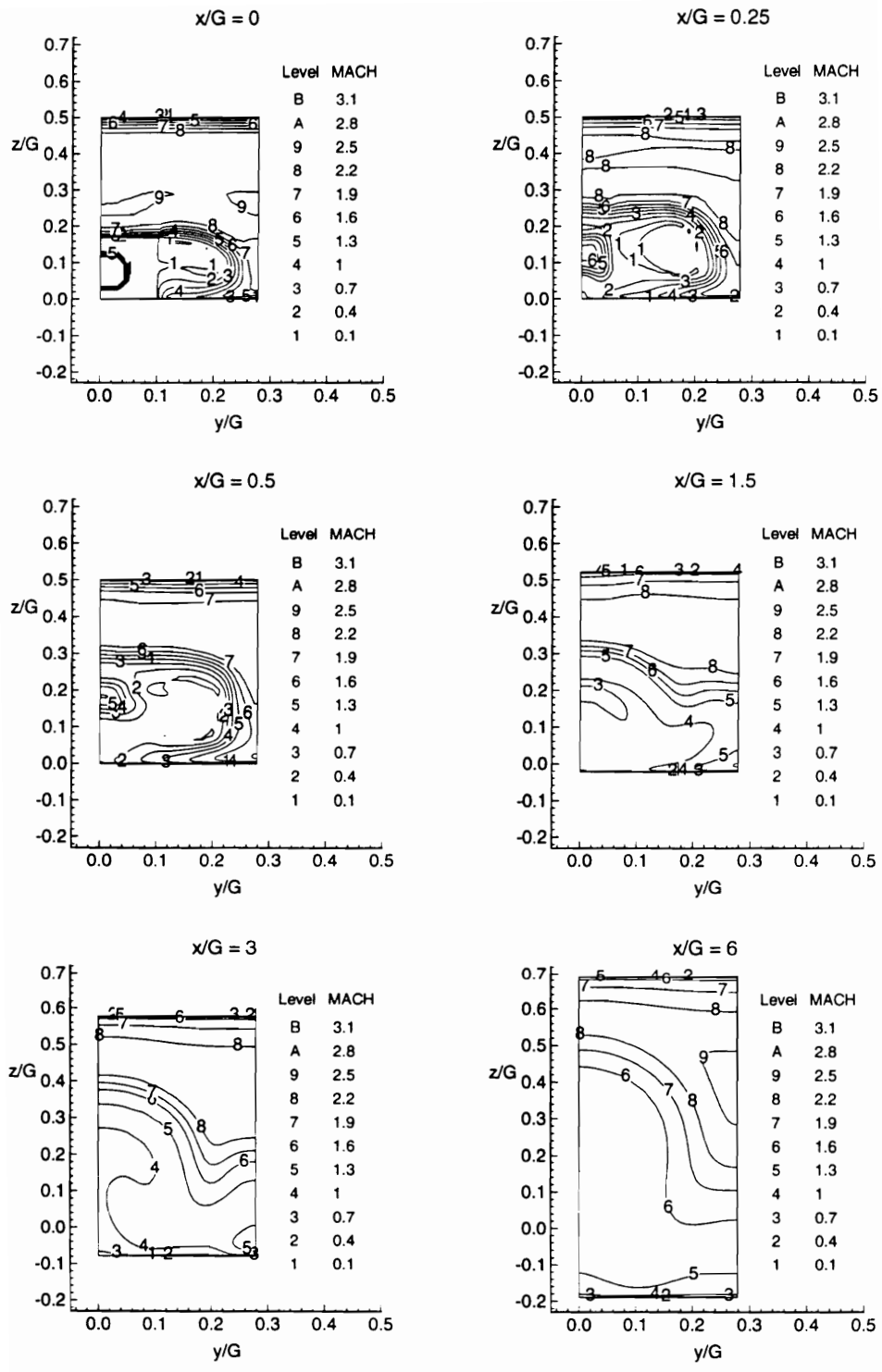

Figure 5.22 Mach Number Contours for the Reacting Flow Case.

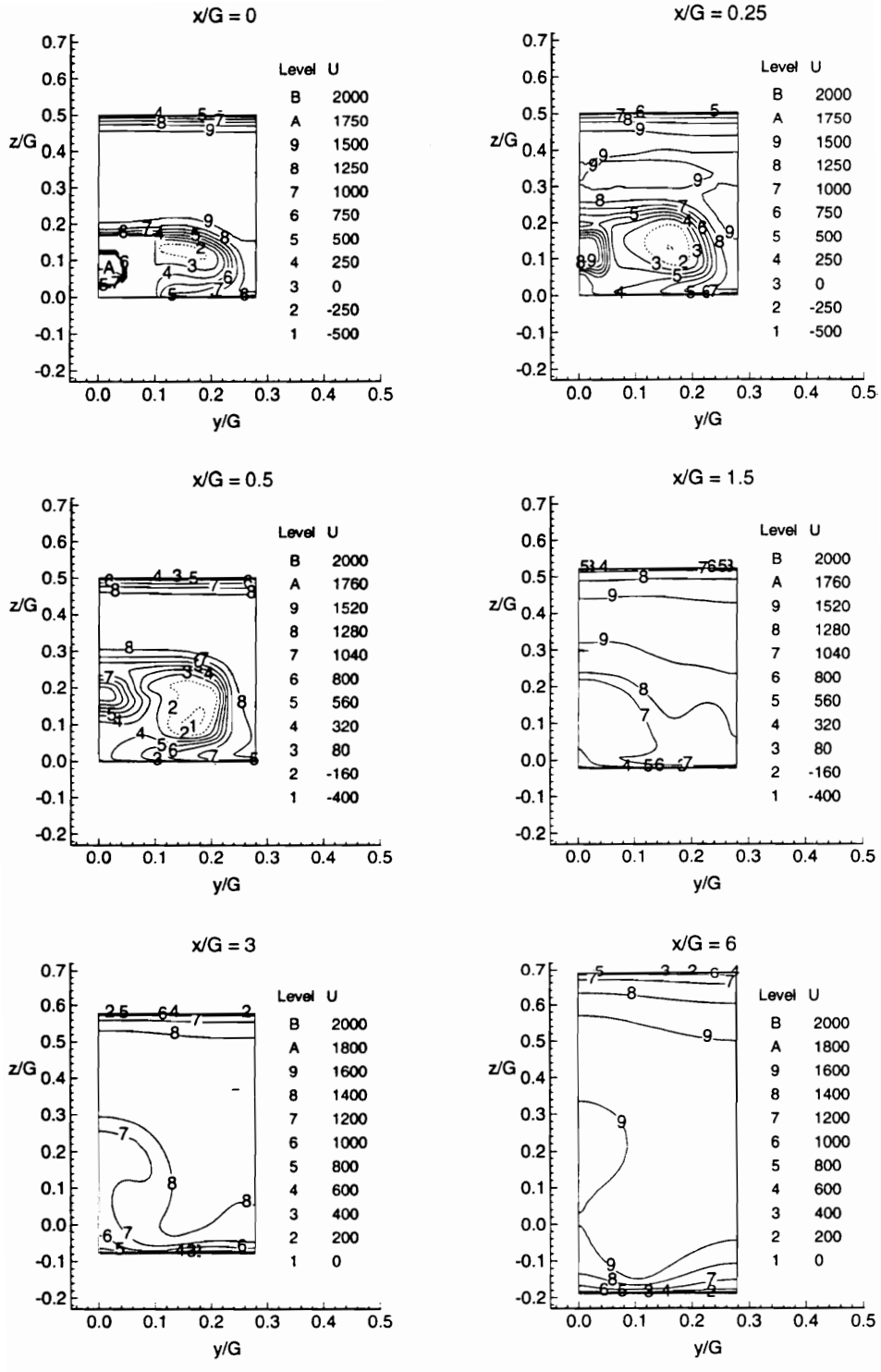

Figure 5.23 The Axial Velocity (m/s) Contours for the Reacting Flow Case.

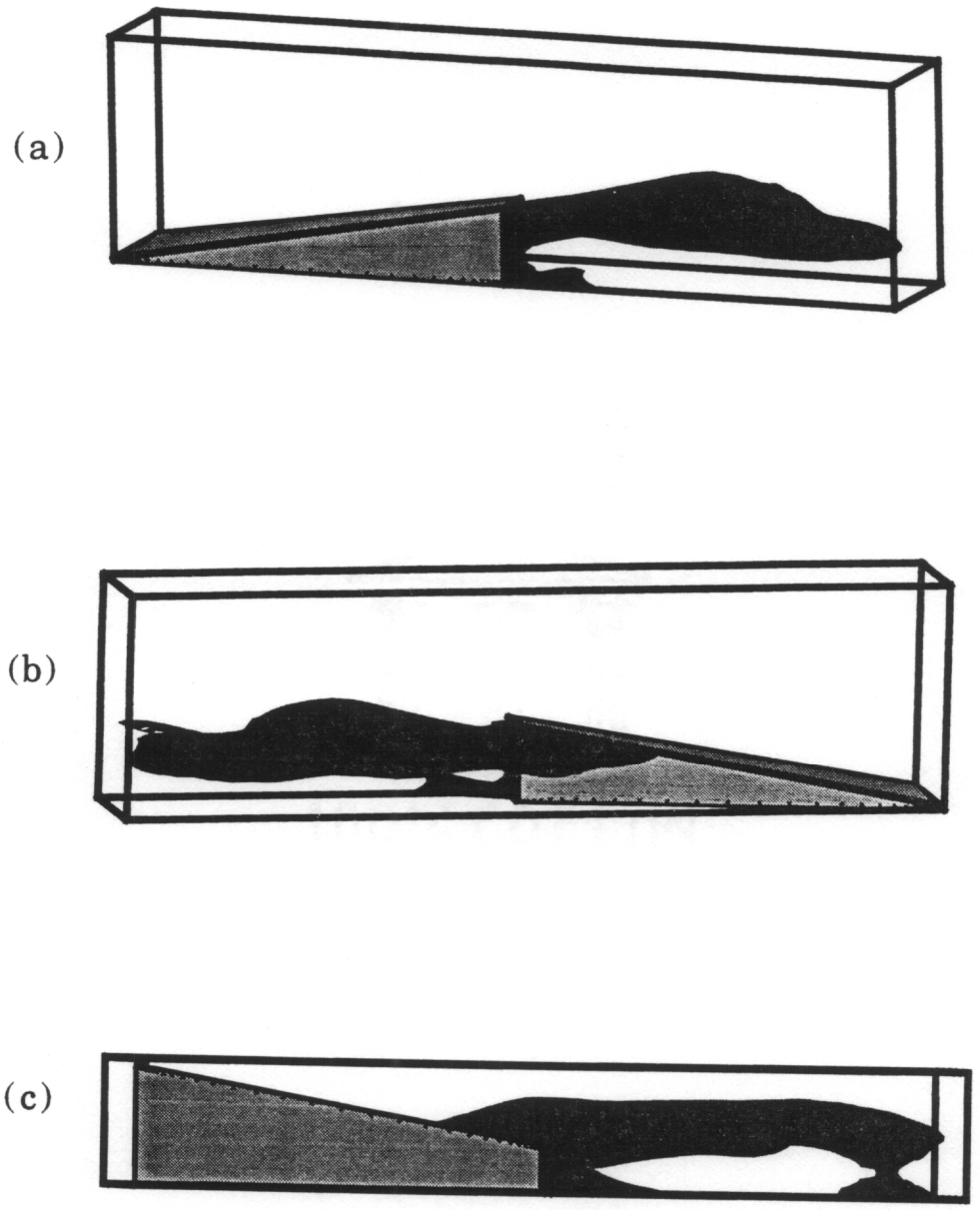

Figure 5.24 The Recirculation Region as Viewed From (a) Jet Centerline (b) Interstice Centerline (c) Top.

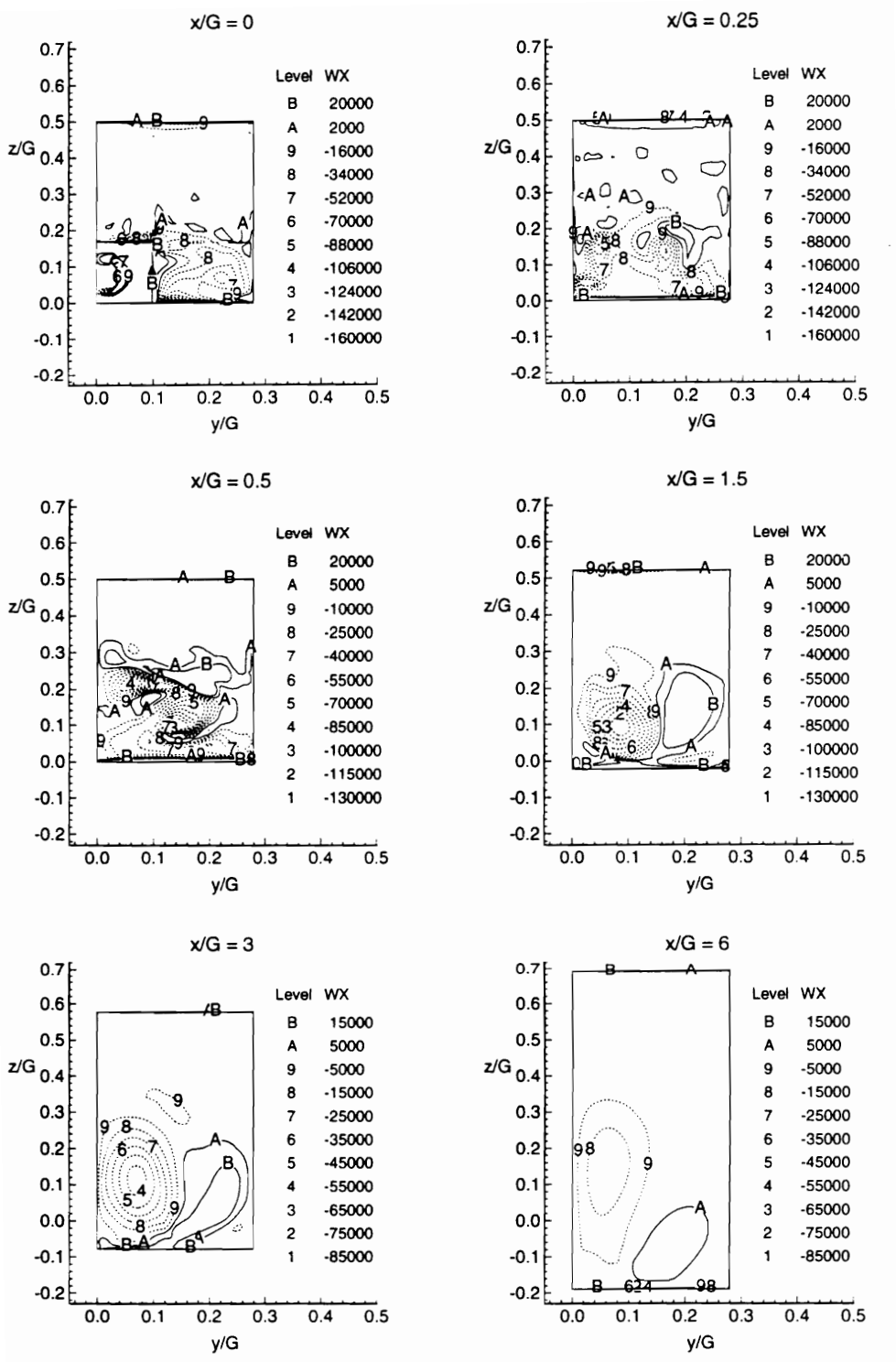

Figure 5.25 Axial Vorticity (1/s) Contours for the Reacting Flow Case.

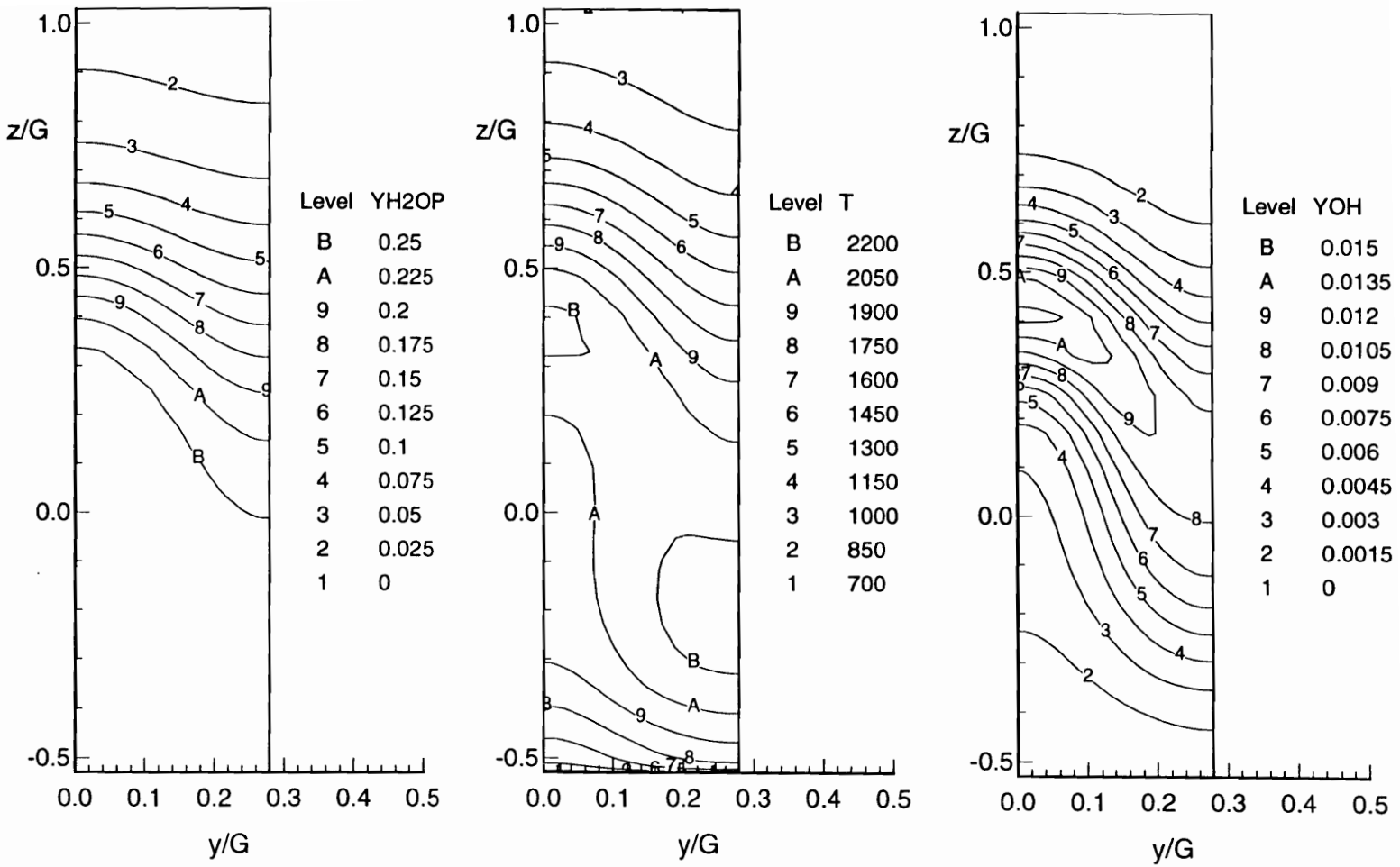

Figure 5.26 Contours of Static Temperature(K), and Mass Factions of Water Product and Hydroxyl Radical at x/G = 15.4.

5.4 Comparison of Computational Results With the Experiments

The results of the calculations, presented in the previous sections, provided insight into the flowfield structure for the swept-compression ramp with and without fuel. In the sections below, the calculated results are compared to the experimentally determined wall pressures, pitot pressures, and the Mie scattering images, to judge the validity of the calculated flowfield structure.

5.4.1 Wall Pressures

The calculated and experimental pressures along the interstice centerline on the injector side of the combustor are shown in Fig. 5.27. The agreement between the numerically and experimentally determined pressures for the no fuel case is within a few percent over most of the combustor. The comparison for the $\phi = 0.7$ case shows that the numerically determined pressures are identical for both the 7 and 19 reaction models. The jagged peaks in the computational pressure traces are due to a localized reflected shock system that exists between the outer boundary of the fuel plume and the interstice centerline. The computationally determined pressures under predict the experimental values in the near field. In the farfield, the agreement improves to within a few percent.

The calculated and experimental pressures along the interstice centerline on the side of the combustor opposite of the injectors are shown in Fig. 5.28. As it was for the other side of the combustor, the agreement between the numerically and experimentally determined pressures for the no fuel case is within a few percent over most of the combustor. For the reacting case, the pressure match in the far field of the injectors is good.

Upstream of the ramp base, the calculated wall pressures are in agreement with the experimentally determined wall pressures. The experimental pressure measurements along the fuel injector and interstice centerlines showed that no pressure rise occurred at the closest measurement location upstream of the base of the ramp (x/G = -0.19). As was shown in Fig. 5.24 a recirculation region extended upstream of the injectors along the side

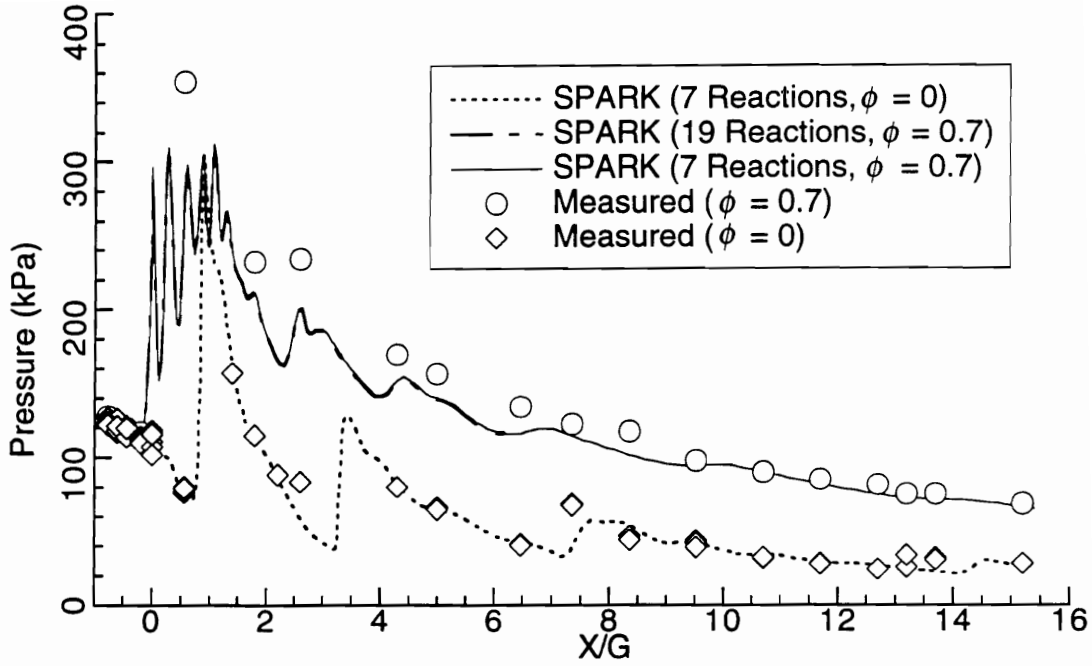

Figure 5.27 Comparison of the Wall Pressure Along the Interstice of the Injector Wall.

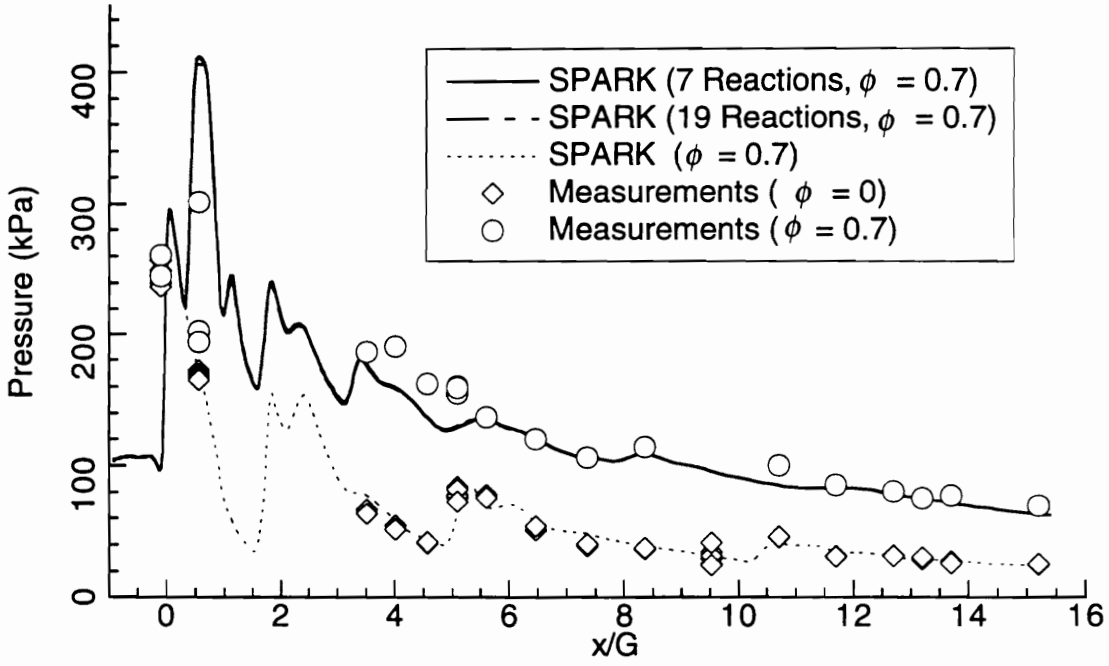

Figure 5.28 Comparison of the Wall Pressure Along the Interstice of the Wall Opposite of the Fuel Injectors.

of the ramps to x/G = -0.2. However, the calculations show that the disturbance did not extend to the ramp top, or the interstice centerline at the x/G = -0.19 measurement location.

5.4.2 Comparison of Mie Scattering and Computational Results

The Mie scattering flow visualization discussed in Chapter 4 was used to visualize the distribution of the combustion products across the combustor. The Mie scattering photographs were compared to the calculations of the mass fraction of water product Y_{H_2O} formed as a result of combustion in the reacting cases.

The experimentally determined images of the product plumes from the two center ramps were used for comparison. The computational results were reflected about the center line of the injector, and the Mie scattering images of the two center plumes were extracted to form an average image for a single injector by folding and averaging about the vertical centerline of the combustor.

The Mie scattering images are compared with the water product mass fraction contour plots in Fig. 5.29 for x/G = 3.1, and Fig. 5.30 for x/G = 6.1. Recall from the discussion in Chapter 3 that the outer edge of the Mie scattering image is relatively insensitive to the final gray scale adjustment. However, the contrast within the fuel jet was a function of the cut-off values used in the final gray scale adjustment. Thus, the details within the plume are less certain than the outer boundary of the fuel jet. As shown in Fig. 5.29, at x/G = 3.1 the penetration of the calculated product plume is close to that for the Mie scattering image at the fuel jet centerline. The plume shown in the Mie scattering image of the fuel plume is wider than the calculated plume. In addition, the calculated water product contours display a notch in the contours at y/G = ±0.2 which is not shown in the Mie scattering images. At x/G = 6.1, the penetration is approximately the same for the calculations and the experiment at the fuel jet centerline, and the differences between the calculations and experiment are less pronounced at the interstice. Comparisons cannot be made near the injector wall because of the effect of light reflected from the walls.

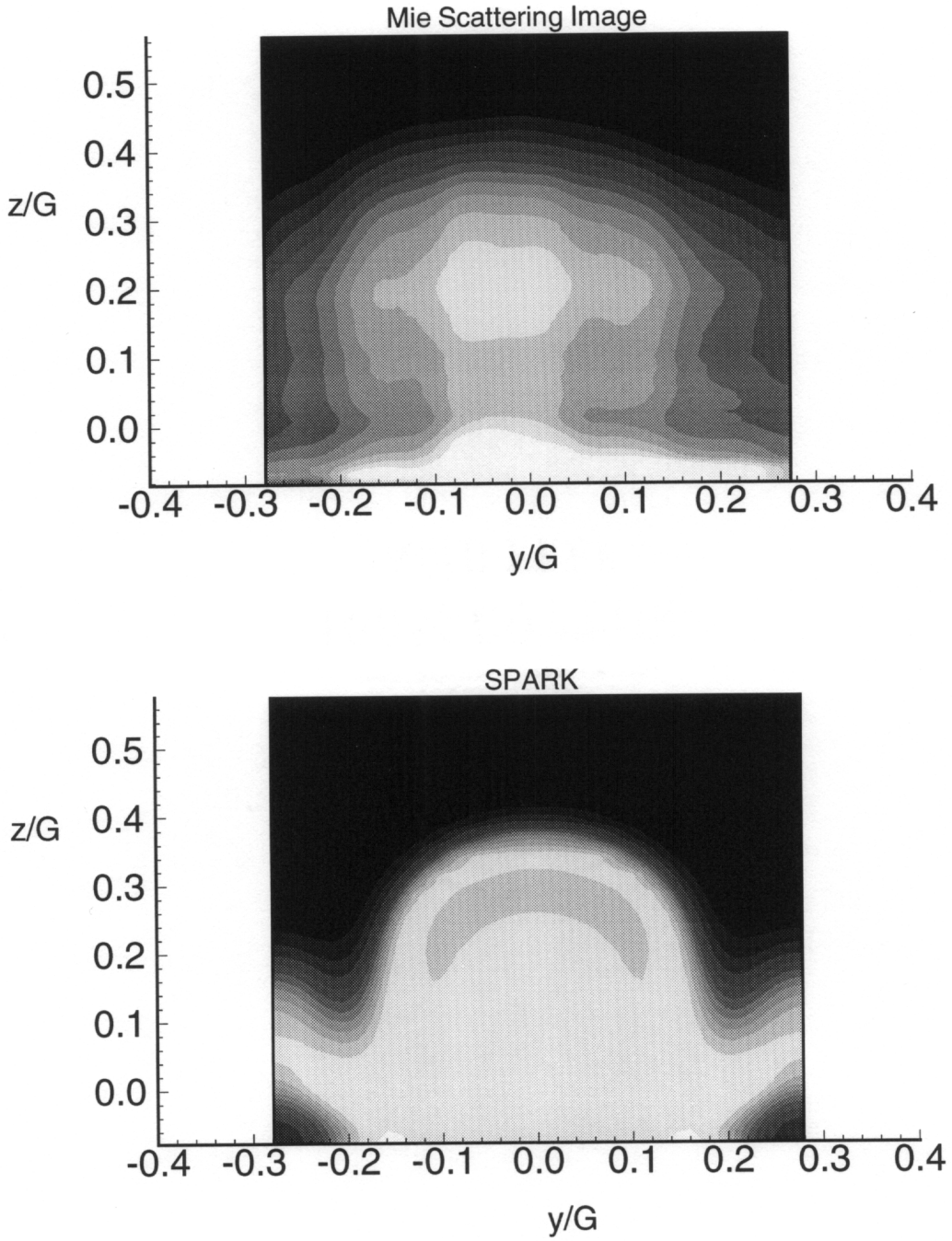

Figure 5.29 Comparison of Mie Scattering and Calculated Water Product Mass Fraction at x/G = 3.1.

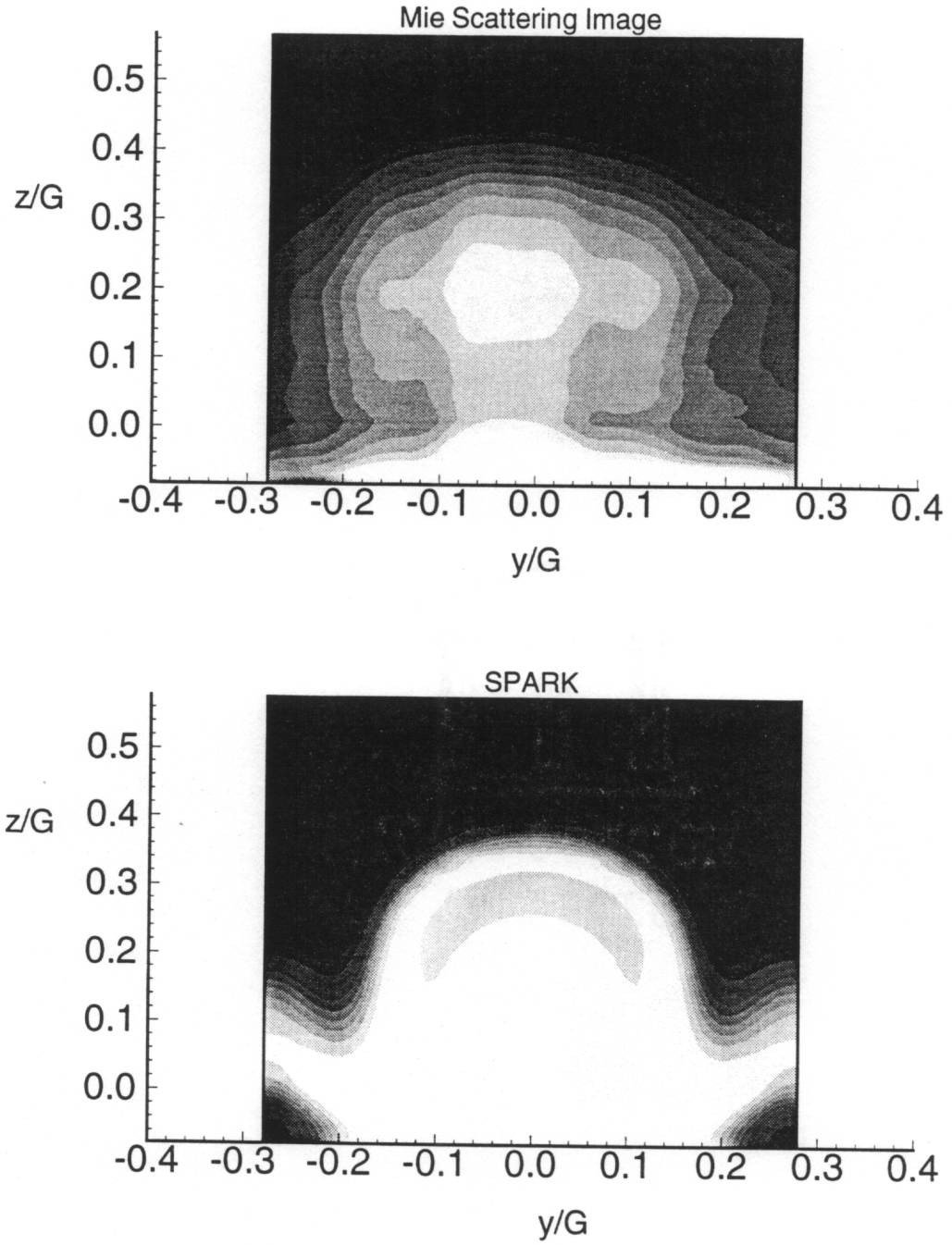

Figure 5.29 Comparison of Mie Scattering and Calculated Water Product Mass Fraction at x/G = 3.1.

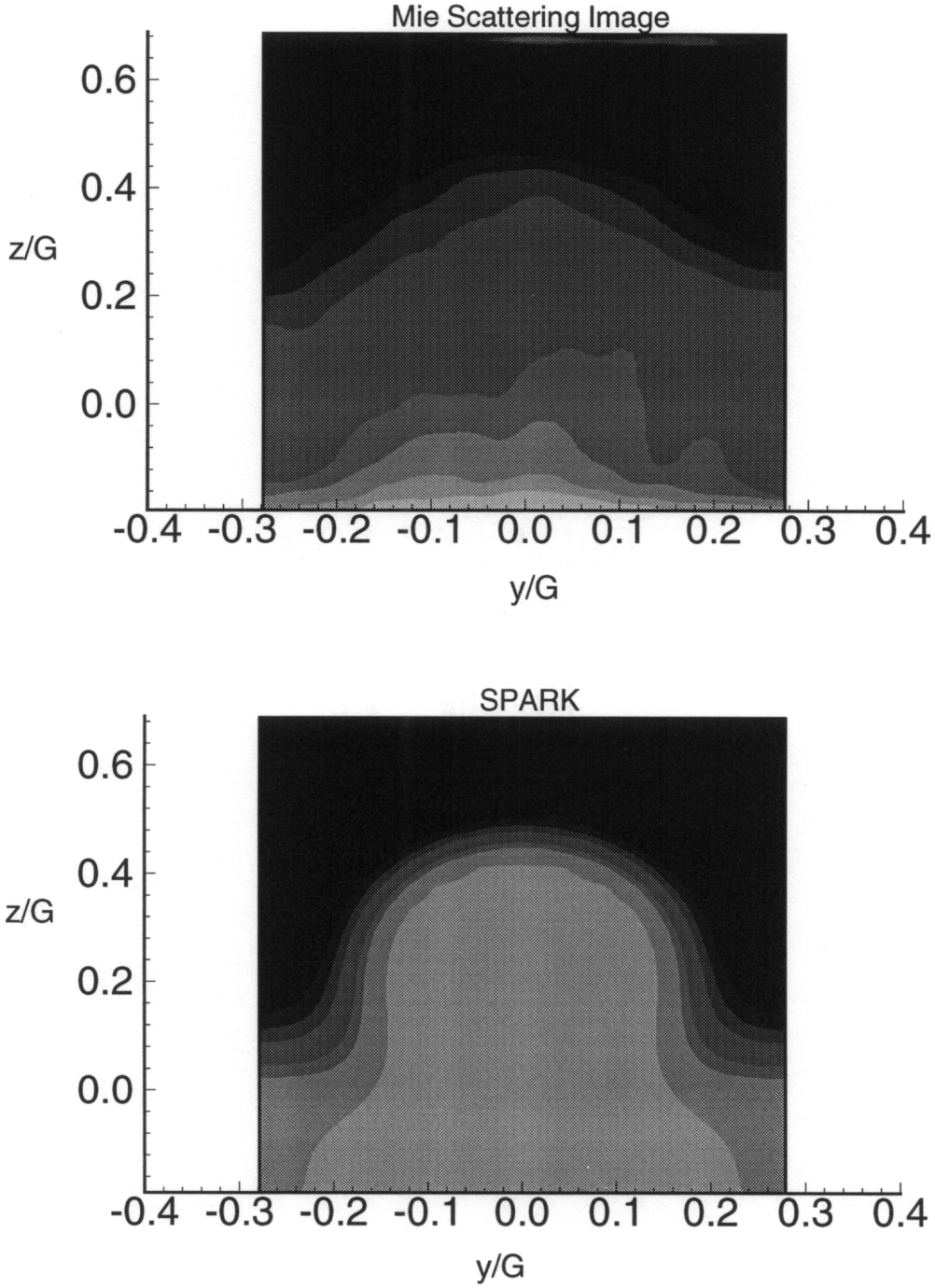

Figure 5.30 Comparison of Mie Scattering and Calculated Water Product Mass Fraction at x/G = 6.1.

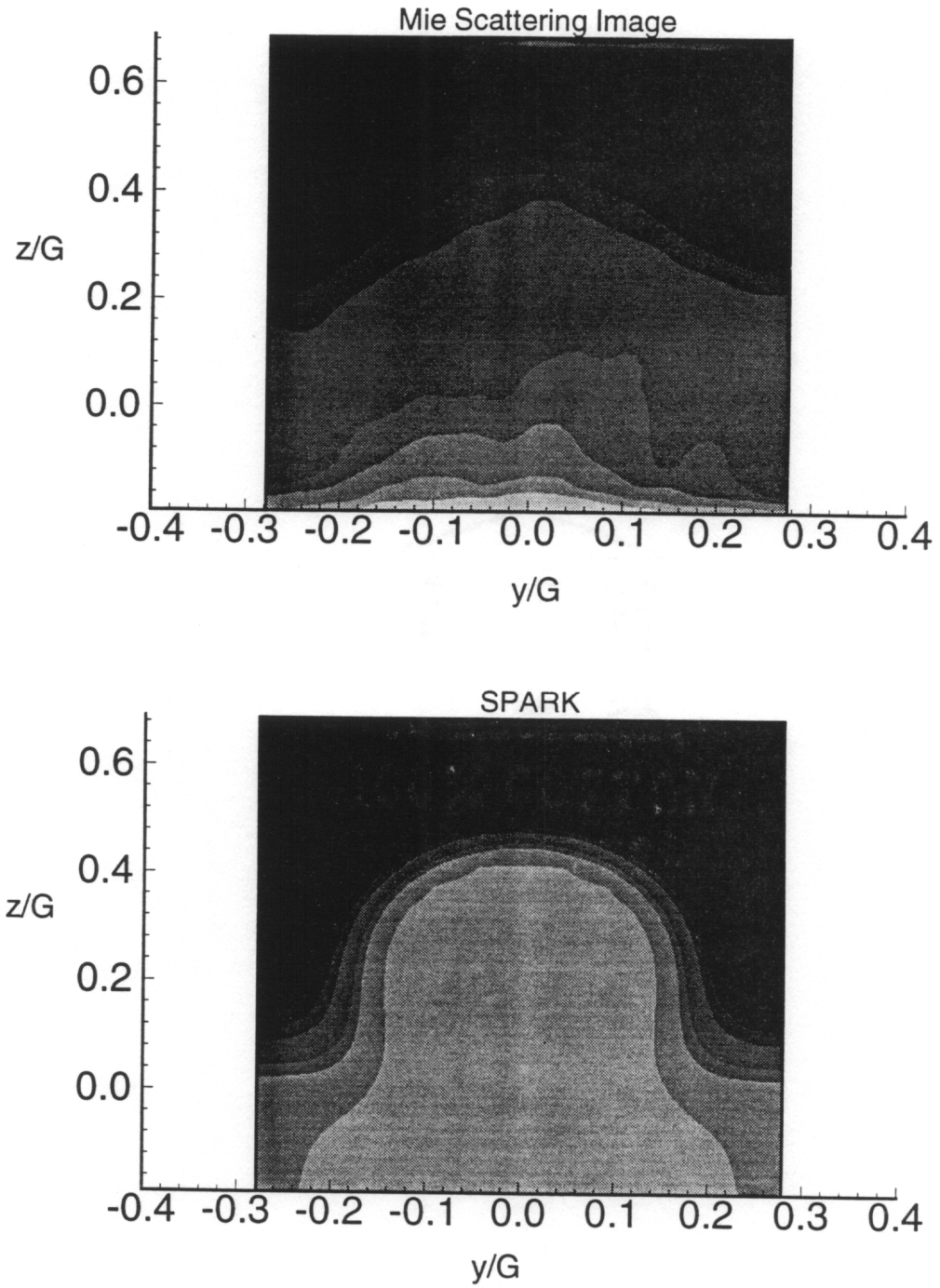

Figure 5.30 Comparison of Mie Scattering and Calculated Water Product Mass Fraction at x/G = 6.1.

Considering the limitations on the experimental images, the comparison of the images and the calculations show that they are in agreement at the outer edge of the fuel jet. As discussed in Chapter 3, further improvements in the imaging technique, and the understanding of the light scattering (particle size distribution, particle refractive index) are needed before quantitative concentration measurements can be made.

5.4.3 Pitot Pressure Comparisons

The measured and calculated pitot pressures for the reacting flow case along the interstice centerline of the combustor are compared in Fig. 5.31. The pitot profile shapes are also similar for the computational and the experimental pitot pressures. Although the computational pitot pressure is consistently lower than the experimentally determined pitot pressure, the experimental and computational pitot pressures are within 15 % of each other. The peak pitot pressure occurred closer, by approximately 0.08 Gap

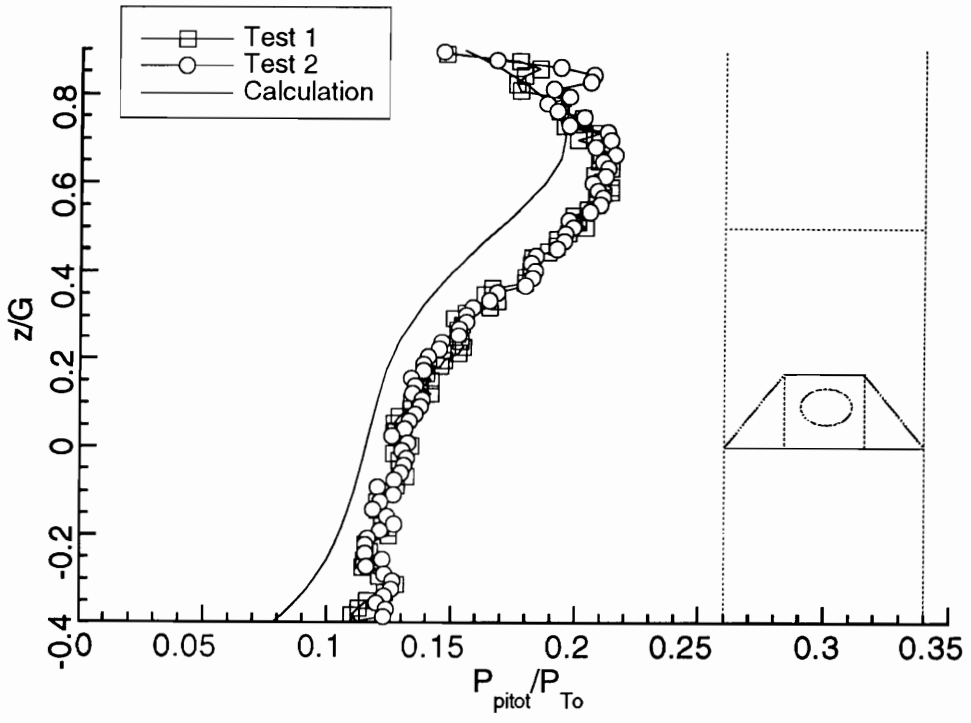

Figure 5.31 Comparison of Calculated and Measured Pitot Pressures Along the Interstice Centerline at x/G = 14.1 (ϕ = 0.7).

lengths (6.3 mm), to the injector wall in the experiments than it did in the computations. Since the pitot pressure is less in the reacting layer, this result implies the penetration of the reacting fuel is slightly less than the calculated value at this location.

5.5 Mixing and Combustion Efficiencies

The mixing efficiency, η_m, which is defined as the ratio of the mass of fuel that would react if complete combustion occurred to the mass of fuel injected. The mixing efficiency, η_m, was calculated by the following expressions:

$$\eta_m = \frac{\dot{m}_{H_2,MIX}}{\dot{m}_{H_2,Inj}} = \frac{\int \rho u \alpha_{H_2} dA}{\dot{m}_{H_2,Inj}}$$

where $\alpha_{H2} = Y_{H2}$ For $Y_{H2} \le Y_{H2,Stoic}$

and $\alpha_{H2} = \left(\frac{1 - Y_{H2}}{1 - Y_{H2,Stoic}} \right) Y_{H2,Stoic}$ For $Y_{H2} > Y_{H2,Stoic}$

where Y_{H2} is the mass fraction of hydrogen, $Y_{H2,Stoic}$ is the stoichiometric mass fraction of H_2, and $\dot{m}_{H_2,Inj}$ is the mass of hydrogen injected.

A plot of the mixing efficiencies calculated over the first section of the combustor is shown in Fig. 5.32. The laminar solution had the lowest mixing efficiency. Although fuel penetrated to the opposite side of the duct in the laminar case, the lateral spreading was small, resulting in the lowest mixing efficiency. The mixing efficiency for the turbulent mixing case was greater than that for the laminar case due to the greater lateral spreading of the jet. Figure 5.32 also shows that combustion had a detrimental effect on mixing efficiency in these calculations. The mixing efficiency was approximately 20% lower for the turbulent reacting case than it was for the turbulent mixing case. Most of the difference in the mixing efficiency occurred over the first 1.5 gap lengths, although the difference slowly increased over the rest of the combustor.

As discussed in Chapter 1, there are several mechanisms that can decrease the mixing rates in the reacting flow compared to the mixing rates

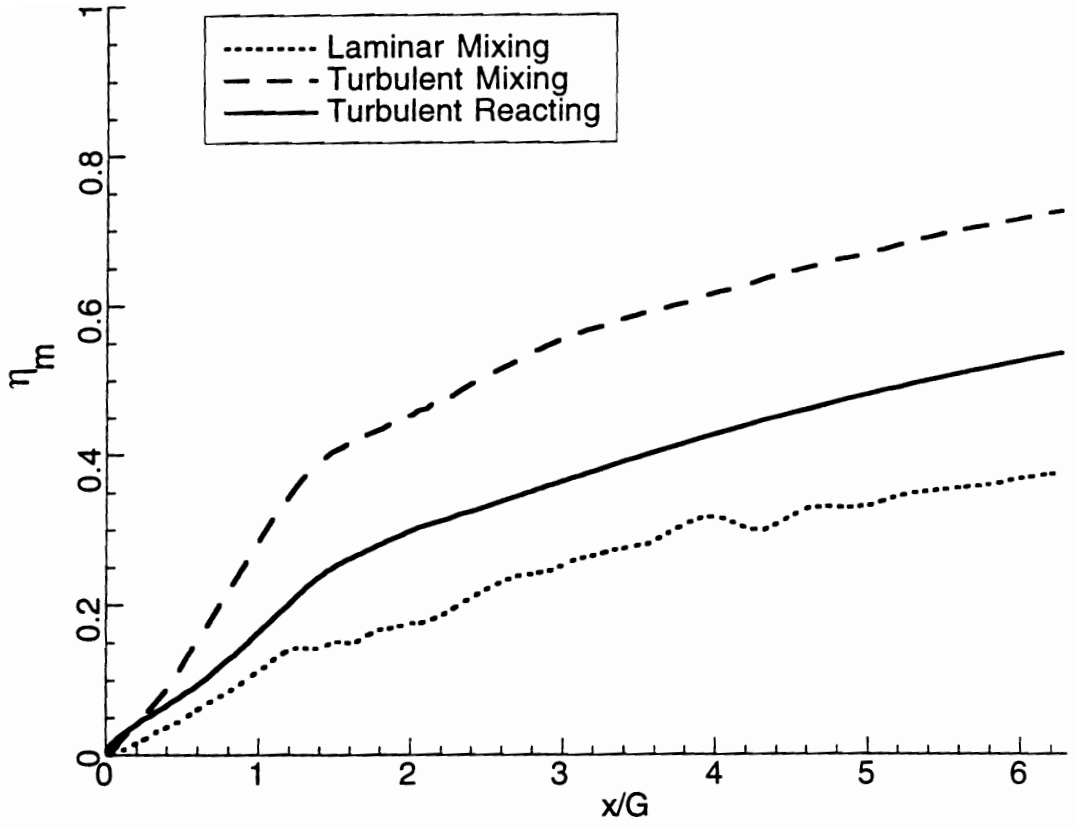

Figure 5.32 Calculated Mixing Efficiencies for the Swept Compression Ramp ($\phi = 0.7$).

in the non reacting case. One mechanism is the reduction in mass entrainment caused by the high temperature at the fuel/air interface. The other two mechanisms are illustrated in Fig. 5.33, which shows the pressures and velocity vectors at the exit plane of the injectors for the mixing and reacting cases. The fuel jet was underexpanded for both the reacting and non-reacting cases, but the fuel jet is less underexpanded in the reacting flow case. Perhaps the most important difference between the reacting and the non-reacting flows is the large difference in the vortical flow patterns at the ramp exit. The vortex in the interstice region for the non-reacting case is closely tied to the ramp corner. In contrast, the higher pressure in the interstice region leads to a much weaker axial vortex which is centered further away from the center of the fuel jet.

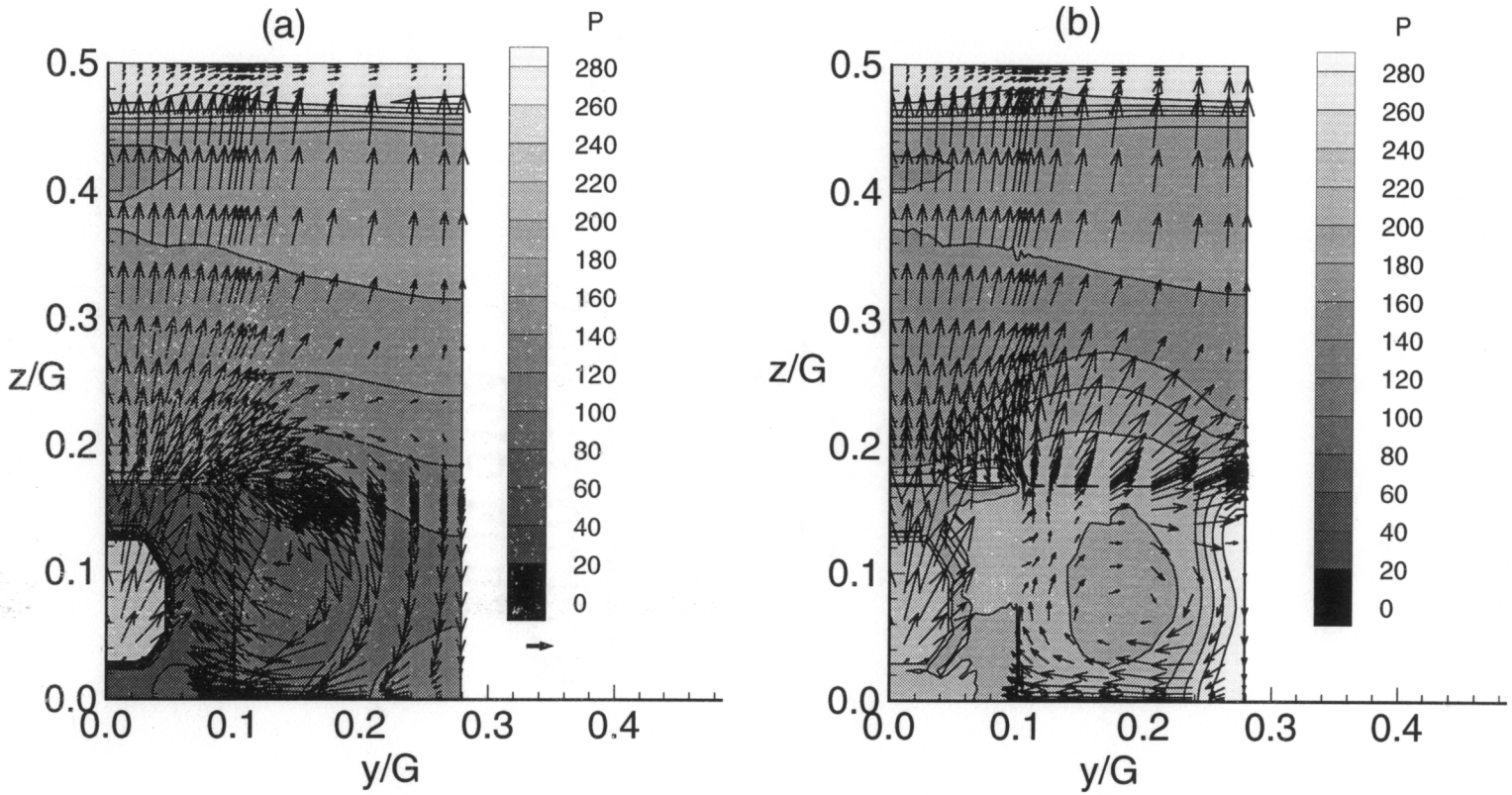

Fig 5.33 Pressure contours [kPa] and velocity vectors at the exit of the fuel injector for
(a) Nonreacting Mixing Case (b) Reacting Case

The calculated combustion efficiencies are compared with the mixing efficiency in Fig. 5.34. Two different definitions were used to calculate the combustion efficiency. The first definition of combustion efficiency, η_{c1}, is the ratio of the mass of hydrogen that has been converted to water, to the total hydrogen injected. The second definition, η_{c2}, is the ratio of the chemical energy released in the combustor to the amount of energy that would be released if all of the fuel reacted. The two values of the combustion efficiency are close to the mixing efficiency. Thus, the flow is said to be "mixing limited." In other words, reaction occurs where the fuel and air mix, with little delay due to chemical kinetics. This does not mean that one can determine the amount of fuel which will react from a study of the mixing alone, because, as shown earlier, the heat release affects the mixing rates.

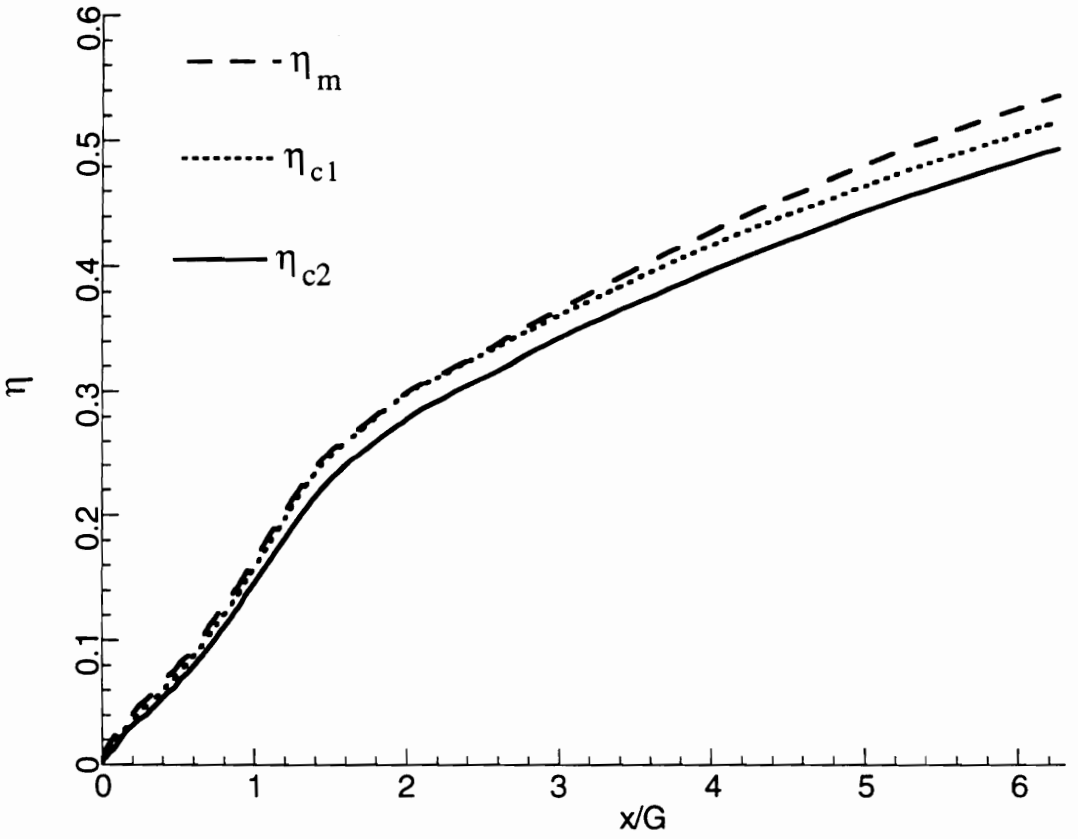

Figure 5.34 Comparison of Calculated Mixing and Combustion Efficiencies for the Reacting Flow Case.

5.6 Computed Stream Thrust Components

The calculated stream thrust for the swept ramp combustor is shown in Fig. 5.35, and the calculated components of the thrust for the swept ramp combustor are shown in Table 5.3. The net internal thrust produced in the combustor, assuming vacuum on the external walls, is the difference between the stream thrust at the entrance and exit of the combustor. Note that since only 1/8th of the combustor is modeled the thrust components are 1/8th of the total combustor thrust. The stream thrust drops upstream of the ramp base due to the skin friction and the pressure on the forward facing surface of the injector ramps. Calculations of the pressure integral in this region show that the pressure drag was 25 N of the 30 N of drag upstream of the ramp base, while the rest of the drop was due to skin friction. The slight increase in the stream thrust just upstream of the ramp in the reacting flow case was caused by the increase of pressure on the portion of the rearward facing sides of the ramp which are in the recirculation zone.

The stream thrust increased at the ramp base for both cases. The small increase for the no fuel case was due to the pressure at the base of ramp acting on the fluid. The change in the stream thrust in the reacting case was caused by the momentum of the fuel and the ramp base pressure. As shown in Table 5.3, the contribution of the ramp base pressure is slightly greater than half of the 39 N force produced at the ramp base, while the rest is due to the momentum of the fuel. The high pressure on the base of the ramp did not cancel the pressure drag on the forward facing part of the ramp. However, the combination of jet momentum and base pressurization produced positive net thrust in this region of the combustor.

The stream thrust dropped over the constant area section of the combustor due to skin friction. The stream thrust then increased in the expanding combustor duct for both cases due to the increase in the momentum of the flow. The small dip in the stream thrust at x/G = 6.1 occurred at the interface between the two computational grids. It is thought that the loss of momentum was caused by the switch from 39 to 20 points in

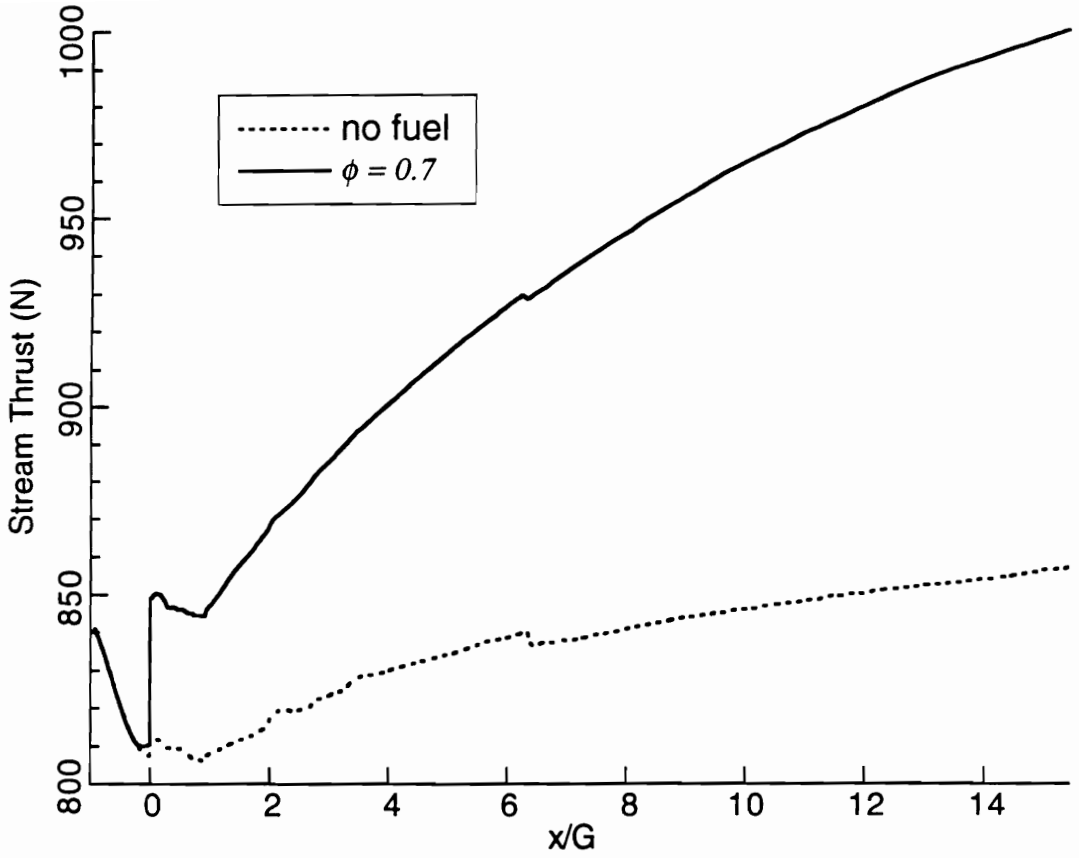

Figure 5.35 Stream Thrust for the Swept Ramp Combustor (1/8 of the width of the Combustor).

the crossflow direction which occurred when passing the solution between the two grids. The total internal thrust, calculated by the difference in the stream thrust between the combustor inlet and exit, is only 17 N for the no fuel case and 159 N for the $\phi = 0.7$ case.

The total skin friction in the combustor duct was calculated by subtracting the pressure integral and fuel momentum from the net thrust produced in the combustor. This result was checked with an integration of the skin friction forces[117] and agreed to within 1%. The calculated skin friction increased by approximately 20 % with combustion of the fuel. Note that this calculation did not include the effects of the side walls, which were not modeled. Hence, the actual skin friction should be higher because of the larger wetted surface area.

Table 5.3 Calculated Thrust Components (N) for the Swept Compression Ramp (1/8th of Combustor Width)

	No Fuel		$\phi = 0.7$	
Component	Force (N)	Fraction %	Force (N)	Fraction %
Pressure Integral Upstream of Ramp Base	-25	-153	-22	-14
Ramp Base Pressure Integral	3.1	19	20	13
Combustor Duct Pressure Integral	94	577	209	131
Fuel Jet Momentum	0	0	19	12
Skin Friction	-56	-344	-67	-42
Total Internal Thrust	16.3	100	159	100

The breakdown of the fractions of the force components in Table 5.3 shows the relative importance of the various force components. The calculated internal thrust for the no fuel case is small in magnitude compared to the force components that compose it. Recall that the exterior forces and the inlet drag have been neglected, so that the positive internal thrust for the no fuel case does not imply that a scramjet can produce thrust without fuel. For both cases the largest positive term is the combustor duct pressure integral. The ramp base pressure increase due to combustion nearly cancels out the pressure integral upstream of the ramp base. The skin friction represents a large loss (42 % of the total combustor thrust). While the fuel jet momentum represents about 12 % of the thrust.

The pressure integrals for the combustor duct are compared to the experimental values in Table 5.4. The experimental values are the average of 4 tests with ϕ =0.7± 0.09. The experimental and computational values agree within the uncertainty of the experimental values. This result was expected considering the agreement between the calculated and experimental pressures (see Fig. 5.27 and 5.28).

Table 5.4 Comparison of the Calculated and Experimental Pressure Integrals (N) in the Combustor Duct.

	No Fuel	$\phi = 0.7$
Experimental	765±45	1695±95
Computational	752	1672

5.7 Heat Transfer Calculations

5.7.1 Method

The heat transfer was computed for the swept-compression ramp for both the no fuel, and the reacting flow case. The heat transfer was computed directly from the temperature gradient at the wall. The thermal conductivity was evaluated by using the specific heat, viscosity, and the definition of the Prandtl number.

In order to reduce the amount of time required to solve for the large scale characteristics of the complex reacting flowfield, the grid spacing for the upstream grid was large enough that the first node from the wall was outside the laminar sublayer ($z+ > 10$ for the first node). Therefore, it was expected that errors would exist in the calculated heat flux due to the grid spacing. Further reductions in the grid size would have allowed better resolution of the flow near the wall, but would have been prohibitively expensive to run. Although some error is expected due to grid spacing, the results of the heat flux calculations for the upstream grid are examined below to provide qualitative insight into the variation of the wall heat flux and the effect of the flowfield on the heat flux.

In the second section of the combustor, the combustor geometry and the flowfield were much simpler than that in the first section. This allowed the node spacing in the axial and spanwise locations to be increased. The node spacing in the transverse direction was decreased in an effort to better resolve the boundary layer flow. Also, the boundary layer thickness was greater in the second section of the combustor. Therefore, the boundary layer was resolved better in the second section of the combustor and the calculated heat fluxes are expected to be closer to the actual heat fluxes than those for the first section of the combustor.

The imposed wall temperatures used for the CFD calculations are temperatures shown in Fig. 5.36. Recall that the wall temperatures were set at a constant 670 K for the first section of the combustor ($x/G < 6.3$). In the second section of the combustor ($x/G > 6.3$) a linear fit of the experimentally determined wall temperatures was used for the calculations. The actual wall temperatures in the second section of the combustor were less than 670 K for

the no fuel case and the opposite wall of the combustor in the reacting case. The curve fit of the injector wall of the combustor resulted in a higher temperature (≈820 K) at the start of grid 2. In hindsight, it is thought that the estimated temperature used for the calculations in the first section of the combustor was lower than the actual wall temperatures.

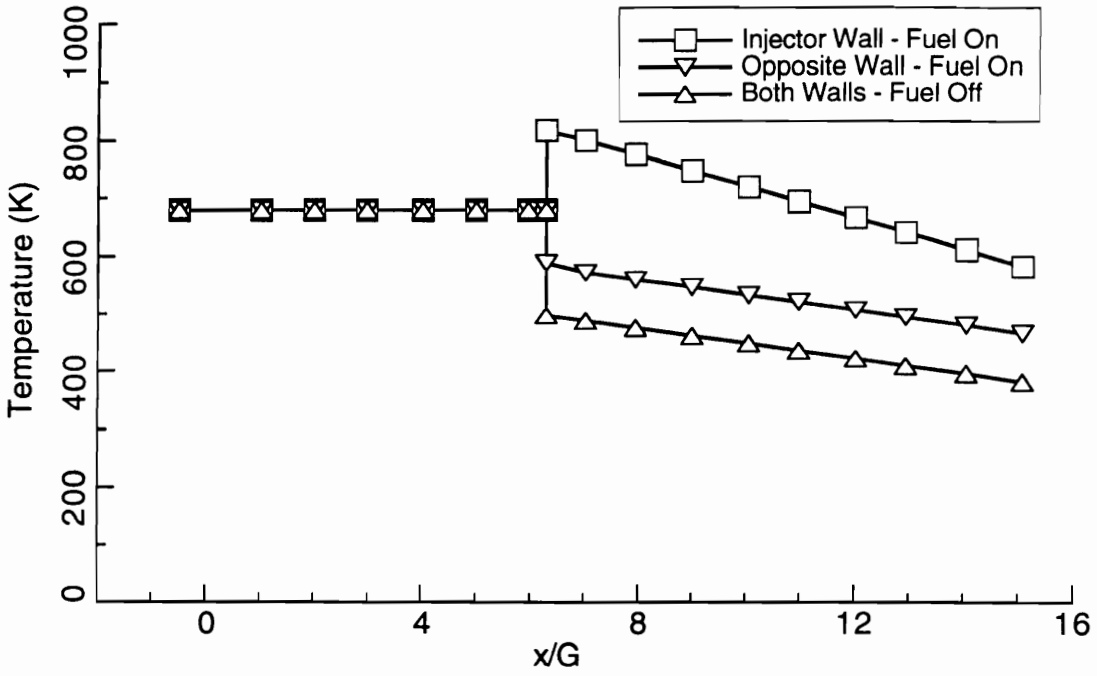

Figure 5.36 Wall Temperatures Used in the CFD Calculations.

5.7.2 Calculated Heat Transfer Results

The results for the no fuel case are shown in Fig. 5.37 and 5.38. Downstream of x/G = 1.5, the calculated heat flux varies little in the spanwise location. The heat flux plots show that the maximum heat flux on the injector wall is located downstream of the line where the reflected shock hit the top wall of the combustor. Similar increases in the heat flux due to the interaction of the shock waves with the flowfield near the wall can be observed at locations where the ramp shock reflected off of the walls. Localized axial oscillations in the heat flux occurred near the reflections of the shock waves with the wall. The oscillation was most severe at the shock reflection at x/G = 7.2. It is thought that this problem can be alleviated by

improving the axial resolution of the grid, and lowering the grid aspect ratio (axial spacing/transverse spacing) in this area.

As the solution was passed from the upstream grid to the downstream grid (Fig. 5.37 to 5.38), the calculated heat flux increased. The increase of the heat transfer at the start of the second grid was caused by two effects. The first is the wall temperature drop between the first and second grids. The second reason is that a finer grid was used near the wall in the second section of the combustor to improve the heat transfer prediction. It is thought that the heat flux is under-predicted in the upstream portion of the combustor due to the coarser grid.

The heat flux plots for the reacting case are shown in Fig. 5.39 and 5.40. As expected from the plots of the flowfield variables, the calculated heat fluxes were higher on the injector wall than they were on the opposite wall. The highest heat fluxes are calculated to be at approximately x/G = 1.8 and y/G = 0.1. Referring to Fig. 5.17 and 5.19, which show the OH mass fraction, and static temperature, it can be seen that the flame front, and thus the highest temperature is closest to the wall at this location. At locations further downstream, the pocket of oxygen between the flame and the wall was totally consumed so that the closest approach of the flame front to the wall is at the outer edge of the fuel jet near the interstice. This is reflected in the heat transfer contours in the region downstream of x/G > 5 that had higher heat fluxes at the interstice centerline than at the injector centerline.

The relative increase of the heat flux between the first and second sections of the combustor was less along the injector wall than for the opposite wall. However, recall that the wall temperature used for the calculations increased between the first and second sections of the injector wall. Thus, although the heat flux prediction increased due to grid refinement, the increase in the heat flux is less than it was for the opposite wall because of the decrease in the temperature difference.

The adiabatic wall temperature and the film coefficients were calculated from the numerical flow field solutions for the interstice and

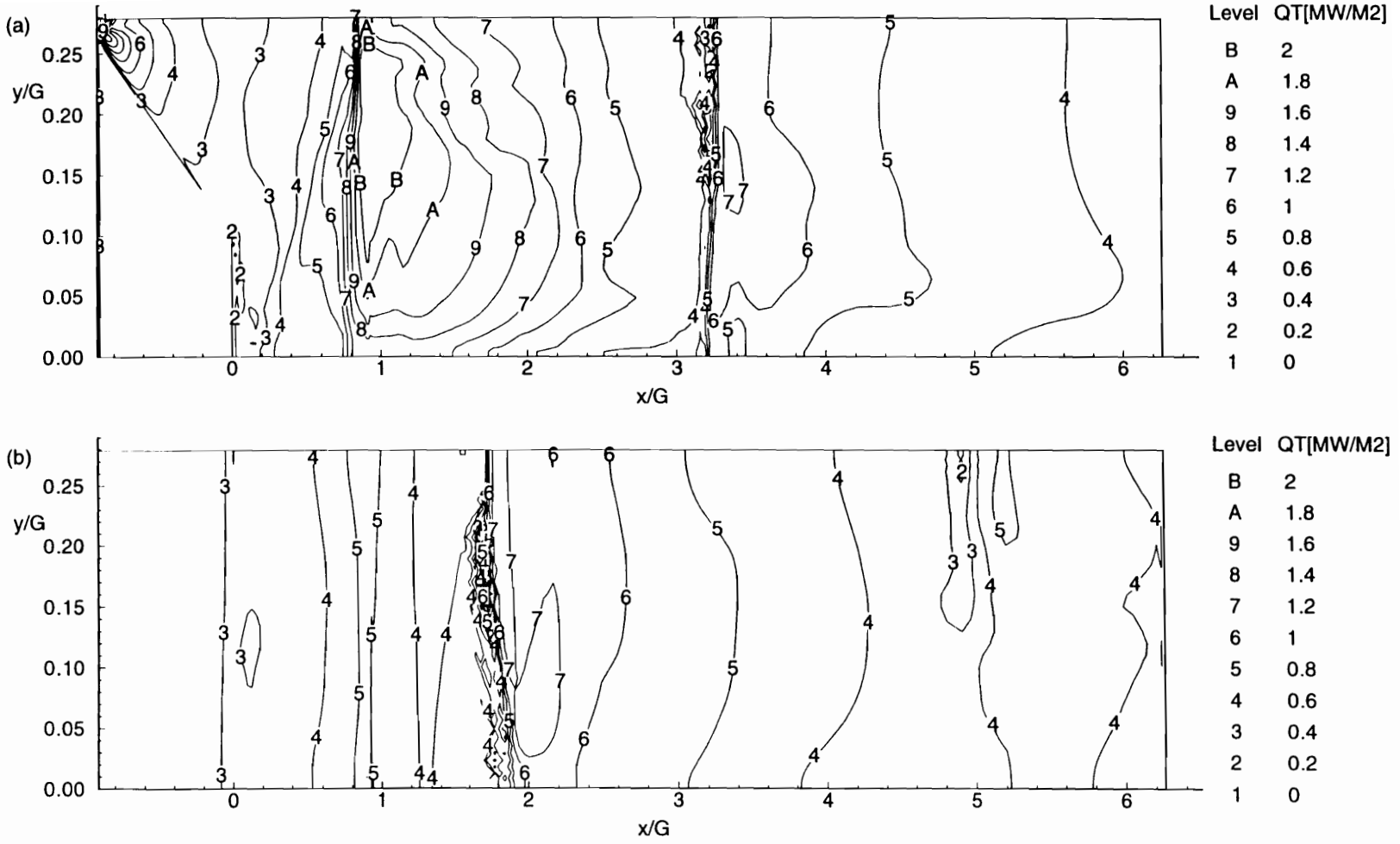

Figure 5.37 Heat Flux for the No Fuel Case in the First Section of the Combustor:(a) Injector Wall (b) Opposite Wall.

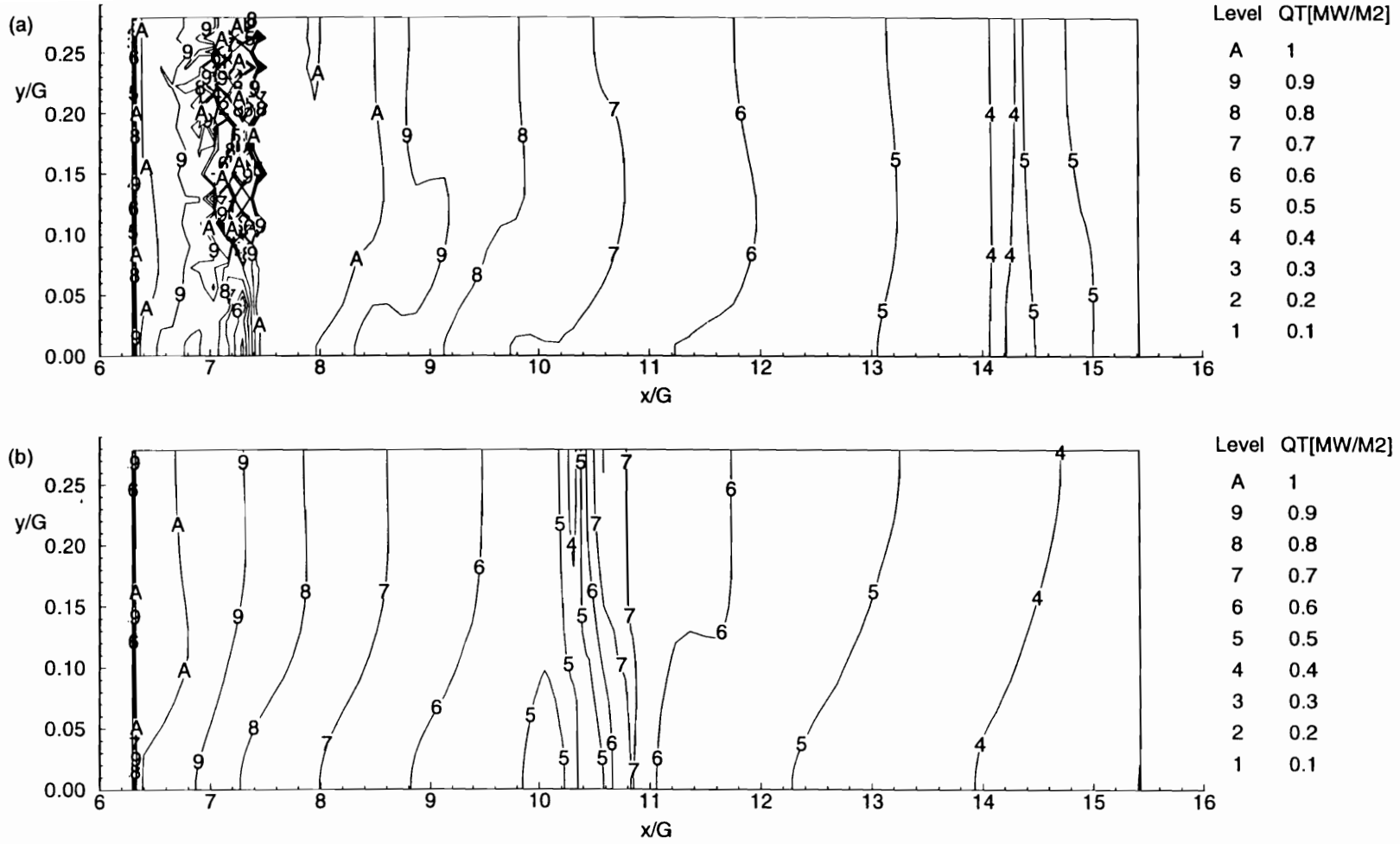

Figure 5.38 Heat Flux for the No Fuel Case (2nd Half of Combustor): (a) Injector Wall (b) Opposite Wall.

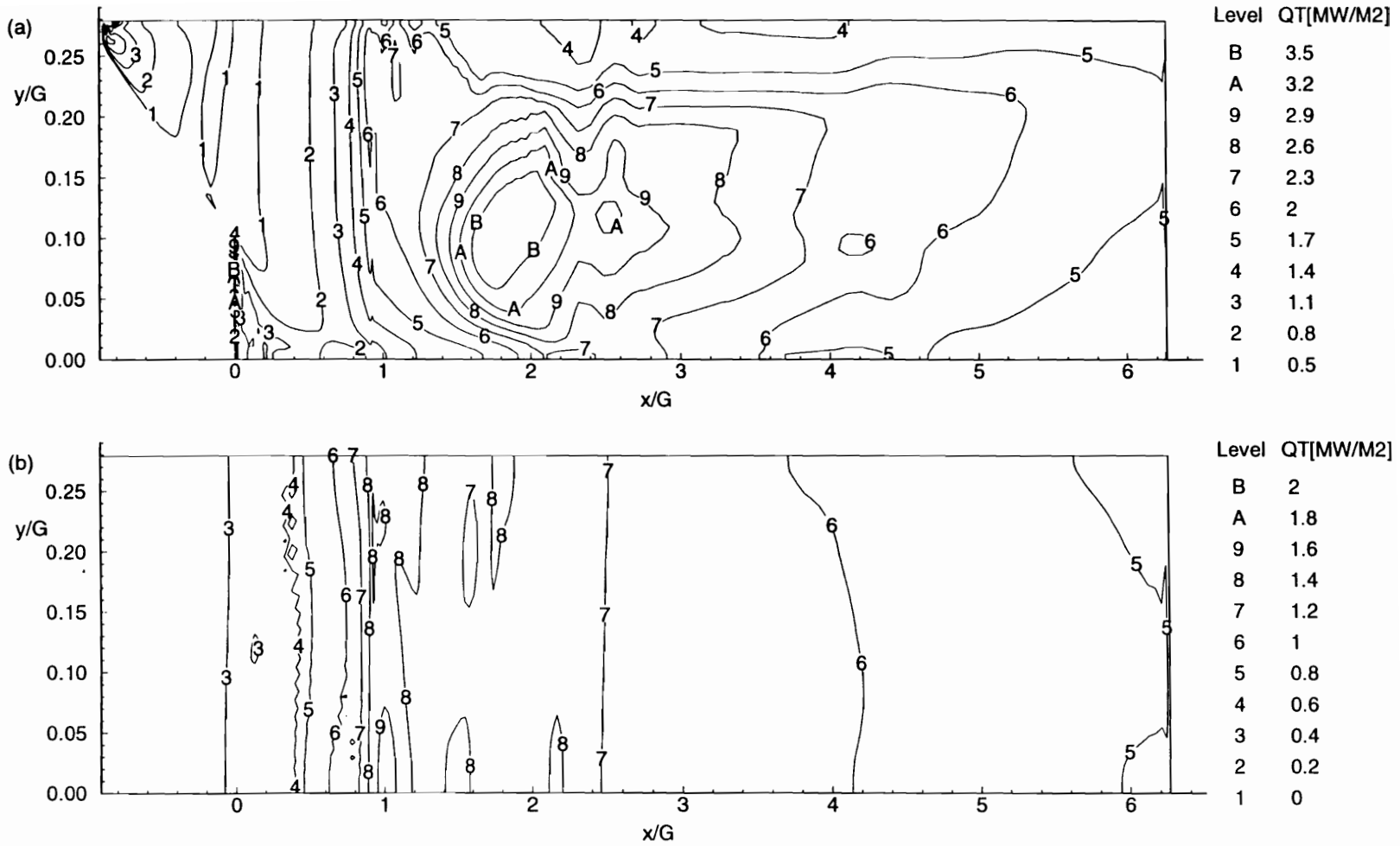

Figure 5.39 Heat Flux for the Phi = 0.7 Case (First Section) (a) Injector Wall (b) Opposite Wall

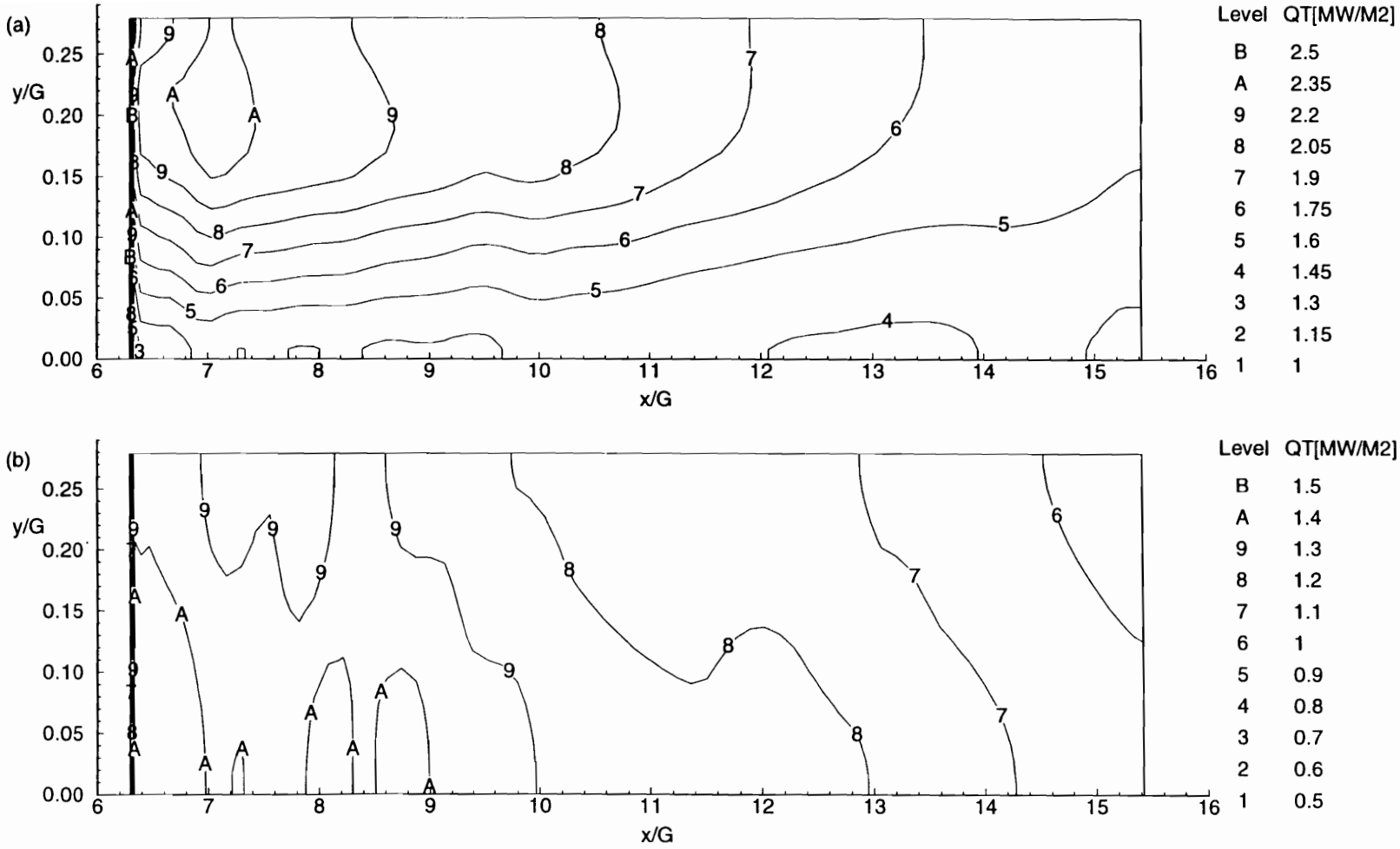

Figure 5.40 Heat Flux for the Phi = 0.7 Case (Second Section of the Combustor) (a) Injector Wall (b) Opposite Wall

injector centerlines. The adiabatic wall temperature, T_{aw}, was calculated from the following expression:

$$T_{aw} = T\left(1 + r\frac{U^2}{2C_p}\right) \quad (5\text{-}5)$$

where U is the velocity vector, and the recovery factor, r, was set equal to $(Pr)^{1/3}$. For the constant turbulent Prandtl number (0.9) used here the recovery factor was 0.966. Selecting the edge of the thermal boundary layer was a challenge because of the complex nature of the flow field. Therefore, at selected points along the wall, the velocity and temperature profiles were examined to find the edge of the thermal boundary layer, and equation 5-5 was used to determine the adiabatic wall temperature.

The calculated adiabatic wall temperatures along the interstice and injector centerlines are shown in Fig. 5.41. The wall opposite of the injectors was not effected by the combustion products due to the lack of penetration, resulting in a nearly constant adiabatic wall temperature of approximately 1880 K. In contrast, T_{aw} along the injector wall varied greatly because of the proximity of the burning fuel jets to the outer edge of the boundary layer. Along the interstice centerline T_{aw} increased dramatically between x/G = 3 and x/G = 5 due to the close approach of the combusting fuel jet to the wall. Further downstream, T_{aw} was nearly constant. Along the fuel jet axis, the adiabatic wall temperature increased downstream of x/G = 1.4, due to the close approach of the burning fuel jet to the wall. The maximum adiabatic wall temperature along the injector centerline occurred at x/G = 2, and then decreased because of flame quenching near the wall. Along the injector centerline for x/G > 4, the flow near the wall consisted of fuel rich combustion products that were heated by reaction and turbulent diffusion along the rest of the combustor.

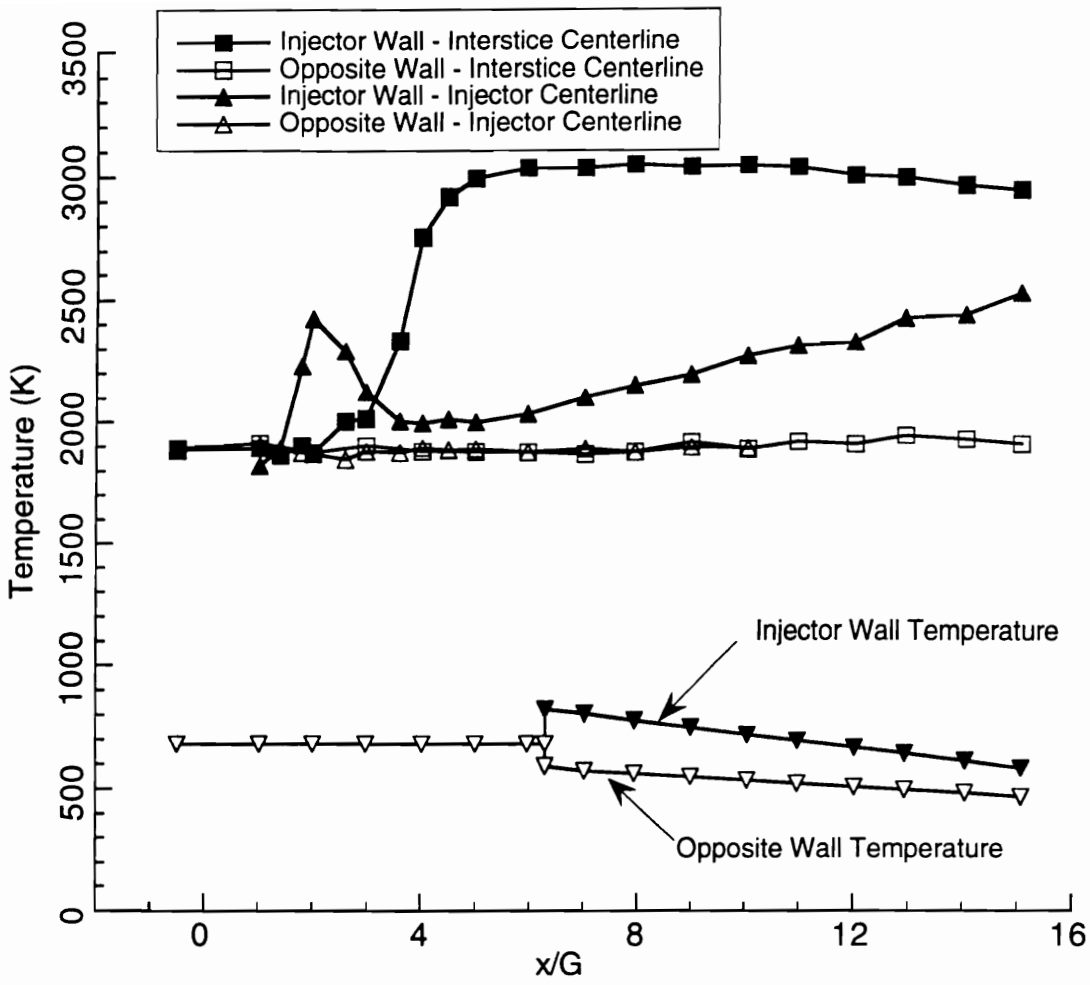

Figure 5.41 Calculated Adiabatic Wall Temperatures Along With the Imposed Wall Temperature for the Reacting Flow Case.

The film coefficient calculated from the definition of the film coefficient, $h = \frac{q}{T_{aw} - T_w}$, is shown in Fig. 5.42 along the fuel injector, and interstice centerlines, on both walls of the combustor. In the first section of the combustor the film coefficient decreased at approximately the same rate along the interstice centerline on the injector wall, and the opposite wall. The film coefficient on the injector centerline on the injector wall increased between x/G = 2 and x/G = 2.6. It is thought that the reason for the increase in the film coefficient in this region is the higher thermal conductivity at the wall, which was largely due to the high thermal conductivity of hydrogen at

the wall. Note that Fig. 5.15 showed that there was little hydrogen at the wall along the injector centerline at x/G = 1.5, in contrast, directly downstream at x/G = 3, the gas at the wall was approximately 40 % hydrogen by volume. A finer grid near the wall was used for x/G > 6.3. As shown in the computed contour plots for the heat flux, the heat flux increased between grid 1 and grid 2. Thus, the computed film coefficient also increased at the boundary between the two grids. Therefore, the computed film coefficient in the first section of the grid was expected to be lower than the actual film coefficient due to the coarse grid, while the film coefficient for the second grid is expected to be closer to the actual film coefficient. In the second section of the combustor, the film coefficient was within a ±10 % band along the four centerlines.

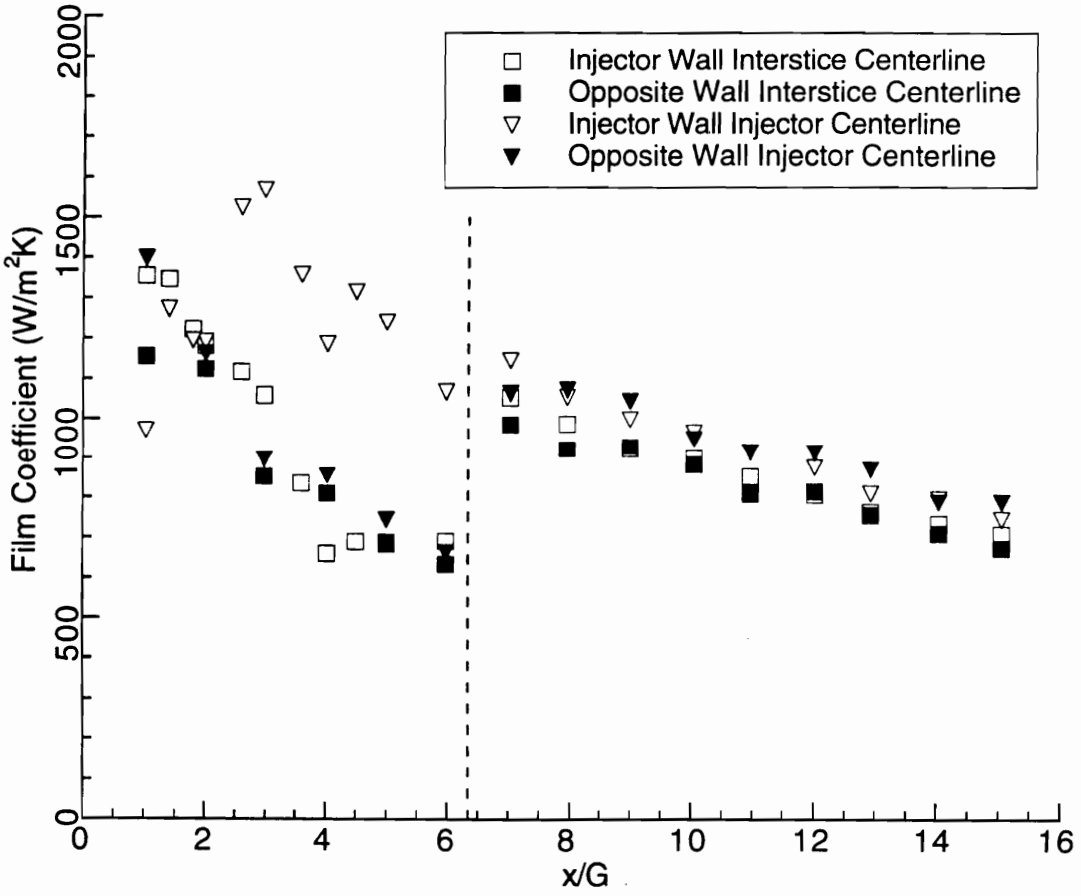

Figure 5.42 The Film Coefficient for the Reacting Flow Case ($\phi = 0.7$)

The wall heat fluxes along the fuel jet, and interstice centerlines are shown in Fig. 5.43 and 5.44 for the injector wall and the opposite wall respectively. Recall that the wall heat flux is the product of the film coefficient and the difference between the adiabatic wall temperature and the wall temperature. Referring to Fig. 5.42 - 5.43 it is seen that over most of the injector side of the combustor the heat flux was highest where the wall temperature difference was the highest. At the end of the first grid, the flux was higher along the interstice centerline because of the higher temperature difference, even though the film coefficient was higher along the injector centerline. In the second section of the combustor, the difference in the heat fluxes was clearly due to the larger adiabatic wall temperature at the interstice centerline.

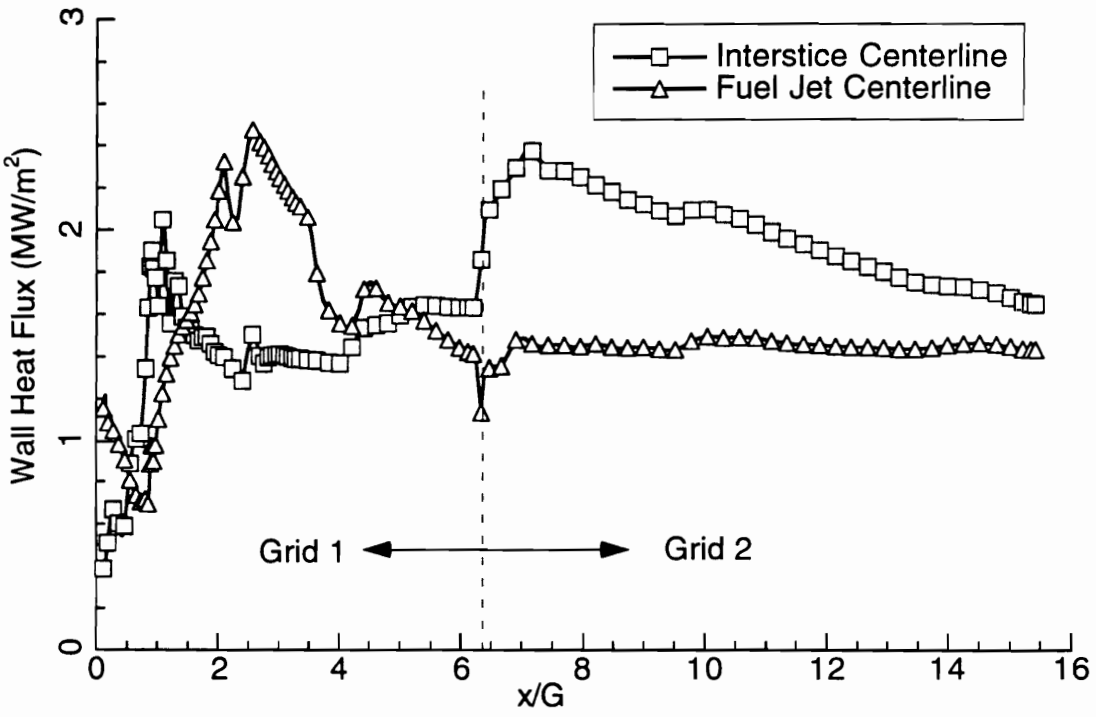

Figure 5.43 Calculated Heat Flux Along the Injector Wall ($\phi = 0.7$).

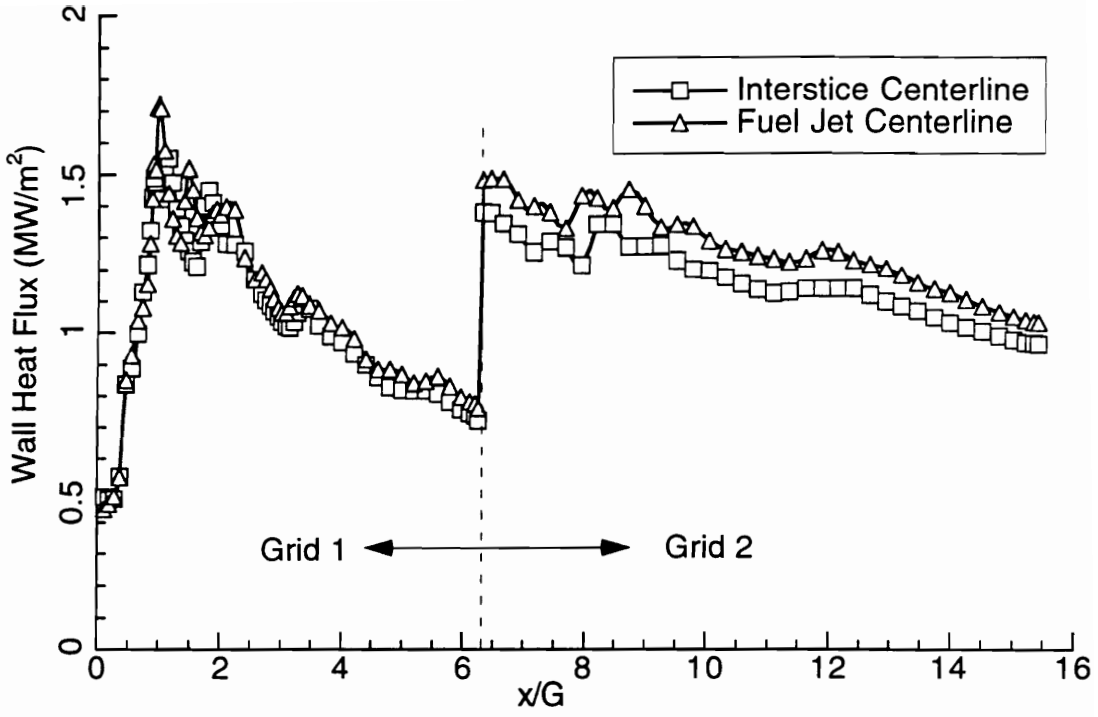

Figure 5.44 Calculated Heat Flux Along the Opposite Wall.

5.7.3 Comparison of Calculated and Experimental Heat Fluxes

The wall heat transfer measurements for the no fuel case are shown in Fig. 5.45, and 5.46. In the first section of the combustor (x/G < 6.2) the heat flux was severely under-predicted by the calculations. In the downstream section of the combustor, the calculated heat fluxes are much closer to the experimental values. Along the injector wall the calculations are within the uncertainty of the heat flux measurements for some of the measurements.

The calculated heat transfer measurements with fuel injection are compared to the experimental measurements in Fig. 5.47, and 5.48 for the injector and opposite walls of the combustor, respectively. As expected, the calculated heat transfer was much less than the experimentally determined heat transfer in the upstream region. However, the trends of the calculated and experimental heat fluxes are the same. In the downstream section of the combustor the calculated heat fluxes are close at most of the gage locations. At the interface between the two grids the relative increase of the heat flux in the calculations was less than that for the opposite wall. However, recall that

the wall temperature increased at the interface between the two grids, thus lowering the temperature difference between the flow and the wall. As shown in Fig. 5.48, along the injector wall the heat transfer was under predicted by a factor of 4 in the first section of the combustor. The calculated heat transfer along the interstice was greater along the interstice centerline than the injector centerline. At x/G = 7 the heat flux was calculated to be 50 % higher at the interstice centerline than it was at the injector centerline. A large difference was not seen between the heat flux at the interstice and injector centerlines in the experiments. It is thought that the lateral penetration of the fuel could have been greater than that predicted by the calculations, resulting in consumption of the oxygen near the wall at the interstice, and a reaction zone which lifted off of the wall. Note that a wider fuel plume is also consistent with the Mie scattering images.

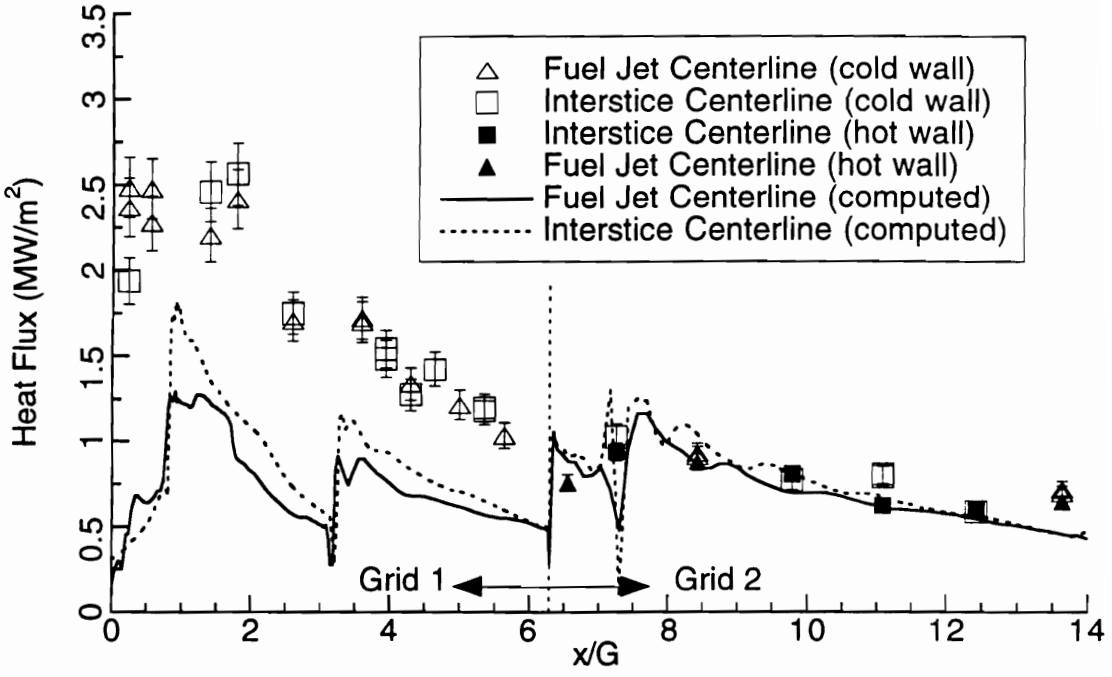

Figure 5.45 Comparison of the Computed and Measured Heat Fluxes Along the Injector Wall (No Fuel Case)

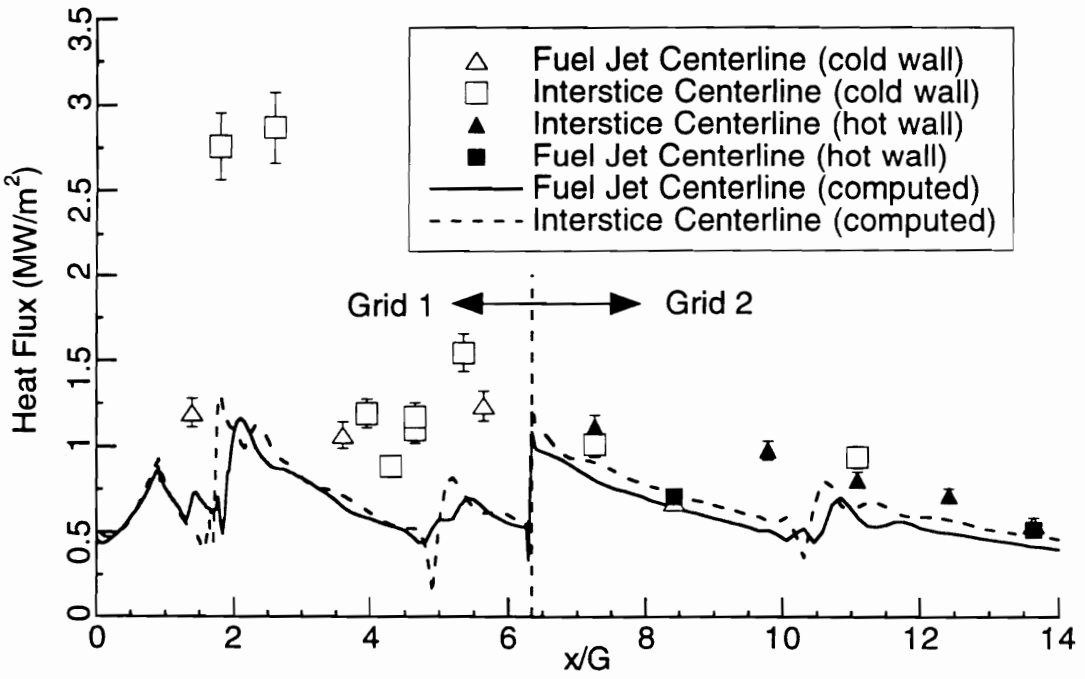

Figure 5.46 Comparison of the Computed and Measured Heat Fluxes Along the Wall Opposite of the Injectors (No Fuel Case)

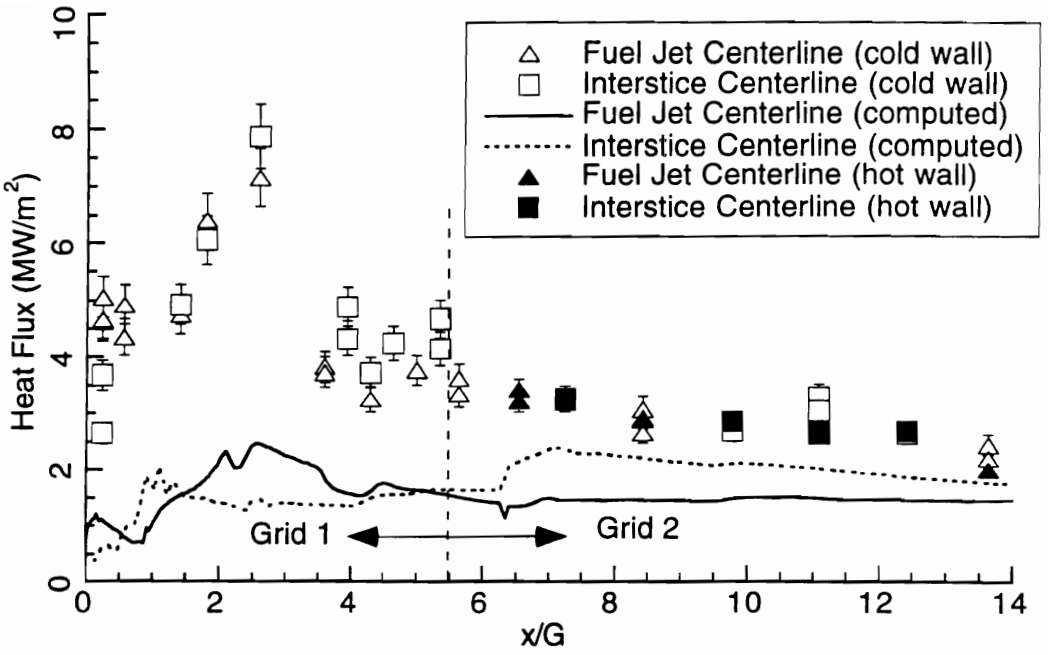

Figure 5.47 Comparison of the Computed and Measured Heat Fluxes Along the Injector Wall (ϕ = 0.7).

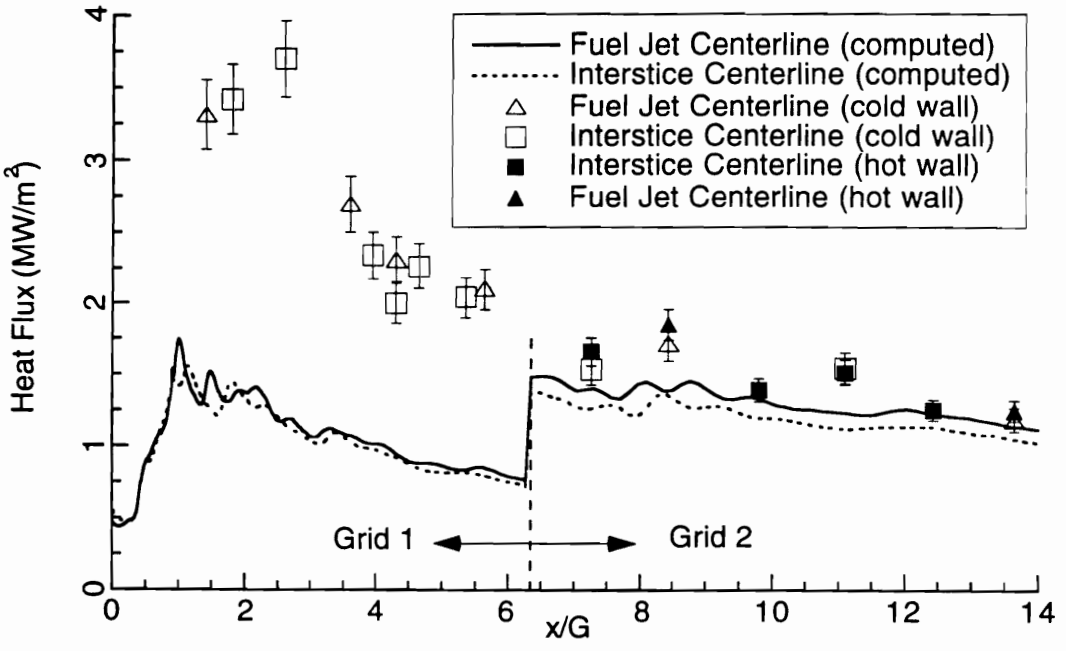

Figure 5.48 Comparison of the Computed and Measured Heat Fluxes Along the Wall Opposite of the Injectors (ϕ = 0.7).

5.8 Expansion Ramp Results From Other Studies

5.8.1 Reacting Flow Case

As part of the joint investigation of the reacting flow fields downstream of swept-ramp fuel injectors calculations of the reacting flow field downstream of the expansion-ramp injectors were attempted by Eklund.[107] Figure 5.49 shows the temperature contours along the jet centerline from this effort. The contour plots are shown at different phases of the calculation. Early in the calculation, autoignition occurred in the boundary layer at the jet centerline and interstice centerline. In the second temperature profile shown in Fig. 5.49 the ignition point moved further upstream to x/G = 3, which is just downstream of the location where ignition occurred in the experimental case. As the calculation continued, the flame front moved forward and eventually anchored near the fuel injectors. Parabolized Navier-Stokes calculations at Mach 2 performed by Davis[63] also showed flameholding in the nearfield of the injectors. Recall that in the experimental tests of the expansion ramps autoignition did not occur, and piloting was required to initiate combustion. Also, in the experimental case, flameholding occurred far downstream of the ramps. Thus, the calculated flowfield did not resemble the experimental case.

The challenge of modeling the reacting flowfield is more difficult for the expansion-ramp case than it was for the autoigniting compression ramp case. In the experimental case the flame was established near the injectors until the pilot was turned off. After the pilot was turned off, the flamefront moved downstream into the expanding combustor duct. This sequence of events leading to the establishment of flameholding in the experimental case can not be realistically modeled in the steady calculations made with the SPARK code. Recall that the calculations for this study were made using a local time step. Time accurate calculations could provide new insight on the sequence of events leading up to establishment of the flame in the duct. However, the required use of global time steps would result in prohibitively large amounts of computer time, because the size of the time step would be limited by the smallest grid spacing.

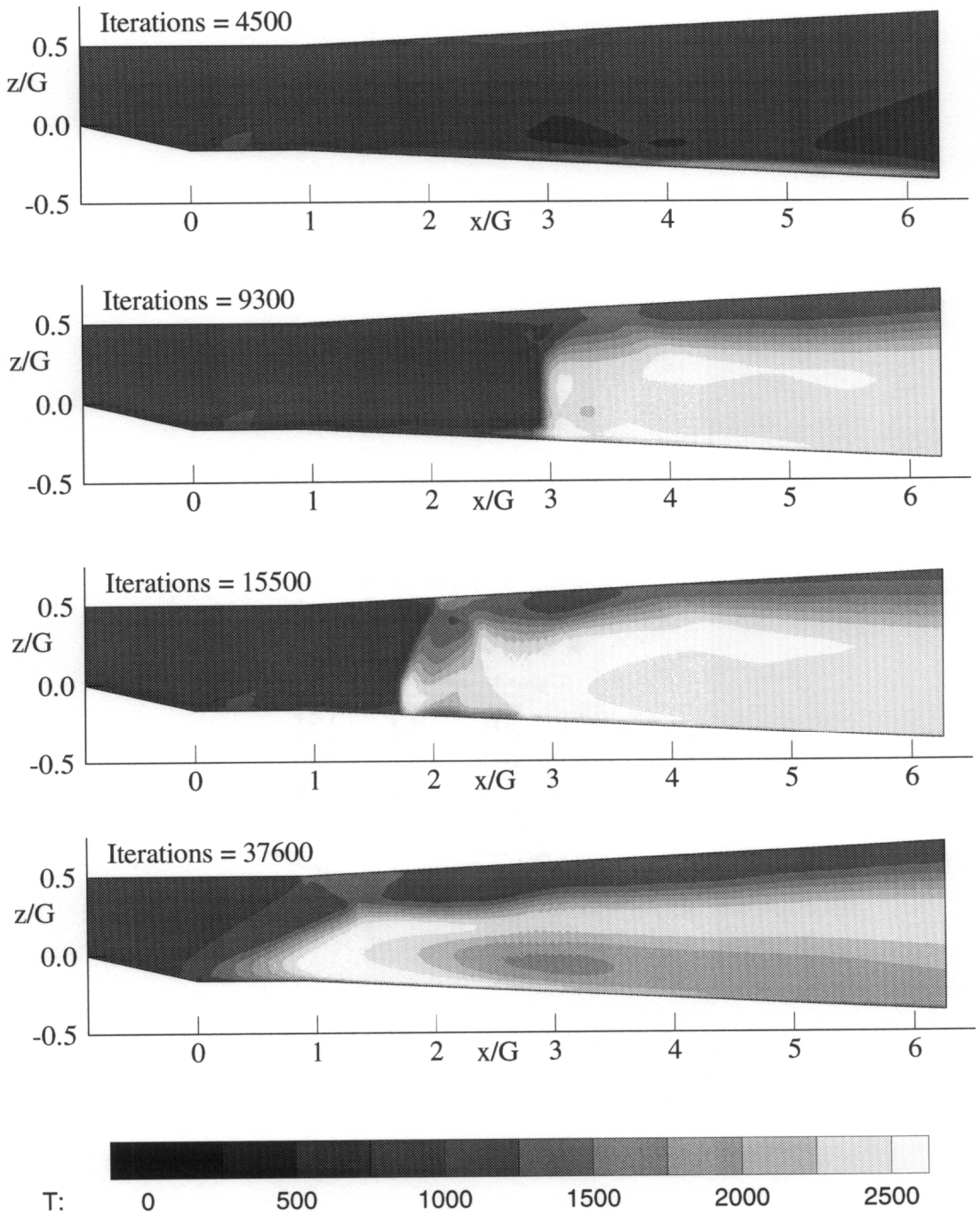

Fig. 5.49 Temperature (K) Contour Plots Along the Interstice Centerline for Expansion Ramp.

5.8.2 Non-Reacting Mixing Case

Calculations of the mixing without reaction in the expansion ramp combustor were performed by Eklund et al.[107] Figure 5.50 shows the mixing efficiency for the swept-compression and the swept-expansion ramp injectors at an equivalence ratio of 1. The mixing efficiency was greater for the swept-compression ramp than it was for the swept-expansion ramp. Other calculations by Davis[63] show that the vorticity generated by the swept expansion ramp was lower than that for the swept-compression ramp. The passage of the oblique shock downstream of the ramps further increased the vorticity further, and thus increased the mixing rate, however the overall mixing efficiency was lower for the swept expansion ramp. In addition, the injector for the swept-expansion ramp was located further from the opposite wall so that penetration was inhibited. For the combustor geometry used in

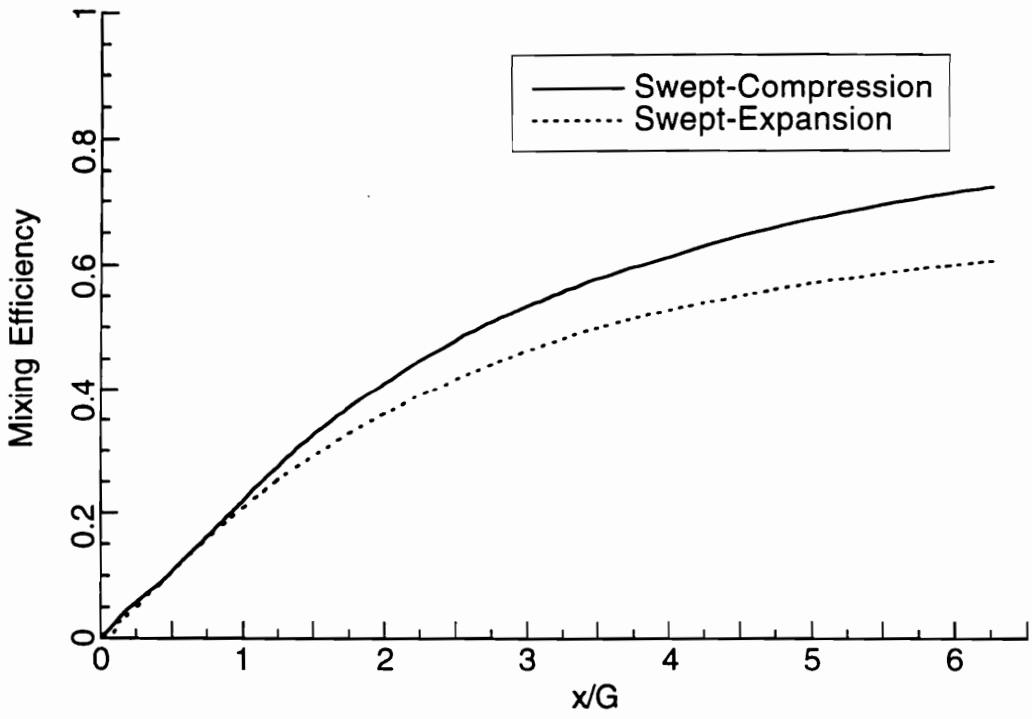

Figure 5.50 The Calculated Mixing Efficiencies for Non-Reacting Flow for $\phi = 1$ (from Eklund et al.[107]).

the present study, combustor geometry used in the present study, the centers of the expansion-ramp fuel injectors were located 40 % farther from the opposite wall than the compression ramp injectors were.

Considering the above discussion of the non-reacting mixing efficiency, the expansion-ramp would be expected to perform much worse than swept-compression ramp. However, recall from the experiments that the swept-expansion ramps clearly outperformed the swept-compression ramp injectors. Recall that for the swept-compression ramp injectors the mixing efficiency was lower for the reacting case than it was for the non-reacting case. In the experimental tests with the compression ramp, a diffusion flame extended from the injectors along the length of the combustor. In contrast, combustion did not occur in the near field of the swept expansion ramp, allowing the fuel and air to premix before combustion began. Once combustion began in the expansion-ramp model, it occurred rapidly because of the premixing that had occurred between the fuel and airstream.

Chapter 6

Summary and Conclusions

A combined experimental and computational study of two different swept-ramp injector configurations was conducted. The objectives of the study were to determine the effect of mixing augmentation, resulting from the streamwise vortices generated by injector ramps, on scramjet engine operation characteristics, combustion, and heat transfer. In the experiments, hydrogen was injected from the base of swept compression and swept expansion ramps at a Mach number of 1.7. The direct-connect tests simulating flight at approximately Mach 6.6 had the following inflow conditions: M = 2.63, T_T = 1940 K, and P = 1 atm.

The experimental effort included combustor wall pressure and heat flux measurements for the two injector configurations. Measurements of the heat flux were made by both cooled Gardon gages and surface thermocouples. A unique side-view laser light sheet technique was developed and used to obtain qualitative images of the combustion products at selected planes in the closed combustor downstream of the swept compression ramp injectors. In addition, a miniature refractory probe was developed to determine the pitot pressure at the exit of the combustor.

Three-dimensional computations were made for mixing and reacting cases of the swept-compression ramp injector using the SPARK computer code. The flow field calculations were compared to the experimentally determined values of wall pressure, heat flux, pitot pressure, and Mie scattering flow visualization.

The following conclusions can be drawn as a result of the investigation:

1. The experimental tests demonstrated combustor performance with parallel injection comparable to that reported using normal injection. This unusually rapid parallel jet mixing and combustion was obtained using swept-compression ramp injectors with near-parallel injection. Although the calculated mixing efficiency for the non-reacting flow was greater for the swept-compression ramp injector design than for the swept-expansion ramp

injector, combustor performance was even better for the expansion ramp injectors. Once combustion began in the expansion-ramp model, it occurred rapidly because of the additional premixing that had occurred between the fuel and airstream. With this configuration, most of the combustion occurred within six gap lengths downstream of the injectors. This rapid heat release demonstrated that for the test conditions used in this study the combustor could be shortened by forcing the fuel and air to premix before ignition.

2. The flowfield structure was altered significantly by the effects of the combustion heat release. The detrimental effect of combustion on the mixing and resultant effects on the performance was demonstrated by the numerical calculations performed for the swept compression ramp injectors at the test conditions used in this study. The heat release associated with combustion was shown to reduce the longitudinal vorticity. Further evidence for the decrease in mixing with combustion was shown by comparing the combustor performance, which was determined experimentally by pressure integrals, for the two injector configurations.

3. The experiments and calculations showed that the injectors were effective in promoting lateral spreading of the fuel jets. The incomplete penetration of the fuel jets in the direction normal to the walls was a major limiting factor in the amount of mixing that could occur for both configurations. In addition the proximity of the burning shear layer to the injector wall led to increased heat transfer on the injector wall.

4. The reacting flow field downstream of the two types of swept ramp injectors led to large heat fluxes. However, the effect of the flow structure on the heat flux was not principally through a large increase in the film coefficient caused by the vortical flow. It was instead due to the proximity of the reacting fuel jet to the wall, which led to high adiabatic wall temperatures near the wall.

In addition to the conclusions, the following observations were made as a result of the investigation:

1. Auto-ignition occurred during tests of the swept-compression ramp combustor. Auto-ignition did not occur during tests of the swept expansion

injector configurations. Thus, a silane/hydrogen pilot was necessary to initiate combustion.

2. The ramps were effective isolators in that combustion occurred downstream of the injectors with little upstream propagation of the pressure rise due to combustion.

3. Pressure distributions and calculated combustion efficiencies showed that the fuel began to react immediately downstream of the swept-compression ramp injectors and a diffusion flame occurred along the combustor length. In contrast, for the swept expansion ramp combustor, pressure distributions and calculated combustion efficiencies showed that the fuel did not begin to react for a distance of at least two gap lengths downstream of the injectors. The length of this ignition delay region decreased as ϕ increased.

4. The calculated combustion efficiency did not increase for $\phi > 1$ for either injector configuration, suggesting that the mixing was limited by the penetration of the fuel across the combustor. Mie-scattered images obtained for the swept-compression ramp configuration confirmed that incomplete fuel penetration occurred.

5. Combustor pressure integrals for the combustor duct were approximately the same for both injector configurations, while the nozzle pressure integral was greater for the swept expansion ramp injector because of the larger combustor exit pressure. The difference in the nozzle pressure integral was responsible for the better performance of the swept expansion ramp injector.

6. Severe heat fluxes (up to 9 MW/m^2) were measured along the injector wall of both combustors. In contrast, the heat flux was much less on the opposite wall.

7. The highest heat transfer in the swept compression ramp occurred downstream of the region of maximum pressure at the same location (x/G=2.6) for all equivalence ratios.

8. The location of the maximum measured heat transfer in the expansion ramp combustor was further downstream ($3.4 \leq x/G \leq 4.34$) and followed the movement of the flame front as the equivalence ratio varied. In addition, the

maximum heat transfer in the expansion ramp combustor occurred close to the maximum pressure.

9. Large differences were observed between the flow structure in the turbulent and laminar mixing calculations. In the laminar mixing case, complete transverse penetration of the fuel jet occurred by x/G = 6. In contrast, penetration was much less for the turbulent case, but the lateral spreading was much greater. Since complete transverse penetration did not occur in the experimental reacting case, laminar calculations were thought to be inadequate.

10. The calculated mixing and combustion efficiencies were within 5 % for the reacting flow. Thus, combustion was mixing limited.

11. Comparison with the measured and calculated pressures in the near field of the injectors showed that the calculations had under-predicted the measured pressures. Agreement between the experimental and calculated pressures was good in the far field.

12. Comparison of the calculated water product mass fraction and the Mie scattering showed that the prediction of the fuel penetration was good.

13. The calculated and experimental pitot pressures were within 15 % of each other.

14. The heat flux was severely under predicted by the calculations in the first section of the combustor due to inadequate grid resolution. In the second section of the combustor, where the grid resolution was better, the calculated heat fluxes were closer to the measured heat fluxes. Agreement was best along the opposite wall of the combustor. On the injector side, the calculations predicted that the heat flux was higher at the interstice centerline than it was at the injector centerline. However, in the region downstream of x/G = 7, large differences were not seen between the heat flux at the interstice and injector centerlines in the experimental measurements.

Chapter 7
Recommendations

This chapter is divided into two sections. The first section consists of recommendations for further experimental studies. The second section consists of recommendations for improvements in the experimental and computational procedures used in the research.

7.1 Recommendations for Future Studies

The results of the present study show that while the injectors are effective in promoting combustion, performance can be improved. Suggestions for further improvements are presented in the following section.

The results of this study show that the failure of the fuel jet to lift off the wall and penetrate completely across the flow was a major limiting factor for the mixing. In addition to reduced mixing rates, the proximity of the burning shear layer to the injector wall increased the wall heat transfer on the injector wall. Future work should focus on increasing the transverse penetration of the fuel. One approach suggested by cold flow studies is the use of non-axisymetric fuel injector nozzles. In particular, a tapered-slot nozzle with a horizontal throat showed increased penetration in cold-flow tests[140]. Another option suggested by a study with unswept ramp injectors[65] is to use normal or angled wall injectors downstream of the ramp injectors to increase the longitudinal vorticity. It is also thought that further improvements are possible through ramp geometry modifications (height, ramp, angle, sweep angle, and spacing). However, the losses for a given injection scheme need to be carefully considered.

The effect of combustion has been shown computationally in this dissertation to reduce the mixing efficiency in the ramp injectors considered in this study. It is thought that the required combustor length could be shortened considerably by controlling where combustion occurs in a configuration with an ignition delay. Therefore, it is suggested that the degree of mixing which occurs before combustion should be studied in the swept-expansion ramp combustor. By controlling where combustion is

initiated along the combustor (possibly by a plasma torch or shock-induced combustion), the amount of mixing which occurs upstream of the flame front can be varied. Thus, the tradeoff between the degree of premixing required to produce rapid combustion and the added length of combustor required to premix the fuel and air could be studied.

Little is known about the effects of combustion on slot film and transpiration cooling. Since it is thought that the adverse pressure gradients associated with heat release may destroy the film, slot film cooling should be first attempted in regions with a favorable pressure gradient. Since the maximum heat fluxes for the swept compression ramp do occur in a favorable pressure gradient, it is recommended that slot film cooling should be explored first in the swept compression ramp combustor, and compared with transpiration cooling. For the expansion ramp it is recommended that transpiration film cooling should be studied, because the location of heat release was a strong function of ϕ, and the maximum heat transfer occurred in an adverse pressure gradient, which could have adverse effects on the integrity of the film from a slot injector.

7.2 Recommendations For Improvements of Experimental and Computational Techniques

Although the Gardon gages used in this study produced a direct measurement of the heat flux, interpretation of the gage output was not always straight forward as evidenced by the discussion in Appendix C. For low conductivity materials, such as steel, the heat flux can be calculated from the transient wall temperature history, provided that accurate measurements of the wall temperature are made. Unfortunately, the surface thermocouples used for this investigation often failed. The rate of thermocouple failure was much greater in the hot, low conductivity section of the combustor. It is recommended that more reliable methods of wall temperature measurement be explored. Suggested methods include better surface thermocouples with insulation designed for use at higher surface temperatures. Other surface temperature measurement techniques such as fluorescence, and infrared imaging offer the promise of planar measurement, but require further development of optical access. In particular, optical access for infrared

surface temperature measurements is difficult because hygroscopic infrared window materials are incompatible with the humid combustor environment. Another alternative is the high frequency heat flux microsensor developed by VATELL.[80]

The side view Mie scattering technique developed for this research was successful in obtaining qualitative images of the water product. However there is room for improvement in the technique. It is recommended that a linear reticon camera be added to the bottom of the combustor to normalize the images for the variation of the incident light intensity. Another improvement would be the replacement of the camera scanner, mirror, and CCD camera by a single linear reticon camera. This would allow faster scanning which would result in more images for a given test time, and would also eliminate the vertical striations in the raw images. Further improvements in the understanding of the silica particle size distribution are needed for quantitative interpretation of the Mie scattering results. However, the effort required to obtain the information on the silica particles can be greater than that required to apply quantitative spectroscopic techniques (degenerate four wave mixing, CARS, PLIF, absorption, and emission measurements, ect.) to the flow field instead. In general the information obtained by spectroscopic techniques would be of greater value but were not attempted because of the optical access requirements.

The refractory pitot probe developed for this study showed that refractory probes show promise of instream pitot pressure measurements with much smaller probes than those which were used in previous experiments. In addition, the refractory probe did not introduce cooling water into the flowfield. Oxidation is a major limiting factor in the application of refractory probes to continuos testing. It is recommended that probes should be constructed out of refractory materials coated with oxidation resistant coatings for future tests. Possible material combinations are rhenium coated with iridium and Mo-Si_2.

The results from about 40 % of the experimental tests were neglected because the combustor inlet conditions (temperature, pressure, and oxygen fraction) were not close enough to the target conditions. In addition, the

uncertainty analysis, presented in Appendix A, showed that the uncertainty associated with the heater mass flow rates (measured by ASME standard orifices) caused larger uncertainties in the oxygen fraction, total temperature, and equivalence ratio, which were dependent on the mass flows. It is recommended that the orifices be replaced by choked venturis, which have an uncalibrated uncertainty of 1 % with a small total pressure loss (≈10 % of P_T). An additional advantage of the choked venturi is that the differential pressure transducers could be eliminated. Major improvements in the number of "good" tests obtained from the direct connect supersonic combustor test facility would be possible with the addition of automatic controls and fast acting valves to the heater supply lines.

The development of a method to directly measure of the thrust in the direct connect combustor is desirable for two reasons. The first reason is that thrust is a direct measurement of the performance. The second reason is that the difference between the thrust and the pressure integral in a duct section is the integrated skin friction. Initial efforts using strain gages inside the flange bolts to measure the thrust have shown limited success.[102] It is recommended that this technique be extended to include separate measurements on sections of the combustor and nozzle, in order to measure both the thrust and the total skin friction from the sections of the combustor/nozzle.

Computationally, improvement in the grid resolution, and the turbulence model is desirable. Also, a major limitation for the computations was the large amount of computer time that was required for a reacting flow calculation (up to 350 cpu-hr on the CRAY-2 computer). The slow solution convergence can be speeded up by using multigrid algorithms employed in recently developed Navier-Stokes codes.

References

1. Swithenbank, J., Eames, I., Chin, S., Ewan, B., Yang, Z., Cao, J., and Zhao, X., "Turbulent Mixing in Supersonic Combustion Systems,"AIAA 89-0260.
2. Hannun, N. and Berkopec, F., "Fueling the National Aerospace Plane With Slush Hydrogen," AIAA 89-5014.
3. Czysz, P., and Murthy, S.N.B., "Energy Analysis of Propulsion Systems for High Speed Vehicles," AIAA 89-0182.
4. Sabin,C.M., "An Analytical and Experimental Investigation of the Plane, Incompressible, Turbulent Free-Shear Layer with Arbitrary Velocity Ratio and Pressure Gradient," Transactions of the ASME D., Vol. 87, pp. 421-428, 1965.
5. Brown, G. L., and Roshko, A., "On Density Effects and Large Structure in Turbulent Mixing Layers," Journal of Fluid Mechanics, Vol. 64, pp. 775-816, 1974.
6. Bogdanoff, D.W., "Compressibility Effects in Turbulent Shear Layers,"AIAA Journal, Vol. 21, No. 6, pp. 926-927, 1983.
7. Papamoshou, D., and Roshko A. , "The Compressible Turbulent Shear Layer: an Experimental Study, " Journal of Fluid Mechanics, Vol. 197, pp. 453-477, 1988.
8. Papamoshou, .D., "Structure of the Compressible Turbulent Shear Layer," AIAA 89-0126.
9. Gutmark, E., Schadow, K.C., and Wilson, K.J., " Effect of Convective Mach Number on Mixing of Coaxial Circular and Rectangular Jets," Phys. of Fluids, Vol. 3, pp. 29-36, 1991.
10. Fourgette, D. C., Mungal, M. G., and Dibble, R. W., "Time Evolution of the Shear Layer of an Axisymmetic Jet," AIAA Journal, Vol. 29, No. 7, pp. 1123-1130, 1991.
11. Fourgette, D. C., Mungal, M. G.,´Barlow, R. S., and Dibble, R. W., "Concentration Measurements in a Supersonic Shear Layer," AIAA 91-0627.
12. Lau, J. C., Morris, P. J., and Fisher, M. J., "Measurements in Subsonic and Supersonic Free Jets Using a Laser Velocimeter", Journal of Fluid Mechanics, Vol. 93, pp. 1-27, 1979.
13. Papamoshou, .D., "Communication Paths in the Compressible Shear Layer," AIAA-90-0155.
14. Nixon, D., Keefe, L. R., and Kuhn, G. D., "The Effects of Compressibility on a Supersonic Mixing Layer," AIAA-90-0706.

15. Hussani, M. Y., Collier, F. and Bushnell, D. M., "Turbulence Alteration Due to Shock Motion," IUTAM Symposium, Turbulent Shear Layer Interactions, Springer-Verlag, New York,1985.

16. Schetz, J. A., and Billig, F. S., "Penetration of Gaseous Jets Injected Into a Supersonic Stream," Journal of Spacecraft and Rockets, Vol. 3, No. 11, pp. 1658-1665, 1966.

17. Rogers, R. C., "A Study of the Mixing of Hydrogen Injected Normal to a Supersonic Airstream," NASA TN D-6114, 1971.

18. Hyde, C., Smith, B., Schetz, J., and Walker, D., "Turbulence Measurements for Heated Gas Slot Injection in Supersonic Flow," AIAA 89-1868.

19. Walker, D. A., Campbell, R. L., and Schetz, J. A., "Turbulence Measurements for Slot Injection in Supersonic Flow," AIAA-88-0123.

20. Thomas, R. H., Schetz, J. A., and Billig, F. S., "Gaseous Injection in High Speed Flow," Ninth International Syposium On Air Breathing Engines," Athens Greece, 1989.

21. McMurtry, P. A., Riley, J. J., and Metcalfe, R. W., "Effects of Heat Release on the Large Scale Structure in Turbulent Mixing Layers," Journal of Fluid Mechanics, Vol. 199, pp. 297-332, 1989.

22. Hermanson, J. C. , and Dimotakis, P. E., "Effects of Heat Release in a Turbulent, Reacting Shear Layer," Journal of Fluid Mechanics, Vol. 199, pp. 333-375, 1989.

23. Eklund, D. R.,Fletcher, D. G.,Harfield, R. J., McDaniel, J. C., Northam, G. B., Dancey, C. L., and Wang, J. A., "Computational/ Experimental Investigation of Staged Injection into a Mach 2 Flow," AIAA Journal Vol. 31, No. 5, 1994.

24. King, P. S., Thomas, R. H., and Schetz, J.A., "Combined Tangential-Normal Injection into a Supersonic Flow," AIAA 89-0622, 1989.

25. McClinton, C. R.,"The Effect of Injection Angle on the Interaction Between Sonic Secondary Jets and a Supersonic Airstream," NASA TN D-6669, 1972.

26. Mays, R. B., Thomas, R. H., and Schetz, J. A., "Low Angle Injection into a Supersonic Flow," AIAA 89-2461.

27 Fuller, E. J., Mays, R. B., Thomas, R. H., and Schetz, J. A., "Mixing Studies of Helium in Air at Mach 6," AIAA-91-2268.

28. Cox, S. K., Fuller, R. P., Schetz, J. A., Walters, R. W., "Vortical Interactions Generated by an Injector Array to Enhance Mixing in Supersonic Flow," AIAA 94-0708.

29. Gutmark, E., Schadow, K.C., Wilson, K. J., "Noncircular Jet Dynamics in Supersonic Combustion," Journal of Propulsion and Power, Vol. 5, No 5., pp. 529-533, pp. 240-249, 1989.

30. Gutmark, E., Schadow, K.C., Wilson, K. J., "Subsonic and Supersonic Combustion Using Noncircular Injectors," Journal of Propulsion and Power, Vol. 7, No. 2, pp. 240-249, 1991.

31. Gutmark, E., Bowman, H. L., and Schadow, K. C. " Flow and Acoustic Features of a Supersonic Tapered Nozzle," Experiments in Fluids ,Vol. 13, pp. 49-55, 1992.

32. Samimy, M., Reeder, M., and Zaman, K., " Supersonic Jet Mixing Enhancement by Vortex Generations," AIAA 91-2263.

33. Zaman, K. B. M. Q., "Effect of 'Delta Tabs' on Mixing and Axis Switching in Jets From Asymmetric Nozzles," AIAA 94-0186.

34. Yu, K., Kraeutle, K., Wilson, K., Parr, T., Smith, R., Gutmark, E., and Shadow, K., "Supersonic Flow Mixing and Combustion Using Ramp Nozzle," AIAA 92-3840.

35. King, C. J., Krothapalli, A., and Strykowski, P. J., " Streamwise Vorticity Generation in Supersonic Jets with Minimal Thrust Loss," AIAA 94-0661.

36. Cutler, A. D., and Levey, B. S., " Vortex Breakdown in a Supersonic Jet, " AIAA-91-1815.

37. Levy , B. S., " An Experimental Investigation of a Supersonic Vortical Flow, " M.S. Thesis, School of Engineering and Applied Science, George Washington University, 1991.

38. Kraus, D. K., "An Experimental Investigation of Mixing Enhancement in a Simulated Scramjet Combustor By Use of Swirling Jets," M.S. Thesis George Washingon University, 1993.

39. Kraus, D. K. and Cutler, A. D., "Mixing Enhancement by Use of Swirling Jets," AIAA-93-3126.

40. Cutler, A. D., Levey, B. S., and Kraus, D. K., "An Experimental Investigation of Supersonic Swirling Jets," AIAA 93-2922.

41. Metwally, O. M., Settles, G. S., and Horstman, C. C., "An Experimental Study of Shock Wave/Vortex Interaction," AIAA Paper 89-0082.

42. Kumar, A., Bushnel, D. M., Hussaini, M. Y., " Mixing Augmentation Technique for Hypervelocity Scramjets", Journal of Propulsion and Power, Vol. 5, No. 5, 1989.

43. Wood, C., and Schetz, J., "Effects of Unsteady Shock Impingement On High-Speed Gaseous Mixing," AIAA 91-5091.

44. Yang, J., Kubota, T., and Zukoski, E. E., "An Analytical and Computational Investigation of Shock-induced Vortical Flows," AIAA 92-0316.

45. Marble, F. E., Hendricks, G. J., and Zukoski, E. E., "Progress Toward Shock Enhancement of Supersonic Combustion Processes," AIAA 87-1880.

46. Waitz, I.A., Marble, F. E., Zukoski, E. E., "A Systematic Experimental and Computational Investigation of a Class of Contoured Wall Fuel Injectors," AIAA 92-0625.

47. Waitz, I.A., Marble, F. E., Zukoski, E. E., "Vorticity Generation by Contoured Wall Injectors," AIAA 92-3550.

48. Northam, G. B., Greenberg, I., and Byington, C.S., "Evaluation of Parallel Injector Configurations for Supersonic Combustion," AIAA 89-2525.

49. Capriotti, D.P., Northam, G. B., Greenberg, I., and Byington, C. S., "Evaluation of Parallel Injector Configurations for Mach 3 Combustor Conditions," 26th JANNAF Combustion Meeting, 1989.

50. Northam, G. B., Capriotti, D.P., Byington, C. S., and Greenberg, I., "Evaluation of Parallel Injector Configurations For Mach 2 and Mach 3 Combustor Inlet Conditions," 8th National Aerospace Plane Technology Symposium,"Monterey, Calif., 1990.

51. Northam, G. B., Capriotti, D.P., Byington, C. S., and Greenberg, I., "Mach 2 and Mach 3 Mixing and Combustion in Scramjets," AIAA 91-2394.

52. Northam, G. B., Greenberg, I., Byington, C.S., and Capriotti "Evaluation of Parallel Injector Configurations for Mach 2 Combustion," Journal of Propulsion and Power, Vol. 8, No. 2, 1992

53. Drummond, J. P., Carpenter, M. H., Riggins, D. W., Adams, M. S., "Mixing Enhancement in a Supersonic Combustor," AIAA 89-2794.

54. Riggins, D. W., Mekkes, G. L., McClinton, C. R., and Drummond, J. P., "A Numerical Study of Mixing Enhancement in a Supersonic Combustor," AIAA 90-0203.

55. Drummond, J. P., "Mixing Enhancement of Reacting Parallel Fuel Jets in a Supersonic Combustor," AIAA 91-1914.

56. Riggins, D. W. and McClinton, C. R., "A Computational Investigation of Flow Losses in a Supersonic Combustor," AIAA 90-2093.

57. Riggins, D. W., McClinton, C. R., "Analysis of Losses in Supersonic Mixing and Reacting Flows," AIAA 91-2266.

58. Moon, Y., "Numerical Study of Supersonic Combustors by Multi-Block Grids With Mismatched Interfaces," AIAA 90-5204.

59. Hartfield, R. J., Hollo, S. D., and McDaniel, J. C., "Experimental Investigation of a Supersonic Swept Ramp Injector Using Laser Induced Iodine Fluorescence," AIAA 90-1518.

60. Donohue, J. M., Haj-Hariri, H. and McDaniel, J. C., "Vorticity Generation Mechanisms in Parallel Injection Schemes For Supersonic Mixing," AIAA 92-3286.

61. Donohue, J. M., McDaniel, J. C., and Haj-Hariri, H., "Experimental and Numerical Study of Swept Ramp Injection into a Supersonic Flowfield," AIAA 93-2445.

62. Davis, D. O. and Hingst, W. R., "Progress Toward Synergistic Hypermixing Nozzles," AIAA 91-2264.

63. Davis, D. L. ," Numerical Analysis of Techniques For Efficient Generation of Vorticity in Supersonic Flows, " AIAA 92-0828, 1992.

64. Hamovich, Y., Gartenberg, E., Roberts, A. S., and Northam, G. B., "An Investigation of Wall Injectors for Supersonic Mixing Enhancement,"AIAA-94-2940.

65. Stouffer, S. D., Vandsburger, U., and Northam, G. B., "Comparison of Wall Mixing Concepts For Scramjet Combustors," AIAA 94-0587.

66. McClinton, C. R., "Interaction Between Step Fuel Injectors On Opposite Walls in a Supersonic Combustor Model", NASA TP 1174, 1978.

67. Rogers, R. C., "Effects of Fuel Temperature on Supersonic Mixing and Combustion of Hydrogen," AIAA 77-17, 1977.

68. Billig, F. S., and Grenleski, S. E., "Heat Transfer In Supersonic Combustion Processes," 4th international Heat Transfer Conference, Versailles France, 1970.

69. Guy, R. W., Mackley, E. A., "Initial Wind Tunnel Tests at Mach 4 and 7 of a Hydrogen-Burning, Airframe Integrated Scramjet," 4th ISABE Meeting, Lake Buena Vista Florida, 1979.

70. Diskin, G. S., Jachimowski, C. J., Northam, G. B., and Bell, R. A., "Mach 2 Combustion Characteristics of Hydrogen /Hydrocarbon Fuel Mixtures," 24th Jannaf Combustion Meeting, 1987.

71. Morgan, R. C., and Stalker, R. J. "Shock Tunnel Measurements of Heat Transfer in a Model Scramjet," Journal of Spacecraft and Rockets, Vol. 23, No. 5, pp. 470-475, 1986.

72. Baker, N. R, Northam, G. B., Stouffer, S. D., and Capriotti, D. P., "Evaluation of Scramjet Nozzle Configurations and Film Cooling for Reduction of Wall Heating," AIAA-93-0744.

73. Olsen, G. C, Nowak, R. J., Holdin, M. S., and Baker, N. R., "Experimental Results for Film Cooling in 2-D Supersonic Flow Including Coolant Delivery Pressure, Geometry, and Incident Shock Effects," AIAA Paper 90-0605.

74 Byington, C.S., Northam, G.B., and Capriotti, D.P., "Transpiration Cooling in the Locality of a Transverse Fuel Jet for Supersonic Combustors," AIAA 90-2341.

75. General Applied Sciences Laboratories, "Engineering Analysis and Design Calculations of The NASA-Langley Research Center Hydrogen-Air Vitiated Heater with Oxygen Replenishment," NASA CR-132381, 1968.

76. Kidd, C. T., "Recent Developments in High Heat-Flux Measurement Techniques at the AEDC," ISA Paper #90-156, 1990.

77. Merski, N. R., "A Relative-Intensity Two-Color Phosphor Thermography System," NASA TM-104123, 1991.

78. Chin, J. H., "Effect of Uncertainties in Thermocouple Location on Computing Surface Heat Fluxes," ARS Journal, pp. 273-274, February, 1962.

79. Wiese, K.L., Bonne, M.A., Friedmann, F.A., and Assanis, D.N.: "Combustion and Heat Transfer Studies in a Direct-Injection Diesel Engine," SAE Paper 891902, September, 1989.

80. Hager, J. M., Langley, L. W., Onishi, S., and Diller, T. E., " High Temperature Heat Flux Measurements," AIAA 91-0165.

81. Gardon, R., "An Instrument for the Direct Measurement of Intense Thermal Radiation", The Review of Scientific Instruments, Vol. 24, No. 5, pp. 366-370, 1953.

82. Gardon, R., "A Transducer for the Measurement of Heat-Flow Rate," ASME Journal of Heat Transfer, Vol. 82, pp. 396-398, 1960.

83. Roeser, W. F., and Dahl, A. I. , " Reference Tables for Iron-Constantan And Copper-Constantan Thermocouples," Journal of Research of the National Bureau of Standards, Vol. 20, pp. 337-355, 1938.

84. Goldsmith, Alexander, "Handbook of Thermophysical Properties of Solid Materials," MacMillan Co. N.Y., 1961.

85. Carroll, John, M., "The Thermal Conductivity of Thermocouple Grade Constantan Rod," NASA-CR-56932, 1964.

86. Mie, G. , Ann. Physik, Vol. 25, p 377, 1908.

87. van de Hulst, H. C., "Light Scattering by Small Particles," Dover Publications, New York, 1981.

88. McGregor, I., "The Vapor Screen Method of Flow Visualization," Journal of Fluid Mechanics, Vol. 11, No 4, pp. 481-511, 1961.

89. Clemens, N.T., Mungal, M. G., Berger, T. E., and Vandsburger, U., "Visualizations of the Structure of the Turbulent Mixing Layer Under Compressible Conditions," AIAA-90-0500.

90. Messersmith, N. L., Dutton, J. C., and Krier, H., "Experimental Investigation of Large Scale Compressible Mixing Layers," AIAA Paper-91-2444.

91. Cattafesta III, L. N., and Settles, G. S., "Experiments on Shock/Vortex Interaction," AIAA-92-0315, 1992.

92. Wey, C. C. , Ghorashi, B., Marek, C. J., and Wey, C., "An Imaging System for PLIF/Mie Measurements for a Combusting Flow," 6th International Symposium on Heat and Mass Transfer, Miami, Florida, 1990.

93. Smith, M. W., and Northam, G. B., "Instantaneous Planar Visualization of Reacting Supersonic Flows Using Silane Seeding,"AIAA 91-1690.

94. Zachariah, M. R., Chin, D., and Semerjian, H. G., "Silica Particle Synthesis in a Counterflow Diffusion Flame Reactor," 22nd International Symposium on Combustion, Seattle, WA, 1988.

95. Precision Visuals, Inc, "PV-WAVE Command Language Reference Manual", Precision Visuals Inc., 1992.

96. Rogers, R.C, Weidner, E.H., and Bittner, R.D., "Quantification of Scramjet Mixing in the Hypervelocity Flow of a Scramjet," AIAA-94-2518, 1994.

97. Lagen, N. T., and Seiner, J. M., "Evaluation of Water Cooled Supersonic Temperature and Pressure Probes For Application to 2000 F Flows, " NASA Technical Memorandum, 102612, 1990.

98. Ivanov, V. Y., Nechiporenko, Y. P., Yefimenko, L., N., Yurchenko, M.I. "High Temperature Oxidation Protection of Tungsten," NASA TT F-583, 1969.

99. Harding, J. T., Kazaroff, J. M., Appel, M. A., "Iridium-Coated Rhenium Thrusters by CVD," NASA TM 101309, 1988.

100. Anderson, G. Y., and Gooderum P. B., "Exploratory Tests of Two Strut Fuel Injectors for Supersonic Combustion," NASA TN D-7581, 1974.

101. van Driest, E. R, "The Problem of Aerodynamic Heating," Aeronautical Engineering Review, Oct. 1956.

102. Calayag, B.R., "The Measurement of Thrust Produced by a Scramjet in a Direct-Connect Research Facility," MS Thesis, George Washington University, 1994.

103. DeTurris, D.J., Schetz, J. A., and Hellbaum, R.F., "Direct Measurements of Skin Friction in a Scramjet Combustor," AIAA 90-2342.

104. Fiueira da Silva, L. F., Deshaies, B., and Champion, M., "Numerical Study of Ignition Within Hydrogen-Air Supersonic Boundary Layers, " AIAA Journal Vol. 31, No. 5, pp. 884-890.

105. Bellet, J. C., Donzier, H. P., Soustre, J., and Manson, N., "Influence of Aerodynamic Field of Hydrogen and Ethylene in Supersonic Flow," 12th International Combustion Symposium, 1970, pp. 595-602.

106. Rubins, P. M., and Rhodes, R. P., "Shock Induced Combustion with Oblique Shocks: Comparison of Experiment and Kinetic Calculations,"AIAA Journal, Vol. 1, No. 12, 1963.

107. Eklund, D. R.; Stouffer, S. D., "A Numerical and Experimental Study of a Supersonic Combustor Employing Swept Ramp Fuel Injectors," AIAA 94-2819.

108. Drummond, J. P., and Hussaini, M. Y., "A Detailed Numerical Model of a Supersonic Mixing Layer," AIAA 86-1427, 1986.

109. Drummond, J. P., "A Two-Dimensional Numerical Simulation of a Supersonic, Chemically Reacting Mixing Layer," NASA TM-4055, 1988.

110. Drummond, J. P., "Numerical Simulation of a Supersonic Reacting Mixing Layer," AIAA 87-1325.

111. Carpenter, M. H., "Three-Dimensional Computations of Cross-Flow Injection and Combustion in a Supersonic Flow," AIAA 89-1870.

112. Baldwin, B. S., and Lomax, H. "Thin Layer Approximation and Algebraic Model for Separated Turbulent Flows," AIAA 78-257, 1978.

113. Eggers, J. M., "Turbulent Mixing of Coaxial Compressible Hydrogen-Air Jets," NASA TN D-6487, 1971.

114. Eklund, D. R., Northam, G. B., and Fletcher, D. G., "A Validation Study of the SPARK Navier-Stokes Code for Nonreacting Scramjet Combustor Flowfields," AIAA 90-2360, 1990.

115. Jachimowski, C. J.," An Analytical Study of the Hydrogen-Air Reaction with Application to Scramjet Combustion," NASA Technical Paper 2791, 1988.

116. Jachimowski, C. J., "An Analysis of Combustion Studies in Shock Expansion Tunnels and Reflected Shock Tunnels, " NASA TP 3224, 1992.

117. Eklund, D. R., Personal Communication, NASA Langley Research Center, August 1994.

118. Kline, S. J., and McClintock, "Describing Uncertainties in Single Sample Experiments", Mechanical Engineering Vol 75, No. 1, pp 3-8, 1953.

119. ASME Research Committee on Fluid Meters, " Flowmeter Computation Handbook", ASME, 1971.

120. Andrews, E.H., Torrence, M.G., Anderson, G.Y., Northam, G. B., and Mackley, E.A., "Langley Mach 4 Scramjet Test Facility", NASA TM 86277, 1985.

121. Vidal, R.J., "A Resistance Thermometer for Transient Surface Temperature Measurements," ARS Meeting, Buffalo, N.Y., Sept., 1956.

122. Cook, W.J., and Felderman, E.J., "Reduction of Data from Thin-Film Heat Transfer Gages: A Concise Numerical Technique", AIAA Journal, Vol. 4, No. 3, 1966.

123. Kidd, C. T. "Coaxial Surface Thermocouples: Analytical and Experimental Considerations for Aerothermal Heat-Flux Measurement Applications", ISA Paper # 90-126, 1990.

124. Patankar, S.V., "Numerical Heat Transfer and Fluid Flow," Hemisphere, Washington D.C., 1980.

125. Kirchoff, G., "Vorlesungen uber die Theorie der Warme" , Barth, Leipzig, 1894.

126 Ozisik, M. N., "Heat Conduction", Wiley, New York 1979.

127. Borell, G. J., and Diller, T. E., " A Convection Calibration Method for Local Heat Flux Gages, " ASME Journal of Heat Transfer, Vol. 109, pp 83-89, 1987.

128. Brookley, C. E., " The Circular Foil Heat Flux Gage," Thermogage, Inc., Frostburg, Md. 21532

129. Brookley, C. E., " A Method For the Rapid Calibration of Circular foil Calorimeters to 500 BTU/ft^{2}s," Thermogage, Inc. Frostburg, Md.

130. Clayton, W. A., "High Temperature Circular Foil Heat Flux Gage," Hy-Cal Engineering Report, TR-417, Hy-Cal Engineering El Monte, Ca., 1981.

131. Rubesin, M. W., "The Effect of an Arbitrary Surface-Temperature Variation Along a Flat Plate on the Convective Heat Transfer in an Incompressible Boundary Layer," NACA Technical Note 2345, 1951.

132. Westkaemper, J. C., "On the Error in Plug-Type Calorimeters Caused by Surface Temperature Mismatch," Journal of the Aeronautical Sciences," Vol. 28., pp. 907-908, 1961.

133. Conti, Raul, "Heat Transfer Measurements at a Mach Number of 2 in the Turbulent Boundary layer on a Flat Plate Having a Stepwise Temperature Distribution," NASA Technical Note D-159, 1959.

134. Woodruff, L.W., Hearne, L.,F., and Keliher, T.J., "Interpretation of Asymptotic Calorimeter Measurements," AIAA Journal, Vol. 5, No. 4, pp. 795-797, 1967.

135. Praharaj, S.C., and Foster, L.D., "Orbital Flight Test Shuttle External Tank Flowfield and Aerothermal Analysis," AIAA-84-1750.

136. Neuman, R.D., Erbland, P.J. and Kretz, L.O., "Instrumentation of Hypersonic Structures: A Review of Past Applications and Needs of the Future," AIAA 88-2612.

137. Paik, S. W., "Simultaneous Direct Measurements of Skin Friction and Heat Flux in a Supersonic Flow," Ph. D. Dissertation, VPI &SU, 1993.

138. Blevins R. D., "Fluid Dynamics Handbook," Van Nostrand Reinhold Company, New York 1984.

139. Rosenow, W.M., Hartnett, J.P., and Ganic, E. N., "Handbook of Heat Transfer Fundamentals, " McGraw-Hill New York, 1985.

140. Northam, G. B., Stouffer, S. D., Haimovich, Y., Eklund, D. R.: "Comparison of Mixing Concepts for Scramjet Combustors," XII ISABE, Meeting, Melbourne Australia, September, 1995.

141. Anderson, D. A., Tannehill, J. C., and Pletcher, R. H., "Computational Fluid Mechanics and Heat Transfer," McGraw-Hill, New York, 1984

142. White, J. A., "Elliptic Grid Generation With Orthogonality and Spacing Control on an Arbitrary Number of Boundaries," AIAA-90-1568.

143. Northam, G. B., and Anderson, G. Y., " Supersonic Combustion Research at Langley," AIAA 86-0159.

144. Rogers, R. C., "Influence of Fuel Temperature on Supersonic Mixing and Combustion of Hydrogen," AIAA 77-0017.

Appendix A

Uncertainty Analysis For The Facility and Combustor Wall Measurements

A.1 Introduction

The uncertainty analysis of the facility conditions and the heat flux measurements is presented in this section. The method of Kline and McClintock[118] was used to express the desired uncertainty in terms of the individual measured uncertainties. In this method, if the measurement of a variable, x, is dependent on the measurement of independent variables, $x_1, x_2, \ldots, x_n$, which have uncertainties ($w_1, w_2, \ldots, w_n$) specified to the same confidence, then the total uncertainty, w_x, given with the same confidence can be expressed as follows:

$$w_x = \left[\left(\frac{\partial X}{\partial x_1} w_1 \right)^2 + \left(\frac{\partial X}{\partial x_2} w_2 \right)^2 + \cdots + \left(\frac{\partial X}{\partial x_n} w_n \right)^2 \right]^{1/2} \qquad \text{(A-1)}$$

For the uncertainty analysis presented here the confidence interval was chosen as two standard deviations.

Because all measurements (facility and data) were made with a computer based data acquisition system, the uncertainty associated with the data acquisition system are discussed first. Then the uncertainty of the tunnel conditions (total temperature, total pressure, oxygen content) will be discussed, followed by a discussion of the uncertainty in the combustor wall temperature and pressure measurements and the pitot pressure measurements. The uncertainty in the heat flux measurements is discussed in detail in Appendix C.

A.2 Uncertainty in the Data Acquisition System

A modified Neff 620200 data acquisition system was used during the experiments. The specifications for this modified system are given below:

Resolution = 14 bits (13 bits + 1 sign bit)

Full scale data ranges (FS) = $\pm$ 4, 8,16,32,64, or 128 mV
(software selectable on each channel)

Static accuracy = 0.02% FS $\pm$ 2μV
Gain Stability = 0.002 % FS/ °C
Zero Stability = $\pm$ 1 μV/ °C
Total Noise = $[((N_1A)^2 + (N_2)^2)^{1/2}] / A$

Where N_1 = 1 μV
N_2 = 2500 μV
A = 10.24 V/ FS

The data system underwent an auto-calibration each time it was turned on. The data system was kept in the air conditioned environment of the test cell control room, so that the maximum variation in its temperature was limited to ± 5 K. Therefore, the components of the uncertainty, expressed as a percent of full scale, caused by the above effects can be calculated as follows:

Resolution uncertainty = w_r = 1/ (2^{+13}) x 100 % = 0.012 %
Gain stability = w_{gs} = 0.002 % FS/ °C x 5 °C = 0.01 %
Zero stability = w_{zs} = (0.5 μV/ °C x 5 °C / FS) x 100 % = (5μV / FS) x 100 %
Static accuracy = w_{sa} = 0.02 % + (2 μV/ FS) x 100 %
Noise = w_n = (noise/ FS) x 100 %

The components of the uncertainty were calculated and are tabulated in Table A.1 along with the total normalized uncertainty of the data system, w_{ds}, which was calculated from the following equation:

$$w_{ds} = [w_r^2 + w_{gs}^2 + w_{zs}^2 + w_{sa}^2 + w_n^2]^{1/2} \qquad (A\text{-}2)$$

Table A.1 Components of the Data System Uncertainty.

Range mV	w_r % FS	w_{gs} % FS	w_{zs} % FS	w_{sa} % FS	w_n % FS	w_{ds} %FS
4	0.012	0.01	0.025	0.070	0.035	0.08
8	0.012	0.01	0.013	0.045	0.027	0.06
16	0.012	0.01	0.006	0.033	0.025	0.04
32	0.012	0.01	0.003	0.026	0.024	0.04
64	0.012	0.01	0.002	0.023	0.024	0.04
128	0.012	0.01	0.001	0.022	0.024	0.04

A.3 Facility Conditions

The purpose of this section is twofold. First, to provide an uncertainty analysis of the facility parameters relevant to the investigation. Also, because no uncertainty analysis has been published for this facility in the past, the second purpose of this section is to present the detailed methodology of the uncertainty analysis as a tool for future investigations. For convenience the final results of the uncertainty analysis is summarized at the end of this section in Table A.6. Because the other facility parameters are dependent on the mass flow rates, the uncertainty in the mass flow rates is calculated first.

A.3.1 Uncertainty in the Mass Flow Rates

All of the flow rates were measured by ASME-standard flange tap orifices. The pressure drop across the orifices was small enough that the mass flow rates can be calculated by equation A-3 from reference 119.

$$\dot{m} = D^2 I \sqrt{\rho \Delta P} = \frac{D^2 I}{\sqrt{R}} \sqrt{\frac{P \Delta P}{T}} \qquad (A\text{-}3)$$

Where ρ = Density of the gas upstream of the orifice

P = Pressure upstream of orifice

D = Actual inside pipe diameter

d = Orifice diameter

I = Principal meter constant = f(d/D,D)

ΔP = Pressure drop across the orifice

R = Ideal gas constant

The percentage uncertainty of the flow rates for each gas can be calculated from the following equation:

$$\frac{w_{\dot{m}}}{\dot{m}} = \left[\left(\frac{w_I}{I} \right)^2 + \left(\frac{2 w_D}{D} \right)^2 + \left(\frac{w_P}{2P} \right)^2 + \left(\frac{w_{\Delta P}}{2 \Delta P} \right)^2 + \left(\frac{w_T}{2T} \right)^2 \right]^{1/2} \qquad (A\text{-}4)$$

In order to evaluate the uncertainty in the mass flow measurements, the individual component uncertainties are calculated for each gas in the sections below.

A.3.1.1 Orifice Uncertainty

As shown in equation A-4, there are two contributions to the total uncertainty of the mass flow that depend on the geometry of the orifice/pipe installation; uncertainty in the meter constant, I, and uncertainty in the inside pipe diameter, D. The meter constant, I, which is tabulated in reference 119, is a function of D, and β (β = d/D). The uncertainty of I is listed in reference 119 for known orifice/pipe diameters. Since I changes with the ratio β, and there is uncertainty in β, the uncertainty of I was calculated from the following equation:

$$w_I = \left[w_{IT}^2 + \left(\frac{\partial I}{\partial \beta} \right)^2 w_\beta^2 \right]^{1/2} \qquad \text{(A-5)}$$

Where: w_{IT} = value of uncertainty of I given in reference 119.

w_B = uncertainty in the ratio β = d/D.

The orifice diameters were all measured to within ± 0.13 mm. Seamless carbon steel pipe was used for the heater gas flows. The uncertainty of the inside pipe diameters was assumed to be ± 0.76 mm. The calculated percentage uncertainties are given in Table A.2 shown below. Also tabulated is the percentage uncertainty in I which was calculated by the methods outlined in reference 119.

Table A.2 Orifice Diameters and Resultant Uncertainties.

Gas	D (mm)	d (mm)	I	w_D %	w_I %
Air	102.3	41.2	35.419	0.075	1.8
H_2	52.5	13.1	13.440	1.45	3.4
O_2	77.9	20.8	15.3581	0.98	2.5
H_2 (Fuel)	40.9	14.8	28.513	1.9	3.7

A.3.1.2 Inlet Gas Temperatures

The inlet gas temperatures for the heater and fuel systems were all measured with standard type T thermocouples mounted upstream of the orifice plate. The uncertainties were due to the assumed uncertainty for type T thermocouples and the uncertainties in the data system. The uncertainty

for the measurement of a typical inlet condition of 300 K is calculated in the following equation:

$$w_T = \left[\left(\frac{\partial T}{\partial V} w_{ds} \right)^2 + w_{tc}^2 \right]^{1/2} \qquad (A\text{-}5)$$

Uncertainty in the data system (8 mV Range) = $w_{ds} = \pm 0.0048$ mV
Thermocouple uncertainty = $w_{tc} = \pm 1.0$ K

Thermocouple sensitivity = $\left(\frac{\partial T}{\partial V} \right)^{-1} = 0.0409 \text{mV/K}$

Substituting the values listed above shows that the percentage uncertainty in temperature measurement at 300 K equals 0.28 % of the measurement

A.3.1.3 Uncertainty in Pressure and Differential Pressure Measurements

The pressure transducers which were used to measure the upstream pressures in the flow lines, as well as the transducer which measured heater total pressure, were all regularly calibrated with a dead weight tester which was traceable to NIST and is linear within 0.1 %. The error due to the calibration procedure itself was less than 0.20 % for all pressure calibrations. The differential pressure calibrations were accomplished with a Mensor gage which had an accepted uncertainty of 0.04 % of the full scale range of 207 kPa (30 psid). The total uncertainty in the pressure measurements, w_p, can be calculated by the following equation:

$$w_P = \left[\left(\frac{\partial P}{\partial V} w_{ds} \right)^2 + (w_{cal})^2 + (w_{ps})^2 + (w_t)^2 \right]^{1/2} \qquad (A\text{-}6)$$

Where w_{cal} = calibration uncertainty
w_{ps} = uncertainty in the pressure standard
w_t = transducer uncertainty
wp = the total uncertainty in the pressure measurement.

The components of the uncertainty as well as the total uncertainty for each of the pressure measurements are shown in Table A.3.

Table A.3 Uncertainties in the Pressure Measurements.

Pressure	Data range mV	w_{ds} mV	Sensitivity kPa/mV	w_t kPa	w_{cal} kPa	w_{ps} kPa	w_p kPa
Air P	16	0.006	344.9	17.9	8.27	4.14	20.0
Air ΔP	16	0.006	2.52	0.121	0.069	0.083	0.165
H_2 P	16	0.006	347.7	17.9	8.27	4.14	20.0
H_2 ΔP	32	0.012	3.15	0.241	0.138	0.083	0.290
O2 P	16	0.006	347.7	17.9	8.27	4.14	20.0
O2 ΔP	32	0.012	3.43	0.241	0.138	0.083	0.290
H_2 Fuel P	16	0.006	461.7	24.1	8.27	4.14	25.5
H2 Fuel ΔP	16	0.006	3.81	0.834	0.138	0.083	0.200
PTotal	16	0.006	230.2	8.62	5.52	2.76	11.0

A.3.1.4 Total Mass Flow Uncertainty

The total uncertainty in the mass flow measurements was calculated by equation A-4 using the component uncertainties developed in the sections above. The uncertainty for the facility mass flows (also shown) at the set condition of T_T = 1944 K (3500 R), P_T = 2.79 MPa, (405 psi), oxygen fraction = 20.95 % are presented in Table A.4.

Table A.4 Percentage Uncertainties of Facility Mass Flows.

Gas	Mass Flow (kg/s)	% Uncertainty
Air	2.75	2.4
O_2	1.0	3.2
Heater H_2	0.082	4.4
Model H_2	(ϕ dependent)	5.3

Note that the uncertainty in the determination of the mass flows is dominated by the first two terms in equation A-4. In fact, the contribution to the uncertainty of the other terms is negligible compared to the first two terms for the two hydrogen flow rates. Much of this uncertainty could be removed by an in-situ calibration of the orifices. However, this was not attempted due to the large mass flow rates. Another alternative, which would improve the mass flow measurement uncertainty, is a choked venturi. An additional advantage of a choked venturi is that it eliminates the requirement of differential pressure transducer.

A.3.2 Uncertainty of the Vitiated Heater Total Temperature.

No direct measurement was made of the total temperature of the vitiated air exiting the heater. Instead, the total temperature was calculated from measurements of the heater total pressure, the area of the facility nozzle, and the mass rates of hydrogen, oxygen, and air to the heater. Initially, two different total temperatures are calculated; one based on the adiabatic flame temperature of the hydrogen/oxygen/air mixture in the heater, and the total temperature based on the total mass flow in the heater, the throat area of the facility nozzle, and the total pressure in the heater. A lengthy iteration procedure, which is discussed in detail in reference 120, was used account for the effects of heat loss to the heater walls to obtain the total temperature. This iteration procedure was coded into the data acquisition software and the total temperatures was calculated for each data cycle.

The total temperature uncertainty was calculated from the following equation:

$$w_T = \left[\left(\frac{\partial T}{\partial A} \right)^2 w_A^2 + \left(\frac{\partial T}{\partial P} \right)^2 w_P^2 + \left(\frac{\partial T}{\partial \dot{m}_{O_2}} \right)^2 w_{\dot{m}_{O_2}}^2 + \left(\frac{\partial T}{\partial \dot{m}_{H_2}} \right)^2 w_{\dot{m}_{H_2}}^2 + \left(\frac{\partial T}{\partial \dot{m}_{air}} \right)^2 w_{\dot{m}_{air}}^2 \right]^{1/2} \qquad \text{(A-7)}$$

As discussed above, an iteration procedure was used to calculate the total temperature from the measured variables. The partial derivatives in equation A-7 were each calculated from the computer code which was used to calculate the total temperature. First, ideal values of the mass flows, throat area, and total pressure which produce the correct oxygen content and total temperature were selected. Then, while maintaining four of the independent variables constant at the 'ideal' values, the other independent variable was adjusted to determine the effect of that variable on the total temperature. Figure A.1 shows the curves developed by this procedure. The ordinate is the calculated total temperature corresponding to the fraction of the ideal value of the variable (shown on the abscissa) which is being adjusted. The partial derivatives were calculated from the slopes of the curves which were close to linear for each of the curves over the range of variation of the independent variables.

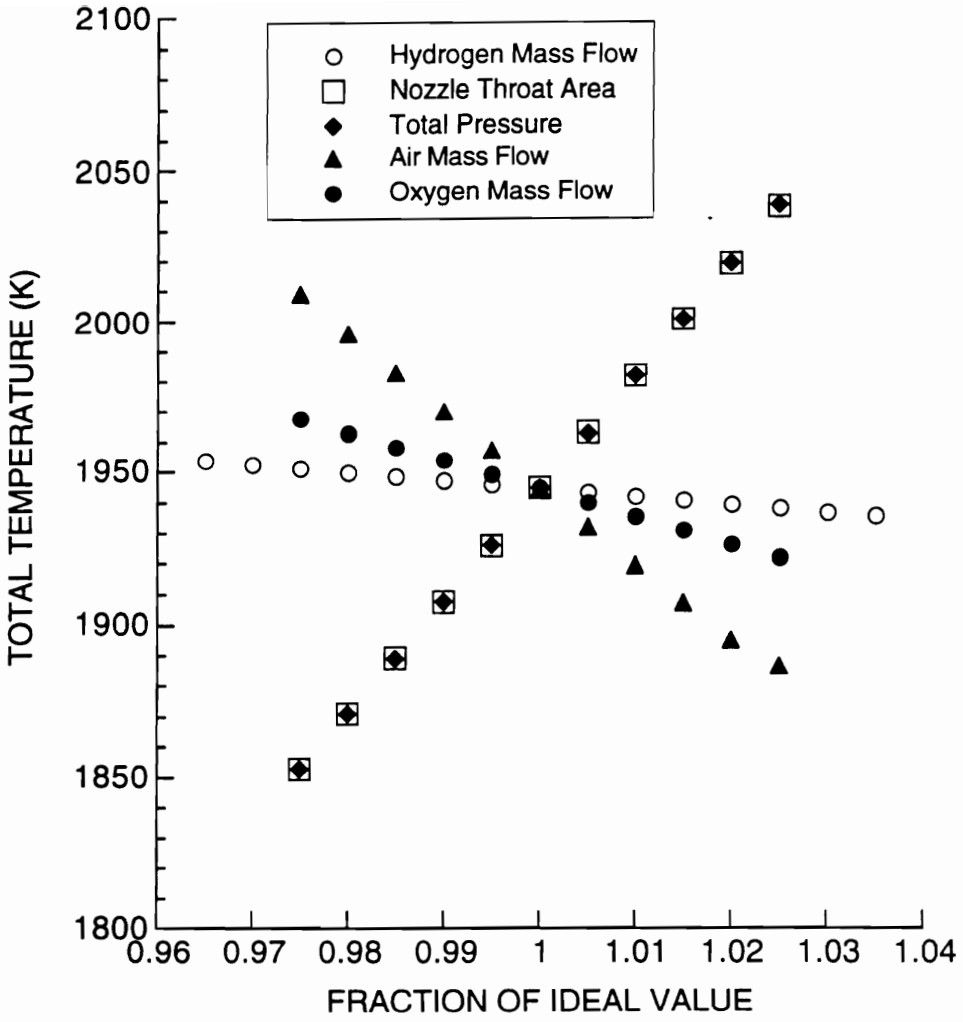

Figure A.1 The Effect of the Variation of the Independent Variables on the Calculated Facility Total Temperature.

The partial derivatives of temperature with respect to the independent variables are given along with the uncertainty of the individual variables in Table A.5.

Table A.5 The Uncertainty Components for the Total Temperature

Independent Variable	Partial Derivative	Uncertainty of Variable	Component of Uncertainty (K)
Throat Area	2.26 K/mm^2	11.6 mm^2	26
Pressure	1.31 K/kPa	11.0 kPa	14
H_2 Flow rate	3200 K/kg/s	0.00036 kg/s	12
O_2 Flow rate	916 K/kg/s	0.032 kg/s	29
Air Flow rate	915 K/kg/s	0.066 kg/s	60

The component uncertainties were summed as in equation A-7, and the uncertainty in the calculated total temperature was determined to be ±74 K at the heater total temperature of 1944 K.

A.3.3 Oxygen Volume Fraction

The chemical balance for the heater mass flows is shown in the following equation:

$$y(0.2095O_2 + 0.7905N_2) + xH_2 + zO_2 \rightarrow 0.7905yN_2 + xH_2O + (0.2095y + z - 0.5x)O_2 \quad \text{(A-8)}$$

Where : y = Air flow rate (ideal rate = 0.0950 kg-mol/s)
x = H_2 flow rate (ideal rate = 0.0407 kg-mol/s)
z = O_2 flow rate (ideal rate = 0.0312 kg-mol/s)

The heater was designed to obtain complete combustion of the hydrogen. The hydrogen in the heater is injected from multiple injectors in the presence of pure oxygen. Also, the heater is operated fuel lean; for this investigation ϕ = 0.398 in the heater. Therefore, combustion is considered to be complete in the heater. With this assumption, the volume fraction of oxygen in the vitiate gases is a function only of the three mass flows into the heater, and is expressed by the following equation:

$$\%O_2 = \frac{(0.2095y + z - 0.5x)}{(0.5x + y + z)} \quad \text{(A-9)}$$

The uncertainty in the volume fraction of oxygen can be calculated by equation A-10.

$$w_{\%O_2} = \frac{1}{(0.5x+y+z)^2}\left[\begin{array}{l}(0.6048y+z)^2 w_x^2 + (0.6048x - \\ 0.7905z)^2 w_y^2 + (x+0.7905y)^2 w_z^2\end{array}\right]^{1/2} \quad \text{(A-10)}$$

The individual uncertainties (w_x, w_y, and w_z) used in equation A-10 were calculated from the percent uncertainty of the mass flows which were calculated earlier. At the ideal operating point of the heater, assuming complete combustion of the hydrogen, the uncertainty of the calculated value of the volume fraction of oxygen is ±0.0092. Therefore, the percent oxygen at the ideal operating point of the heater is 20.95±0.92 %.

A.3.4 Fuel/Air Equivalence Ratio

The fuel/air equivalence ratio for the combustor model is defined by the following equation: $$\phi = \frac{FA}{FA_{stoic}} = \frac{1}{FA_{stoic}}\frac{\dot{m}_{H_2}}{\dot{m}_{O_2}} \quad \text{(A-11)}$$

which is expressed in terms of molar flow rates to the heater and the model in the following equation: $$\phi = \frac{v}{(0.419y+2z-x)} \quad \text{(A-12)}$$

Where: v = Combustor H_2 flow rate (moles/s)

x,y,z = Vitiated heater H_2, air, and O_2 flow rates (moles/s)

The uncertainty in the equivalence ratio can then be calculated from the following equation:

$$w_\phi = \frac{\left[(0.419y+2z-x)^2 w_v^2 + v^2\left(w_x^2 + 0.1756w_y^2 + 4w_z^2\right)\right]^{1/2}}{(0.419y+2z-x)^2} \quad \text{(A-13)}$$

The percentage uncertainty of ϕ from equation A-13 is 7.0 % at all values of ϕ.

A.3.5 Summary of the Facility Measurement Uncertainty

The results of the uncertainty analysis of the facility parameters is summarized in Table A.6.

Table A.6 Summary of the Facility Measurements

Measurement	Ideal Value	Uncertainty	% Uncertainty
Total Temperature	1944 K	± 74 K	± 3.8 %
Total Pressure	2.79 MPa	± 0.011 MPa	± 0.395 %
Oxygen Fraction	0.2095	±0.0093	±4.4 %
ϕ	0.5	±0.035	7.0 %
ϕ	0.75	±0.053	7.0 %
ϕ	1.0	±0.070	7.0 %
ϕ	1.25	±0.088	7.0 %

A.4 Uncertainty of Combustor Wall Measurements

A.4.1 Uncertainty of Combustor Wall Pressure Measurements

Combustor wall pressures were measured with an Electronically Scanned Pressure (ESP system 780-B) measurement system built by Pressure Science Incorporated. The range of pressures measured along the combustor walls was accommodated by using modules with two full scale differential pressure measurement ranges: 310 kPa, and 517 kPa. The static error ban, w_{se}, of the modules is ± 0.1 % of full scale. The ESP modules were auto-calibrated at the start of each series of test runs and the uncertainty of the pressure measurement due to calibration and quantatization errors in the A/D, w_{qc}, is 0.2 % of full scale.

Pressure taps in the model walls were connected to the ESP measurement modules in the test cell by approximately 1.3 m of Tygon tubing. The temperature variation in the test cell was typically up to ± 15 K during a series of tests. This temperature change causes a change in the sensitivity, and the zero shift of the modules. This effect could be removed by recalibrating between tests. However, the time required to recalibrate was too long to be practical and the uncertainty due to temperature change was

tolerated. The uncertainty in the sensitivity and the zero shift were each 0.036 % of the full scale pressure per degree K. Therefore, the components of the overall pressure measurement uncertainty due to thermal sensitivity and thermal zero shift (w_{ts} and w_{zs}) were each 0.54 % of full scale.

The total uncertainty of the pressure measurement is calculated in equation A-14:

$$w_p = \left(w_{ts}^2 + w_{zs}^2 + w_{se}^2 + w_{qc}^2\right)^{1/2} \qquad \text{(A-14)}$$

The uncertainty of pressure calculated form equation A-14 is ±0.80 % of the full scale pressure. Therefore, the uncertainty is ± 2.5 kPa (±0.36 psi) for the 310 kPa pressure range and ± 4.1 kPa (±0.60 psi) for the 517 kPa pressure range.

A.4.2 Uncertainty of the Wall Temperature Measurements

Wall temperature measurements were made with standard type K thermocouples. Assuming that the thermocouple is at the surface, the uncertainty is the combination of the quantatization error of the data system and the calibration uncertainty of the thermocouple.

The standard calibration uncertainty for type K thermocouples is 0.75 % of the temperature, and the quantatization uncertainty for type K thermocouples on the 64 mV scale was ± 0.64 K. Therefore the total uncertainty of the wall temperature is expressed as :

$$\omega_T = \left[\pm 0.75 + \frac{0.64}{T}\right]\%$$

A.5 Uncertainty of the Pitot Pressure Measurements

The uncertainty in the measured pitot pressure profiles comes from two sources: the uncertainty in pressure measurement and the uncertainty in the position measurement. Both the pressure and position signal were measured using a 12 bit A/D card. The uncertainty components of the pitot pressure are listed below:

Uncertainty of pressure standard = ± 0.45 kPa

Non-linearity = 0.00061x689.47 Pa = ±0.42 kPa

Hysteresis = 0.00046 x 689.47 Pa = ±0.32 kPa

Data quantatization = ± 1.4 kPa

Thermal zero shift = ± 7.1 kPa

Thermal sensitivity shift = ± 5.0 kPa

Summing the components above gives an uncertainty of ± 8.8 kPa in the pitot pressure measurement which is ±0.3 % of the vitiated heater total pressure with the heater fully on.

The uncertainty components for the probe position are listed below:

Uncertainty of initial position = ± 1mm

Uncertainty due to data quantatization = ± 0.248 mm

Power supply drift = ± 1.3 mm

The resultant total uncertainty for the position measurement was ± 1.6 mm or ±0.02 gap lengths.

Appendix B

Conversion of Surface Temperature History to Heat Flux

Most of the previous research which used the conversion of surface temperature to heat transfer has been associated with short run time facilities (shock tubes) and used assumptions of constant thermal properties, and a semi-infinite solid. With these assumptions, the methods of Vidal[121] or Cook and Felderman[122] can be used to determine the heat flux. Kidd[123] shows that the time which a wall of thickness, l, and conductivity, k, can be considered semi-infinite can be determined from the following relationship: $t < \left(\frac{l^2}{3.2k}\right)$. Therefore for the 1/2 inch thick walls used in the combustor, the wall can be considered semi-infinite for 13 and 4 seconds for the stainless steel and carbon steel walls, respectively. For the case of longer run times the semi-infinite assumption is not valid. Therefore other methods must be employed to extract the heat flux from the surface temperature.

Kidd[123] used a finite-difference method which does not assume semi-infinite walls to determine the wall heat transfer from surface thermocouple measurements. A similar approach was used for this study. The development and validation of this code for a case with temperature-dependent thermal properties will be presented in the sections below.

B.1 Code Development

The non-linear, heat conduction problem with temperature-dependent thermal properties is shown in equation B-1.

$$\frac{\partial}{\partial x}\left(k\frac{\partial T}{\partial x}\right) = \rho C \frac{\partial T}{\partial t} \qquad \text{(B-1)}$$

Over a large temperature range, the density, specific heat, and the thermal conductivity are functions of temperature, which make equation B-1 nonlinear. The one-dimensional heat conduction equation was rewritten in

the following form which neglects the variation of thermal conductivity with x, but allows k, C, and ρ to vary with temperature.

$$k\frac{\partial^2 T}{\partial x^2} = \rho C\ \frac{\partial T}{\partial t} \qquad \text{(B-2)}$$

Equation B-2 was then written in the common implicit finite-difference form which is shown in equation B-3 and corresponds to the grid representation shown in Fig. B.1

$$K_{i-1}T_{i-1}^{n+1} + (K_{i-1} + K_{i+1})T_i^{n+1} + K_{i+1}T_{i+1}^{n+1} = \frac{(\rho C)_i \Delta x^2}{\Delta t}\left(T_i^{n+1} - T_i^n\right) \qquad \text{(B-3)}$$

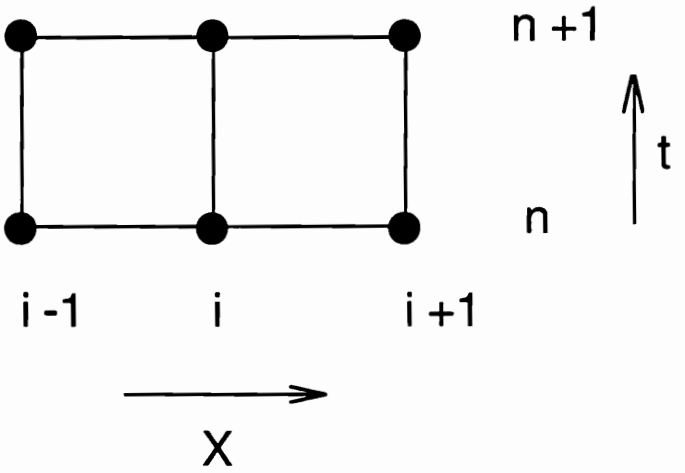

Figure B.1 Computational Grid for Finite-Difference Code

In equation B-3 the superscript is used to denote increments of time and the subscripts are used to denote spatial increments. For simplicity constant Δx and Δt were used for the finite difference grid. The thermal properties were curve-fitted to account for variation with temperature. The terms $K_{i\pm1}$ represent an effective conductivity between node i and the adjacent nodes. As suggested by Patankar[124] the thermal resistance was used to determine the effective thermal conductivity between two nodes. Therefore, the terms $K_{i\pm1}$ can be determined by equation B-4:

$$K_{i\pm1} = \frac{2k_i k_{i\pm1}}{k_i + k_{i\pm1}} \qquad \text{(B-4)}$$

Considering equation B-3 again, the thermal conductivity terms are multiplied by the temperatures at time n+1, while the density and the specific heat are multiplied by the temperature at both times n and n+1. Therefore, the effective thermal conductivity was evaluated at the temperatures at time n+1 and the product of density and specific heat is evaluated at times n and n+1 and then averaged. In equation B-3 the thermal properties used in the calculation of the temperatures at time n+1 are dependent on the temperature at time n+1. Therefore, equation B-3 was solved using the properties at time n first. Then the estimate of temperature at time n+1 was used to update the thermal properties and allow a second determination the temperature at time n+1. This process was repeated four more times at each time step. Experience obtained while developing the code has shown that, by the last iteration, the calculated temperatures at time n+1 are the same as that calculated in the preceding iteration.

The boundary conditions used for the code were a specified internal wall temperature (from the surface thermocouple measurement) and an insulated outer wall. The outer wall was not actually insulated in this study, but, for the materials and run times used in this study, the amount of heat transfer from the outer wall during the test was insignificant.

The result of solving equation B-3 is the determination of the temperature distribution across the wall as a function of time. To properly determine the heat transfer, the entire temperature history up to the test point of interest was required. After obtaining the temperature distribution, the heat transfer can be calculated from equation (B-5):

$$q = \frac{K_0}{\Delta x}(T_0^{n+1} - T_1^{n+1}) + \frac{\rho C \Delta x}{2}\frac{\left(T_0^{n+1} - T_0^{n}\right)}{\Delta t} \qquad \text{(B-5)}$$

where T_0 is the measured internal wall temperature. The first term in the equation B-5 is due to the temperature gradient in the metal and the second term is due to thermal capacity of the wall material. As the grid spacing decreases the second term decreases compared to the first term. For the grid

spacing used during this study the contribution of the second term was less than one percent of the total wall heat transfer.

Several equally spaced grids were tried and a spacing of 50 nodes over the 12.7 mm wall was selected. With this spacing the determination of the heat flux was rapid. Typically less than one-half second on the Convex C-2 vector computer at NASA was required per thermocouple for a ten second test.

B.2 Code Validation

After creating the finite difference code it was necessary to determine how well it models the heat flux. An analytical solution of the non-linear problem of heat transfer with temperature-dependent thermal properties was used to validate the finite difference code. First the analytical closed-form solution was used to determine the surface temperature history caused by a known heat flux. Then this surface temperature history was used as the input temperature history to the finite difference heat conduction code. The calculated heat flux was then compared to the known heat flux which was used as an input to the analytical solution.

The equation for the one-dimensional heat conduction problem with temperature-dependent thermal properties was shown in equation B-1. If k, ρ, or C vary as a function of temperature then equation B-1 is non-linear. The Kirchhoff transformation[125] was used to linearize equation B-1 for the variation of the conductivity with temperature. The Kirchhoff transformation is shown in equation B-6.

$$U = \int_{T_o}^{T} \frac{k(\eta)}{k_o} d\eta \qquad \text{(B-6)}$$

Further details of the Kirchhoff Transformation can be found in reference 126.

A test case for the validation was designed with the properties of the Kirchhoff transformation in mind. The problem was that of one-dimensional conduction with one side adiabatic and a constant flux (4.54 MW/m^2) to the other side. A hypothetical material with thermal properties which varied linearly with temperature as shown in equations B-7 to B-9 was used to allow

variation of the thermal conductivity and specific heat while maintaining constant α.

$$k = k_0 (1 + \beta T) \qquad \text{(B-7)}$$

$$C = C_0 (1 + \beta T) \qquad \text{(B-8)}$$

$$\rho = \text{constant} \qquad \text{(B-9)}$$

The coefficients k_0, C_0, and ρ in equation B-7 and B-8 were chosen to represent the properties of stainless steel at room temperature. The only thing that is artificial about the 'material' used for the validation is that the same linear dependence with temperature was used for both the conductivity and specific heat. In general the variation with temperature of the conductivity and specific heat are not the same.

After applying the Kirchoff transformation to the boundary conditions they become:

$$k_0 \frac{\partial U}{\partial x} = q_0 \qquad \text{at } x = l \qquad \text{(B-10)}$$

$$k_0 \frac{\partial U}{\partial x} = 0 \qquad \text{at } x = 0 \qquad \text{(B-11)}$$

where q_0 is the specified heat flux.

The solution for the heated surface temperature is given in equations B-12 and B-13:

$$U = \frac{q_0}{k_0}\left[\frac{\alpha t}{L} + L\left(\frac{1}{3} - \frac{2}{\pi^2}\sum_{n=1}^{\infty}\left(\frac{1}{n^2} e^{-\alpha n^2 \pi^2 t / L^2}\right)\right)\right] \qquad \text{(B-12)}$$

$$U = (T - T_o) + \frac{\beta}{2}(T^2 - T_o^2) \qquad \text{(B-13)}$$

The wall temperature calculated from the analytical solution is shown in Fig. B.2. This temperature trace was sampled at 20 Hz and 5 Hz and was used as the boundary condition for the finite difference code. The numerically calculated heat fluxes are also plotted in Fig. B.2. After an initial 12 % overshoot, the calculated values of the heat flux quickly settled to the known input flux. The heat flux calculated from the 20 Hz temperature trace settles faster than that calculated from the 5 Hz data trace. However, even at the 5 Hz data rate, which was the experimental data rate, the finite difference code adequately models the problem of transient conduction with temperature-dependent thermal properties, if the heat flux is relatively steady with time.

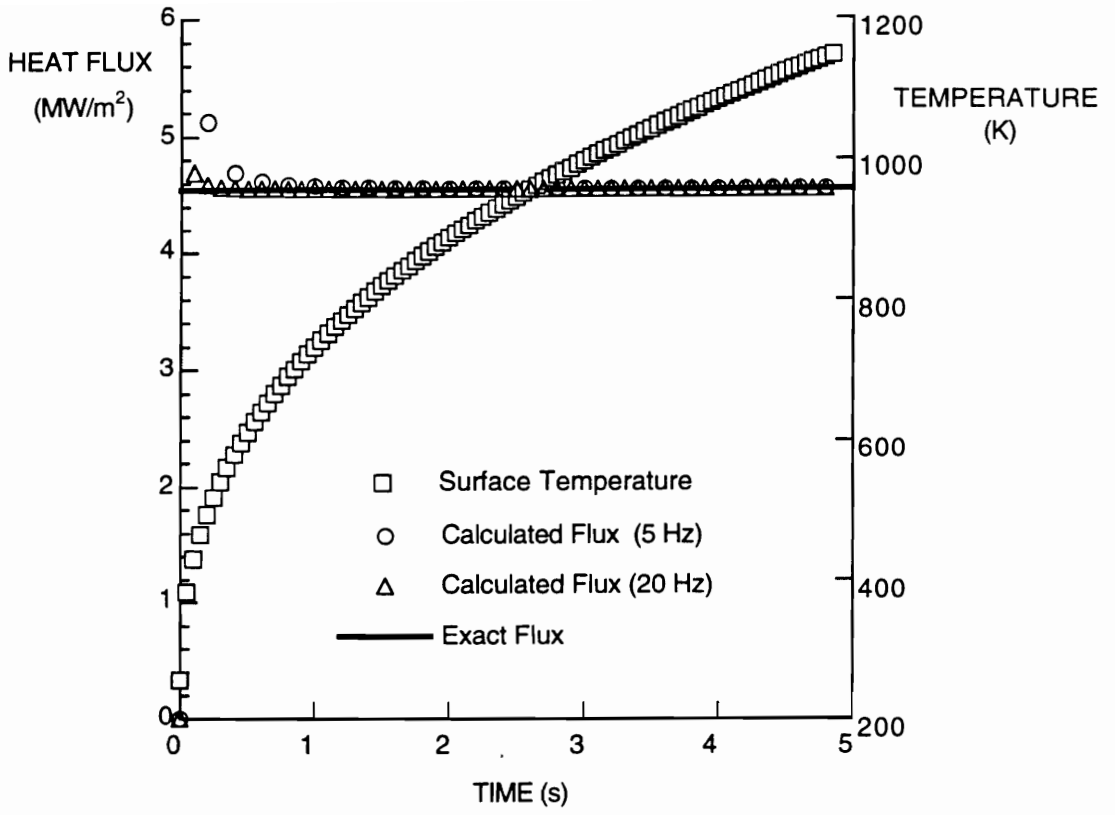

Figure B.2 Validation of the Finite-Difference Code.

B.3 Conversion of Wall Temperature From the Heat Flux

A modified version of the code was used to calculate the wall temperature corresponding to a known surface heat flux. The modified code used a known heat flux history flux as the boundary condition at the internal wall surface instead of the fixed temperature boundary condition.

B.4 Uncertainty Sources in the Hot Wall Heat Flux

The results of the test case presented above show that the heat flux can be accurately predicted at times greater than four data cycles after the start of a large transient. If the region near a transient is avoided, the errors due to the code are negligible. The major term in the heat flux calculation

(equation B-5) is $q = \frac{K_0}{\Delta x}(T_0^{n+1} - T_1^{n+1})$ thus, the only sources of uncertainty are the temperature measurement and thermal conductivity. The thermal properties for the steel were found from handbooks and had an uncertainty of ± 5%.

The uncertainty of the temperature measurement was determined in Appendix A, and had a total uncertainty of $T = \left[\pm 0.75 + \frac{0.64}{T}\right]\%$. The first term of the temperature is the bias uncertainty of the thermocouple caused by calibration. The effect of the bias uncertainty is a constant shift of the temperature vs. time curve. In other words the temperature is within a ± 0.75 % band. Thus the bias term of temperature measurement causes a small error in the thermal properties. However, the uncertainty in the thermal properties is much larger than this term, so that it can be neglected in comparison. The second term in the temperature uncertainty is due to the quantatization uncertainty which is random, and oscillates between positive and negative values. Furthermore, the magnitude of this term decreased as the temperature difference between the surface and the first node increased.

An examination of the temperature difference of the surface temperature and the first node for several of the tests showed that the magnitude of the temperature difference was about 20 K, at four data cycles after the fuel on transient. Thus the uncertainty of the heat flux due to the temperature uncertainty was ≈(0.64/20) or ± 3 % of the heat flux.

The total uncertainty of the hot wall heat flux is the RMS sum of the uncertainty due to the conductivity and the temperatures and is ± 5.8 % of the heat flux.

Appendix C

Uncertainty Analysis and Installation Effects in the Use of Gardon Heat Flux Gages

The uncertainty in the direct heat flux measurements performed during this study is due to several sources. The first source is the uncertainty in the calibration of the sensor itself. The second source is due to quantatization errors in the data acquisition system. The third source is a nonlinearity effect which occurs at high gage temperatures due to the departure of the gage from idealized behavior. The fourth source is due to wall temperature mismatch effects. Each of the effects will be discussed in the sections below.

C.1 Gage Calibration

Direct calibrations of Gardon gages in a convective flow have been performed by Borrel and Diller[127] at flux levels which were three orders of magnitude less than those encountered during this study. The calibration method used at higher fluxes is not a direct calibration with a known convective heat flux since there are presently no national standards for convection heat transfer. Instead a radiation calibration was performed by the manufacturer. The heat flux gages were calibrated by comparing the output of the gages with the output of a secondary standard when exposed to the same radiant heat source.[128] The secondary standard was calibrated using a dual blackbody cavity method[129] and was found to have an uncertainty of ± 3 % of the reading.

The standard deviation of the heat flux for the no fuel cases, normalized by the average heat flux at each gage location was examined to access the gage repeatability and drift. The tunnel conditions for the tests are tabulated in Appendix E. The facility total temperature and pressure are ideally the same for each test. If the gages are repeatable with little drift in the sensitivity, the wall heat flux should be the same for the same tunnel conditions. Differences between the tunnel conditions are due to the

uncertainty of the measured facility conditions and the difference between the indicated and the target tunnel conditions.

The normalized standard deviation of the no fuel heat flux was less than 4 % for all gages, and less than 2.5 % for most of the gages. Table E.3 in Appendix E shows that the standard deviation of the measured total temperature, and pressure for the heater were 2.6%, and 0.9%, respectively, of the average values. For the expansion ramp combustor, the normalized standard deviation of the heat flux with no fuel was less than 3% for all gages.

Considering the uncertainty of the indicated pressure and temperature (Appendix A) as well as the deviation of the measured tunnel conditions from the target conditions, the standard deviation of the gages is acceptable. In other words, the gages are as repeatable as the facility. In addition, no trend in the flux with no fuel vs. time was observed, indicating that there was little drift in the gage calibration.

C.2 Data Quantatization Uncertainty

The average sensitivity of the gages, was 0.57 $MW/m^2/mV$. The heat fluxes were measured using the 16 mV full scale range of the amplifiers which had an uncertainty of ± 0.0064 mV. Therefore, the uncertainty in the heat flux measurement due to the A/D system was only ± 0.0037 MW/m^2. Thus, the error due to quantatization is negligible for most of the measurements.

C.3 Non-Idealized Gage Behavior

In Chapter Three (section 3.3.1) the following form was derived for the sensitivity of the gage at low (Te <470 K) gage temperatures:

$$S = \frac{\Delta EMF}{q} = A'\left[\frac{1+\beta(T_c+T_e)}{1+\gamma(T_c+T_e)}\right] \qquad \text{(C-1)}$$

where A', β, and γ are constants, and $\beta \approx \gamma$. Thus, at low temperatures the sensitivity is temperature-independent. However, the derivation leading to this equation neglects two effects; conduction by the center wire, and the third order terms of the thermoelectric potential.

Clayton[130] proposed the following form of correction to account for center-wire conduction:

$$CF = 1/(1+Ck_w/K) \qquad \text{(C-2)}$$

where C is a constant, and k_W/k is the ratio of the wire to the foil conductivity. Including the center wire correction term and the third-order term in the thermoelectric potential, the expression for the gage sensitivity can be expressed as:

$$S = \frac{\Delta EMF}{q} = \left[\frac{a_1(T_c - T_e) + a_2(T_c^2 - T_e^2) + a_3(T_c^3 - T_e^3)}{Ak_o(1+0.5\alpha(Tc+Te))(T_c - T_e)}\right]\left[\frac{1}{1+C\frac{k_w}{k}}\right] \qquad \text{(C-3)}$$

To investigate the effects of center wire conduction and the third order thermoelectric potential term, the sensitivity calculated by equation C-3 was plotted vs. foil edge temperature in Fig. C.1. The center-wire conduction constant was set to 0.025 as suggested by Clayton[130]. The set of curves plotted in Fig. C.1 were plotted for the theoretical maximum temperature difference between the center and edge (260 K) as well as 1/2 and 1/4 of this temperature difference.

Figure C.1 shows that the sensitivity is a function of both the foil temperature gradient (or flux) and the foil edge temperature. At low temperatures (T <420 K), the gage sensitivity is within 2 % of the sensitivity at the 300 K edge temperature. As the edge temperature increases, the sensitivity decreases. The sensitivity decreases most rapidly with edge temperature for the high heat flux case. This is expected because the higher heat flux leads to higher temperatures at the center of the foil which causes a larger contribution from the third order term in the thermoelectric potential, in addition to an increase due to the center-wire effect (see equation C-3).

It should be noted that a change of the sensitivity with the edge temperature was not expected at the start of this research. The only other known report of this effect is the investigation by Clayton[130]. Other researchers have apparently neglected this effect.

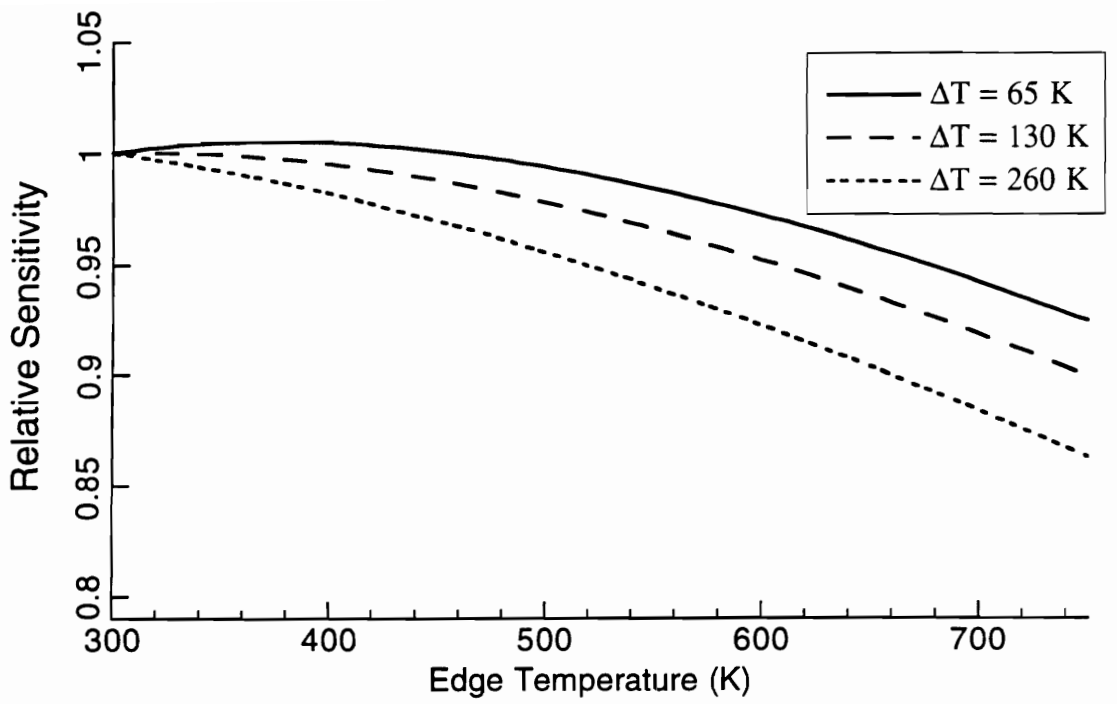

Figure C.1 Sensitivity of Gardon Gage as a Function of the Foil Edge Temperature and the Difference Between the Foil Edge and Foil Center (Sensitivity at 300 K = 1).

A correction factor can be calculated if the temperature at the edge of the foil is measured in addition to the indicated flux. The measured heat flux from the gage is calculated by :

$$q_{meas} = \frac{\Delta EMF}{S(T_e = 300K)} \quad \text{(C-4)}$$

While the actual heat flux can be expressed as:

$$q = \frac{\Delta EMF}{S(T_e)} \quad \text{(C-5)}$$

Thus, while the actual sensitivity depends on the edge temperature, the assumed sensitivity is that with an ambient edge temperature. A correction to the indicated flux is formed by dividing equation (C-5) by (C-4):

$$q = \frac{(S(T_e = 300K))}{(S(T_e))} q_{meas} \quad \text{(C-6)}$$

where the numerator and denominator of (C-6) are calculated from equation (C-3).

Half of the heat flux gages used in this study had an auxiliary thermocouple on the edge of the foil. For these gages, the sensitivity correction factor, calculated from equation (C-6), was determined for each gage for all of the test points in this investigation. The foil edge temperatures and the sensitivity correction factor are plotted vs. the measured heat flux. In general, the edge temperature increases as the heat flux increases. The scatter in the temperature vs. flux curve is largely due to the fact that the results for 14 different gages, each with different cooling effectiveness because of different cooling line lengths (thus different pressure drops, and flow rates) are shown. Note that up to 16 gages (including other instrumentation) were attached to the same cooling water manifolds which were at common line pressure. Although no measurements of the cooling water flow rates through the gages were attempted, variations were expected.

The effect of the edge temperature variation on the sensitivity correction factor is also shown in Fig. C.2. At measured heat fluxes below 3 MW/m^2, the sensitivity is within 2% of the assumed sensitivity. As the heat flux increases the sensitivity factor increases to an observed maximum of +12 %. Therefore, at the highest edge temperature the actual measured flux could be up to +12 % higher than the measured flux. Note that the scatter in the correction factor also increased with the measured flux.

Half of the gages which were used did not include auxiliary thermocouples. The only differences between the two types of gages (other than the absence of the auxiliary thermocouple) is the foil diameter, which is half the size for the gages with no auxiliary thermocouples. Therefore, the relationship of the edge temperature to the applied flux is expected to be the same for both types of gages, so that the sensitivity correction factor for the gages without an auxiliary thermocouple would be close to the band of factors shown in Fig. C.2 at the same flux levels.

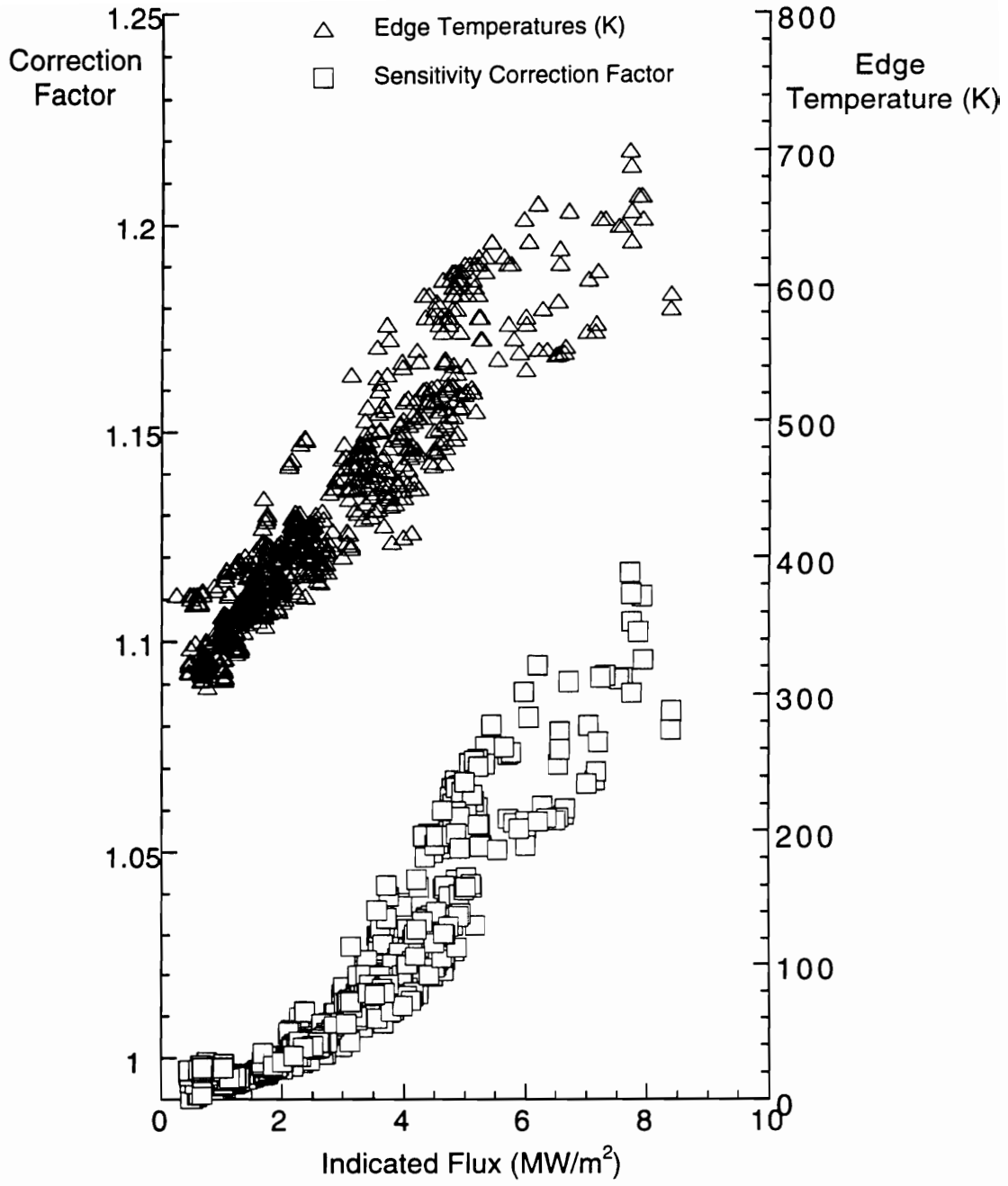

Figure C.2 Gardon Gage Edge Temperature and Sensitivity Correction Factor vs. Heat Flux.

A piecewise curve fit of the correction factor in Fig. C.3 gives the following expression for the uncertainty due to temperature sensitivity of the gage:

Flux Range	Correction Factor
0-3 MW/m^2	$[-0.93+0.45q]\% \pm 1\%$
3-8 MW/m^2	$[-4.4+1.8q]\% \pm 2\%$

where q is the measured heat flux in MW/m^2.

Since only half of the gages had an edge temperature measurement, a method was needed to correct the sensitivity of the gages with no thermocouples. It was assumed that the relationship between the sensitivity correction factor established above could be used for all of the gages (including those without thermocouples) if the possible random error was increased by a factor of two. Therefore, the effects of gage sensitivity change with temperature were split into a bias correction term and a random uncertainty term as shown below:

Flux Range	Bias Correction	Random Uncertainty
0-3 MW/m^2	$[-0.93+0.45q]\%$	$\pm 2\%$
3-8 MW/m^2	$[-4.4+1.8q]\%$	$\pm 4\%$

Therefore, all of the gages were corrected for the bias part of the sensitivity factor listed above, and were assumed to have a random uncertainty equal to that listed.

C.4 Temperature Mismatch Effects

C.4.1 Background

A cooled Gardon gage installed in a hot wall creates a disturbance in the wall temperature profile as shown in Fig. C.3. The temperature drops in a step between the hot wall and the cooled copper gage body. Note that in the gages used for this research the gage body diameter was 4-8 times the sensing foil diameter. The temperature rises parabolically between the edge of the foil and the center of the foil. Depending on the magnitudes of the heat flux and the temperature mismatch between the uncooled wall and the edge of the gage foil, the temperature at the center of the foil can be higher or lower than the uncooled wall temperature upstream of the gage.

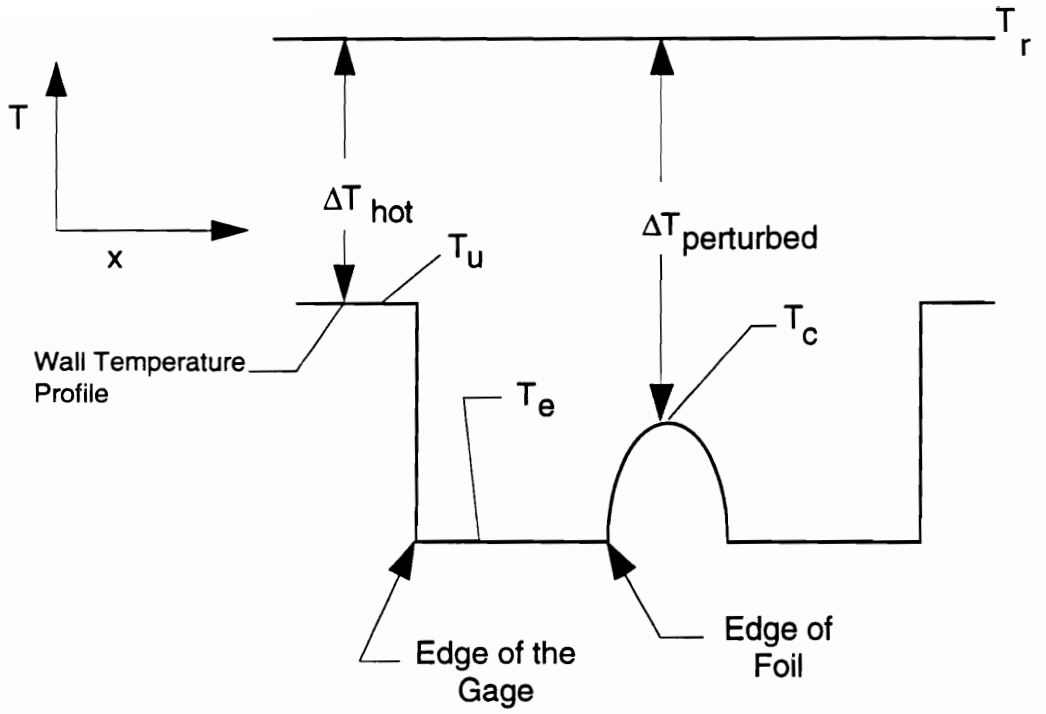

Figure C.3 Wall Temperature Disturbance Due to Installation of a Cooled Gardon Gage in an Uncooled Wall.

It is expected that the heat flux measured by a cooled gage in an uncooled wall is higher than the heat flux to the uncooled wall upstream of it. Recall that the convective heat transfer to a wall can be expressed as:

$$q = h(T_r - T_w) \qquad \text{(C-7)}$$

where h is the film coefficient, Tr is the recovery temperature, and Tw is the wall temperature. Thus, the temperature discontinuity along the wall affects the heat transfer in two ways. First, an obvious increase in the heat flux occurs due to the increase in the difference between the recovery and wall temperatures. Second, it is expected that the film coefficient will change due to the temperature discontinuity.

The temperature-mismatch problem has been studied in the past. Many of the studies have focused on the problem of the change in the film coefficient caused by a single step change in the wall temperature profile.

Rubesin[131] studied the problem of heat transfer to a wall with a step change temperature. The flow conditions considered were an incompressible, constant property, flat plate boundary layer, with a 1/7 power velocity boundary layer. Rubesin used a linear superposition of solutions to model the step change in temperature. Although the magnitude of one of the terms in his corrections was later proved to be erroneous[132], Rubesin showed that the film coefficient at the center of a non-isothermal wall plug differed from that for an isothermal wall. In particular, he showed that the film coefficient increased when a step change in temperature increased the temperature difference between the wall and the fluid. Conversely, when the step change in wall temperature decreased the temperature difference between the fluid and the wall, the film coefficient dropped.

Conti[133] experimentally studied the problem of heat transfer from a Mach 2 boundary layer to a wall with a stepwise temperature change. He found that a superposition of solutions could be used to model the change in heat transfer which was due to the change in the film coefficient with the wall temperature distribution.

Simultaneous measurements of skin friction and heat flux were conducted by Paik[137] in a Mach 2 boundary layer flow. The gage was actively heated to study the effect of temperature mismatch. Large changes in both the Stanton number and skin friction coefficient were observed as the temperature mismatch between the gage and the wall increased.

Woodruff et al.[134] presented an analysis of the change in the film coefficient caused by the temperature profile along an uncooled wall with a Gardon gage installed in it. The temperature profile along the wall is similar to the one shown in Fig. C.3. The authors considered the effect of the temperature disturbance for both laminar and turbulent flat plate boundary layers. The correction for the film coefficient was of the form:

$$\frac{h}{h_{iso}} = 1 + H_1\left[\frac{T_u - T_e}{T_r - T_c}\right] + H_2\left[\frac{T_c - T_e}{T_r - T_c}\right] \qquad \text{(C-8)}$$

where: h is the average film coefficient at the gage surface
h_{iso} is the film coefficient for an isothermal wall
T_r is the recovery temperature
T_u is the undisturbed wall temperature
T_e and T_c are the edge and center temperatures of the foil

In equation C-8, the second term is a correction due to the drop of temperature between the wall and the gage, and the third term is due to the increase in the foil temperature from the edge to the center of the foil. The factors H_1 and H_2 are functions of the radius of the foil and the distance of the foil from the start of the boundary layer. The term H_1 is always positive and the term H_2 is always negative. For the case of heat transfer from a hot fluid to a cold gage the terms in parenthesis are positive. Therefore, the effect of the drop in temperature at the gage surface is to increase the film coefficient while the increase of the foil temperature from the edge to the center decreases the film coefficient as previously shown by Rubesin.[131]

Researchers have used correction factors such as equation C-8 to correct their data for gage-wall temperature mismatch effects in simple well-characterized flows.[135] However, one must view such correction procedures with caution since the development of such relations require that assumptions (boundary layer on a flat plate) must be made about the flow over the gage and the wall. The major limitation in the application of corrections factors such as that in equation C-8 is described by Neuman et al.[136] in a review of past instrumentation of hypersonic vehicles:

"*Thus, the project engineers were forced to try to analytically correct for the resulting non-isothermal wall modification to the heat flux. To do this, they used the aeroheating model that they were attempting to verify with their measurements.*"

Therefore, unless the flow field is known *a priori* the effects of the temperature mismatch on the film coefficient cannot be calculated.

C.4.2 Observed Temperature Mismatch Effects

Since the flowfield in a scramjet combustor is not simple, correction factors for the film coefficient were not calculated. Instead, temperature mismatch effects were examined by two methods. First, by directly comparing the hot and cold wall heat fluxes at axial locations where there were both functioning surface thermocouples and cooled heat flux gages in symmetrical locations about the centerline of the combustor. This is possible in the second half of the combustor where the carbon-steel eroding thermocouples functioned as desired. The second method was to examine the change in the flux measured by the gage as the temperature mismatch between the cooled gage surface (measured by the auxiliary thermocouple) and the hot wall increased. In the first half of the combustor, which was machined out of stainless steel, the surface thermocouples failed. Therefore, an estimate was made of the hot wall temperature by using the measured cold wall heat flux as an input to a finite difference code (see Appendix B) and calculating the wall temperature. Since the cold wall heat flux was higher than the hot wall flux, this estimate of the hot wall temperature was higher than the actual wall temperature.

Figure C.4 shows a comparison of the cold wall heat flux (measured by a Gardon gage) and the hot wall heat flux (calculated from the wall temperature history) during a typical run with the swept compression ramps. The measurements were at x/G = 8.43, which is in the second half of the combustor where the wall material is carbon steel. The heat flux gage and the thermocouple were mounted at the same axial location, and were in line with the two center fuel jets which are symmetric about the centerline of the combustor. The temperatures of the hot wall and the edge of the foil are also shown along with the equivalence ratio.

As expected, the tunnel wall was hotter than the cooled heat flux sensor edge through the entire test. Before the fuel was turned on, the hot wall heat flux was lower than the cold wall heat flux. During the fuel-on transient, the hot wall flux was initially slightly higher than the cold wall flux. Recall from the discussion of the program in Appendix B that the calculated hot wall flux overshoots the actual heat flux for the first few data

cycles near a transient. As the wall temperature increased, the hot wall heat flux decreased by about 20 % during the fuel-on portion of the test. If the test time were longer the wall temperature would continually increase, further lowering the heat flux. The edge temperature of the cooled heat flux gage also increased during the test but at a much slower rate than the combustor wall. Thus, the temperature mismatch between the edge of the gage and the combustor wall increased with time. The calculated adiabatic wall temperature at this location was 2150 K, resulting in a temperature mismatch at the start of the fuel on period of about $\Delta T/T_{aw}$ =7% and $\Delta T/T_{aw}$ = 15 % at end of the test. At the same time the temperature of the edge increased slightly so that ΔT decreased by 2 %. However, in contrast to the hot wall heat flux, the cold wall heat flux was relatively steady during the fuel on period, increasing rather than decreasing by less than 5% during the test. It is thought that the change in the cold wall flux was mainly due to an increase in the film coefficient.

In the first half of the combustor, which was constructed of stainless steel, the temperature mismatch is more severe because of the higher heat fluxes and the lower thermal conductivity of the walls. Therefore, there is a larger difference between the measured cold wall heat flux and the hot wall heat flux.

Figure C.5 shows the measured cold wall heat flux and edge temperature for a gage installed in the stainless steel wall at x/G = 4. The hot wall temperature, which was calculated by using the measured cold wall heat flux as the input to the finite difference code, is also shown. Since the cold-wall flux is used, the calculated hot wall temperature is an over-estimate. However, the temperature trace is illustrative of the high combustor temperatures which are reached in the combustor and lead to severe temperature mismatch between the gage edge and the hot wall. Note that the measured cold wall heat flux changed little as the temperature mismatch between the gage and the wall increased.

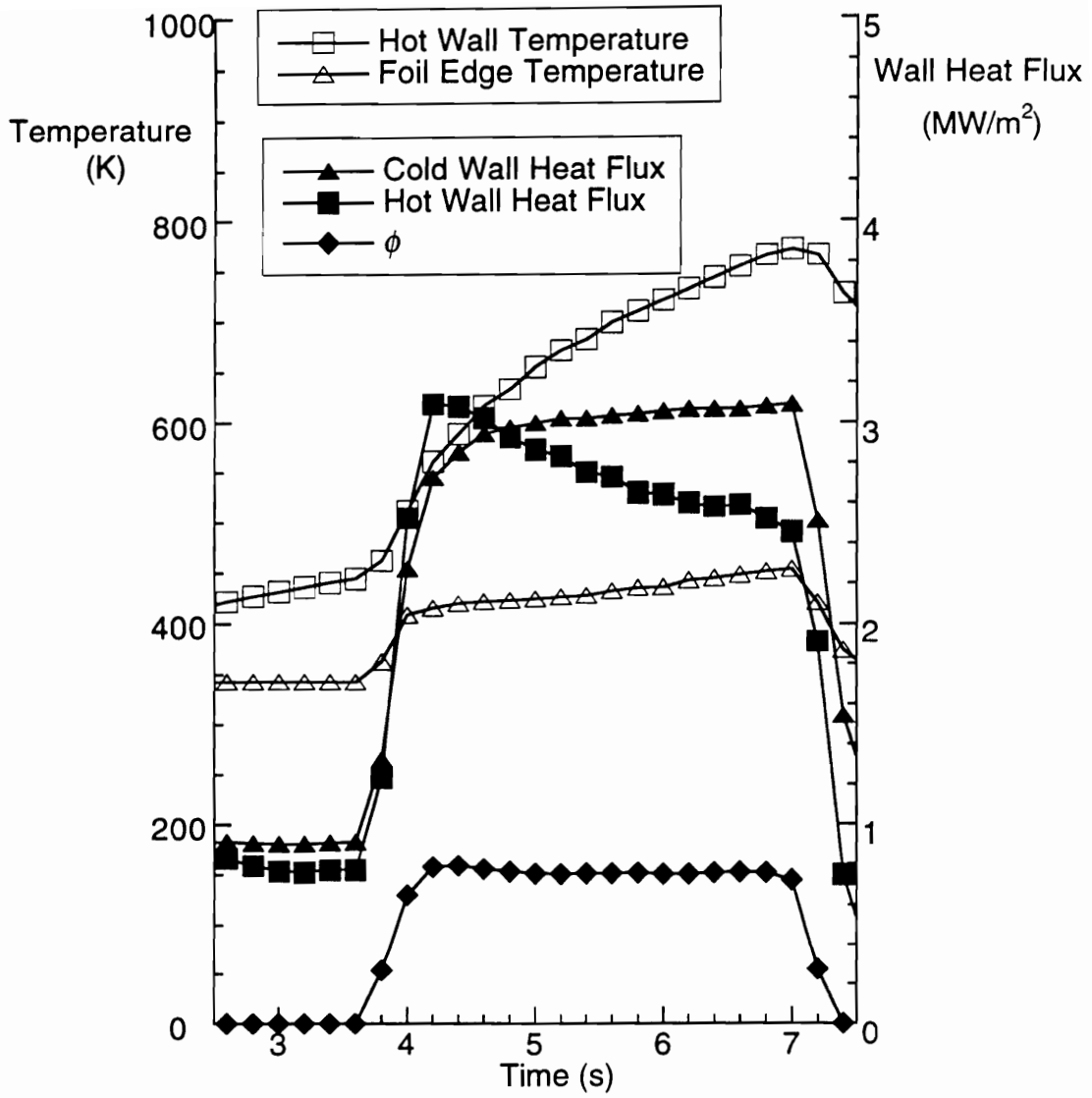

Figure C.4 Comparison of Hot Wall and Cold Wall Heat Fluxes and Temperatures During a Typical Test (Swept-Compression Ramp, $\phi = 0.74$, x/G = 8.43, Injector Centerline, $T_{aw} = 2150$ K).

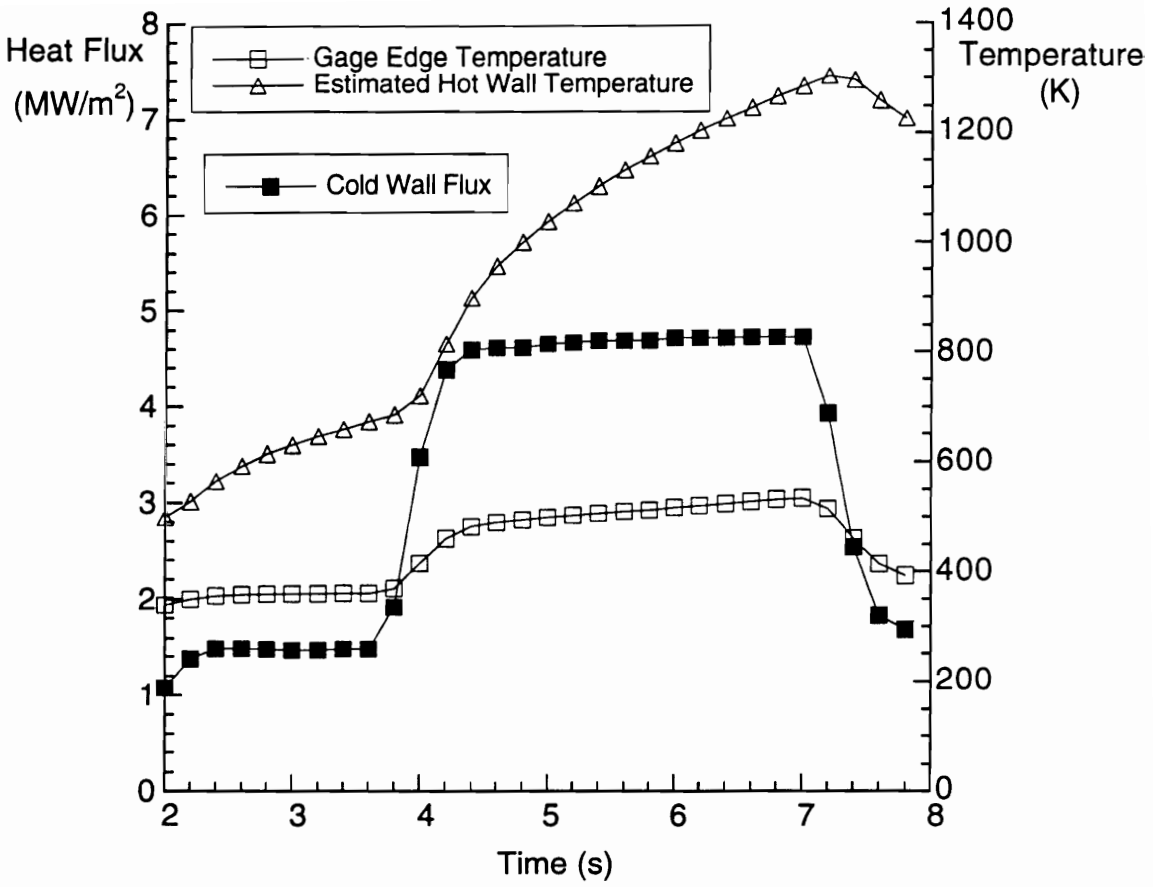

Figure C.5 Comparison of the Calculated Hot Wall Temperature and the Gage Temperature in the Stainless Steel Portion of the Combustor (Swept-Compression Ramp, $\phi = 0.74$, x/G = 4, Interstice Centerline, $T_{aw} = 2750$ K).

Figure C.6 shows the cold wall fluxes for the same test at several axial locations along the combustor. The change in the measured heat flux is less than ± 5% for each of the gages while the fuel is on. Further examination of the all of the measured cold wall heat fluxes for each of the tests also showed that the measured cold wall heat flux changed less than ± 5% during the fuel-on period. The output of some of the gages decreased while the output of others increased with time during the fuel on period.

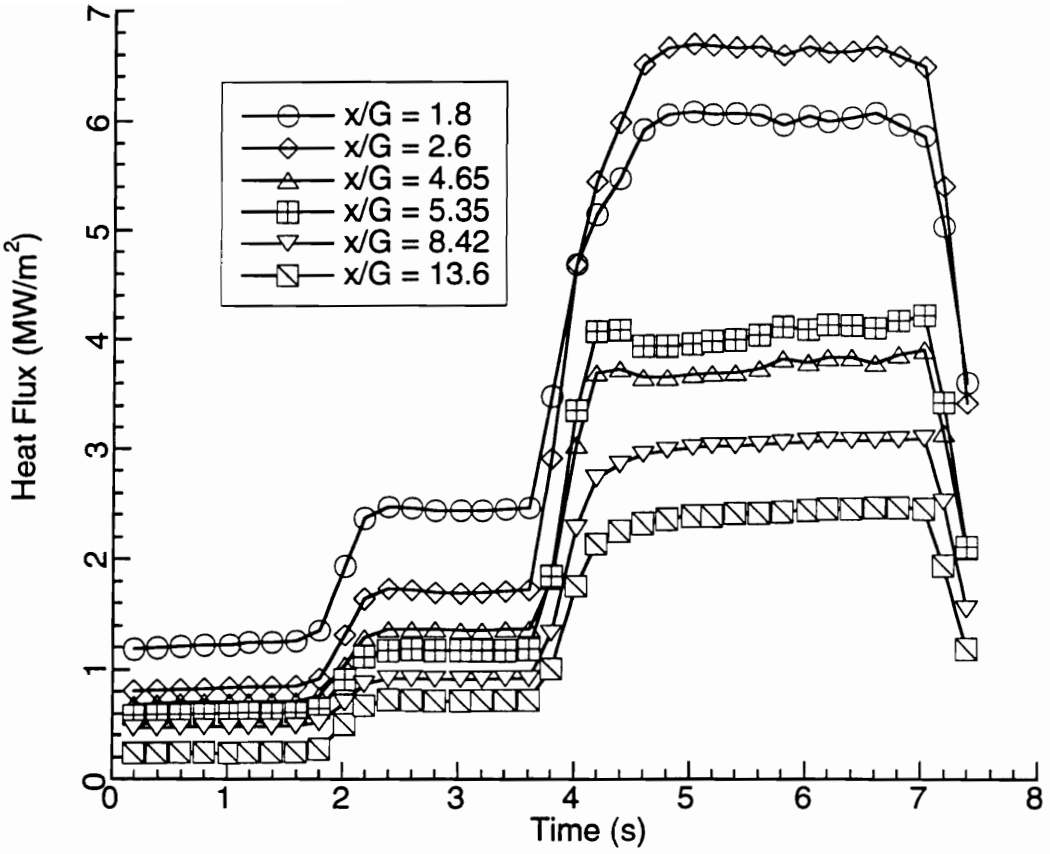

Figure C.6 Cold Wall Fluxes at Several Axial Locations in the Combustor Wall (Swept-Compression Ramp, ϕ = 0.74).

In summary, the difference between the measured cold wall heat flux and the hot wall heat flux is large, and continually increases as a result of the continuously increasing temperature difference between the gage and wall during a test. Differences of up to 25 % have been observed between the hot and cold wall heat fluxes in the carbon steel portion of the combustor. For the stainless steel section of the combustor, the difference is expected to be larger. However, the examination of the cold wall heat fluxes showed that little change occurred in the cold wall heat flux during the fuel on period, even though the magnitude of the temperature drop between the hot wall the gage increased appreciably. Therefore, the uncertainty in the cold wall heat flux uncertainty associated with the selection of the data cycle (and thus temperature mismatch) during a test at which data was extracted was less

than ± 5%. Note that for many of the tests the change of the heat flux was less than 5 % during the fuel on period, so that ± 5 % is the maximum observed difference during tests.

C.5 Summary of Heat Transfer Measurement Uncertainty

The uncertainty of the hot wall heat flux, which is the heat flux to the uncooled wall, discussed in Appendix B, was less than ± 5.8 %.

The cold wall flux, is the heat flux to a cooled gage which has a surface temperature of 300-700 K. The cold wall heat flux uncertainties were discussed above and are summarized below:

Calibration uncertainty = ± 3 %
Data quantatization = ± 0.0035 MW/m^2
Temperature mismatch effects < ± 5 %
Gage sensitivity correction:

Flux Range	Correction Factor
0-3 MW/m^2	± 2 %
3-8 MW/m^2	± 4 %

The summation of the uncertainty terms by the method discussed in Appendix A gives an uncertainty of ± 6.6 % for fluxes less than 3 MW/m^2, and ± 7.1 % for fluxes larger than 3 MW/m^2.

In the heat flux results presented in Chapter 4 both hot wall and cold wall heat fluxes are plotted.

Appendix D

Pitot Probe Stress and Heat Transfer Analysis

A brief summary of the design calculations for the pitot pressure probe is presented in the sections below:

D.1 Stress Analysis

The assumed conditions at the exit of the combustor were: P=83 kPa, M=1.8, T_T= 2700 K, and γ= 1.28.

The force per length on a cylinder in a cross-flow can be calculated as follows: $$\frac{F}{L} = C_D D\left(\frac{1}{2}\rho U^2\right) = \frac{C_D D}{2}\left(\gamma P M^2\right) \quad \text{(D-1)}$$

The drag coefficient, C_D, for a cylinder at Mach 1.8 is given in reference 138 as 1.35. Substituting the values into D-1 gives: F/L = 3.0 N/mm

A free body diagram of the probe support is shown in Fig. D.1.
where x1 = 100 mm, x2 = 126 mm, x_{max} = 183 mm. Solving this statically indeterminate problem by singularity functions gives the following for the bearing reaction forces and the moment at the center of the support:

R1 = 214 N

R2 = 42.3

M_{max}=5.0 N-m.

The maximum normal stress, σ, in the tube occurs at the center of the tube and was calculated from equation D-2.

$$\sigma = \frac{M_{max} r}{I} \quad \text{(D-2)}$$

where M_{max}, I is the moment of inertia, and r is the radius of the probe.

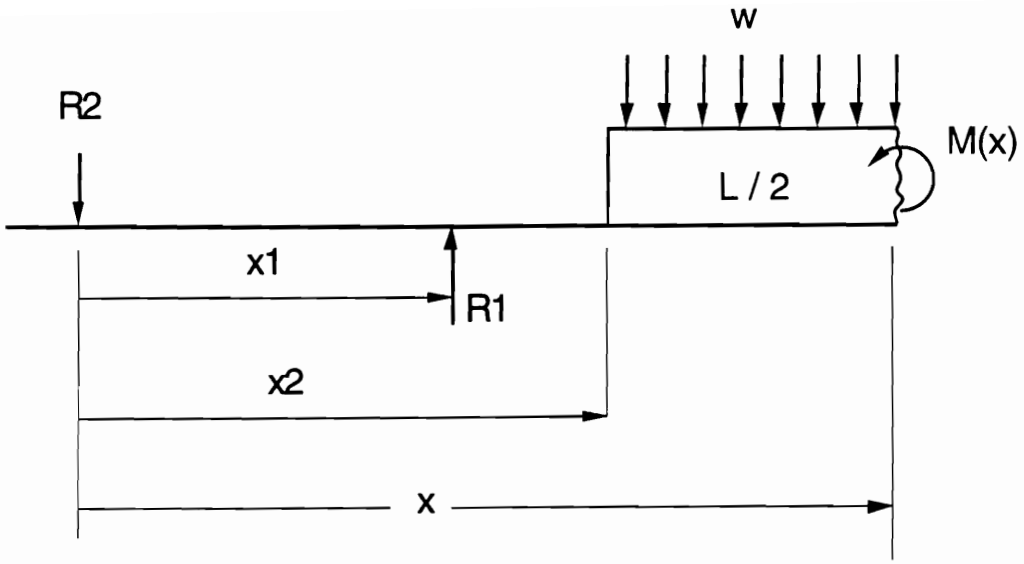

Figure D.1 The Free Body Diagram for the Probe Support

The inner and outer diameters of the tube are 10.3 mm, and 12.7 mm, respectively. The normal stress due to aerodynamic loading can be calculated by substituting the maximum moment and the moment of inertia into D.2. Thus, σ = 44 MPa, which is much less than the yield strength of stainless steel at 800 K (214 MPa).

D.2 Heat Transfer Analysis

The conservative assumption was made that the entire probe support circumference was exposed to the stagnation point heating. The problem of stagnation point heating was analyzed using the method of van Driest.[101] The heat flux to the probe was assumed to be steady-state (no transient conduction effects). Therefore, the heat flux at the inside wall was calculated by the ratio of the diameters and the heat flux to the outer wall:

$$q_{wi} = \frac{d_o}{d_i} q_{wo} \qquad \text{(D-3)}$$

The calculated stagnation point and inside wall heat fluxes for assumed outside wall temperatures are given in Table D.1.

Table D.1 The Stagnation Point and Inside Wall Heat Fluxes for the Probe Support Tube.

Temperature (K)	qwo (MW/m^2)	qwi (MW/m^2)
333	2.95	3.63
555	2.61	3.22
778	2.37	2.93

The temperature gradient across the tube wall was calculated as follows:

$$\Delta T = \frac{q_{wi}}{U_1} \qquad \text{(D-4)}$$

and:

$$U_1 = \frac{k}{r_i \ln\left(\frac{r_o}{r_i}\right)} \qquad \text{(D-5)}$$

To provide a starting point for the design the internal wall temperature was set at 420 K. The outside wall temperature and the heat flux at the internal wall corresponding to the assumed inside wall temperature were calculated by iterating between equation D-4 and the fluxes in Table D.1. The resultant outside temperature and internal wall heat flux were found to be 615 K, and 3.1 MW/m^2, respectively.

The convection at the internal wall was calculated assuming turbulent flow through an annulus and water at an assumed temperature of 305 K. The inside and outside diameters of the annulus were 7.9 mm, and 10.3 mm, respectively. The velocity of the water was set at 12 m/s. Correlations for the Nusselt number for turbulent flow through a circular annulus are given in reference 139 in the following form:

$$Nu = f\left[\mathrm{Re}, \mathrm{Pr}, \frac{D_o}{D_i}\right] \qquad \text{(D-6)}$$

For the assumed velocity and water properties the film coefficient, h, was calculated to be 0.045 MW/m^2K. Therefore, the inside wall temperature required at the internal wall was calculated from Newton's law of cooling:

$$T_{wi} = \frac{q_{wi}}{h} + T_\infty \qquad \text{(D-7)}$$

The internal wall temperature required to convect the internal wall heat flux (at an estimated internal wall temperature of 420 K) away was calculated to

be 370 K which was slightly lower than the assumed inside wall temperature. To provide an added margin of safety, it was decided to increase the water pressure at the exit of the probe support to 1.4 MPa, thus increasing the boiling point of the water to 468 K. This increases the maximum temperature difference between the wall and the fluid without boiling by a factor of over 2.5. Therefore, the estimates of stagnation point heating can be off by a factor of 2.5 without boiling the water.

The pressure drop required to maintain flow velocities of 12 m/s through the annulus and the transition piece were calculated to be 0.5 MPa. In addition to the probe, there were 4 m of flexible tubing at the inlet and exit of the probe as well as fittings, and transition pieces. The design pressure difference was set at 1.0 MPa, and the mass flow was measured in the actual design to be 0.42 kg/s, corresponding to a velocity in the annulus of 13 m/s, which is higher than the design velocity of 12 m/s, providing an additional margin of safety. The average temperature change of the water was calculated to be only 6 K assuming that the entire cylinder is exposed to the stagnation heating. Therefore the water-cooled design was considered to be adequate.

Appendix E
Test Conditions for Combustor Tests

The test conditions for the surface measurements presented in Chapter 4 are shown in Tables E.1-E.4. The data were given a run-batch-cycle designation. Each series of individual tests was assigned a run number, individual tests were assigned a batch number, and each time was a data cycle.

Table E.1 Tunnel Conditions For Expansion-Ramp Tests With No Fuel.

Run	Batch	Cycle	T_T (K)	P_T (kPa)	%O_2
25	2	13	1931.	2809.	21.54
25	4	11	1929.	2822.	20.98
25	5	11	1932.	2823.	21.33
25	6	10	1944.	2811.	21.3
25	7	11	1950.	2824.	20.95
25	8	11	1923.	2836.	20.86
25	11	11	1969.	2822.	21.06
26	2	10	1958.	2822.	20.88
26	3	10	1964.	2819.	20.66
26	4	11	1982.	2822.	21.27
26	5	11	1954.	2821.	21.65
26	6	10	1965.	2815.	20.89
26	7	11	1963.	2824.	20.7
26	9	11	1967.	2817.	21.4
26	10	10	1954.	2824.	20.44
27	3	12	1969.	2789.	20.87
27	4	11	1979.	2787.	21
27	5	11	1972.	2784.	21.21
27	6	12	1952.	2796.	20.98
27	7	13	1940.	2799.	20.77
28	2	11	1910.	2792.	20.56
28	3	11	1944.	2771.	20.77
28	4	11	1932.	2771.	21.09
28	5	11	1928.	2771.	21.19
Average			1951.	2807.	20.99
Standard Deviation			19.3	20.1	0.29

Table E.2 Tunnel Conditions for the Expansion Ramp Tests With Fuel

Run	Batch	Cycle	T_T (K)	P_T (kPa)	$\%O_2$	ϕ
25	2	30	1918	2816	21.66	0.98
25	4	34	1932	2832	21.08	1.27
25	5	34	1952	2834	21.20	1.38
25	6	28	1967	2822	21.28	0.97
25	7	33	1984	2833	21.00	0.74
25	8	34	1934	2849	20.89	0.47
25	11	34	1962	2833	21.10	0.72
26	2	30	2004	2829	21.06	0.71
26	3	30	1971	2827	21.00	0.70
26	4	31	1983	2831	21.46	0.88
26	5	30	1974	2830	21.77	1.04
26	6	31	1967	2820	21.09	1.08
26	7	28	1987	2833	20.83	1.40
26	9	31	1968	2826	21.52	1.09
26	10	31	1966	2840	20.85	1.18
27	3	30	1997	2800	21.04	0.91
27	4	31	1987	2796	21.24	0.95
27	5	30	1976	2795	21.39	1.12
27	6	29	1943	2814	21.21	1.21
27	7	29	1954	2809	21.04	0.62
28	2	31	1903	2793	20.86	0.99
28	3	31	1917	2784	21.06	1.27
28	4	31	1927	2774	21.41	1.27
28	5	30	1944	2771	21.47	0.72
Average			1959	2816	21.19	
Standard Deviation			26.9	21.3	0.26	

Table E.3 Tunnel Conditions For the Compression Ramp Tests With No Fuel

Run	Batch	Cycle	T_T (K)	P_T (kPa)	% O_2
37	2	17	1833	2748	20.00
37	3	26	1937	2781	21.60
37	4	19	1857	2737	22.00
37	5	20	1943	2762	21.10
37	6	20	1937	2757	20.05
37	7	15	1839	2753	21.95
37	8	20	1923	2751	21.20
37	9	17	1829	2731	21.60
37	10	20	1923	2762	21.30
38	2	13	1890	2731	21.51
38	3	36	1847	2727	21.66
38	4	34	1844	2720	21.16
39	2	35	1948	2727	21.16
39	5	36	1914	2721	20.95
39	6	33	1946	2718	20.65
39	7	37	1946	2713	20.82
41	4	40	1926	2745	21.51
42	4	36	1952	2785	20.38
42	3	36	1910	2769	21.10
42	5	39	1995	2791	20.02
42	7	37	1961	2785	20.02
42	9	31	1973	2777	20.05
42	11	30	1947	2787	21.60
Average			1914	2751	21.02
Standard Deviation			49.0	25.1	0.65

Table E.4 Tunnel Conditions For the Compression Ramp Tests With Fuel

Run	Batch	Cycle	T_T (K)	P_T (kPa)	$\%O_2$	ϕ
37	2	32	1953	2782	20	1.28
37	3	38	1942	2787	21.7	1.07
37	4	38	1894	2753	21.9	1.16
37	5	35	1952	2769	21.4	1.03
37	6	36	1956	2767	20.46	0.97
37	7	28	1932	2771	21.64	0.76
37	8	36	1975	2762	21.1	0.83
37	9	34	1944	2758	21.3	0.61
37	10	34	1926	2767	21.36	0.50
38	2	30	1954	2748	21.51	1.21
38	3	50	1932	2743	21.64	1.20
38	4	53	1955	2749	20.89	1.26
39	2	48	1959	2735	21.28	1.02
39	5	49	2003	2733	20.83	0.79
39	6	48	1971	2728	20.83	0.62
39	7	53	1983	2722	21.09	0.51
41	4	55	1945	2756	21.76	1.17
42	3	48	1903	2775	21.2	1.01
42	4	46	1935	2791	20.58	0.80
42	5	55	1990	2799	20.3	0.58
42	7	44	1977	2789	20.21	0.52
42	9	41	1984	2784	20.1	1.42
42	11	42	1943	2794	21.7	1.23
Average			1953	2764	21.08	
Standard Deviation			26.5	22.3	0.58	

Appendix F

A Case of Downstream Flameholding With the Swept Compression Ramp Injectors

In Chapter 4 it was stated that for all but one of the 23 test runs with the swept compression ramp injectors flameholding occurred near the injectors. For one case flameholding occurred in the expanding duct downstream of the injector ramps. The cause of downstream flameholding during this run is not understood at this time. Nor is it known whether or not downstream flameholding would ever occur again. The reason for discussing this seemingly "odd" run was the huge change in engine performance which occurred when the combustor operated in this mode.

F.1 Evidence of Downstream Flameholding

The downstream flameholding occurred during run 42 batch 3. The tunnel and fuel conditions during run were:

Total Temperature = 1903 K
Total Pressure = 2.775 MPa
Oxygen Fraction = 21.2 %
Equivalence Ratio = 1.01

Although the total temperature for this run was lower than it was for most of the runs with the swept compression ramps, the facility parameters are all within 2 standard deviations of the average values shown in Table E4.

The wall pressures and heat fluxes from this run are shown in Fig. F.1-F.3. Figure F.1 shows the combustor wall pressure distribution for the run with downstream flameholding along with that for several other tests with the same equivalence ratio. In contrast to the other runs which exhibited flameholding near the injectors, the pressure rise for "downstream flameholding" did not begin until $x/G > 1.4$. The maximum measured pressure for this run occurred at $x/G = 2.2$, far into the expanding combustor duct. In addition the pressures over the rest of the combustor are significantly higher for the case with downstream flameholding.

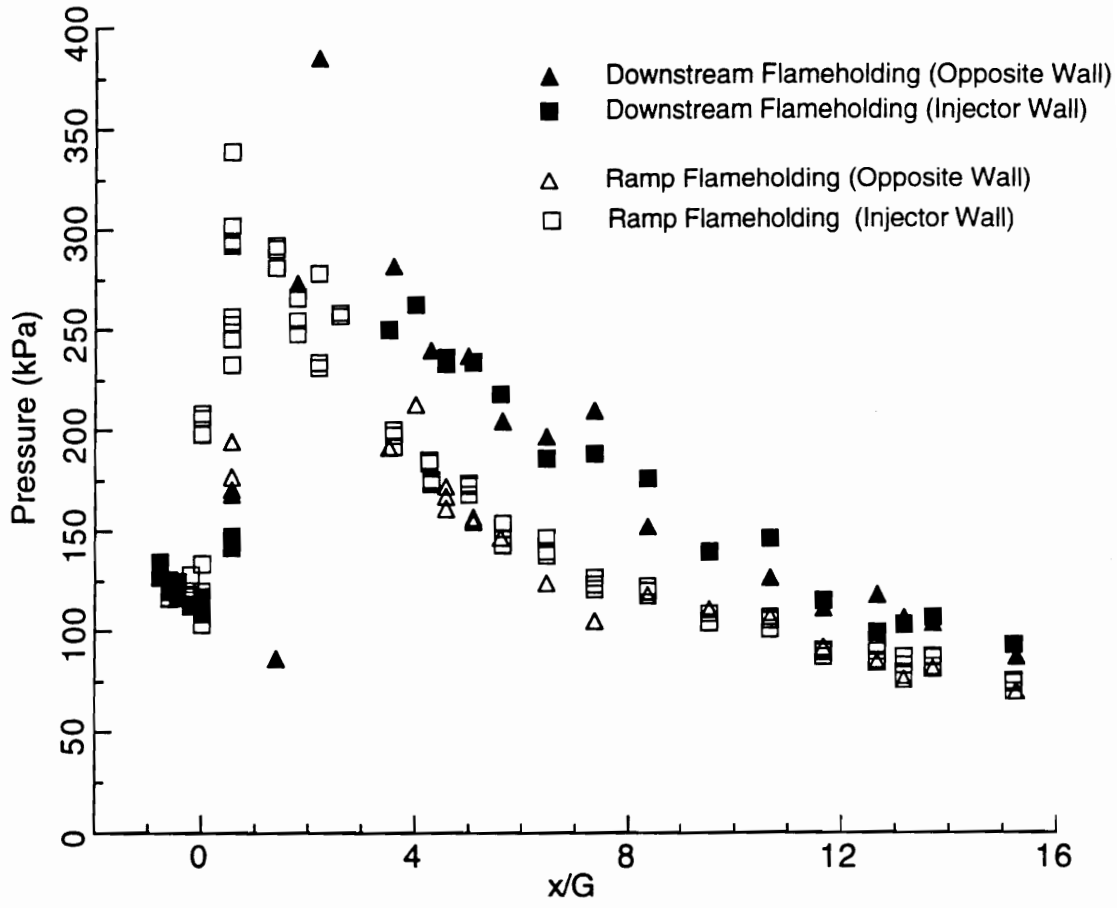

Figure F.1 Pressure Distributions for the Swept Compression Ramps With $\phi = 1$.

In addition to the pressure traces , the measured heat fluxes also show that downstream flameholding occurred during run 42 b3. The combustor ducts downstream of the injector block section were flipped (relative to the previous tests with the swept-compression ramps) for this test as well as all of the other tests during run 42 to measure the fluxes on the wall opposite of the fuel injector. Figure F.2 shows the heat fluxes on the wall opposite of the injectors for the case that exhibited downstream flameholding along with the flux distributions for the rest of the tests that were conducted with the same instrumentation layout. The other tests were conducted during the same day and had equivalence ratios of $0.6<\phi<1.4$. In the case that exhibited

downstream flameholding, the fluxes were lower than those for all of the ramp flameholding cases for x/G ≤1.8. Conversely the fluxes for x/G ≥ 2.6 were higher for the case with downstream flameholding.

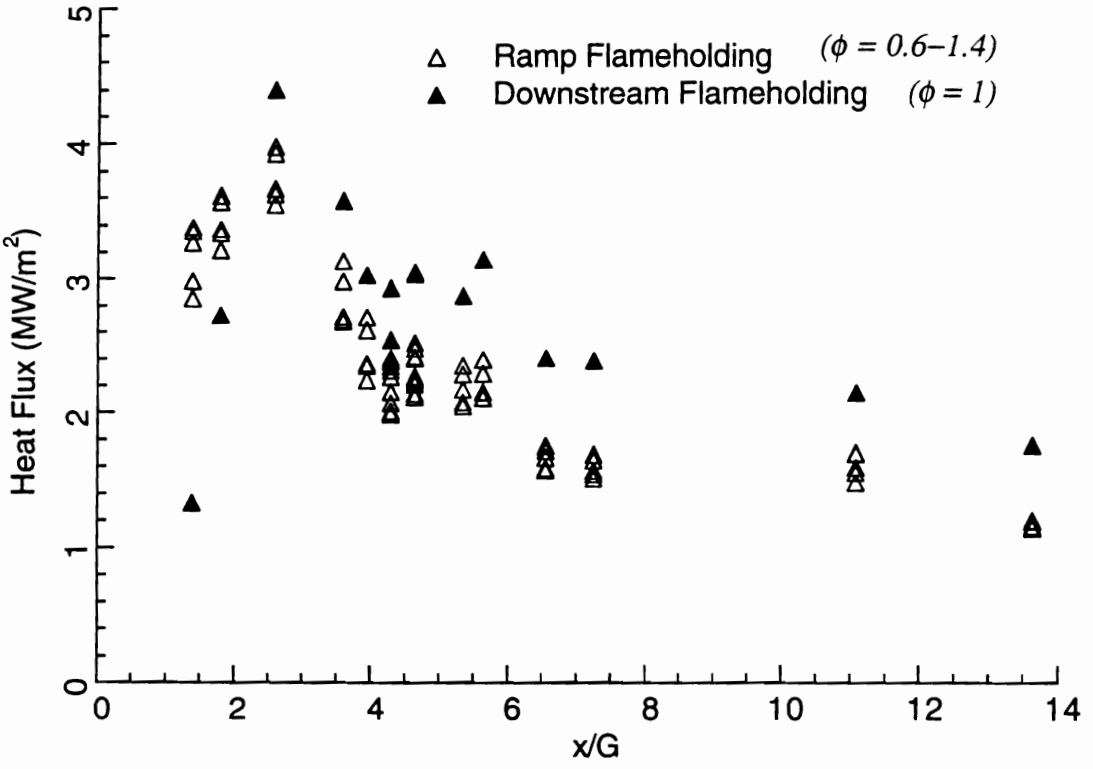

Figure F.2 Wall Heat Flux Opposite of the Fuel Injectors with Ramp Flameholding and Downstream Flameholding.

The last evidence of downstream flameholding is shown in Fig. F.3, which shows the injector wall heat fluxes at two spanwise locations at x/G= 0.23. Because the downstream ducts were flipped, these were the only two heat flux gages on the injector wall for this series of tests. In contrast to the cases with ramp flameholding, the heat flux measured directly downstream of the injectors for the downstream flameholding case decreased below that for the case of no fuel. In fact, the measured heat flux was actually negative. At the interstice (y/G = 0.27) a slight increase above the no fuel value was seen for the downstream flameholding. However, the heat flux was lower than it was for all of the other equivalence ratios at the same location. It is thought

that the slight increase in heat flux at the interstice is due to a pressure rise associated with injection rather than combustion.

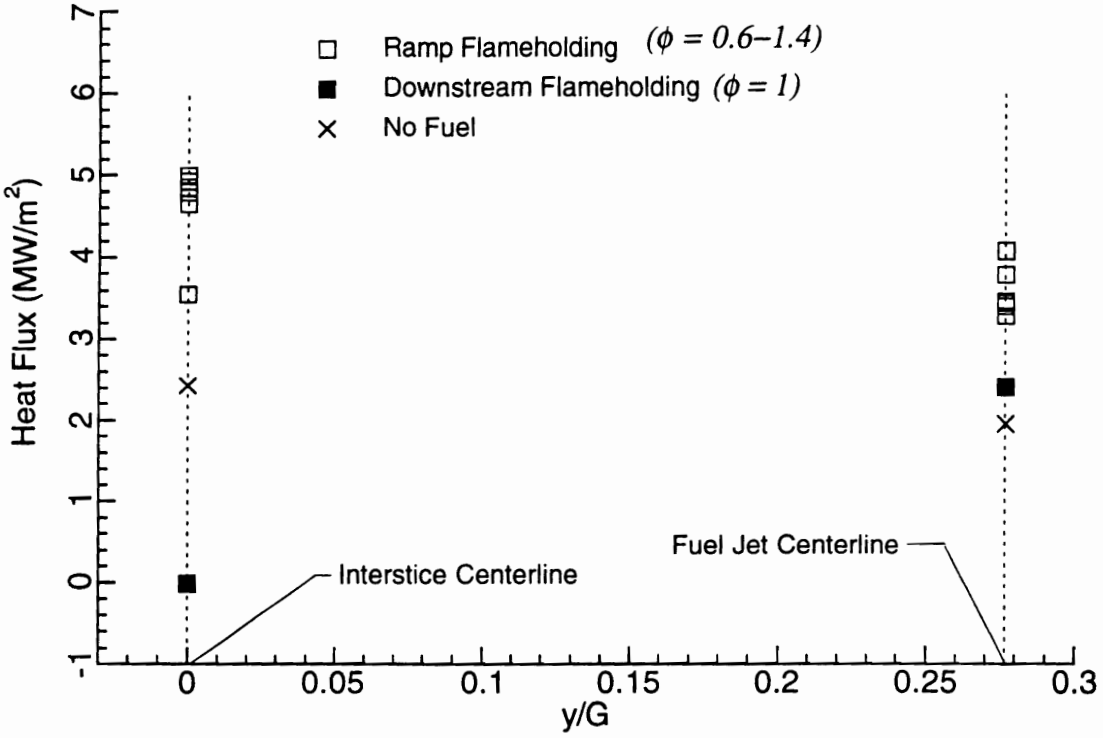

Figure F.3 Wall Heat Fluxes on the Injector Side of Combustor at x/G = 0.23 for Ramp Flameholding and Downstream Flameholding.

In summary, the pressure traces and the heat fluxes both show, that for one case, flameholding occurred downstream of the injectors rather than in the nearfield of the injectors. The large performance gain associated with this different mode of flameholding will be discussed in the next section.

F.2 Performance With Downstream Flameholding

The pressure integrals for the downstream flameholding are shown along with those with the same equivalence ratio in Table F.1. The case with downstream flameholding had a 41 % higher pressure integral than did the ramp flameholding case. Considering the large differences between the pressure traces for the two types of flameholding, the higher pressure integral is expected for downstream flameholding. Also, note that the total pressure integral for the swept-compression ramp is higher than that for the

expansion-ramp results shown in Chapter 4. Therefore, the change in flameholding location caused a huge change in the performance of the swept-compression ramps.

Table F.1 Pressure Integrals for $\phi = 1$ with Ramp Flameholding and Downstream Flame Holding. ($\Delta F = F_f - F_{nf}$).

Type of Flameholding	Combustor ΔF	Nozzle ΔF	Total ΔF
Ramp Flameholding	1030	1190	2220
Downstream Flameholding	1530	1600	3130

The combustion efficiency (calculated by the one-dimensional code) for the case with downstream flameholding was approximately 95 % in contrast to only 62 % for the ramp flameholding case.

The test results shown for this case show that the effect of delaying the onset of stable combustion by 1.5 gaps increases the performance dramatically. The results also imply that mixing is detrimentally effected by combustion near the injectors. The calculations of the flowfield in Chapter 5 showed that the mixing efficiency for the turbulent reacting case was less than that for the turbulent mixing case. The largest difference in the over all mixing efficiency occurred in the first 1.5 gap lengths. The effect of downstream flameholding on the mixing in unswept injectors has also been discussed by Riggins and McClinton.[57]

As noted earlier, it is not known whether or not downstream flameholding would occur again in 23 tests, 230 tests, or ever again with this set of injectors. However, the results from these tests imply that at least for scramjet combustors which are largely mixing-limited, that the controlling the location of ignition and flameholding can be an important strategy in controlling the mixing. Indeed the results imply that the optimum flameholding location, from the standpoint of subsequent mixing is in the farfield of the injectors.

Vita

Scott David Stouffer was born in Hagerstown, Maryland on April 17, 1963. He grew up in the nearby town of Boonsboro, and graduated from Boonsboro High School in 1981 in the bottom half of his class. After high school he attended Hagerstown Junior College, where he graduated in 1983 first in his class. In the fall of 1983 he enrolled in the Mechanical Engineering Department of VPI, and graduated with his BS degree in the fall of 1985. He enrolled in the graduate program in Mechanical Engineering at VPI in 1986. His MS thesis "The Development and Operating Characteristics of an Improved Plasma Torch Flameholder for Supersonic Combustion Applications", conducted under the direction of Dr. Walter O'Brien, was completed in 1989. After receiving his MS degree, he enrolled in the Ph.D. program in Mechanical Engineering at VPI, and completed his course work in 1990. In 1991 he moved to Hampton, to complete his dissertation research at the NASA Langley Research Center working with Burt Northam of the Reacting Flow Group. While at NASA he also participated in other projects connected with dealing with SCRAMJET mixing, combustion, performance, and heat transfer. Following graduation he will find a rewarding position in research and development at a yet to be determined company.

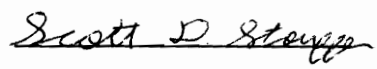

Scott David Stouffer